PhD-FSTM-2024-081
The Faculty of Science, Technology and Medicine

DISSERTATION

Defence held on 15/10/2024 in Luxembourg

to obtain the degree of

DOCTEUR DE L'UNIVERSITÉ DU LUXEMBOURG

EN PHYSIQUE

by

Kunmin Wu
Born on 22 March 1995 in HuNan of birth, (China)

DISSIPATION IN MESOSCOPIC QUANTUM SYSTEMS: QUANTUM FRICTION AND BRAIDING IN DISSIPATIVE-DRIVEN MAJORANA BOXES

Dissertation defence committee

Dr Thomas Schmidt, dissertation supervisor
Professor, Université du Luxembourg

Dr Patrik Recher
Professor, Technische Universität Braunschweig

Dr Ludger Wirtz, Chairman
Professor, Université du Luxembourg

Dr Andreas Michels
Professor, Université du Luxembourg

Dr Reinhold Egger, Vice Chairman
Professor, Universität Düsseldorf

University of Luxembourg
UNIVERSITÉ DU LUXEMBOURG
Faculty of Science, Technology and Medicine

Dissipation in mesoscopic quantum systems

Quantum friction and braiding in dissipative-driven Majorana boxes

Kunmin Wu

Supervisor: Prof. Dr. Thomas L. Schmidt

A thesis presented for the degree of
Doctor of Physics

December 19, 2024

Contents

Part I

Quantum friction between metals in the hydrodynamic regime

Chapter 1

From the Casimir effect to quantum friction

1.1 The Casimir-Polder effect

The Casimir effect, also known as the Casimir-Polder effect, provides strong evidence for the existence of quantum fluctuations. This phenomenon, which results in an attractive force between two closely spaced neutral conducting plates, highlights the physical implications of vacuum fluctuations predicted by quantum field theory. The debate between "modern" and "old" quantum physics arises from the evolution of our understanding of these fluctuations. Early quantum theories did not fully account for the complexities of vacuum fluctuations and zero-point energy. In contrast, modern quantum field theory incorporates these fluctuations as a fundamental aspect, leading to observable effects like the Casimir effect. Quantum fluctuations, including the transient creation and annihilation of virtual electron-positron pairs, are a direct consequence of the Heisenberg uncertainty principle, which underscores the probabilistic nature of quantum mechanics.

In 1948, H. B. Casimir predicted that two parallel neutral plates in a vacuum would experience an attractive force due to the presence of zero-point energy [1]. This force arises because moving one plate infinitely far away from the other would result in a change in the zero-point energy, even though the energy required to make such a move is infinite. Casimir's theoretical analysis showed that the energy difference between the two configurations is finite. For large separations between an atom and a wall, Casimir identified that the force, $\delta E_{\text{Casimir}}$, can be expressed as [2]

$$\delta E_{\text{Casimir}} = \frac{3}{8\pi}\frac{\alpha}{R^4}, \tag{1.1}$$

where α is the polarizability and R is the distance between the plates. Subsequently, Lifshitz clarified that the Casimir-Polder force and the van der Waals force represent

the long-range and short-range limits, respectively, of the same underlying interaction [3–5]. This interaction arises from the attraction between induced dipole moments due to quantum mechanical fluctuations.

The first experimental attempt to measure the Casimir effect was conducted by Marcus Sparnaay [6], but the experimental uncertainty was too large to reconcile the experimental observations with the theories. After approximately four decades, Steve Lamoreaux conducted the first direct and high-accuracy measurements of the Casimir force using a torsion pendulum [7]. The results of these measurements were consistent with theoretical predictions, deviating by no more than 5%. One year later, Ref. [8] reported another highly accurate measurement of the Casimir force between a metallized sphere with a diameter of 196 µm and a flat plate using an Atomic Force Microscope (AFM). In this static AFM setup, the sphere is rigidly attached to a cantilever and is positioned close to the plate. The resulting surface force causes a deflection in the cantilever. The root mean square deviation of 1.6 pN between theoretical predictions and experimental results corresponds to a 1% deviation at the smallest separation between the two objects. This small discrepancy confirms that the Casimir-Polder effect is now a well-established quantum phenomenon.

1.2 Quantum friction: the non-equilibrium counterpart of the static Casimir effect

The static Casimir effect describes the attractive force between two relatively stationary objects resulting from quantum field fluctuations. This effect can also be understood in terms of atom-field interactions. Near a material object, the local density of electromagnetic states is modified by the boundary conditions imposed by the object's interface, such as the presence of an evanescent wave near the interface. Polarizable entities, like atoms and molecules, interact with these altered electromagnetic fields, resulting in an attractive force between the atoms and the interface. When two objects move relative to each other, three distinct scenarios arise based on their acceleration: 1) varying acceleration, 2) constant acceleration, and 3) zero acceleration. The first two scenarios are associated with different quantum effects. Specifically, varying acceleration is linked to the dynamical Casimir effect [9, 10], while constant acceleration is related to the Fulling-Davis-deWitt-Unruh effect [9]. Both effects involve the excitation of particles (such as atoms) due to the creation of real and entangled photons as a result of their relative motion.

When an atom moves parallel to an interface at a constant velocity, as shown in Fig. 1.1, its interactions with material objects modify nearby electromagnetic fluctuations, leading to forces that both attract the particle toward the interface and decelerate its motion.

The latter specific force component is known as quantum friction [11–14] at the absolute zero, which is denoted as $\vec{F}_x$ in Fig.1.1. Relative motion is crucial for breaking time-reversal symmetry in this system, which in turn leads to the occurrence of dissipation and quantum friction. However, the theoretical description of quantum friction remains controversial and debatable [12, 15, 16]. Recent theoretical studies over the past decade [17–21] have shown that equilibrium-based or perturbative approaches may not always be appropriate for describing this phenomenon. To the best of our knowledge, there has yet to be a clear and definitive experimental confirmation of the quantum frictional force, although numerous proposals and experiments [22–24] have been conducted on the topic.

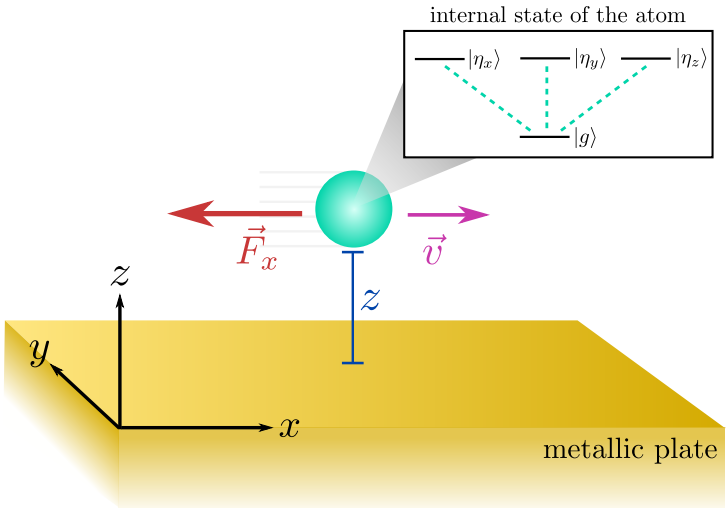

Figure 1.1: **The quantum friction system.** The system comprises an atom moving parallel to the interface between a metallic plate and a vacuum. The atom is regarded as a two-level system, and quantum friction should oppose the motion of the moving atom.

However, developing a comprehensive theoretical framework for quantum friction is an important goal for researchers. This effect is universal and becomes particularly significant in nanoscale systems, such as when a probing tip scans the surface of a material. Understanding quantum friction can provide new insights into how quantum fields interact with matter. Additionally, the principles of quantum friction have potential applications in emerging technologies like nanotechnology. As we develop smaller and more precise devices, understanding quantum friction is crucial for designing effective systems. In some cases, the dissipation caused by quantum friction can even be beneficial.

Understanding quantum friction, both theoretically and experimentally, is essential

for advancing our knowledge in this field. As a result, many theoretical studies have focused on this topic in recent years. Various theoretical methods have been explored to investigate quantum friction. However, because the system is in a non-equilibrium state, conventional methods that address typical fluctuation problems are not applicable. Theoretical approaches used to study quantum friction encompass functional methods based on time-dependent perturbation theory [25], path integrals [26], macroscopic quantum electrodynamics [27] and generalized fluctuation theorems [21,28]. Additionally, several other methods have been proposed to observe this frictional force. For example, researchers have explored the interplay between quantum friction and decoherence [29,30] and its impact on the Berry phase [24] as an indirect way to find evidence of the phenomenon, even if the force itself is not directly measured.

This study focuses on the interaction between an atom moving at a constant velocity parallel to and above the interface and the field, as depicted in Fig. 1.1. The moving atom is modeled as a two-level system consisting of one ground state and three degenerate excited states, as described in the inset of Fig. 1.1. Due to the boundary conditions at the interface between the metallic plate and the vacuum, quantum fluctuations cause the electric field to behave like an evanescent wave near the interface. This leads to questions about how the interaction between an atom's electric dipole moment and the fluctuating electromagnetic field is affected, especially since the presence of the material modifies this field. This work employs time-dependent perturbation theory to find the answer.

The time-dependent perturbation theory [31, 32] allows for the examination of non-equilibrium dynamics, which is particularly important for studying dissipative processes that break time-reversal symmetry, such as quantum friction. These processes typically involve the transfer of energy and momentum in non-equilibrium states, and time-dependent perturbation theory accurately captures these interactions. In the case of quantum friction, the interaction between a moving atom and a metallic plate is mediated by plasmon polaritons. These are virtual electromagnetic states that represent the coupling between plasmons and photons (sometimes referred to as dressed photons). Time-dependent perturbation theory helps us understand how these virtual states contribute to energy dissipation and friction.

1.3 Hamiltonian of the quantum friction system

To apply time-dependent perturbation theory, it is essential to first identify the complete Hamiltonian of the system shown in Fig. 1.1. In this system, an atom is moving parallel

to the interface between a plate and a vacuum. The total Hamiltonian is given by

$$H_{\mathrm{QF}} = \underbrace{H_{\mathrm{atom}} + H_{\mathrm{plate}}}_{H_0} + V(t), \tag{1.2}$$

where H_{atom} represents the Hamiltonian of the atom, H_{plate} represents the Hamiltonian of the metallic plate, and $V(t)$ denotes the interaction between the atom and the plate through the plasmon polaritons. In the interaction picture, the unperturbed Hamiltonian, denoted as H_0 includes both the atom and the fermionic system of the plate, as described in Eq. (1.2). As aforementioned, the presence of the metallic plate leads to a non-zero expectation value of the electromagnetic field near the interface in the vacuum. Consequently, the interaction Hamiltonian $V(t)$ in Eq. (1.2) accounts for the interaction between this electromagnetic field and the atom, which is modeled as a two-level system.

In a two-level atomic system with a transition energy characterized by the Bohr transition frequency ω_b, the Hamiltonian can be expressed as

$$H_{\mathrm{atom}} = -\frac{1}{2}\omega_b \chi_z, \tag{1.3}$$

where χ_z denotes the Pauli operator associated with the atomic states. For the quantum states of an atom, we consider the unique ground state $|g\rangle$, which is typically represented by the $1s$ orbital in a hydrogen-like atom. The lowest excited state, on the other hand, corresponds to the $2p$ orbital, which is actually degenerate and comprises three distinct sublevels. The lowest energy levels can be described as the ground state and the first excited state of a three-dimensional harmonic oscillator [25]. The atom's polarization, determined by the linear combination of the excited $2p$ states, can be uniquely described by a normalized three-dimensional vector $\boldsymbol{\eta}$. The components in the unit vectors from the basis of $\boldsymbol{\eta}$ satisfy $\sum_{\boldsymbol{\eta}} \eta_i \eta_j = \delta_{ij}$, where the sum is taken over the orthonormal basis of three vectors. For example, in a standard orthonormal basis, the atomic polarization state $|\boldsymbol{\eta}\rangle$ is represented by the unit vectors $|\boldsymbol{\eta}_1\rangle = (1,0,0)$, $|\boldsymbol{\eta}_2\rangle = (0,1,0)$, $|\boldsymbol{\eta}_3\rangle = (0,0,1)$ in real space.

In the two-level system model of an atom, the interaction with the electromagnetic field is characterized by the transition dipole moment operator $\boldsymbol{D}$. In the interaction picture, the matrix elements of the dipole moment operator between the ground state $|g\rangle$ and the excited state $|\boldsymbol{\eta}\rangle$ represent the transition amplitude between these two states. This transition can exhibit oscillatory behavior, reflecting the time evolution of the system.

$$\begin{aligned} \boldsymbol{D}(t) &= \boldsymbol{\eta} d \left(e^{-i\omega_b t} |g\rangle\langle \boldsymbol{\eta}| + e^{i\omega_b t} |\boldsymbol{\eta}\rangle\langle g| \right) \\ &= \boldsymbol{\eta} d \left(\cos(\omega_b t)\chi_x + \sin(\omega_b t)\chi_y \right) \end{aligned} \Rightarrow \begin{cases} \langle \mathrm{g}|\boldsymbol{D}(t)|\boldsymbol{\eta}\rangle = \boldsymbol{\eta} d e^{-i\omega_b t}; \\ \langle \boldsymbol{\eta}|\boldsymbol{D}(t)|\mathrm{g}\rangle = \boldsymbol{\eta} d e^{i\omega_b t}, \end{cases} \tag{1.4}$$

where d denotes the magnitude of the transition dipole moment, and d is the dipole coupling associated with the atom polarizability $\alpha = 2d^2/\omega_b$. In the Hamiltonian, the effect of the external electric potential is described by the interaction between the dipole moment and the electric field.

$$V(t) = \boldsymbol{D}(t) \cdot \boldsymbol{\nabla}\hat{\Phi}(t), \tag{1.5}$$

where $\hat{\Phi}(t)$ represents the quantized electric potential in the vacuum at the atom's location. To properly describe dissipative dynamics, the frictional force needs to be extracted from or considered within this interaction.

To determine the quantized electric potential modified by the presence of a plate, one must first identify the Hamiltonian H_{plate}. This Hamiltonian depends on the model used for the fermions in the plate. In this study, we will focus on the effects arising from spatial dispersion in the plate, where the energy spectrum varies as a function of the wavenumber. This direction is particularly important because a previous study [33] highlighted that *nonlocality*, including spatial dispersion effects, can significantly impact scenarios where the atom is moving at relatively low velocities. Incorporating spatial dispersion into the analysis increases the inaccuracies associated with the local thermal equilibrium approximation, leading to a larger deviation from the full non-equilibrium results [21, 33]. However, some well-known and extensively studied models for fermion many-body systems, such as the Drude model and the simple Hubbard model, do not exhibit spatial dispersion.

Historically, it has been believed that generic many-body quantum systems behave like classical fluids on long time and length scales. In the 1950s, L.D. Landau pioneered Fermi liquid theory [34–36], initially applied to liquid ^{3}He at very low temperatures. This groundbreaking work soon showed that the theory could also be applied to other fermion many-body systems, notably the conduction electrons in metals and graphene. Fermi liquid theory has since become a crucial framework for understanding many properties of metals. Additionally, some theoretical works [37, 38] have developed the hydrodynamic aspects of interacting fermion systems and extended the theory to account for spatial variations and collective behavior.

The electron hydrodynamics, or quantum hydrodynamic model, provides a streamlined way to describe the collective behavior of electrons in a metal. This model simplifies the analysis by avoiding unnecessary complexity while still allowing for the examination of how the electron fluid responds to external perturbations. It is particularly useful for studying transient phenomena and non-equilibrium effects. Consequently, the model serves as an effective framework for investigating how spatial dispersion influences quantum friction.

In the next chapter, we will analyze how electron interactions within the plate, as described by the hydrodynamic model, generate a static electric field in the vacuum, following the framework outlined in G. Barton's review [39]. Subsequently, we will integrate this hydrodynamic model with an approach for quantum friction, which is based on dipole interactions with the atom as described in Eq. (1.5) and employs time-dependent perturbation theory [25]. This combined approach enables a relatively straightforward analytical treatment by starting from the equations of motion for the fields and the microscopic degrees of freedom of the material. It will provide insight into the microscopic mechanisms underlying this contactless dissipation.

Chapter 2

The static hydrodynamic regime in conductors

The system consists of a semi-infinite plate and an atom moving horizontally above the interface. In some previous studies, the electron dynamics within the semi-infinite plate were described by the Drude model [28], which primarily considers electron-electron and electron-atom interactions and results in no dispersion. To explore the force with the dispersive limit in the electrons of the plates, one can use the hydrodynamic (HD) model. The HD model offers the advantage of accurately incorporating non-local Coulomb interactions within the metal without introducing excessive complexity. It is applicable to clean metals at intermediate temperatures, where the scattering length due to (momentum-conserving) electron-electron collisions is smaller than that of electron-impurity and electron-phonon interactions [40–42].

Certainly, dispersion becomes relevant at small distances from the surface and when the charge carriers in the material cover distances larger than the interatomic separation. This has been demonstrated to be particularly relevant for phenomena such as quantum friction [33]. The HD model serves as a valuable platform for understanding how quantum friction behaves when there is a non-negligible dispersion in the plate. In this section, we will demonstrate how to evaluate the static potential from the semi-infinite plate in the HD regime, following the review by G. Barton [39].

2.1 The sound speed in the classical hydrodynamic model

In the HD model, the free electron gas has an electron number density of n, an effective electron mass of m, and a pressure of P. Due to fluctuations such as vacuum fluctuation, there is a deviation of the electron number density, Δn, and simultaneously a deviation

of the hydrodynamic pressure, ΔP.

$$\Delta n = -n\,\boldsymbol{\nabla}\cdot\boldsymbol{\xi}, \qquad \Delta P = -nmv_s^2\boldsymbol{\nabla}\cdot\boldsymbol{\xi}, \tag{2.1}$$

where v_s is the sound velocity in the neutral medium or the compressional wave speed, and $\boldsymbol{\xi}$ is the displacement vector of an electron's coordinate from its equilibrium position (see Fig. 2.1).

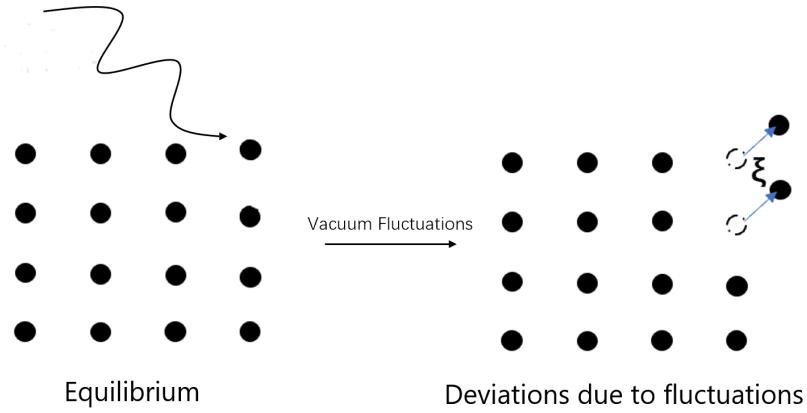

Figure 2.1: **Deviations in the HD model.** This is a brief sketch illustrating how the density deviation is expressed in the HD model. The black dots represent hydrodynamic particles, and $\boldsymbol{\xi}$ denotes the displacement vector from equilibrium.

Collisions between electrons in the HD regime are adiabatic, meaning that energy transforms into work done rather than thermal variation during collisions. As a consequence, the pressure follows a polytropic process equation for the adiabatic case, i.e.: PV^{Γ} is constant, where Γ is the ratio of specific heats at constant pressure and volume ($\Gamma \equiv C_p/C_v$). With a slight transformation, the adiabatic polytropic process formula becomes $P = K\rho^{\Gamma} = K(mn)^{\Gamma}$, where K is another constant. Thus, the pressure deviation caused by the inhomogeneous distribution of electrons can be expressed as:

$$\Delta P = \frac{dP(n)}{dn}\Delta n = \left(\Gamma\frac{P}{n}\right)\Delta n = mv_s^2\Delta n = -nmv_s^2\boldsymbol{\nabla}\cdot\boldsymbol{\xi}. \tag{2.2}$$

The sound speed or compressional wave speed is defined as $v_s^2 = \Gamma P/(mn)$.

To understand the sound speed in this scenario, one can draw a parallel with the concept of sound speed in the conventional HD model, which is defined as the speed at which a compressional wave propagates in a certain medium. In the electronic HD model,

the deviation or configuration of electrons can be "transmitted" to surrounding electrons. Thus, the sound speed here is analogous to how quickly an electron can influence its neighboring electrons or how rapidly phonons/energy propagate between electrons.

At absolute zero temperature, v_s can be expressed in terms of the Fermi velocity, as given in Ref. [39].

$$v_s^2 = 3v_f^2/5 \text{ for high frequencies,} \tag{2.3}$$

$$v_s^2 = v_f^2/3 \text{ for low frequencies.} \tag{2.4}$$

When considering high oscillating frequencies, the Fermi electron gas cannot reach equilibrium within one oscillating period. Thus, the plasmon can penetrate the interface and reach the material's bulk modes. For low-frequency waves, there will be static screening on the material's surface, and this case is referred to as surface modes.

The pressure gradient deviation acts as the force pulling the electrons back to their equilibrium position, and one can conceptualize this model as a simple harmonic oscillation between the neighboring electrons. With the expression of the pressure deviation in Eq. (2.1),

$$\boldsymbol{\nabla}\left(\Delta P\right) \equiv -m\omega^2\boldsymbol{\xi} \Rightarrow mv_s^2\nabla^2\left(\boldsymbol{\xi}\right) = -m\omega^2\boldsymbol{\xi}. \tag{2.5}$$

By using a plane-wave ansatz $\boldsymbol{\xi}(\boldsymbol{r}) \propto e^{i\boldsymbol{k}\cdot\boldsymbol{r}}$,

$$-mv_s^2k^2\boldsymbol{\xi} = -m\omega^2\boldsymbol{\xi} \Rightarrow v_s = \frac{\omega}{k} = \frac{1}{k}\sqrt{\frac{\kappa}{m}}, \tag{2.6}$$

where $k = |\boldsymbol{k}|$, ω is the frequency of the imaginary oscillator and κ is the oscillator constant. When the oscillator constant κ is large, the oscillator between electrons is "stiff" and "heavy", resulting in a fast sound speed v_s. The limit $v_s \to 0$ means no oscillators between electrons, and this case should correspond to the Drude model without a relaxation rate.

2.2 The electric potential and the displacement potential

In addition to the deviation in the HD model, one should also take into account the Coulomb interaction between electrons. In this work, we consider the non-relativistic case ($c \to \infty$), such that the Maxwell-Faraday Equation ($\boldsymbol{\nabla} \times \boldsymbol{E} = -(1/c)(\partial\boldsymbol{B}/\partial t)$), in Gaussian units) implies that the magnetic interaction or Hall effect can be neglected. Beginning with the Gauss's law and Δn in Eq. (2.1), one can consider the electron deviation causing

$$\boldsymbol{\nabla}\cdot\boldsymbol{E} = 4\pi e\Delta n = -4\pi ne\boldsymbol{\nabla}\cdot\boldsymbol{\xi} \quad (z \leq 0). \tag{2.7}$$

Here, $z \leq 0$ signifies being inside the plate in the system sketched in Fig. 1.1, while $z > 0$ represents being in the vacuum above the plate.

We introduce the displacement potential (Ψ and $\boldsymbol{\xi} = -\boldsymbol{\nabla}\Psi$), and it leads the Gauss's law in Eq. (2.7) to

$$\nabla^2\Phi = -4\pi ne\nabla^2\Psi, \quad (z \leq 0), \tag{2.8}$$

where Φ is the static electric potential ($\boldsymbol{E} = -\boldsymbol{\nabla}\Phi$). The equation of motion in the electronic HD model consists of the Coulomb interaction and the gradient of the pressure deviation.

$$nm\ddot{\boldsymbol{\xi}} = ne\boldsymbol{E} - \boldsymbol{\nabla}(\Delta P) \quad (z \leq 0). \tag{2.9}$$

The ansatz for displacement field vectors is defined with time dependence as $\boldsymbol{\xi}(t) \propto e^{-i\Omega t}$ in normal modes of an oscillating system, such that the equation of motion becomes

$$-\Omega^2 nm\boldsymbol{\xi} = -ne\boldsymbol{\nabla}\Phi + \boldsymbol{\nabla}(nmv_s^2\nabla^2\Psi) \tag{2.10}$$

$$\Rightarrow \Phi = -\frac{m}{e}(\Omega^2 + v_s^2\nabla^2)\Psi \quad (z \leq 0). \tag{2.11}$$

As shown in Eq. (2.8), one can replace Φ by Ψ once the Laplace operator is applied on both sides in Eq. (2.11).

$$\nabla^2\Phi = -\frac{m}{e}\nabla^2(\Omega^2 + v_s^2\nabla^2)\Psi \tag{2.12}$$

$$\nabla^2(\Omega^2 - \omega_p^2 + v_s^2\nabla^2)\Psi(z \leq 0) = 0, \tag{2.13}$$

where ω_p is the plasma frequency: $\omega_p^2 \equiv 4\pi ne^2/m$. For the static electric potential in the vacuum ($z > 0$), $\nabla^2\Phi(z > 0) = 0$. To find the electric potential Φ, one can first solve the fourth derivative of the displacement potential in Eq. (2.13), then calculate Φ through the Gauss's law in Eq. (2.8).

In the system, which is half-filled by the metallic slab shown in Fig. 1.1, one can use the following ansatz for both potentials.

$$\Psi = e^{i\boldsymbol{k}\cdot\boldsymbol{r}(x,y)}\psi(z), \qquad \Phi = e^{i\boldsymbol{k}\cdot\boldsymbol{r}(x,y)}\phi(z). \tag{2.14}$$

Because the interface breaks the symmetry along the z-axis, one can assume the fields have a plane wave in the x-y plane and an evanescent wave exponentially decaying from the interface. Therefore, we define the coordinates as $(\boldsymbol{r}(x,y), iz)$ in real space and $(\boldsymbol{k}(k_x,k_y), ik_z)$ in momentum space. Due to the Laplace equation in the vacuum, $k_z = |\boldsymbol{k}|$, and hereafter we use k to denote k_z and the magnitude of $\boldsymbol{k}$.

With the ansatz in Eq. (2.14), the differential equations (2.8) and (2.13) can be rewritten as

$$-\frac{e}{m}\phi(z\leq 0)=\left(\Omega^2-v_s^2k^2+v_s^2\frac{d^2}{dz^2}\right)\psi(z\leq 0), \tag{2.15}$$

$$\left(-k^2+\frac{d^2}{dz^2}\right)\left(\Omega^2-\omega_p^2-v_s^2k^2+v_s^2\frac{d^2}{dz^2}\right)\psi(z\leq 0)=0. \tag{2.16}$$

These differential equations are valid inside the plate, but outside the plate (vacuum), ϕ is determined by the Laplace equation:

$$\nabla^2\Phi=0\ \Rightarrow -k^2e^{i\boldsymbol{k}\cdot\boldsymbol{r}}\phi(z\geq 0)+e^{i\boldsymbol{k}\cdot\boldsymbol{r}}\frac{d^2}{dz^2}\phi(z\geq 0)=0, \tag{2.17}$$

$$\phi(z\geq 0)=\phi(z=0^+)\,e^{-kz}, \tag{2.18}$$

where k is the modulus of $\boldsymbol{k}$, i.e.: $k=\sqrt{k_x^2+k_y^2}$. As anticipated, the electric potential $\phi(z\geq 0)$ in the vacuum exponentially decays from the interface, representing the evanescent wave. To study quantum friction, we need to compute the static electric potential $\phi(z\geq 0)$ in Eq. (2.18).

This half-space system also imposes three boundary conditions for Ψ and Φ. Firstly, Ψ should vanish at infinity, i.e., $\psi(z\to\pm\infty)=0$. This also applies to the electric potential: $\phi(z\to\pm\infty)=0$. The second boundary condition arises from the continuity of the electric field through the interface at $z=0$.

$$\phi(z=0^+)=\phi(z=0^-),\qquad \left.\frac{\partial\phi(z)}{\partial z}\right|_{z=0^-}=\left.\frac{\partial\phi(z)}{\partial z}\right|_{z=0^+}. \tag{2.19}$$

For the displacement potential, the third boundary condition arises because the electrons cannot escape the plate, so the z-component of the displacement vector ξ_z vanishes at the interface.

$$\xi_z(z=0^-)=-\left.\frac{\partial\psi(z)}{\partial z}\right|_{z=0^-}=0. \tag{2.20}$$

In the vacuum, there is no displacement potential $\psi(z)$, and $\phi(z)$ behaves like an evanescent wave. However, within the plate, $\psi(z)$ comprises not only the evanescent wave from the surface but also the plane wave in the bulk. In the subsequent calculation of the potential inside the plate, we will illustrate the computation of two modes and subsequently determine the electric potential in the vacuum.

2.3 Surface and bulk modes

Inside the plate, the ansatz of the displacement potential is defined as follows.

$$\psi(z \leq 0) = \psi(z = 0^-)e^{pz} \tag{2.21}$$

$$\Rightarrow \frac{d}{dz}\psi(z \leq 0) = p\psi(z \leq 0). \tag{2.22}$$

Therefore, the fourth derivative equation (2.16) becomes

$$\left(-k^2 + p^2\right)\left(\Omega^2 - \omega_p^2 - v_s^2 k^2 + v_s^2 p^2\right)\psi(z \leq 0) = 0. \tag{2.23}$$

Two solutions can be identified, which are

$$p = k, \tag{2.24}$$

$$p^2 = \frac{1}{v_s^2}(-\Omega^2 + \omega_p^2 + v_s^2 k^2). \tag{2.25}$$

Given that this concerns the interior of the plate ($z \leq 0^-$), we exclusively take the positive real values for p to ensure the convergence of $\psi(z \leq 0)$ as z approaches $-\infty$. The solution $p = k$ results in local effects since it lacks explicit dependence on the sound velocity v_s, resulting in the emergence of the evanescent wave mode. The other solution for p in Eq. (2.25) is non-local and can be split into two modes: a surface mode and a bulk mode.

As mentioned earlier, the surface mode behaves like an evanescent wave, while the bulk mode should appear as a plane wave, both determined by the frequency Ω. When $\Omega^2 \leq \omega_p^2 + v_s^2 k^2$, Eq. (2.25) yields a real value for p, corresponding to the surface mode. Conversely, when $\Omega^2 > \omega_p^2 + v_s^2 k^2$, Eq. (2.25) produces a complex value for p, representing the bulk mode.

$$\Omega_s^2 = \omega_p^2 + v_s^2 k^2 - v_s^2 p_s^2, \tag{2.26}$$

$$\Omega_b^2 = \omega_p^2 + v_s^2 k^2 + v_s^2 p_b^2, \tag{2.27}$$

where p_s and p_b are real numbers, and the subscripts s and b represent the surface and bulk modes, respectively. In physical interpretation, we can refer to $\sqrt{\omega_p^2 + v_s^2 k^2}$ as the effective plasma frequency in the hydrodynamic regime. Therefore, if an incident wave has frequencies lower than the effective plasma frequency, it will be screened out at the surface. Conversely, if the incident wave possesses frequencies higher than the effective plasma frequency, it can penetrate the material and interact with the bulk modes.

In both modes, the fourth derivative equation (2.16) can be expressed as

$$\text{surface modes: } \left(-k^2+\frac{d^2}{dz^2}\right)\left(-v_s^2p_s^2+v_s^2\frac{d^2}{dz^2}\right)\psi_s(z\leq 0)=0, \tag{2.28}$$

$$\text{bulk modes: } \left(-k^2+\frac{d^2}{dz^2}\right)\left(v_s^2p_b^2+v_s^2\frac{d^2}{dz^2}\right)\psi_b(z\leq 0)=0. \tag{2.29}$$

They result in the following solutions.

$$\psi_s(z\leq 0)=C_1'e^{kz}+C_2'e^{p_sz}, \tag{2.30}$$

$$\psi_b(z\leq 0)=C_1e^{kz}+C_2\cos(p_bz)+C_3\sin(p_bz), \tag{2.31}$$

where C and C' are constants determined by the boundary conditions. The boundary conditions in Eq. (2.20), which arise from the constraint that no electrons escape the plate, result in both modes to

$$\psi_s(z\leq 0)=N_k\left(p_se^{kz}-ke^{p_sz}\right), \tag{2.32}$$

$$\psi_b(z\leq 0)=M_k\left[\cos(p_bz)+C\left(e^{kz}-\frac{k}{p_b}\sin(p_bz)\right)\right]. \tag{2.33}$$

where N_k and M_k are the normalizing constants for the surface and bulk modes, respectively. The normalizing constant is utilized for quantization purposes.

2.3.1 The electric potential of the surface mode

Since quantum friction is concerned with the electric potential, Eq. (2.15) can be employed to derive $\phi(z\leq 0)$ from $\psi(z\leq 0)$. In the surface mode, we obtain ϕ_s from ψ_s in Eq. (2.32).

$$-\frac{e}{m}\phi_s(z\leq 0)=\left(\Omega_s^2-v_s^2k^2+v_s^2\frac{d^2}{dz^2}\right)N_k\left(p_se^{kz}-ke^{p_sz}\right), \tag{2.34}$$

$$\Rightarrow \phi_s(z\leq 0)=-\frac{m}{e}N_k\left[\Omega_s^2p_se^{kz}-\left(\Omega_s^2-v_s^2k^2+v_s^2p_s^2\right)ke^{p_sz}\right]. \tag{2.35}$$

According to the expression in Eq. (2.26), $\phi_s(z\leq 0)$ can be simplified to

$$\phi_s(z\leq 0)=-\frac{m}{e}N_k\left(\Omega_s^2p_se^{kz}-\omega_p^2ke^{p_sz}\right). \tag{2.36}$$

At the interface, one can determine $\phi_s(z=0^-)=-(mN_k/e)\left(\Omega_s^2p_s-\omega_p^2k\right)$. Since the field must remain continuous across the interface, $\phi_s(z=0^-)=\phi_s(z=0^+)$.

Consequently, the static electric potential in a vacuum, as given in Eq. (2.18), is expressed as

$$\phi_s(z>0) = -\frac{m}{e} N_k \left(\Omega_s^2 p_s - \omega_p^2 k\right) e^{-kz}. \tag{2.37}$$

The last boundary condition demands the continuity of $d\phi_s/dz$ across the interface, the electric potential in the plate (Eq. (2.36)) and in vacuum (Eq. (2.37)) provide

$$\frac{d}{dz}\phi_s(z=0^+) = \frac{d}{dz}\phi_s(z=0^-) \tag{2.38}$$

$$\Rightarrow -\frac{m}{e} N_k(-k) \left(\Omega_s^2 p_s - \omega_p^2 k\right) = -\frac{m}{e} N_k p_s k \left(\Omega_s^2 - \omega_p^2\right) \tag{2.39}$$

$$\Rightarrow 2\Omega_s^2 p_s - \omega_p^2 (p_s + k) = 0. \tag{2.40}$$

Then, using the expression of Ω_s in Eq. (2.26), we can obtain

$$2p_s \left(\omega_p^2 + v_s^2 k^2 - v_s^2 p_s^2\right) - \omega_p^2 (p_s + k) = 0 \tag{2.41}$$

$$\Rightarrow p_s^3 - \left(k^2 + \frac{\omega_p^2}{2v_s^2}\right) p_s + \frac{\omega_p^2}{2v_s^2} k = 0. \tag{2.42}$$

To solve the above cubic polynomial, we need a trial solution for p_s. A useful strategy here is to consider the obvious solution from Sec. 2.3: $p = k$ in Eq. (2.24). Therefore, $p_s = k$ can also be a solution to the above equation, resulting in

$$(p_s - k)\left(p_s^2 + k p_s - \frac{\omega_p^2}{2v_s^2}\right) = 0. \tag{2.43}$$

Once more, we exclusively consider the positive root for p_s because $\phi_s(z \leq 0)$ should converge as z approaches $-\infty$.

$$p_s = \frac{1}{2}\left(-k + \sqrt{k^2 + \frac{2\omega_p^2}{v_s^2}}\right). \tag{2.44}$$

p_s in Eq. (2.44) allows us to express Ω_s^2 in Eq. (2.26) as

$$\Omega_s^2(k) = \frac{1}{2}\left(\omega_p^2 + v_s^2 k^2 + v_s k\sqrt{(2\omega_p^2 + v_s^2 k^2)}\right) \tag{2.45}$$

$$= \frac{1}{4}\left(\left(2\omega_p^2 + v_s^2 k^2\right) + v_s^2 k^2 + 2v_s k\sqrt{(2\omega_p^2 + v_s^2 k^2)}\right) \tag{2.46}$$

$$= \frac{1}{4}\left(\sqrt{(2\omega_p^2 + v_s^2 k^2)} + v_s k\right)^2 \tag{2.47}$$

Thus, we find a dispersion relation for the surface mode:

$$\Omega_s(k) = \frac{1}{2}\left(\sqrt{2\omega_p^2 + v_s^2 k^2} + v_s k\right). \tag{2.48}$$

This dispersion equation indicates dispersion when v_s is non-zero.

Accordingly, one can express the dispersion relation in Eq. (2.48) in terms of p_s as given in Eq. (2.44).

$$\Omega_s = v_s k + v_s p_s \tag{2.49}$$

Using Eq. (2.37), (2.44), and (2.45), one can determine the electric potential induced by surface modes outside the semi-infinite plate. Furthermore, the surface-mode limit ($\Omega_s^2 < \omega_p^2 + v_s^2 k^2$) is satisfied automatically as long as the dispersion relation of Ω_s in Eq. (2.48) holds true.

2.3.2 The electric potential of the bulk mode

Analogous to the calculation in the surface mode, we begin by computing ϕ_b inside the plate by substituting $\psi_b(z \leq 0)$ from Eq. (2.33) into Eq. (2.15).

$$\phi_b(z \leq 0) = -\frac{m}{e}\left((\Omega_b^2 - v_s^2 k^2)\psi_b + v_s^2 \frac{d^2}{dz^2}\psi_b\right) \tag{2.50}$$

$$= -\frac{m}{e} M_k \left[\left(\Omega_b^2 - v_s^2 k^2 - v_s^2 p_b^2\right)\cos(p_b z) + C\Omega_b^2 e^{kz}\right. \tag{2.51}$$

$$\left. + C\left(\Omega_b^2 - v_s^2 \frac{k^3}{p_b} + v_s^2 k p_b\right)\sin(p_b z)\right].$$

At the interface, the bulk mode gives

$$\phi_b(z = 0^-) = -\frac{m}{e} M_k \left[(1 + C)\,\Omega_b^2 - v_s^2 k^2 - v_s^2 p_b^2\right]. \tag{2.52}$$

Thus, in vacuum, the static electric potential from Eq. (2.18) becomes

$$\phi_b(z > 0) = \phi_b(z = 0^+)e^{-kz} = -\frac{m}{e} M_k \left(\omega_p^2 + C\Omega_b^2\right) e^{-kz}. \tag{2.53}$$

To evaluate the unknown constant C in Eq. (2.53), one can use the boundary conditions ensuring continuity across the interface. Here, we employ the expression of Eq. (2.50) for $\psi_b(z \leq 0^-)$.

$$\frac{d}{dz}\phi_b(z \geq 0)\big|_{z=0^+} = \frac{d}{dz}\phi_b(z \leq 0)\big|_{z=0^-} \tag{2.54}$$

$$\Rightarrow M_k \left(\omega_p^2 + C\Omega_b^2\right) k = -\left[\left(\Omega_b^2 - v_s^2 k^2\right)\frac{d}{dz}\psi_p\big|_{z=0^-} + v_s^2 \frac{d^3}{dz^3}\psi_p\big|_{z=0^-}\right]. \tag{2.55}$$

Since no electrons escape the plate, $(d\psi_p/dz)|_{z=0^-} = 0$. With $\psi_p(z \leq 0)$ from Eq. (2.33), one can derive the expression for the constant C as follows.

$$M_k(\omega_p^2 + C\Omega_b^2)k = -\frac{m}{e} M_k C v_s^2 \left(k^3 + k p_b^2\right), \tag{2.56}$$

$$C = -\frac{\omega_p^2}{\Omega_p^2 + v_s^2 k^2 + v_s^2 p_b^2}. \tag{2.57}$$

Since the frequency in the bulk mode, Ω_b, can be expressed as shown in Eq. (2.27), one can express the constant C as

$$C = -\frac{\omega_p^2}{2\Omega_p^2 - \omega_p^2}. \tag{2.58}$$

Therefore, the potentials from the bulk mode in Eqs. (2.33) and (2.53) become

$$\psi_b(z \leq 0) = M_k \left[\cos(p_b z) - \frac{\omega_p^2}{2\Omega_p^2 - \omega_p^2}\left(e^{kz} - \frac{k}{p_b}\sin(p_b z)\right)\right], \tag{2.59}$$

$$\phi_b(z \geq 0) = -\frac{m}{e} M_k \omega_p^2 \left(\frac{\Omega_p^2 - \omega_p^2}{2\Omega_p^2 - \omega_p^2}\right) e^{-kz}. \tag{2.60}$$

Eq. (2.60) represents the final result for bulk modes in vacuum with frequency $\Omega_b > \sqrt{\omega_p^2 + v_s^2 k^2}$.

Additionally, there exists another mode known as the transverse mode. This mode arises from a more general expression of the displacement field, $\boldsymbol{\xi}$.

$$\boldsymbol{\xi} = -\boldsymbol{\nabla}\Psi - \boldsymbol{\nabla} \times \boldsymbol{A}, \tag{2.61}$$

where $\boldsymbol{A}$ is a vector potential. $\boldsymbol{A}$ can be non-zero in the semi-infinite plate, and a chosen gauge is $\boldsymbol{\nabla} \cdot \boldsymbol{A} = 0$. To prevent the singularity of $\boldsymbol{\nabla} \cdot \boldsymbol{A}$ at the surface, we set $A_z(z = 0^-) = 0$. Once more, we express the position vector in the form $(\boldsymbol{r}(x, y), z)$, and the vector potential can be expressed as

$$\boldsymbol{\nabla} \cdot \boldsymbol{A} = 0,\ |\boldsymbol{A}| \propto e^{i\boldsymbol{k}\cdot\boldsymbol{r}+kz} \Rightarrow \boldsymbol{A} = \begin{pmatrix} -k_y \\ k_x \\ 0 \end{pmatrix} L e^{i\boldsymbol{k}\cdot\boldsymbol{r}+kz}, \tag{2.62}$$

where L is a normalizing constant. Therefore, $\boldsymbol{\xi}$ can be written as

$$\boldsymbol{\xi} = -\boldsymbol{\nabla}\Psi - \left[\boldsymbol{\nabla}\left(\boldsymbol{\nabla} \cdot \boldsymbol{A}\right) - \nabla^2 \boldsymbol{A}\right] \tag{2.63}$$

$$= -\boldsymbol{\nabla}\left(\Psi - \boldsymbol{\nabla} \cdot \boldsymbol{A}\right) \tag{2.64}$$

$$= -\boldsymbol{\nabla}\left[e^{i\boldsymbol{k}\cdot\boldsymbol{r}}\left(\psi(z) - ikLe^{kz}\right)\right], \quad (z \leq 0). \tag{2.65}$$

However, gauge invariance implies that $\psi' = \psi - ikLe^{kz}$ plays the same role as ψ. Thus, transverse modes simply result in a shift in the z component of Ψ, and there is no need to consider them.

2.4 Quantization of the electric static potential in vacuum

With the classical solutions, Eqs. (2.37) and (2.60), we can now quantize the potential in vacuum using a standard elementary approach, expressing it as a Hermitian field operator:

$$\Phi(z \geq 0) = \int d\boldsymbol{k}\; e^{i\boldsymbol{k}\cdot\boldsymbol{r}} a_{\boldsymbol{k}} \phi_s(z) + \int d\boldsymbol{k} \int dp e^{i\boldsymbol{k}\cdot\boldsymbol{r}} a_{\boldsymbol{k}p} \phi_b(z) + h.c., \tag{2.66}$$

$$\begin{aligned}\Phi(z \geq 0) = &-\frac{m}{e} N_k \int d\boldsymbol{k}\; e^{i\boldsymbol{k}\cdot\boldsymbol{r}-kz} a_{\boldsymbol{k}} (\Omega_s^2 p_s - \omega_p^2 k) \\ &- \frac{m}{e} M_k \int d\boldsymbol{k} \int dp\; e^{i\boldsymbol{k}\cdot\boldsymbol{r}-kz} a_{\boldsymbol{k}p} \omega_p^2 \frac{\Omega_b^2 - \omega_p^2}{2\Omega_b^2 - \omega_p^2} + h.c.,\end{aligned} \tag{2.67}$$

where $\boldsymbol{k} = (k_x, k_y)$. The first and second contributions arise from the surface and bulk modes, respectively. The bosonic operators in Φ obey the following commutation relation:

$$\left[a_{\boldsymbol{k}}, a^\dagger_{\boldsymbol{k}'}\right] = \delta(\boldsymbol{k}' - \boldsymbol{k}), \qquad \left[a_{\boldsymbol{k}p}, a^\dagger_{\boldsymbol{k}'p'}\right] = \delta(\boldsymbol{k}' - \boldsymbol{k})\delta(p' - p). \tag{2.68}$$

As shown in Appendix A, the normalizing constants can be determined as follows.

$$N_k^2 = \frac{\omega_p^2 (2\Omega_s^2 - \omega_p^2)^2}{16\pi^2 mn\Omega_s k^3 (\omega_p^2 + 2\Omega_s^2)(\Omega_s^2 - \omega_p^2)^2}, \tag{2.69}$$

$$M_k^2 = \frac{v_s^4 p_b^2 (2\Omega_b^2 - \omega_p^2)^2}{4\pi^3 mn\Omega_b (\Omega_b^2 - \omega_p^2)^2 ((2\Omega_b^2 - \omega_p^2)^2 - 4v_s^2 k^2 \Omega_b^2)}. \tag{2.70}$$

This results in the quantized potential in Eq. (2.67) becoming

$$\begin{aligned}\Phi(z \geq 0) = &-\int d\boldsymbol{k} e^{i\boldsymbol{k}\cdot\boldsymbol{r}-kz} a_{\boldsymbol{k}} \omega_p^2 \sqrt{\frac{1}{4\pi k\Omega_s(\omega_p^2 + 2\Omega_s^2)}} \\ &- \int d\boldsymbol{k} \int dp e^{i\boldsymbol{k}\cdot\boldsymbol{r}-kz} a_{\boldsymbol{k}p} \frac{v_s^2 p_b \omega_p}{\pi\sqrt{\Omega_b((2\Omega_b^2 - \omega_p^2)^2 - 4v_s^2 k^2 \Omega_b^2)}} + h.c..\end{aligned} \tag{2.71}$$

For the Hamiltonian of the plate in the hydrodynamic regime, we can start with its classical energy from the equation of motion in Eq. (2.9).

$$E = \int_{-\infty}^{\infty} d\boldsymbol{r} \int_{-\infty}^{0} dz \left(\frac{1}{2} nm \left(\boldsymbol{\nabla}\dot{\Psi}\right)^2 + \frac{1}{2} nmv_s^2 \left(\nabla^2\Psi\right)^2 + \frac{1}{2} ne\Phi\nabla^2\Psi\right). \tag{2.72}$$

On the right-hand side, the first term represents the kinetic energy of electrons per unit volume. The second contribution is the hydrodynamic compressional energy density, and the last term represents the electrical energy per unit volume. The Hamiltonian can be deduced by substituting the quantized Φ and Ψ into E.

$$H_{\mathrm{HD}} = \int d\boldsymbol{k}\ \Omega_s(k)\left(a^\dagger_{\boldsymbol{k}}a_{\boldsymbol{k}} + \frac{1}{2}\right) + \int d\boldsymbol{k}\ \int dp\ \Omega_b(k,p)\left(a^\dagger_{\boldsymbol{k}p}a_{\boldsymbol{k}p} + \frac{1}{2}\right). \tag{2.73}$$

This constitutes a standard scalar field of oscillations, where the first and second integrals describe surface modes and bulk modes, respectively. The term with a factor of 1/2 in each integral represents the so-called zero-point energy.

Given that quantum friction is a low-frequency phenomenon (i.e., the contribution to the lowest order in velocity can be obtained from the zero-frequency response of both the material and the atom [28]), and considering that we are in the non-retarded and near-field regimes, small frequencies will have a dominant effect. Therefore, only surface modes will be relevant to quantum friction.

In the interaction picture, one can apply the Heisenberg equation of motion,

$$a_{\boldsymbol{k}}(t) = e^{-i\Omega_s(k)t}a_{\boldsymbol{k}}, \tag{2.74}$$

and the quantized vacuum field becomes:

$$\hat{\Phi}(\boldsymbol{r},z,t) = -\int d\boldsymbol{k}\ e^{i\boldsymbol{k}\cdot\boldsymbol{r}-kz}a_{\boldsymbol{k}}(t)e^{-i\Omega_s t}\omega_p^2\sqrt{\frac{1}{4\pi k\Omega_s(\omega_p^2+2\Omega_s^2)}} + h.c.. \tag{2.75}$$

After extracting the semi-infinite material information into $\phi_k^2 = \omega_p^4/[4\pi k\Omega_s(\omega_p^2+2\Omega_s^2)]$, our quantized electric potential can be rewritten as

$$\hat{\Phi}(\boldsymbol{r},z,t) = -\int d\boldsymbol{k}\ e^{i\boldsymbol{k}\cdot\boldsymbol{r}-i\Omega_s(k)t-kz}a_{\boldsymbol{k}}(t)\phi_k + h.c.. \tag{2.76}$$

Here, ϕ_k represents the surface-mode shape or eigenmode, encoding information regarding the internal degrees of freedom of the material, and its square has units of velocity. Additionally, $\Omega_s(k)$ follows the dispersion relation in Eq. (2.48).

2.4.1 The non-dispersive limit

In the non-dispersive limit, $v_s \to 0$. In this scenario, electrons inside the plate are more "isolated", and there is only Coulomb's repulsive force between them. As a result, many physical quantities become familiar if one is well-versed in the Drude model. For instance,

the frequency in surface modes tends to $\Omega_s = \omega_p/\sqrt{2}$, which corresponds to the surface plasmon resonance in the Drude model.

Another notable observation is that the potential of bulk modes vanishes due to the v_s-dependence of the normalizing constant M_k in Eq. (2.70). Consequently, the quantized potential changes to:

$$\hat{\Phi}(z \geq 0) = -\int d\boldsymbol{k} e^{i\boldsymbol{k}\cdot\boldsymbol{r}-kz} a_{\boldsymbol{k}} \sqrt{\frac{\omega_p}{4\sqrt{2}\pi k}} + h.c.. \tag{2.77}$$

This quantized potential corresponds to the Drude model without a relaxation rate.

2.5 Summary for the HD model

In this chapter, we follow the approach outlined in Ref. [39] to illustrate the evaluation of the quantized electric potential in the quantum-friction system depicted in Fig. 1.1. In the non-relativistic limit within the HD regime, we begin with the density and pressure deviations in Eqs. (2.1), Gauss's law in Eq. (2.7), and the equation of motion in Eq. (2.9). Subsequently, we evaluate the classical potentials ϕ_s and ϕ_b in Eqs. (2.37) and (2.60), respectively, under the boundary conditions in the half-space system. The HD regime yields an effective plasma frequency $\sqrt{\omega_p^2 + v_s^2 k^2}$, which is associated with the sound speed v_s. In this context, the sound speed describes how quickly the deviation/configuration can propagate between neighboring electrons.

In Sec. 2.4, the potentials from both modes are quantized as Eq. (2.71). Given that quantum friction is primarily associated with surface modes, we focus solely on Φ_s in Eq. (2.76) to compute the quantum friction on the moving atom. Additionally, the HD regime provides the dispersion relation in Eq. (2.48), enabling the study of quantum friction within the dispersive limit. This dispersion relation will play a crucial role in the subsequent analysis of quantum friction.

Chapter 3

Time evolution of the dressed states in the quantum friction system

This chapter will focus on illustrating the time-dependent perturbation theory, which is applied to find the dressed states or atom-field states, in the system sketched in Fig. 1.1. In this process, we assume the interaction Hamiltonian as the perturbed Hamiltonian and calculate the system states with perturbative orders. These system states yield the expectation values in different perturbative orders. This method can be adopted when two systems are weakly coupled, which is suitable in the scenario of a moving atom above the interface.

To recap from Sec. 1.3 in the introduction chapter, the Hamiltonian in the interaction picture is given by

$$H_{\mathrm{QF}} = H_{\mathrm{atom}} + H_{\mathrm{HD}} + V(t), \tag{3.1}$$

$$V(t) = \boldsymbol{D}(t) \cdot \boldsymbol{\nabla}\hat{\Phi}(t), \tag{3.2}$$

where $\boldsymbol{D}$ is the dipole operator. For the moving atom, one can consider it as a two-level system with a ground state $|g\rangle$ and three degenerate excited states $|\boldsymbol{\eta}\rangle$.

$$H_{\mathrm{atom}} = -\frac{1}{2}\omega_b \chi_z, \tag{3.3}$$

where ω_b is the Bohr transition frequency, and χ_z is the Pauli operator in the manifold of the atom states $\{|g\rangle, |\boldsymbol{\eta}\rangle\}$.

As shown in Eq. (1.4), the dipole operator of this atom can be written as

$$\boldsymbol{D}(t) = \boldsymbol{\eta} d \left(\cos(\omega_b t)\chi_x + \sin(\omega_b t)\chi_y\right), \tag{3.4}$$

where $\boldsymbol{\eta}$ is a unit vector from a set $\{\boldsymbol{\eta}\}$ of an orthonormal basis in real space. The dipole operator in Eq. (3.4) gives

$$\langle \mathrm{g}|\boldsymbol{D}(t)|\boldsymbol{\eta}\rangle = \boldsymbol{\eta} d e^{-i\omega_b t},\ \langle \boldsymbol{\eta}|\boldsymbol{D}(t)|\mathrm{g}\rangle = \boldsymbol{\eta} d e^{i\omega_b t}. \tag{3.5}$$

The other part of the interaction Hamiltonian $V(t)$ in Eq. (3.2) is the quantized electric potential in the vacuum, $\hat{\Phi}$ which is discussed in the previous chapter 2. For the plate in the HD regime, $\hat{\Phi}$ can be taken as in Eq. (2.76), and it leads to

$$V(t) = \int_0^\infty dk \int_{-\pi}^{\pi} k d\theta \left(\boldsymbol{D}(t)\cdot i\vec{k}\right) e^{i\boldsymbol{k}\cdot\boldsymbol{r} - i\Omega_s t - kz} a_{\boldsymbol{k}}(t)\phi_k + h.c., \tag{3.6}$$

where $\vec{k} = (k_x, k_y, ik_z)$.

The quantum friction is against the movement of the atom, and when the atom is moving along the x-axis, the force operator is as follows.

$$F_x(t) = -\frac{\partial}{\partial x} V(t) \tag{3.7}$$

$$= \int_0^\infty dk \int_{-\pi}^{\pi} k d\theta \left(\boldsymbol{D}(t)\cdot\vec{k}\right) k\cos(\theta) e^{i\boldsymbol{k}\cdot\boldsymbol{r} - i\Omega_s t - kz} a_{\boldsymbol{k}}(t)\phi_k + h.c., \tag{3.8}$$

where $k_x = k\cos(\theta)$. As we consider the atom moving at a constant velocity v along the x-axis from the origin at the plane $z = z_0$, the position vector in the horizontal plane should be $\boldsymbol{r} = (vt, 0)$. The fact that the moving atom breaks time-reversal symmetry results in a dissipative force as

$$F_x(t) = \int_0^\infty dk \int_{-\pi}^{\pi} d\theta \left(\boldsymbol{D}(t)\cdot\vec{k}\right) k^2\cos(\theta) e^{ik\cos(\theta)vt - i\Omega_s t - kz} a_{\boldsymbol{k}}(t)\phi_k + h.c., \tag{3.9}$$

If the atom is moving backwards, $\boldsymbol{r} = (-vt, 0)$, the force operator becomes $F_x(-t)$ in Eq. (3.9).

$$F_x(-t) = \int_0^\infty dk \int_{-\pi}^{\pi} d\theta \left(\boldsymbol{D}(t)\cdot\vec{k}\right) k^2\cos(\theta) e^{-ik\cos(\theta)vt - i\Omega_s t - kz} a_{\boldsymbol{k}}(t)\phi_k + h.c.. \tag{3.10}$$

By writing $-\cos(\theta) = \cos(\pi - \theta)$, one can prove this force operator is an odd function of the time or the atom velocity v, i.e.: $F_x(-t) = -F_x(t)$. This is anticipated, as quantum friction always opposes the atom's movement.

The following sections in this chapter aim to find the coupled states of the system and calculate the expectation friction in perturbative orders. As shown in Eq. (3.9), the

force operator involves the states of the atom $\{|g\rangle, |\boldsymbol{\eta}\rangle\}$ and the interaction photons, or the plasmon polaritons, $\{|\text{vac}\rangle, |\text{k}_1\rangle, |\text{k}_1, \text{k}_2\rangle, \ldots\}$, corresponding to the dipole operator $\boldsymbol{D}$ and the bosonic operator $a_{\boldsymbol{k}}$, respectively. Because of the dispersion relation (2.48) in the HD regime, the state of interaction photons can be determined solely by their wavenumber. Thus, the dressed state is defined as

$$|\varphi(t)\rangle = |\text{atom}, \text{photon}\rangle = |\text{atom}\rangle \otimes |\text{photon}\rangle, \tag{3.11}$$

where $|\text{atom}\rangle \in \{|\text{g}\rangle, |\boldsymbol{\eta}\rangle\}$ and $|\text{photon}\rangle \in \{|\text{vac}\rangle, |\text{k}\rangle, |\text{k}_1, \text{k}_2\rangle, \ldots\}$.

3.1 Time-dependent perturbation theory

Time-dependent perturbation theory can be applied when the total Hamiltonian includes a perturbed Hamiltonian proportional to a small perturbation constant. In the quantum friction Hamiltonian in Eq. (3.1), one can consider the dipole coupling d as the perturbative constant.

$$H_{\text{QF}}(t) = H_0 + dW(t), \tag{3.12}$$

where the unperturbed Hamiltonian $H_0 = H_{\text{atom}} + H_{\text{HD}}$, and $W(t) = V(t)/d$. For such a Hamiltonian, its ansatz can be defined as

$$|\varphi(t)\rangle = \sum_{n=0} b_n(t) e^{-i\omega_n t} |\varphi_n\rangle. \tag{3.13}$$

In the unperturbed system, the time dependence in the ansatz can also be expanded using the above formula, but b_n should be time-independent.

With the state function in Eq. (3.13), the time-dependent Schrödinger equation conveys that

$$i\frac{\partial}{\partial t}|\varphi(t)\rangle = H_{\text{QF}}|\varphi(t)\rangle \tag{3.14}$$

$$\Rightarrow i\sum_{n=0} \dot{b}_n(t) e^{-i\omega_n t}|\varphi_n\rangle + \sum_{n=0} \omega_n b_n(t) e^{-i\omega_n t}|\varphi_n\rangle = H_0|\varphi(t)\rangle + dW(t)|\varphi(t)\rangle. \tag{3.15}$$

Because $\sum_{n=0} \omega_n b_n(t) e^{-i\omega_n t}|\varphi_n\rangle = H_0|\varphi(t)\rangle$ in the unperturbed system, the perturbed Hamiltonian acting on the state function should give

$$i\sum_{n=0} \dot{b}_n(t) e^{-i\omega_n t}|\varphi_n\rangle = dW(t)|\varphi(t)\rangle. \tag{3.16}$$

To extract the time differential function $\dot{b}_n(t)$ on the left-hand side, one can compute

$$\langle\varphi_m|i\sum_{n=0}\dot{b}_n(t)e^{-i\omega_n t}|\varphi_n\rangle = \langle\varphi_m|dW(t)|\varphi(t)\rangle \tag{3.17}$$

$$\Rightarrow \dot{b}_m(t) = -id\sum_{n=0}W_{mn}b_n(t)e^{i\omega_{mn}t}, \tag{3.18}$$

where the transition amplitude $W_{mn} = \langle\varphi_m|W(t)|\varphi_n\rangle$, and frequency difference $\omega_{mn} = \omega_m - \omega_n$. In the above differential equation, the function $b_m(t)$ depends on the constant perturbation d, such that a general form of $b_m(t)$ can be written as an expansion of perturbative coefficients.

$$b_m(t) = \sum_{j=0} d^j b_m^{(j)}(t). \tag{3.19}$$

For the perturbative order j, the differential equation (3.18) gives

$$d^j\dot{b}_m^{(j)}(t) = -id\sum_{n=0}W_{mn}d^{j-1}b_n^{(j-1)}(t)e^{i\omega_{mn}t} \tag{3.20}$$

$$\Rightarrow b_m^{(j)}(t) = \sum_{n=0}\mathcal{F}_{mn}^{(j-1)}(t), \tag{3.21}$$

$$\text{where } \mathcal{F}_{mn}^{(j-1)}(t) = -i\int_{-\infty}^{t} ds\; W_{mn}b_n^{(j-1)}(s)e^{i\omega_{mn}s}. \tag{3.22}$$

To make the perturbative order j self-consistent in Eq. (3.22), the zeroth perturbative coefficient $b_m^{(0)}$ should be time-independent. Because the state should be normalized at any time, one can use $b_0(t=0) = b_0^{(0)} = 1$.

The state function in Eq. (3.13) can be expressed using perturbative coefficients.

$$|\varphi(t)\rangle = \sum_{n=0}\sum_{j=0}c_n^{(j)}(t)e^{-i\omega_n t}|\varphi_n\rangle, \text{ where } c_n^{(j)}(t) = d^j b_n^{(j)}(t). \tag{3.23}$$

For the system inducing quantum friction, we consider its initial state as $|g, \text{vac}\rangle$, meaning the atom is in the ground state and there are no interaction photons. Then, the possible dressed states are $|\varphi_n\rangle \in \{|g, \text{vac}\rangle, |\boldsymbol{\eta}, \boldsymbol{k}\rangle, |g, \boldsymbol{k}_1\boldsymbol{k}_2\rangle, |\boldsymbol{\eta}, \boldsymbol{k}_1\boldsymbol{k}_2\boldsymbol{k}_3\rangle, \ldots\}$, and one can write its

state function (3.11) as an expansion of the perturbative coefficients $c_n^{(j)}(t)$ in Eq. (3.23)

$$|\varphi(t)\rangle = \left(1 + \sum_{j=1} c_0^{(2j)}(t)\right)|\mathrm{g}, \mathrm{vac}\rangle + \sum_{\eta}\int d\boldsymbol{k}\ \left(\sum_{j=1} c_1^{(2j-1)}(t)\right)|\boldsymbol{\eta}, \boldsymbol{k}\rangle \tag{3.24}$$
$$+ \frac{1}{2!}\int d\boldsymbol{k}_1 d\boldsymbol{k}_2\ \left(\sum_{j=1} c_2^{(2j)}(t)\right)|\mathrm{g}, \boldsymbol{k}_1\boldsymbol{k}_2\rangle + \ldots.$$

Because we mainly focus on the low perturbative orders, the following state function is primarily used in the calculation of friction.

$$|\varphi(t)\rangle = \left(1 + c_0^{(2)}(t)\right)|\mathrm{g}, \mathrm{vac}\rangle + \sum_{\eta}\int d\boldsymbol{k}\ \left(c_1^{(1)}(t) + c_1^{(3)}(t)\right)|\boldsymbol{\eta}, \boldsymbol{k}\rangle \tag{3.25}$$
$$+ \frac{1}{2!}\int d\boldsymbol{k}_1 d\boldsymbol{k}_2\ c_2^{(2)}(t)|\mathrm{g}, \boldsymbol{k}_1\boldsymbol{k}_2\rangle + \ldots.$$

The subscript in $c_n^{(j)}$ represents the number of interaction photons, and the superscript indicates the perturbative order, which can be understood as the number of transitions between two atom states. Therefore, for the coefficients $c_n^{(j)}$, there is always $n \leq j$, and $(n-j)$ should be even. This property should also apply to the integral $\mathcal{F}_{mn}^{(j)}$ defined in Eq. (3.22), which results in

$$b_0^{(2)} = \mathcal{F}_{01}^{(1)}, \tag{3.26}$$
$$b_1^{(1)} = \mathcal{F}_{10}^{(0)}, \tag{3.27}$$
$$b_1^{(3)} = \mathcal{F}_{10}^{(2)} + \mathcal{F}_{12}^{(2)}, \tag{3.28}$$
$$b_2^{(2)} = \mathcal{F}_{21}^{(1)}. \tag{3.29}$$

3.2 Perturbative coefficients

To obtain the exact state function, we need to calculate the coefficients $b_n^{(j)}$ using Eq. (3.22). Because the initial state gives $b_0^{(0)} = 1$, we begin with the coefficient $b_1^{(1)}$.

$$b_1^{(1)}(t) = \mathcal{F}_{10}^{(0)}(t) = -i\int_{-\infty}^{t} ds\ W_{10}e^{i\omega_{10}s}, \tag{3.30}$$

where $W_{10}(t) = \langle\boldsymbol{\eta}, \boldsymbol{k}|W(t)|\mathrm{g}, \mathrm{vac}\rangle$ is the amplitude from a state with the atom in its ground state and no photons to a state with the atom in its excited state and one

dressed photon with the momentum $\boldsymbol{k}$. Because the operator $W(t) = V(t)/d$ and the interaction Hamiltonian is defined in Eq. (3.6), the element W_{10} can be expressed as

$$W_{10}(t) = \frac{1}{d}\int d\boldsymbol{k}' \, \langle \boldsymbol{\eta}, \boldsymbol{k}| \left(\boldsymbol{D}(t)\cdot i\vec{k}'\right) e^{i\boldsymbol{k}'\cdot\boldsymbol{r} - i\Omega_s t - k'z} a_{\boldsymbol{k}'}\phi_{k'} + h.c.|\mathrm{g}, \mathrm{vac}\rangle. \tag{3.31}$$

Because the bosonic operator follows $a_{\boldsymbol{k}}|\mathrm{vac}\rangle = 0$, only the Hermitian conjugate term remains in the above integrand. Due to the dipole $\boldsymbol{D}(t)$ in Eq. (3.5), the integral turns into

$$W_{10}(t) = \frac{1}{d}\int d\boldsymbol{k}' \, \langle \boldsymbol{\eta}|\boldsymbol{D}(t)|\mathrm{g}\rangle \cdot \left(i\vec{k}'\right)^* e^{-i\boldsymbol{k}'\cdot\boldsymbol{r} + i\Omega_s t - kz}\phi_{k'}\langle \boldsymbol{k}|a^\dagger_{\boldsymbol{k}'}|\mathrm{vac}\rangle \tag{3.32}$$

$$= -i\int d\boldsymbol{k}' \, e^{i\omega_b t}\left(\boldsymbol{\eta}\cdot\vec{k}'\right)^* e^{-i\boldsymbol{k}'\cdot\boldsymbol{r} + i\Omega_s t - k'z}\phi_{k'}\delta(\boldsymbol{k}-\boldsymbol{k}') \tag{3.33}$$

$$W_{10}(t) = -i\left(\boldsymbol{\eta}\cdot\vec{k}\right)^* \phi_k e^{i(\Omega_s+\omega_b)t - i\boldsymbol{k}\cdot\boldsymbol{r} - kz}. \tag{3.34}$$

Due to the movement of the atom, the position vector is $\boldsymbol{r} = (vt, 0)$, where v is the velocity of the atom. Thus, we obtain

$$W_{10}(t) = -i\left(\boldsymbol{\eta}\cdot\vec{k}\right)^* \phi_k e^{-kz} e^{i(\omega'(k)+\omega_b)t}, \tag{3.35}$$

where $\omega'(k) = \Omega_s(k) - k\cos(\theta)v$ represents the frequency changed by the Doppler shift due to the motion of the atom. Then, one can write the coefficient $b_1^{(1)}(t)$ (3.30) as follows.

$$b_1^{(1)}(t) = -\left(\boldsymbol{\eta}\cdot\vec{k}\right)^* \phi_k e^{-kz}\int_{-\infty}^{t} ds \, e^{i(\omega'(k)+\omega_b+\omega_{10})s}. \tag{3.36}$$

To ensure the integral converges at $t = -\infty$, introduce an infinitesimal parameter by setting $\omega_{10} = -i\delta^+$, where δ^+ is infinitesimally small. Thus, the above integral becomes

$$b_1^{(1)}(t) = i\left(\boldsymbol{\eta}\cdot\vec{k}\right)^* \phi_k e^{-kz}\frac{e^{i(\omega'(k)+\omega_b)t}}{\omega'(k)+\omega_b - i\delta^+}. \tag{3.37}$$

After obtaining the coefficient $b_1^{(1)}(t)$, it is possible to compute $b_0^{(2)}$, which corrects the contribution to the ground state, and $b_2^{(2)}$ which are

$$b_0^{(2)} = \mathcal{F}_{01}^{(1)} = -i\int_{-\infty}^{t} ds \, W_{01} b_1^{(1)}(s) e^{i\omega_{01}s}, \tag{3.38}$$

$$b_2^{(2)} = \mathcal{F}_{21}^{(1)} = -i\int_{-\infty}^{t} ds \, W_{21} b_1^{(1)}(s) e^{i\omega_{21}s}. \tag{3.39}$$

In the Appendix B.1, we follow the same algebra calculation and obtain

$$b_0^{(2)} = i\sum_{\boldsymbol{\eta}} \int d\boldsymbol{k} \frac{|\boldsymbol{\eta}\cdot\vec{k}|^2\phi_k^2 e^{-2kz}}{\omega'(k)+\omega_b-i\delta^+} \int_{-\infty}^{t} ds\, e^{\delta^+ s}, \tag{3.40}$$

$$b_2^{(2)} = -\frac{e^{-k_1 z-k_2 z}\left(\vec{k}_2\cdot\vec{k}_1\right)^*\phi_{k_1}\phi_{k_2}}{\omega'(k_1)+\omega'(k_2)-i\delta^+}\left(\frac{e^{i(\omega'(k_1)+\omega'(k_2))t}}{\omega'(k_2)+\omega_b-i\delta^+}+\{k_1\leftrightarrow k_2\}\right). \tag{3.41}$$

As noted earlier, the subscript n in the coefficients $b_n^{(j)}$ represents the number of interaction photons involved in the state function. We can find that the coefficient $b_2^{(2)}$ in Eq. (3.41) indeed depends on two wavenumbers, $\vec{k}_1$ and $\vec{k}_2$, while the coefficient $b_0^{(2)}$ in Eq. (3.40) has no momentum dependence, as expected.

The time integral in the coefficient $b_0^{(2)}$ Eq.(3.40) yields $e^{\delta^+ t}/\delta^+$. As δ^+ is infinitesimally small, we can approximate $e^{\delta^+ t}/\delta^+ \approx (\delta^+)^{-1}+t$. Then, we can determine the frequency shift ($\delta\omega_g$)and the inverse lifetime (γ_g) of the ground state as follows [28].

$$d^2 b_0^{(2)}(t) \approx i d^2 \sum_{\eta}\int d\boldsymbol{k}\, \frac{\left|\boldsymbol{\eta}\cdot\vec{k}\right|^2|\phi_k|^2 e^{-2kz}}{\omega'(k)+\omega_b-i\delta^+}t = -i\delta\omega_g t - \frac{\gamma_g t}{2}. \tag{3.42}$$

γ_g is the decay rate of the ground state, which can also be obtained from Fermi's golden rule.

$$\gamma_g = \sum_{\eta}\int d\boldsymbol{k}\ |V_{01}(t)|^2\,\delta(\omega_b+\omega'(k)), \tag{3.43}$$

The delta function is the nascent delta function found by the Sokhotski-Plemelj theorem in the Appendix C.

The last perturbative coefficient, b_1^3, consists of two parts.

$$b_1^{(3)}(t) = \mathcal{F}_{10}^{(2)}+\mathcal{F}_{12}^{(2)} = -i\int_{-\infty}^{t} ds\, W_{10} b_0^{(2)} e^{i\omega_{10}s} - i\int_{-\infty}^{t} ds\, W_{12} b_2^{(2)} e^{i\omega_{12}s}. \tag{3.44}$$

The first term, which contains the coefficient $b_0^{(2)}$, represents the process via vacuum, while the second term, consisting of the coefficient $b_2^{(2)}$, can be considered as the process via two dressed photons. In the Appendix B.2, one can obtain these two terms via the

expressions of $b_0^{(2)}$ and $b_2^{(2)}$ in Eqs. (3.42) and (3.41), respectively.

$$b_1^{(3)} = \frac{i\phi_k e^{-kz} e^{i(\omega'(k)+\omega_b)t}}{\omega'(k)+\omega_b - i\delta^+}\Bigg[- \frac{\left(\boldsymbol{\eta}\cdot\vec{k}\right)^*}{d^2}\left(i\delta\omega_g + \frac{\gamma_g}{2}\right)\left(t + \frac{i}{\omega'(k)+\omega_b - i\delta^+}\right) \\ + \int d\boldsymbol{k}'\; e^{-2k'z}\frac{\left(\vec{k}\cdot\vec{k}'\right)^*\left(\boldsymbol{\eta}\cdot\vec{k}'\right)^*\phi_{k'}^2}{\omega'(k)+\omega'(k')-i\delta^+}\left(\frac{1}{\omega'(k')+\omega_b-i\delta^+} + \{k\leftrightarrow k'\}\right)\Bigg], \tag{3.45}$$

where the first and second terms are $\mathcal{F}_{10}^{(2)}$ and $\mathcal{F}_{12}^{(2)}$, respectively.

We can now derive the perturbative order term $c_n^{(r)}$ (as given in Eq. (3.23)) up to the third order in the state function $|\varphi(t)\rangle$ (as shown in Eq. (3.25)) from $b_n^{(d)}$ in Eqs. (3.37), (3.41), (3.42) and (3.45).

$$c_1^{(1)}(t,\boldsymbol{k}) = id\left(\boldsymbol{\eta}\cdot\vec{k}\right)^*\phi_k e^{-kz}\frac{e^{i(\omega'(k)+\omega_b)t}}{\omega'(k)+\omega_b-i\delta^+}, \tag{3.46}$$

$$c_0^{(2)}(t) = -i\delta\omega_g t - \frac{\gamma_g t}{2}, \tag{3.47}$$

$$c_2^{(2)}(t,\boldsymbol{k}_1,\boldsymbol{k}_2) = -d^2\frac{e^{-k_1z-k_2z}\left(\vec{k}_2\cdot\vec{k}_1\right)^*\phi_{k_1}\phi_{k_2}}{\omega'(k_1)+\omega'(k_2)-i\delta^+} \\ \times\left(\frac{e^{i(\omega'(k_1)+\omega'(k_2))t}}{\omega'(k_2)+\omega_b-i\delta^+} + \{k_1\leftrightarrow k_2\}\right), \tag{3.48}$$

$$c_1^{(3)}(t) = c_{1,a}^{(3)} + c_{1,b}^{(3)}, \tag{3.49}$$

where $c_{1,a}^{(3)} = d^3\mathcal{F}_{10}^{(2)}$ and $c_{1,b}^{(3)} = d^3\mathcal{F}_{12}^{(2)}$, and their explicit expressions are given by

$$c_{1,a}^{(3)} = -\frac{id\phi_k e^{-kz} e^{i(\omega'(k)+\omega_b)t}}{\omega'(k)+\omega_b - i\delta^+} \left(\boldsymbol{\eta}\cdot\vec{k}\right)^* \left(i\delta\omega_g + \frac{\gamma_g}{2}\right) \tag{3.50}$$

$$\times \left(t + \frac{i}{\omega'(k)+\omega_b - i\delta^+}\right)$$

$$= c_1^{(1)}(t)\, c_0^{(2)}(t) \left(1 + \frac{i/t}{\omega'(k)+\omega_b - i\delta^+}\right), \tag{3.51}$$

$$c_{1,b}^{(3)} = \frac{id^3\phi_k e^{-kz} e^{i(\omega'(k)+\omega_b)t}}{\omega'(k)+\omega_b - i\delta^+} \int d\boldsymbol{k}'\; e^{-2k'z} \frac{\left(\vec{k}\cdot\vec{k}'\right)^* \left(\boldsymbol{\eta}\cdot\vec{k}'\right)^* \phi_{k'}^2}{\omega'(k)+\omega'(k')-i\delta^+} \tag{3.52}$$

$$\times \left(\frac{1}{\omega'(k')+\omega_b - i\delta^+} + \{k \leftrightarrow k'\}\right)$$

$$= -\frac{c_1^{(1)}(t,\boldsymbol{k})}{\left(\boldsymbol{\eta}\cdot\vec{k}\right)^* \phi_k} \int d\boldsymbol{k}'\; e^{kz-k'z} \phi_{k'} e^{-i(\omega'(k)+\omega'(k'))t} \left(\boldsymbol{\eta}\cdot\vec{k}'\right)^* c_2^{(2)}(t,\boldsymbol{k},\boldsymbol{k}'). \tag{3.53}$$

3.3 Summary of the time evolution of the state functions

In this chapter, we have employed time-dependent perturbation theory to compute the state functions within the quantum friction system. The state function $|\varphi(t)\rangle$ is a tensor product of the states of the moving atom and the interaction photons, illustrated in Eq. (3.11). We consider the dipole coupling in the atom, d, as the perturbation constant, and consequently derive the perturbative coefficients up to the third order in Eqs. (3.46)-(3.49). These coefficients encode the information of the HD model through the eigenmodes ϕ_k, while the motion of the atom and the dispersion relation are encapsulated within the frequency $\omega'(k) = \Omega_s(k) - k\cos(\theta)v$, where v represents the velocity of the atom and $\Omega_s(k)$ conforms to the dispersion relation specified in Eq. (2.48).

To calculate the average friction up to the fourth perturbative order, one can compute $\langle\varphi(t)|F_x|\varphi(t)\rangle$, where F_x represents the force operator as defined in Eq. (3.9). The friction is derived as follows.

$$\langle\varphi(t)|F_x|\varphi(t)\rangle \approx 2\mathrm{Re}\Bigg\{\sum_\eta \int d\boldsymbol{k}\; \langle \mathrm{g},\mathrm{vac}|F_x|\boldsymbol{\eta},\boldsymbol{k}\rangle \left[c_1^{(1)}(t) + c_0^{(2)*}(t)c_1^{(1)}(t) + c_1^{(3)}(t)\right] \tag{3.54}$$

$$+ \frac{1}{2}\sum_\eta \int d\boldsymbol{k}_1 d\boldsymbol{k}_2\; \langle \boldsymbol{\eta},\boldsymbol{k}|\hat{F}_x|\mathrm{g},\boldsymbol{k}_1\boldsymbol{k}_2\rangle c_1^{(1)*}(t) c_2^{(2)}(t)\Bigg\}.$$

Because of $F_x \propto d$, Eq. (3.54) encompasses the quantum friction arising from the second and fourth perturbative order forces. In the upcoming chapter, we will calculate the friction forces at the second and fourth perturbative orders, allowing us to assess the impact of dispersion and sound speed on quantum friction.

Chapter 4

Quantum friction between plates in the hydrodynamic regime

Using time-dependent perturbation theory, we have evaluated the state function up to the third perturbative order as shown in Eq. (3.25) with the corresponding perturbative coefficients given in Eqs. (3.46)-(3.49). The expectation value of quantum friction can then be written as $\langle\varphi(t)|F_x|\varphi(t)\rangle$ in Eq. (3.54), and from $\langle\varphi(t)|F_x|\varphi(t)\rangle$ one can identify the contribution to order d^2 which is given by

$$\langle F_x\rangle^{(2)} = 2\mathrm{Re}\sum_{\eta}\int d\boldsymbol{k}\ \langle \mathrm{g},\mathrm{vac}|F_x|\boldsymbol{\eta},\boldsymbol{k}\rangle c_1^{(1)}(t). \tag{4.1}$$

The remaining contribution in Eq. (3.54) is the fourth perturbative order force, which can be divided into two parts: one arising from processes involving a transition through vacuum, $\langle F_x\rangle_0^{(4)}$, and the other involving the creation of two photons, $\langle F_x\rangle_2^{(4)}$.

$$\langle F_x\rangle^{(4)} = \langle F_x\rangle_0^{(4)} + \langle F_x\rangle_2^{(4)}, \tag{4.2}$$

$$\text{where } \langle F_x\rangle_0^{(4)} = 2\mathrm{Re}\sum_{\eta}\int d\boldsymbol{k}\ \langle \mathrm{g},\mathrm{vac}|F_x|\boldsymbol{\eta},\boldsymbol{k}\rangle \left(c_0^{(2)*}(t)\ c_1^{(1)}(t) + c_{1,a}^{(3)}\right), \tag{4.3}$$

$$\langle F_x\rangle_2^{(4)} = 2\mathrm{Re}\Bigg\{\sum_{\eta}\int d\boldsymbol{k}\ \langle \mathrm{g},\mathrm{vac}|F_x|\boldsymbol{\eta},\boldsymbol{k}\rangle c_{1,b}^{(3)} + \frac{1}{2}\sum_{\eta}\int d\boldsymbol{k}_1 d\boldsymbol{k}_2\ \langle \boldsymbol{\eta},\boldsymbol{k}|F_x|\mathrm{g},\boldsymbol{k}_1\boldsymbol{k}_2\rangle c_1^{(1)*}(t,\boldsymbol{k}) c_2^{(2)}(t,\boldsymbol{k}_1,\boldsymbol{k}_2)\Bigg\}. \tag{4.4}$$

The coefficients $c_{1,a}^{(3)}$ and $c_{1,b}^{(3)}$ are give in Eqs. (3.51) and (3.52), respectively. In the

upcoming sections, we will demonstrate the calculation of the second-order force $\langle F_x\rangle^{(2)}$ and the fourth-order force $\langle F_x\rangle^{(4)}$.

4.1 The second-order force

Using the expression for the force operator F_x in Eq. (3.9) and the coefficient $c_1^{(1)}$ in Eq. (3.46), the second-order force in Eq. (4.1) can be written as follows.

$$\langle F_x\rangle^{(2)} = -2\mathrm{Re}\sum_\eta \int_0^\infty dk \int_{-\pi}^{\pi} d\theta\ \phi_k k^2 \cos(\theta) e^{-kz} \times e^{-i\omega'(k)t}\left(\langle \mathrm{g}|D(t)|\boldsymbol{\eta}\rangle\cdot\vec{k}\right) id\left(\boldsymbol{\eta}\cdot\vec{k}\right)^* \phi_k e^{-kz}\frac{e^{i(\omega'(k)+\omega_b)t}}{\omega'(k)+\omega_b-i\delta^+}. \tag{4.5}$$

Here, the Hermitian conjugate vanishes due to the bosonic creation operator, i.e., $\langle \mathrm{vac}|a^\dagger_{\boldsymbol{k}'}|\boldsymbol{k}\rangle = 0$.The dipole operator, as described by Eq. (3.5), leads to

$$\langle F_x\rangle^{(2)} = -2d^2\mathrm{Re}\int_0^\infty dk \int_{-\pi}^{\pi} d\theta\ \phi_k^2 k^2 \cos(\theta) e^{-2kz}\frac{i\sum_\eta|\boldsymbol{\eta}\cdot\vec{k}|^2}{\omega'(k)+\omega_b-i\delta^+}. \tag{4.6}$$

As mentioned around Eq. (3.4), the unit vector $\boldsymbol{\eta}$ is taken from an orthonormal basis, so that $\sum_\eta|\boldsymbol{\eta}\cdot\vec{k}|^2 = |\vec{k}|^2$. To satisfy the Laplace equation in vacuum, we defined the vector $\vec{k} = (k\cos(\theta), k\sin(\theta), ik)$ ensuring that $\nabla^2[\exp(i\vec{k}\cdot\vec{r})] \equiv 0$. This leads to the second-order force

$$\langle F_x\rangle^{(2)} = -4d^2\mathrm{Re}\int_0^\infty dk \int_{-\pi}^{\pi} d\theta\ \phi_k^2 k^4 \cos(\theta) e^{-2kz}\frac{i}{\omega'(k)+\omega_b-i\delta^+}. \tag{4.7}$$

Using the eigenmode of the HD model, $\phi_k = \omega_p^2\Big/\sqrt{4\pi k\Omega_s(k)\left(\omega_p^2+2\Omega_s^2(k)\right)}$, results in

$$\langle F_x\rangle^{(2)} = -d^2\int_0^\infty dk\ \frac{\omega_p^4 k^3 e^{-2kz}}{\pi\Omega_s(k)\left(\omega_p^2+2\Omega_s^2(k)\right)} \times \int_{-\pi}^{\pi} d\theta\ \cos(\theta)\mathrm{Re}\left(\frac{i}{\omega'(k)+\omega_b-i\delta^+}\right). \tag{4.8}$$

In the Appendix C, one can approximate $\mathrm{Re}\left[i\left(\omega'(k)+\omega_b-i\delta^+\right)^{-1}\right]$ to a nascent delta function $-\pi\delta(\omega'(k)+\omega_b)$ when $\delta^+\to 0^+$.

$$\langle F_x\rangle^{(2)} = d^2\int_0^\infty dk\ \frac{\omega_p^4 k^3 e^{-2kz}}{\Omega_s(k)\left(\omega_p^2+2\Omega_s^2(k)\right)}\int_{-\pi}^{\pi} d\theta\ \cos(\theta)\delta\left(\omega'(k)+\omega_b\right). \tag{4.9}$$

Since the integrand with respect to the angle θ in the integral is an even function of θ, the interval of the integral can be halved by simply adding a prefactor of 2. Recalling that the frequency with the Doppler effect is given by $\omega'(k) = \Omega_s(k) - kv\cos(\theta)$, the peak of the delta function $\delta\left(\omega'(k) + \omega_b\right)$ is located at $\cos(\theta) = (\Omega_s(k) + \omega_b)/kv$ which is positive if we assume the atom's velocity v is positive. By substituting that $u = \cos(\theta)$, we obtain the integral with respect to the angle θ as follows.

$$\int_{-\pi}^{\pi} d\theta\ \cos(\theta)\delta\left(\omega'(k) + \omega_b\right) = 2\int_0^1 \frac{du}{\sqrt{1-u^2}}\frac{u}{kv}\delta\left(\frac{\Omega_s(k)+\omega_b}{kv} - u\right) \tag{4.10}$$

$$\times\,\Theta\left(kv - \Omega_s(k) - \omega_b\right),$$

$$= \frac{2(\Omega_s(k)+\omega_b)\Theta\left(kv - \Omega_s(k) - \omega_b\right)}{kv\sqrt{(kv)^2 - (\Omega_s(k)+\omega_b)^2}} \tag{4.11}$$

where $\Theta\left(kv - \Omega_s(k) - \omega_b\right)$ is the Heaviside step function ensuring that $\cos(\theta) = (\Omega_s(k) + \omega_b)/kv \leq 1$. Therefore, the second-order force in Eq. (4.9) is simplified to

$$\langle F_x\rangle^{(2)} = \frac{2d^2\omega_p^4}{v}\int_0^\infty dk\ \frac{k^2 e^{-2kz}}{\Omega_s(k)\left(\omega_p^2 + 2\Omega_s^2(k)\right)}\frac{(\Omega_s(k)+\omega_b)\Theta\left(kv - \Omega_s(k) - \omega_b\right)}{\sqrt{(kv)^2 - (\Omega_s(k)+\omega_b)^2}}. \tag{4.12}$$

As aforementioned in Chapter 2, the HD model exhibits a dispersion relation in the surface modes, as shown in Eq. (2.48).

$$\Omega_s(k) = \frac{1}{2}\left(\sqrt{(2\omega_p^2 + v_s^2k^2)} + v_sk\right) \Rightarrow \begin{cases} k = \dfrac{2\Omega_s^2 - \omega_p^2}{2v_s\Omega_s}, \\ dk = \dfrac{2\Omega_s^2 + \omega_p^2}{2v_s\Omega_s^2}d\Omega_s. \end{cases} \tag{4.13}$$

By defining the following dimensionless variables,

$$\tilde{v} = \frac{v}{v_s}, \qquad \tilde{\omega} = \frac{\omega_b}{\omega_p}, \qquad \tilde{\Omega} = \frac{\Omega_s}{\omega_p}, \qquad \tilde{z} = \frac{z\omega_p}{v_s}, \tag{4.14}$$

we obtain the dispersion relation as

$$k = \frac{2\tilde{\Omega}^2 - 1}{2\tilde{\Omega}}\frac{\omega_p}{v_s}, \qquad dk = \frac{2\tilde{\Omega}^2 + 1}{2\tilde{\Omega}^2}\frac{\omega_p}{v_s}d\tilde{\Omega}. \tag{4.15}$$

From the Appendix D, we substitute the momentum with the dimensionless variable $\tilde{\Omega}$ as follows.

$$\langle F_x\rangle^{(2)} = \frac{d^2\omega_p^4}{2\tilde{v}v_s^4}\int_{1/\sqrt{2}}^{\infty} d\tilde{\Omega}\,\Theta\left(\frac{2\tilde{\Omega}^2-1}{2\tilde{\Omega}}\tilde{v}-\tilde{\Omega}-\tilde{\omega}\right) \times \frac{(\tilde{\Omega}+\tilde{\omega})(2\tilde{\Omega}^2-1)^2 e^{-(2\tilde{\Omega}^2-1)\tilde{z}/\tilde{\Omega}}}{\tilde{\Omega}^4\sqrt{(2\tilde{\Omega}^2\tilde{v}-\tilde{v})^2-4\tilde{\Omega}^2(\tilde{\Omega}+\tilde{\omega})^2}}. \tag{4.16}$$

In the expression in Eq. (4.16), the integral is dimensionless because the Heaviside step function is dimensionless. The dimension of the second-order force is factored out into the prefactor, which corresponds to $d^2\omega_p^2/v_s^4$. This is identical to the dimension of the Casimir-Polder static force, $F_{CP} = -3\alpha c/(2\pi z^5)$ [2], where c is the speed of light and the polarizability is $\alpha = 2d^2/\omega_b$. Thus, the normalized second-order force $\langle f_x\rangle^{(2)} = \langle F_x\rangle^{(2)}/F_{CP}$.

$$\langle f_x\rangle^{(2)} = \frac{\pi\tilde{\omega}\tilde{z}^5 v_s}{6\tilde{v}c}\int_{1/\sqrt{2}}^{\infty} d\tilde{\Omega}\,\Theta\left(\frac{2\tilde{\Omega}^2-1}{2\tilde{\Omega}}\tilde{v}-\tilde{\Omega}-\tilde{\omega}\right) \times \frac{(\tilde{\Omega}+\tilde{\omega})(2\tilde{\Omega}^2-1)^2 e^{-(2\tilde{\Omega}^2-1)\tilde{z}/\tilde{\Omega}}}{\tilde{\Omega}^4\sqrt{(2\tilde{\Omega}^2\tilde{v}-\tilde{v})^2-4\tilde{\Omega}^2(\tilde{\Omega}+\tilde{\omega})^2}}. \tag{4.17}$$

The Heaviside function in the normalized second-order force (4.17) might change the boundary limits of the integral. Therefore, we will perform the analytic calculation of the Heaviside function, followed by numerical analysis.

4.1.1 The Heaviside step function

The Heaviside function in the second-order force $\langle f_x\rangle^{(2)}$ (4.17) will not vanish, when

$$\frac{2\tilde{\Omega}^2-1}{2\tilde{\Omega}}\tilde{v}-\tilde{\Omega}-\tilde{\omega}>0 \Rightarrow 2\tilde{\Omega}^2(\tilde{v}-1)-2\tilde{\omega}\tilde{\Omega}-\tilde{v}>0. \tag{4.18}$$

As defined in Eq. (4.14), all of these dimensionless variables should be positive, so that $\tilde{v}=v/v_s$ must be greater than one to satisfy the non-vanishing Heaviside function. This means that the second-order force vanishes when the atom's velocity v is smaller than the sound speed v_s.

$$\langle f_x\rangle^{(2)}(\tilde{v}<1)=0. \tag{4.19}$$

In perturbation theory up to this order, only one (virtual) photon can be stimulated out of the (dressed) vacuum due to the interaction with the moving atom. When the atom's velocities are too low, the energy supplied by the external source maintaining the particle's constant speed is insufficient to excite the material. Consequently, no friction is generated. A comparable threshold was observed in the case of graphene [43], where for relative velocities between the plates smaller than the Fermi velocity of graphene, no fermion could be stimulated in the material, resulting in the disappearance of the frictional force at the lowest perturbative order.

In the context of the HD model, we offer a straightforward visual interpretation of this outcome in Fig. 4.3. When the atom is in motion, the electrons within the plate will reconfigure to ensure that its reflection (formed by image charges) keeps pace with the atom's movement. The speed at which the electrons can reorganize and propagate through the material is constrained by the sound speed. In scenarios where $v \leq v_s$, the image charge of the atom will match its speed. Consequently, the force between the dipole and its image charge will consistently align along the perpendicular axis, resulting in the elimination of frictional force. From the perspective of energy conservation, the presence of the delta function in Eq. (4.9). establishes a resonant condition. According to the dispersion relation (2.48), this resonance is necessitated by

$$\omega_b + \frac{1}{2}\left(\sqrt{2\omega_p^2 + v_s^2 k^2} - v_s k\right) + (v_s - v\cos\theta)\, k = 0. \tag{4.20}$$

The positivity of the first two terms necessitates that the third term be negative. This inference indicates that $v > v_s$ is a requisite condition for resonance to occur.

We consider the atom's velocity exceeds the sound speed ($\tilde{v} > 1$), and define

$$h(\tilde{\Omega}) = 2\tilde{\Omega}^2\,(\tilde{v} - 1) - 2\tilde{\omega}\tilde{\Omega} - \tilde{v}. \tag{4.21}$$

One can find the root of $h(\tilde{\Omega})$ as follows.

$$\tilde{\Omega}_{\pm} = \frac{\tilde{\omega} \pm \sqrt{\tilde{\omega}^2 + 2\tilde{v}(\tilde{v} - 1)}}{2(\tilde{v} - 1)}. \tag{4.22}$$

Since $\tilde{v} > 1$, we can determine that $\tilde{\omega} < \sqrt{\tilde{\omega}^2 + 2(\tilde{v} - 1)\tilde{v}}$ and the relatively smaller root Ω_- should be negative. Therefore, the Heaviside step function in the second-order force (4.17) will not vanish in the interval

$$\tilde{\Omega} \in \left[\frac{\tilde{\omega} + \sqrt{\tilde{\omega}^2 + 2\tilde{v}(\tilde{v} - 1)}}{2(\tilde{v} - 1)}, \infty\right), \text{ for } \tilde{v} > 1. \tag{4.23}$$

As shown in Eq. (4.17), the lower limit in the integral is $1/\sqrt{2}$, and one can derive the positive root $\tilde{\Omega}_+$ as

$$\tilde{\Omega}_+ = \frac{\tilde{\omega} + \sqrt{\tilde{\omega}^2 + 2\tilde{v}(\tilde{v}-1)}}{2(\tilde{v}-1)} \tag{4.24}$$

$$= \frac{1}{\sqrt{2}} \left(\frac{\tilde{\omega}^2 + 2\tilde{\omega}\sqrt{\tilde{\omega}^2 + 2\tilde{v}(\tilde{v}-1)} + \tilde{\omega}^2 + 2\tilde{v}(\tilde{v}-1)}{2(\tilde{v}-1)^2} \right)^{1/2} \tag{4.25}$$

$$= \frac{1}{\sqrt{2}} \left(\frac{\tilde{\omega}^2 + 2\tilde{\omega}\sqrt{\tilde{\omega}^2 + 2\tilde{v}(\tilde{v}-1)} + \tilde{\omega}^2}{2(\tilde{v}-1)^2} + \frac{\tilde{v}}{\tilde{v}-1} \right)^{1/2}. \tag{4.26}$$

Since $\tilde{v} > \tilde{v} - 1$ for $\tilde{v} > v_s$, it is affirmed that the root $\tilde{\Omega}_+ > 1/\sqrt{2}$. Consequently, the range of the non-vanishing Heaviside step function in Eq. (4.23) is a subset of the interval $[1/\sqrt{2}, \infty)$. This leads to modifications in the boundary of the normalized second-order force, as given by Eq. (4.17), as follows.

$$\langle f_x \rangle^{(2)} = \frac{\pi \tilde{\omega} \tilde{z}^5 v_s}{6\tilde{v}c} \int_{\Omega_+}^{\infty} d\tilde{\Omega}\, \frac{(\tilde{\Omega} + \tilde{\omega})(2\tilde{\Omega}^2 - 1)^2 e^{-(2\tilde{\Omega}^2 - 1)\tilde{z}/\tilde{\Omega}}}{\tilde{\Omega}^4 \sqrt{(2\tilde{\Omega}^2\tilde{v} - \tilde{v})^2 - 4\tilde{\Omega}^2(\tilde{\Omega} + \tilde{\omega})^2}}, \tag{4.27}$$

where the lower limit $\tilde{\Omega}_+ = \left(\tilde{\omega} + \sqrt{\tilde{\omega}^2 + 2\tilde{v}(\tilde{v}-1)}\right)/(2\tilde{v}-2)$ is derived as a consequence of the Heaviside step function.

4.1.2 Numerical analysis of the second-order force

The integral in Eq. (4.27) converges as it approaches infinity and can be numerically solved. For this purpose, we will employ the parameters specified for the model as presented in Table 4.1. The chosen values correspond to typical characteristics of metals and experimental configurations well within the confines of our analysis, specifically, the non-retarded and near-field limits.

In Fig. 4.1, we depict the normalized frictional force (4.27) as a function of the dimensionless velocity of the atom. The expected behavior of the force increasing with velocity and decreasing with the gap distance is evident. While we have previously demonstrated analytically the existence of a threshold leading to a non-vanishing force only for $v > \beta$, the plots in the figure reveal that the force can exponentially diminish even for higher velocities. This effective threshold escalates with the gap distance and diminishes with the plasma frequency ω_p. As mentioned earlier, the sound speed typically has a magnitude around 10^6 m/s, approximately 1% of the speed of light in a vacuum. To

Model parameter	Range
Plasma Frequency (ω_p)	$10^{15} - 10^{16}$ s^{-1}
Sound Speed (v_s)	$10^6 - 10^7$ ms^{-1}
Gap Distance (z)	$10 - 100$ nm
Bohr Transition Frequency(ω_b)	$10^{15} - 10^{16}$ s^{-1}
Dimensionless parameter	**Range**
$\tilde{v}$ (v/v_s)	$1 - 20$
$\tilde{\omega}$ (ω_b/ω_p)	$0.1 - 2$
$\tilde{z}$ ($z\omega_p/v_s$)	$10 - 1000$

Table 4.1: Range of magnitudes considered for the different parameters of the model.

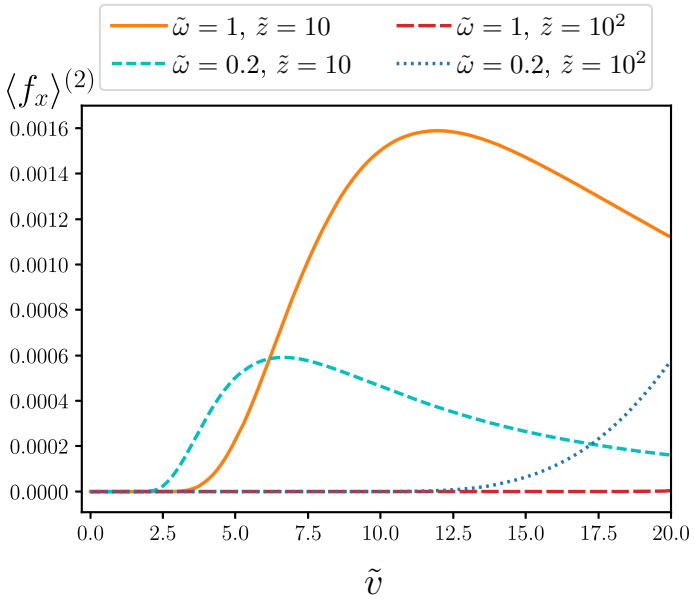

Figure 4.1: **The second-order force as a function of the atom's speed.** The force in Eq. (4.27) is normalized by the static Casimir-Polder force, and the velocity is normalized as $\tilde{v} = v/\beta$, where β represents the sound speed in the material. The parameters are considered as $\tilde{\omega} = \omega_p/\omega_b = 0.2, 1$ and $\tilde{z} = z\omega_p/\beta = 10, 100$. The sound speed is taken as $\beta = 10^6$m/s.

ascertain whether quantum friction may also manifest at lower speeds, we will examine the fourth-order force in perturbation theory in the subsequent sections of this chapter.

4.1.3 The non-dispersive limit

The non-dispersive limit is realized by $v_s \to 0$, which causes the dispersion relation (2.48) to become a momentum-independent surface-plasmon frequency: $\Omega_s = \omega_p/\sqrt{2}$. Accordingly, we can rederive the second-order force from the expression in Eq. (4.12).

$$\langle F_x \rangle^{(2)}_{v_s=0} = \frac{2d^2\omega_p^4}{v}\int_0^\infty dk\, \frac{k^2 e^{-2kz}}{\sqrt{2}\omega_p^3}\frac{(\omega_p/\sqrt{2}+\omega_b)\Theta\left(kv-\omega_p/\sqrt{2}-\omega_b\right)}{\sqrt{(kv)^2-(\omega_p/\sqrt{2}+\omega_b)^2}}. \tag{4.28}$$

The Heaviside function will not vanish, when

$$k > k_0, \text{ where } k_0 = \frac{\omega_p/\sqrt{2}+\omega_b}{v}. \tag{4.29}$$

Since we assume the atom's speed v is positive, the Heaviside function shifts the lower limit of the integral from 0 to k_0.

$$\langle F_x \rangle^{(2)}_{v_s=0} = \frac{\sqrt{2}d^2\omega_p}{v}\int_{k_0}^\infty dk\, k^2 e^{-2kz}\frac{k_0}{\sqrt{k^2-k_0^2}}. \tag{4.30}$$

One can normalize this force using the Casimir-Polder static force $F_{CP} = 3\alpha c/(2\pi z^5)$, and by substituting k with $k' = k/k_0$, we derive the second-order force in the non-dispersive limit as follows.

$$\langle f_x \rangle^{(2)}_{v_s=0} = \frac{\sqrt{2}\pi\omega_p\omega_b z^5 k_0^3}{3vc}\int_1^\infty dk'\, k'^2 e^{-(2zk_0)k'}\frac{1}{\sqrt{k'^2-1}} \tag{4.31}$$

$$= \frac{\sqrt{2}\pi\omega_p\omega_b z^5 k_0^3}{3vc}\left(\mathcal{K}_2(2zk_0) - \frac{\mathcal{K}_1(2zk_0)}{2zk_0}\right), \tag{4.32}$$

where $\mathcal{K}_n(x)$ is the modified Bessel functions of the second kind.

To understand the relative influence of dispersion on the frictional force, we will compare the non-dispersive force (4.32) with the normalized force given in Eq. (4.27). Here, we define the ratio between two forces as σ_f which is given by

$$\sigma_f = \frac{\langle f_x \rangle^{(2)}}{\langle f_x \rangle^{(2)}_{v_s=0}} = \left(\frac{\tilde{v}}{1+\sqrt{2}\tilde{\omega}}\right)^3 \frac{\int_{\Omega_+}^\infty d\tilde{\Omega}\, \frac{(\tilde{\Omega}+\tilde{\omega})(2\tilde{\Omega}^2-1)^2 e^{-\left(2\tilde{\Omega}^2-1\right)\tilde{z}/\tilde{\Omega}}}{\tilde{\Omega}^4\sqrt{(2\tilde{\Omega}^2\tilde{v}-\tilde{v})^2-4\tilde{\Omega}^2(\tilde{\Omega}+\tilde{\omega})^2}}}{\mathcal{K}_2(2zk_0)-\mathcal{K}_1(2zk_0)/(2zk_0)}. \tag{4.33}$$

Fig. 4.2 shows a numerical analysis when $\tilde{z} = 10$ and $\tilde{\omega} = 1$ and 0.2. In this context, we observe that as the speed ratio $\tilde{v}$ increases sufficiently, the dispersion effect becomes

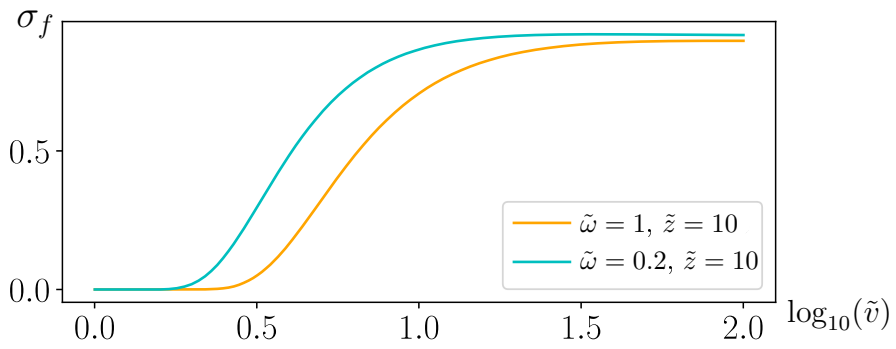

Figure 4.2: **The comparison of non-dispersive limits.** In this figure, we illustrate the ratio of the frictional force in the dispersive and non-dispersive regimes (σ_f defined in Eq. (4.33)) as a function of $\tilde{v}$. The parameters are chosen as follows: $\tilde{\omega} = \omega_p/\omega_b = 0.2, 1$ and $\tilde{z} = z\omega_p/v_s = 10$. The sound speed is taken as $v_s = 10^6$m/s.

negligible, converging towards σ_f tending to one. Based on our numerical simulations, it is indicated that the dispersion effect can be disregarded when the velocity v of the atom exceeds the sound speed v_s by approximately a factor of ten. Hence, we conclude that in materials characterized by a low sound speed, transitioning to the non-dispersive limit is unlikely to significantly affect the results of the frictional force. Conversely, in materials featuring a high sound speed, the frictional force is suppressed by the dispersion effect when the atom's velocity fails to reach a sufficiently high threshold.

4.2 The fourth-order force

We have examined the second-order force in the previous section, and our current focus is on investigating the subsequent higher-order perturbative term, specifically, the fourth-order force. Without loss of generality, we express the fourth-order force as Eq. (4.2), which is comprised of two components: the transition via vacuum, $\langle F_x \rangle_0^{(4)}$ (4.3), and the transition via two photons, $\langle F_x \rangle_2^{(4)}$ (4.4).

4.2.1 The transitions via vacuum

Using the coefficient $c_0^{(2)}$, $c_1^{(1)}$ and $c_{1,a}^{(3)}$ in Eqs. (3.47), (3.46) and (3.51), respectively, the contribution to the fourth-order force associated with the transition via vacuum, as given

in Eq. (4.3), is expressed as follows.

$$\langle F_x\rangle_0^{(4)} = 2\mathrm{Re}\sum_\eta \int d\boldsymbol{k}\ \langle \mathrm{g}, \mathrm{vac}|F_x|\boldsymbol{\eta},\boldsymbol{k}\rangle \tag{4.34}$$

$$\times\left(c_0^{(2)*}(t)\ c_1^{(1)}(t) + c_1^{(1)}(t)\ c_0^{(2)}(t)\left(1+\frac{i/t}{\omega'(k)+\omega_b-i\delta^+}\right)\right)$$

$$= 2\mathrm{Re}\sum_\eta \int d\boldsymbol{k}\ \langle \mathrm{g}, \mathrm{vac}|F_x|\boldsymbol{\eta},\boldsymbol{k}\rangle c_1^{(1)}(t)\left(-\gamma_g t + \frac{ic_0^{(2)}(t)/t}{\omega'(k)+\omega_b-i\delta^+}\right). \tag{4.35}$$

Because of the expression of the second-order force in Eq. (4.1), one can find $\langle F_x\rangle_0^{(4)}$ as

$$\langle F_x\rangle_0^{(4)} = -\gamma_g t\langle F_x\rangle^{(2)} + 2\mathrm{Re}\sum_\eta \int d\boldsymbol{k}\ \langle \mathrm{g}, \mathrm{vac}|F_x|\boldsymbol{\eta},\boldsymbol{k}\rangle \frac{ic_1^{(1)}(t)c_0^{(2)}(t)/t}{\omega'(k)+\omega_b-i\delta^+} \tag{4.36}$$

$$= -\gamma_g t\langle F_x\rangle^{(2)} - 2\mathrm{Re}\left\{\frac{c_0^{(2)}(t)d^2}{t}\int d\boldsymbol{k}\ \phi_k^2\sum_\eta |\boldsymbol{\eta}\cdot\vec{k}|^2 e^{-2kz}\frac{k\cos(\theta)}{(\omega'(k)+\omega_b-i\delta^+)^2}\right\}.$$

Given that the frequency $\omega'(k) = \Omega_s - kv\cos(\theta)$, one can find that

$$\frac{\partial}{\partial v}\left(\frac{1}{\omega'(k)+\omega_b-i\delta^+}\right) = \frac{-\partial\omega'(k)/\partial v}{(\omega'(k)+\omega_b-i\delta^+)^2} = \frac{k\cos(\theta)}{(\omega'(k)+\omega_b-i\delta^+)^2}. \tag{4.37}$$

Hence, $\langle F_x\rangle_0^{(4)}$ can be expressed as

$$\langle F_x\rangle_0^{(4)} = -\gamma_g t\langle F_x\rangle^{(2)} - 2\mathrm{Re}\left\{\frac{c_0^{(2)}(t)}{t}\frac{\partial}{\partial v}\left(\int d\boldsymbol{k}\ \frac{d^2\phi_k^2\sum_\eta|\boldsymbol{\eta}\cdot\vec{k}|^2e^{-2kz}}{\omega'(k)+\omega_b-i\delta^+}\right)\right\}. \tag{4.38}$$

Considering how we approximate the coefficient $b_0^{(2)}$ in Eq. (3.42), the integral in the second term of $\langle F_x\rangle_0^{(4)}$ can be expressed as

$$\langle F_x\rangle_0^{(4)} \approx -\gamma_g t\langle F_x\rangle^{(2)} - 2\mathrm{Re}\left\{\frac{c_0^{(2)}(t)}{t}\times\frac{\partial}{\partial v}\left(\frac{-ic_0^{(2)}(t)}{t}\right)\right\} \tag{4.39}$$

$$= -\gamma_g t\langle F_x\rangle^{(2)} - 2\mathrm{Re}\left\{\left(i\frac{\gamma_g}{2}-\delta\omega_g\right)\times\frac{\partial}{\partial v}\left(-\frac{\gamma_g}{2}-i\delta\omega_g\right)\right\} \tag{4.40}$$

$$= -\gamma_g t\langle F_x\rangle^{(2)} - \left(\delta\omega_g\frac{\partial\gamma_g}{\partial v}+\gamma_g\frac{\partial\delta\omega_g}{\partial v}\right) \tag{4.41}$$

$$\langle F_x\rangle_0^{(4)} = -\gamma_g t\langle F_x\rangle^{(2)} - \frac{\partial}{\partial v}\left(\gamma_g\times\delta\omega_g\right). \tag{4.42}$$

In Eq. (4.42), the contribution of the zero-photon sector to the fourth perturbative order is exponentially small, attributable to the adiabatically stored energy in the Lamb-shifted ground state $\delta\omega_g$ [28]. In the HD model, it becomes evident that this sector will vanish when $v < v_s$, as the expression for γ_g in Eq. (3.43) features a delta function akin to that in $\langle F_x \rangle^{(2)}$ (4.9), which is determined by energy conservation. Consequently, similar to the second perturbative order force, γ_g vanishes, resulting in no contribution from the zero-photon case.

4.2.2 The transition via two interaction photons

The second contribution to the fourth-order force is expressed in Eq. (4.4), which is the sum of two integrals. Using the expression for the coefficient $c_{1,b}^{(3)}$ in Eq. (3.52), the first integral in $\langle F_x \rangle_2^{(4)}$ becomes

$$
\begin{aligned}
&2\mathrm{Re}\sum_{\eta}\int d\boldsymbol{k}\ \langle \mathrm{g}, \mathrm{vac}|F_x|\boldsymbol{\eta},\boldsymbol{k}\rangle c_{1,b}^{(3)} \qquad (4.43)\\
&\quad = 2\mathrm{Re}\sum_{\eta}\int d\boldsymbol{k}\ \langle \mathrm{g}, \mathrm{vac}|F_x|\boldsymbol{\eta},\boldsymbol{k}\rangle c_{1}^{(1)}(t,\boldsymbol{k})\frac{d^2}{\left(\boldsymbol{\eta}\cdot\vec{k}\right)^*}\\
&\quad \times \int d\boldsymbol{k}'\ e^{-2k'z}\frac{\left(\vec{k}\cdot\vec{k}'\right)^*\left(\boldsymbol{\eta}\cdot\vec{k}'\right)^*\phi_{k'}^2}{\omega'(k)+\omega'(k')-i\delta^+}\left(\frac{1}{\omega'(k')+\omega_b-i\delta^+}+\{k\leftrightarrow k'\}\right).
\end{aligned}
$$

Here, we find that the part of the integrand with respect to the momentum $\boldsymbol{k}$ is identical to the second-order force in Eq. (4.1). Therefore, we can use the expression of the second-order force from Eq. (4.6).

$$
\begin{aligned}
&2\mathrm{Re}\sum_{\eta}\int d\boldsymbol{k}\ \langle \mathrm{g}, \mathrm{vac}|F_x|\boldsymbol{\eta},\boldsymbol{k}\rangle c_{1,b}^{(3)} \qquad (4.44)\\
&\quad = -2d^4\mathrm{Re}\int_0^\infty dk\int_{-\pi}^{\pi}d\theta\ \frac{\phi_k^2k^2\cos(\theta)e^{-2kz}}{\omega'(k)+\omega_b-i\delta^+}\\
&\quad \times \int d\boldsymbol{k}'\ e^{-2k'z}\frac{i\left|\vec{k}\cdot\vec{k}'\right|^2\phi_{k'}^2}{\omega'(k)+\omega'(k')-i\delta^+}\left(\frac{1}{\omega'(k')+\omega_b-i\delta^+}+\{k\leftrightarrow k'\}\right).
\end{aligned}
$$

By taking the limit $\delta^+ \to 0$, one can again use the Sokhotski-Plemelj theorem, as illustrated in Appendix C to identify the delta function in the integrals.

$$\mathrm{Re}\int d\boldsymbol{k}d\boldsymbol{k}'\ \left(\lim_{\delta^+\to 0}\frac{i}{\omega'(k)+\omega'(k')-i\delta^+}\right) = -\pi\int d\boldsymbol{k}d\boldsymbol{k}'\ \delta\left(\omega'(k)+\omega'(k')\right). \tag{4.45}$$

We obtain the first term in $\langle F_x\rangle_2^{(4)}$ as follows.

$$\begin{aligned} &2\mathrm{Re}\sum_\eta\int d\boldsymbol{k}\ \langle \mathrm{g},\mathrm{vac}|F_x|\boldsymbol{\eta},\boldsymbol{k}\rangle c_{1,b}^{(3)} \\ &\quad = 2\pi d^4\mathrm{Re}\int_0^\infty dk\int_{-\pi}^{\pi}d\theta\ \frac{\phi_k^2k^2\cos(\theta)e^{-2kz}}{\omega'(k)+\omega_b} \\ &\quad \times\int d\boldsymbol{k}'\ e^{-2k'z}\left|\vec{k}\cdot\vec{k}'\right|^2\phi_{k'}^2\delta\left(\omega'(k)+\omega'(k')\right)\left(\frac{1}{\omega'(k')+\omega_b}+\{k\leftrightarrow k'\}\right). \end{aligned} \tag{4.46}$$

Due to the Bose symmetrization of the integrand, one can replace $2k\cos(\theta)/(\omega'(k)+\omega_b)$ with $k\cos(\theta)/(\omega'(k)+\omega_b)+(\boldsymbol{k}\to\boldsymbol{k}')$.

$$\begin{aligned} &2\mathrm{Re}\sum_\eta\int d\boldsymbol{k}\ \langle \mathrm{g},\mathrm{vac}|F_x|\boldsymbol{\eta},\boldsymbol{k}\rangle c_{1,b}^{(3)} \\ &\quad = \pi d^4\mathrm{Re}\int d\boldsymbol{k}d\boldsymbol{k}'\ \phi_k^2\phi_{k'}^2\left|\vec{k}\cdot\vec{k}'\right|^2e^{-2kz-2k'z}\left(\frac{k\cos(\theta)}{\omega'(k)+\omega_b}+\frac{k'\cos(\theta')}{\omega'(k')+\omega_b}\right) \\ &\quad \times\delta\left(\omega'(k)+\omega'(k')\right)\left(\frac{1}{\omega'(k')+\omega_b}+\{k\leftrightarrow k'\}\right). \end{aligned} \tag{4.47}$$

By employing the expressions for the coefficients $c_1^{(1)}$ and $c_2^{(2)}$ in Eqs. (3.46) and (3.48), respectively, the derivation of the second integral in $\langle F_x\rangle_2^{(4)}$ (4.4) is detailed in Appendix E, which gives

$$\begin{aligned} &\mathrm{Re}\sum_\eta\int d\boldsymbol{k}_1d\boldsymbol{k}_2\ \langle\boldsymbol{\eta},\boldsymbol{k}|F_x|\mathrm{g},\boldsymbol{k}_1\boldsymbol{k}_2\rangle c_1^{(1)*}(t,\boldsymbol{k})c_2^{(2)}(t,\boldsymbol{k}_1,\boldsymbol{k}_2) \\ &\quad = \pi d^4\int d\boldsymbol{k}_1d\boldsymbol{k}_2\ \phi_{k_1}^2\phi_{k_2}^2\left|\vec{k}_1\cdot\vec{k}_2\right|^2e^{-2k_1z-2k_2z}\left(\frac{k_1\cos(\theta_1)}{\omega'(k_2)+\omega_b}+\frac{k_2\cos(\theta_2)}{\omega'(k_1)+\omega_b}\right) \\ &\quad \times\delta\left(\omega'(k_1)+\omega'(k_2)\right)\left(\frac{1}{\omega'(k_2)+\omega_b}+\{k_1\leftrightarrow k_2\}\right). \end{aligned} \tag{4.48}$$

In the integral of Eq. (4.47), one can substitute the dummy variables $\boldsymbol{k} \to \boldsymbol{k}_1$ and $\boldsymbol{k}' \to \boldsymbol{k}_2$. Consequently, the fourth-order force arising from two interacting photons can be represented as the summation of Eqs. (4.47) and (4.50).

$$\begin{aligned}\langle F_x\rangle_2^{(4)} &= \pi d^4 \int d\boldsymbol{k}_1 d\boldsymbol{k}_2 \; \phi_{k_1}^2 \phi_{k_2}^2 \left|\vec{k}_1 \cdot \vec{k}_2\right|^2 e^{-2k_1 z - 2k_2 z} \delta\left(\omega'(k_1) + \omega'(k_2)\right) \qquad (4.49)\\ &\times \left(\frac{k_1\cos(\theta_1)}{\omega'(k_1)+\omega_b} + \frac{k_2\cos(\theta_2)}{\omega'(k_2)+\omega_b} + \frac{k_1\cos(\theta_1)}{\omega'(k_2)+\omega_b} + \frac{k_2\cos(\theta_2)}{\omega'(k_1)+\omega_b}\right)\\ &\times \left(\frac{1}{\omega'(k_2)+\omega_b} + \{k_1 \leftrightarrow k_2\}\right)\\ &= \pi d^4 \int d\boldsymbol{k}_1 d\boldsymbol{k}_2 \; \phi_{k_1}^2 \phi_{k_2}^2 \left|\vec{k}_1 \cdot \vec{k}_2\right|^2 e^{-2k_1 z - 2k_2 z} \delta\left(\omega'(k_1) + \omega'(k_2)\right) \qquad (4.50)\\ &\times \left(k_1\cos(\theta_1) + k_2\cos(\theta_2)\right)\left(\frac{1}{\omega'(k_2)+\omega_b} + \frac{1}{\omega'(k_1)+\omega_b}\right)^2.\end{aligned}$$

The delta function implies that $\omega'(k_2) = -\omega'(k_1)$ and $\Omega_s(k_1) + \Omega_s(k_2) = k_1 v\cos(\theta_1) + k_2 v\cos(\theta_2)$, which results in the following expression.

$$\begin{aligned}\langle F_x\rangle_2^{(4)} &= \frac{\pi d^4}{v} \int d\boldsymbol{k}_1 d\boldsymbol{k}_2 \; \phi_{k_1}^2 \phi_{k_2}^2 \left|\vec{k}_1 \cdot \vec{k}_2\right|^2 e^{-2k_1 z - 2k_2 z} \delta\left(\omega'(k_1) + \omega'(k_2)\right) \qquad (4.51)\\ &\times \left(\Omega_s(k_1) + \Omega_s(k_2)\right)\left(\frac{-2\omega_b}{(\omega'(k_1)+\omega_b)(\omega'(k_1)-\omega_b)}\right)^2.\end{aligned}$$

The delta function in $\langle F_x\rangle_2^{(4)}$, as shown in Eq. (4.51), will not vanish when $\Omega_s(k_1) + \Omega_s(k_2) = k_1 v\cos(\theta_1) + k_2 v\cos(\theta_2)$. Using the dispersion relation in Eq. (2.48), one finds that the delta function implies

$$\sum_{j=1,2} \frac{1}{2}\left(\sqrt{2\omega_p^2 + v_s^2 k_j^2} + v_s k_j - 2k_j v\cos(\theta_j)\right) = 0. \qquad (4.52)$$

Because the plasma frequency ω_p and the sound speed v_s are real and positive, one can prove that

$$\sqrt{2\omega_p^2 + v_s^2 k_j^2} + v_s k_j - 2k_j v\cos(\theta_j) \geq 2v_s k_j - 2k_j v\cos(\theta_j) \qquad (4.53)$$

$$\sqrt{2\omega_p^2 + v_s^2 k_j^2} + v_s k_j - 2k_j v\cos(\theta_j) \geq 2k_j\left(v_s - v\cos(\theta_j)\right). \qquad (4.54)$$

When the atom's velocity is smaller than the sound speed, $v < v_s$, the right-hand side is always positive due to $\cos(\theta_j) \leq 1$. This implies that even the minimal values of the left-hand side in Eq. (4.52) cannot be less than zero. Therefore, the contribution of the fourth-order force in the HD model $\langle F_x\rangle_2^{(4)}$ also vanishes when $v < v_s$.

4.3 Summary

In this chapter, we derive the second and fourth perturbative orders of the frictional force from the force operator in Eq. (3.9) and the corresponding state functions in Eq. (3.25). We determine two delta functions in the forces at both orders: $\delta(\omega'(k)+\omega_b)$ and $\delta(\omega'(k_1)+\omega'(k_2))$. Using the dispersion relation (2.48) from the HD model, we find that these delta functions will vanish when the atom's velocity is less than the speed of sound, denoted as v_s.

In the second-order force (4.9) and the fourth-order force (4.51), the delta functions signify energy conservation. For higher perturbative orders of the force, one would encounter the same type of delta function, imposing analogous energy conservation conditions. For example, the sixth-order term will generate a new delta function $\delta(\omega'(k_1)+\omega'(k_2)+\omega'(k_3)+\omega_b)$, where k_1, k_2 and k_3 represent the momenta of the three interacting photons. Consequently, the frictional force will vanish at all perturbative orders when $v \leq v_s$.

The observed outcomes diverge from those obtained by other models, such as the Drude model for metals [28]. Inherent dissipation within the material leads to a frictional force across all velocities. While the secondary frictional force is found to be negligibly small at low velocities in the local models discussed in the existing literature, no specific threshold is identified.

Incorporating intrinsic dissipation into the model is not essential for the presence of friction at higher velocities in non-local models. However, its absence does establish a velocity threshold, as observed in the case of graphene [43, 44]. In the HD model, we observe this threshold persisting even at the fourth order in perturbation theory. This is in contrast to findings in models that incorporate intrinsic dissipation. Instead, we identify a force that diminishes at low velocities even at higher orders in perturbation theory.

To elucidate the specific velocity threshold in the HD model, we must revisit the definition of the speed of sound within this framework. As previously discussed in Chapter 2, the speed of sound is the maximum velocity at which electron-electron interactions can propagate through the medium in the HD regime. In Fig. 4.3, we initially position a stationary atom above a plate, and an attractive force between them arises due to the Casimir-Polder effect. This can be conceptualized as if there is an electron configuration in the plate that acts as a mirror image of the atom in a vacuum. When the atom moves, this mirror image will also propagate through the plate to keep pace with the atom. The speed of sound represents the maximum velocity of this mirror image propagation. When the atom's velocity exceeds the speed of sound, the frictional force comes into play, as depicted in Fig. 4.3.

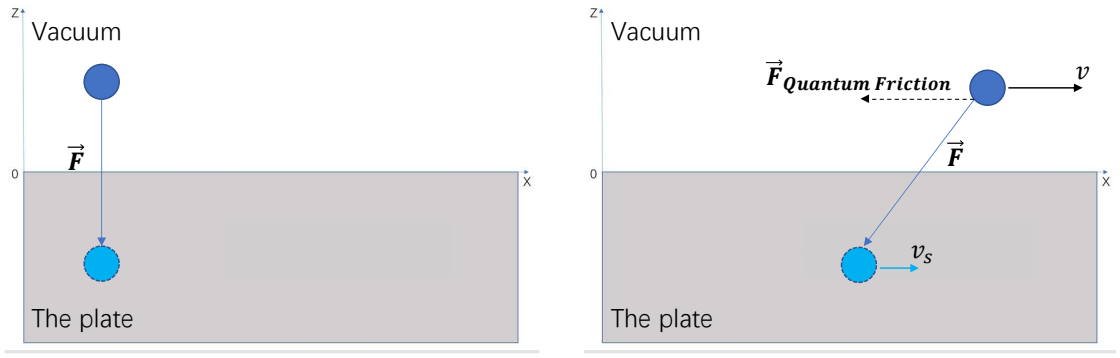

Figure 4.3: $v > v_s$. The left subfigure shows a static atom above the plate with its mirror image inside the plate, creating an attractive force due to the Casimir-Polder effect. In the right subfigure, as the atom moves faster than the speed of sound (v_s), the mirror image's propagation is limited by the speed of sound, resulting in a backward deflection that generates frictional force.

When the atom moves at a velocity higher than the speed of sound, we conduct a numerical analysis of the second-order force by selecting parameters within a reasonable range (see Table 4.1). In Fig. 4.1, the force increases with the atom's velocity as expected. However, the plots shown in Fig. 4.1 reveal that the force can vanish exponentially even for larger velocities. This effective threshold increases with the gap distance z and decreases with the plasma frequency ω_p.

In the non-dispersive limit, the velocity threshold for the occurrence of the frictional force vanishes, and we demonstrate analytically the dispersive effect on the second-order force in Fig. 4.2. The dispersion effect suppresses the friction when the atom's velocity is relatively low. However, when the atom's velocity is approximately an order of magnitude greater than the speed of sound, the dispersive effect becomes negligible.

Part II

Braiding Majorana bound states in a driven-dissipative setup using Majorana-based architectures

Chapter 5

Introduction to non-Abelian braiding for topological quantum computing

A Majorana fermion [45] is a type of exotic fermion first proposed by Ettore Majorana in 1937. This unique fermion is its own antiparticle. In the framework of second quantization, the creation and annihilation operators for a Majorana fermion are equivalent. This implies that Majorana fermions carry zero electric charge. Initially, Majorana fermions were expected to be found in the realms of high-energy and particle physics [46]. To date, it remains an open question whether neutrinos could be Majorana fermions [47].

It has been proposed that the properties of Majorana fermions could emerge in certain quasiparticles within the field of condensed matter physics, such as those found in topological superconductors [48]. In this context, Majorana fermions are quasiparticles localized at specific points or defects within a material. These quasiparticles are known as Majorana bound states (MBSs) because they exhibit the property of self-conjugation, meaning they are their own antiparticles. In simpler terms, MBSs behave like a superposition of electron-like and hole-like excitations, reflecting the unique property of Majorana fermions where each particle is identical to its antiparticle. MBSs are unique in that they have no electric charge and their energy is exactly zero or very close to zero. This distinguishes them from other conventional quasiparticle excitations. Due to these properties, MBSs are sometimes also referred to as Majorana zero modes.

Early proposals for solid-state systems hosting MBSs involve using the edge or surface states of topological insulators that have been coupled to a superconductor [49–53]. Subsequently, research on MBSs has been extended to various experimental platforms. Some of the most promising platforms include heterostructures composed of semiconductor nanowires with Rashba spin-orbit coupling, exposed to a magnetic field and experiencing a superconducting proximity effect [54–67], chains of ferromagnetic

atoms placed on top of a superconductor [68–84], topological insulator nanowires [85–87], and planar Josephson junctions [88–92], among others. Fig. 5.1 presents schematic sketches of these solid-state systems that have the potential to host MBSs.

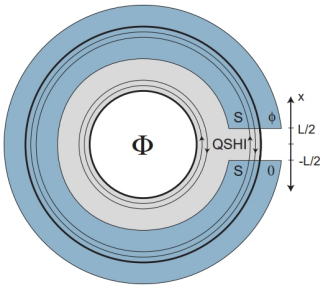

(a) A junction consisting of a superconductor (S) and a quantum spin Hall insulator (QSHI) in the sequence S-QSHI-S [51].

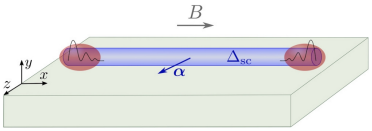

(b) A (blue) nanowire on a (green) superconducting substrate has its spin-orbit-interaction vector, α, along the z-axis and a magnetic field along the perpendicular x-axis [93].

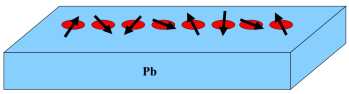

(c) A chain of magnetic nanoparticles with helical spin alignment is placed on a lead (Pb) superconducting substrate [68].

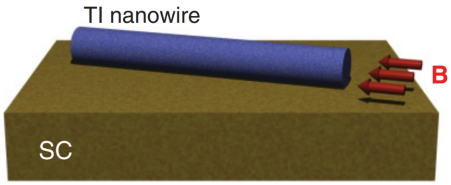

(d) A finite topological insulator (TI) nanowire is proximity-coupled to a bulk s-wave superconductor (SC) and subjected to a longitudinal magnetic field $\boldsymbol{B}$ [85].

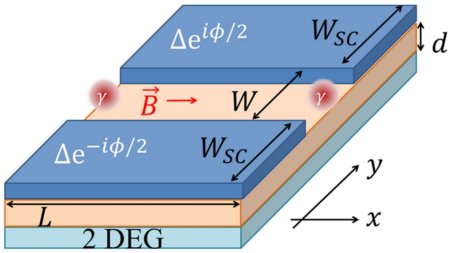

(e) A Josephson junction in a Rashba 2D electron gas (2DEG) is formed by coupling to two s-wave superconductors with phase difference ϕ, while an in-plane magnetic field is applied parallel to the interface [88].

Figure 5.1: **Systems proposed for MBSs**. (a) The junction enters the topological phase when the periodicity ϕ is 4π. Panels (b), (c), and (d) show the paired MBSs at the ends of nanowires. (e) The MBSs are denoted as γ, where the lead width W_{SC} and the junction length L are much larger than the separation W.

To understand MBSs at the ends of chains, we can introduce the Kitaev chain, a well-known toy model described by Kitaev in 2001 [94]. This model involves spinless

Dirac fermions on a one-dimensional chain whose Hamiltonian is given by

$$H_{\text{kitaev}} = -\mu \sum_{n=1}^{N} c_n^\dagger c_n + \sum_{n=1}^{N-1} \left(-t c_n^\dagger c_{n+1} + \Delta c_{n+1}^\dagger c_n^\dagger + \text{h.c.} \right), \tag{5.1}$$

where μ, t, Δ, and N represent the chemical potential, the nearest-neighbor hopping amplitude, the order parameter, and the total number of sites, respectively. On each site, the Majorana fermions γ can be introduced in terms of the Dirac fermions as follows.

$$\left.\begin{aligned} c_n &= \frac{1}{2}\left(\gamma_{n1} + i\gamma_{n2}\right) \\ c_n^\dagger &= \frac{1}{2}\left(\gamma_{n1} - i\gamma_{n2}\right) \end{aligned}\right\} \Rightarrow \begin{cases} \gamma_{n1} = c_n^\dagger + c_n \\ \gamma_{n2} = i\left(c_n^\dagger - c_n\right) \end{cases} \tag{5.2}$$

Rewriting the Hamiltonian (5.1) in terms of the Majorana operators γ gives

$$H_{\text{kitaev}} = -\frac{\mu}{2} \sum_{n=1}^{N} \left(i\gamma_{n1}\gamma_{n2} + 1 \right) + \frac{i}{2} \sum_{n=1}^{N-1} \left[(\Delta + t)\, \gamma_{n2}\gamma_{(n+1)1} + (\Delta - t)\, \gamma_{n1}\gamma_{(n+1)2} \right]. \tag{5.3}$$

We can explore certain limiting cases by choosing the parameters μ, Δ and t. When the superconducting gap is closed, and there is no hopping, i.e., $\Delta = t = 0$, the Kitaev chain does not exhibit a bulk gap or MBSs at the ends. Instead, the Majorana fermions on the same site are coupled in a manner where each site is described by a pairing of the Majorana modes. This coupling is reflected in the Hamiltonian, where the Majorana fermions γ_{n1} and γ_{n2} on the same site interact, as shown in panel (a) of Fig. 5.2.

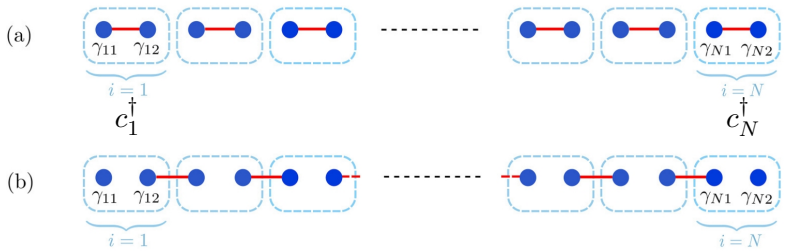

Figure 5.2: **The Kitaev chain** [94]. When $\Delta = t = 0$ in Eq. (5.1), the chain is in a trivial phase with Majorana fermions coupled on the same site (Panel a). For $\Delta = t > 0$ and $\mu = 0$, it becomes topologically non-trivial, with Majorana fermions coupled between neighboring sites (Panel b) [93].

However, a more interesting case arises when $\Delta = t > 0$ and $\mu = 0$. In this scenario, the Hamiltonian (5.3) simplifies to

$$H_{\text{kitaev}} = it \sum_{n=1}^{N-1} \gamma_{n2}\gamma_{(n+1)1}, \tag{5.4}$$

where Majorana fermions at neighboring sites are coupled with strength t. As shown in panel (b) of Fig. 5.2, the MBSs located at the two ends of the Kitaev chain, denoted as γ_{11} and γ_{N2}, are zero-energy states. These MBSs commute with H in Eq. (5.4), indicating that the system is in a topologically nontrivial phase, with one MBS at each end of the chain.

From the perspective of the energy spectrum, the bulk energy spectrum indicates that the bulk gap remains open in this case, which is characteristic of a topologically nontrivial phase. To demonstrate this, we need to express the Hamiltonian (5.1) in momentum space using the transformations $c_n = (1/\sqrt{N}) \sum_k c_k \exp(ikn)$ and $\delta(k-k') = (1/N) \sum_n \exp[-i(k-k')n]$.

$$H_{\text{kitaev}} = \sum_k (-\mu - 2t\cos k)\, c_k^\dagger c_k + \Delta \left(c_k c_{-k} e^{-ik} + c_{-k}^\dagger c_k^\dagger e^{ik} \right). \tag{5.5}$$

Defining the Nambu spinor $C_k = (c_k^\dagger, c_{-k})$, allows us to rewrite this Hamiltonian in the Bogoliubov-de Gennes (BdG) form as follows.

$$H_{\text{kitaev}} = \frac{1}{2} \sum_k C_k^\dagger \mathcal{H}_{\text{kitaev}}(k) C_k + \text{constant}, \tag{5.6}$$

$$\text{where } \mathcal{H}_{\text{kitaev}}(k) = (-\mu - 2t\cos k)\, \tau_z + \Delta\, (\tau_x \cos k + \tau_y \sin k)\,, \tag{5.7}$$

In this expression, $\tau_{x,y,z}$ are the Pauli matrices acting in the particle-hole subspace. The energy spectrum of the Kitaev chain is given by $E(k)^2 = (\mu + 2t\cos k)^2 + \Delta^2$. As shown in Fig. 5.3, the energy spectrum exhibits a closed gap when the pairing parameter is equal to zero. In contrast, for any finite pairing parameter, the energy spectrum is fully gapped. These observations indicate a potential transition between topologically distinct phases.

Compared to the Kitaev chain, which is a theoretical model, a more realistic platform for engineering MBSs is the superconductor-semiconductor heterostructure [63–67]. As illustrated in panel (b) of Fig. 5.1, this system comprises an s-wave superconductor coupled to a semiconductor nanowire of length L, with Rashba spin-orbit coupling

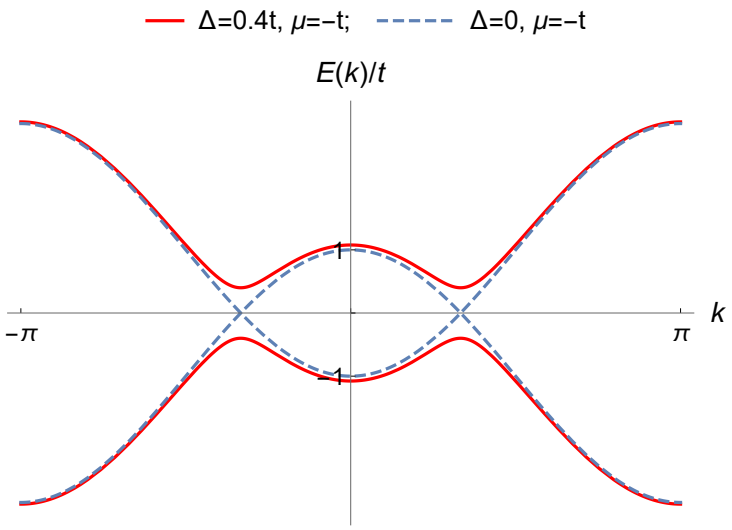

Figure 5.3: **Kitaev Chain Energy Spectrum**. The energy spectrum, normalized by the hopping amplitude t, is closed (indicated by the dashed line) when the gap parameter $\Delta = 0$, which suggests a phase transition or symmetry restoration in the system.

strength denoted by α. The Hamiltonian of the nanowire in this system is given by

$$H_{\text{Semi-SC}} = H_{\text{Semi}} + H_{\text{SC}}, \tag{5.8}$$

$$H_{\text{Semi}} = \int_0^L dx\, \psi_\sigma^\dagger(x) \left(-\frac{\partial_x^2}{2m} - \mu - i\alpha\sigma_z\partial_x + V_x\sigma_x \right)_{\sigma\sigma'} \psi_{\sigma'}(x), \tag{5.9}$$

$$H_{\text{SC}} = \Delta_{\text{ind}} \int_0^L dx\, \left(\psi_\uparrow^\dagger(x)\psi_\downarrow^\dagger(x) + \psi_\downarrow(x)\psi_\uparrow(x) \right), \tag{5.10}$$

where μ, m and Δ_{ind} denote the chemical potential, effective mass, and induced pairing potential, respectively. The Zeeman splitting due to an external magnetic field applied along the x-axis is represented by $V_x = g_{SM}\mu_B B/2$, where g_{SM} represents the Landé g-factor and μ_B denotes the Bohr magneton. In this context, σ denotes the spin index, corresponding to the spin states of the electrons in the nanowire.

Assuming the system is translationally invariant, we can rewrite the Hamiltonian (5.8)

in momentum space using $\psi_\sigma(x) = \int dk\ \psi_\sigma(k) \exp(ikx)$.

$$H_{\text{Semi}} = \int dk\ \psi_\sigma^\dagger(k) \left(\frac{k^2}{2m} - \mu + \alpha k \sigma_z + V_x \sigma_x \right)_{\sigma\sigma'} \psi_{\sigma'}(k), \tag{5.11}$$

$$H_{\text{SC}} = \Delta_{\text{ind}} \int dk\ \left(\psi_\uparrow^\dagger(k) \psi_\downarrow^\dagger(k) + \psi_\downarrow(k) \psi_\uparrow(k) \right). \tag{5.12}$$

Given the Nambu spinor $\Psi^\dagger(k) = (\psi_\uparrow^\dagger(k), \psi_\downarrow^\dagger(-k), \psi_\uparrow(k), \psi_\downarrow(-k))^\dagger$, the Hamiltonian in BdG form can be expressed as

$$H_{\text{Semi-SC}} = \frac{1}{2} \int dk\ \Psi^\dagger(k) \mathcal{H}_{\text{Semi-SC}}(k) \Psi(k) + \text{constant}, \tag{5.13}$$

$$\mathcal{H}_{\text{Semi-SC}} = \left(\frac{k^2}{2m} - \mu \right) \tau_z + \alpha k \sigma_z + V_x \tau_z \otimes \sigma_z + \Delta_{\text{ind}} \tau_y \otimes \sigma_y, \tag{5.14}$$

where $\tau_{x,y,z}$ are the Pauli matrices acting in the particle-hole basis. The energy spectrum can be computed from the BdG Hamiltonian as follows.

$$\begin{aligned} E_\pm^2(k) = &\left(\frac{k^2}{2m} - \mu \right)^2 + \left(V_x^2 + \alpha^2 k^2 \right) + \Delta_{\text{ind}}^2 \\ &\pm 2 \sqrt{\left(\frac{k^2}{2m} - \mu \right)^2 \left(V_x^2 + \alpha^2 k^2 \right) + V_x^2 \Delta_{\text{ind}}^2}. \end{aligned} \tag{5.15}$$

When the condition $V_x^2 = \mu^2 + \Delta_{\text{ind}}^2$ is satisfied, and for any finite value of the induced pairing parameter Δ_{ind} with $\alpha > 0$, the spectrum is always gapped except at a single point where the gap closes at $k = 0$. This gap closing and reopening indicate a topological phase transition from a trivial phase to a topologically nontrivial phase. To demonstrate the emergence of MBSs at both ends of the wire, further steps include observing zero-bias conductance peaks in tunneling experiments or calculating topological invariants. However, this study does not delve into these aspects, as its primary focus is on non-Abelian braiding protocols rather than the detection of MBSs in solid-state systems.

In physics, particularly in the context of quantum computing and anyonic systems, braiding refers to the process of exchanging the positions of particles (or quasiparticles) in a way that causes their quantum states to become intertwined or "braided". The non-Abelian braiding transformation, which can be generalized as a nontrivial rotation operation on quantum states, is essential in topological quantum computing [95–98], where the paths formed by these braids encode information. When braiding involves topological quasiparticles, the encoded information can be protected from noise and errors

due to its topological nature. The non-Abelian braiding of topological quasiparticles represents an ideal theoretical approach and holds great promise for fault-tolerant quantum computing. This complex exchange statistics was initially explored in the context of two-dimensional p-wave superconductors, where vortices in the superconducting order parameter are found to host MBSs [99–101]. In such systems, two MBSs span a two-dimensional low-energy Hilbert space. A cyclic adiabatic transformation, commonly known as "braiding", can act on these two MBSs, implementing a topologically nontrivial unitary transformation within this ground-state subspace. Conventionally, braiding refers to the adiabatic exchange of positions between two MBSs. However, as discussed in this study, other adiabatic processes—such as those occurring within the dark states of a dissipative open system—can also induce non-Abelian topological transformations.

In the experimental realizations, the braiding of MBSs at the ends of one-dimensional systems [94] can be implemented using various techniques, such as T-junctions [102], Y-junctions [103], holonomic entangling [104–107], or by altering superconducting fluxes [99,108]. The schematic diagram [108] shown in Fig. 5.4 illustrates the braiding operation, which is achieved in three steps: $\mathcal{O}_{31}$, $\mathcal{O}_{12}$ and $\mathcal{O}_{23}$. By toggling the Coulomb couplings on and off, the Majorana bound states, indicated by the green and yellow circles, are switched at time $t = 3T$.

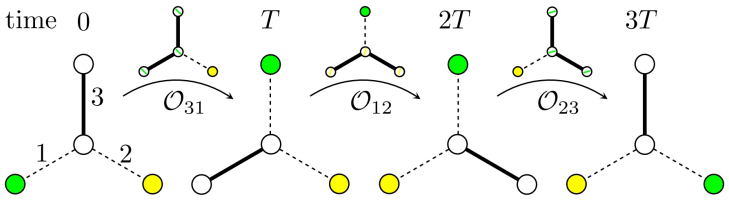

Figure 5.4: **Braiding in the tri-junction** [108]. The circles represent Majorana bound states, with dashed lines indicating turned-on Coulomb couplings and solid lines indicating turned-off couplings. This braiding operation ends with the switching of the Majorana bound states, marked in yellow and green, in real space.

In addition to the closed systems mentioned above, the study of MBSs has also been extended to include open quantum systems [109–111]. Unlike closed systems, an open quantum system interacts with a large external environment, where "large" refers to the extensive number of degrees of freedom within this environment. The interaction between the open system and the external bath can result in the transfer of energy, information, and particles. In certain circumstances, dissipation in an open system can facilitate the detection of MBSs [112–114]. Although most quantum states are prone to decay due to damping, specific "dark states" [115] within the Hilbert space can resist

this dissipation [116–118]. In such cases, damping can stabilize a subspace of dark states that may harbor MBSs. This concept is fundamental to the proposed implementation of a Kitaev chain [94] in dissipative cold-atom systems [110].

The framework of open quantum systems is generally more complex than that of closed quantum systems, where evolution is governed by unitary processes. For open quantum systems, several well-established theories exist, including the non-Hermitian Hamiltonian, the Redfield equation, and the Lindblad master equation [119–122]. In this study, we utilize the Lindblad equation, as it provides a comprehensive and rigorous framework when the Born-Markov approximation is applied. The Lindblad master equation offers a detailed description of the time evolution of the density matrix for an open quantum system while preserving its intrinsic properties. It effectively captures both coherent evolution, driven by the system's Hamiltonian, and incoherent processes, such as dissipation and decoherence, within a unified framework. We will discuss these details further in the upcoming chapter.

5.1 Majorana boxes

The focus of this study is on a reduced open system represented by qubits, with the environment modeled as a bosonic bath. The Majorana qubit is illustrated by the Majorana box, also known as the Cooper-pair box, which was first introduced in Ref. [123]. This system shown in Fig. 5.5 consists of three topological superconductor (TS) nanowires (colored blue), which couple to external leads or quantum dots (colored pink). A floating superconducting bridge (colored orange) connects two of these wires, while the third wire functions as an interface arm, enabling the storage and readout of information within the box using measurement-based implementations of Clifford gates.

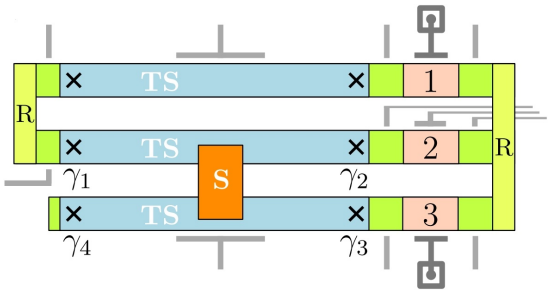

Figure 5.5: **The Majorana box qubit** [123]. TS nanowires (blue) connected by a superconducting bridge (orange) form a floating island hosting four Majorana fermions (crosses). Gate electrodes (gray) control tunneling couplings through semiconductor regions (green), with reference arms (R, light green) completing the interference loop.

In this system, the TS wire is longer than the TS coherence length, which ensures that all MBSs are in a zero-energy state and that their overlaps are negligible. The methods for readout, initialization, and manipulation of the MBSs using quantum dots provide a pathway for implementing single-qubit operations. This qubit design uses the topological protection and non-local properties of MBSs in a network of parallel wires, which do not rely on braiding for quantum gates. However, exploring braiding operations with the Majorana box [124, 125] could unlock new types of quantum operations or enhance the existing design.

Approximately three years later, Matthias Gau [126] demonstrated that a Majorana box, treated as an open quantum system in a bosonic bath, can be stabilized to a desired steady state by adjusting the tunneling couplings between MBSs and quantum dots. Moreover, these steady states can be maintained as coherent states. Nevertheless, it is not immediately evident whether a topological braiding implementation can be achieved in this dissipative-driven Majorana box. This operation requires satisfying two key conditions: the presence of multiple dark states with the same parity, and the maintenance of topological order in the steady state during the braiding process. This work aims to explore the potential of a tunneling system to meet these conditions and contributes to the development of a topological braiding protocol within an open quantum system that incorporates Majorana boxes. To ensure consistency within the literature, the next chapter will revisit the dissipative-driven Majorana box in the context of open systems, building on Gau's research [126, 127].

Chapter 6

The open quantum system employing the Majorana architecture

An open system framework is used to study transport phenomena between the system and its surrounding bath. The Hamiltonian for this setup includes at least the reduced open system, the bath, and the interactions between them. Specifically, in the context of braiding, the reduced system consists of the Majorana box and quantum dots, the bath is a bosonic environment, and the interaction dynamics involve tunneling between the quantum dots and the Majorana box, modulated by the bosonic bath.

The conceptual overview of the Majorana open system is sketched in Fig. 6.1, which encompasses two quantum dots with different energy levels, and one Majorana box. A Majorana box harbors two Kitaev nanowires interfacing with a shared, floating superconductor. The compactness of this setup generates considerable charging energy within the Majorana framework. Furthermore, each MBS is tunnel-coupled to one of two quantum dots, QD1 and QD2. Electrons can be pumped between these dots by an AC voltage. We consider the system to be immersed in an electromagnetic field that primarily alters the tunneling amplitudes' phases between the quantum dots and the MBSs.

In the interaction picture, the Hamiltonian of the open system sketched in Fig. 6.1 is written as

$$H(t) = H_{\text{box}} + H_{\text{QD}} + H_{\text{env}} + H_{\text{drive}}(t) + H_{\text{tun}}. \tag{6.1}$$

The Hamiltonian in Eq. (6.1) is composed of several parts: the Majorana box (H_{box}), the Hamiltonian for the quantum dots (H_{QD}), the Hamiltonian for the bosonic environment (H_{env}), the Hamiltonian for the time-dependent driving field between the quantum dots ($H_{\text{drive}}(t)$), and the Hamiltonian for tunneling between the quantum dots and MBSs

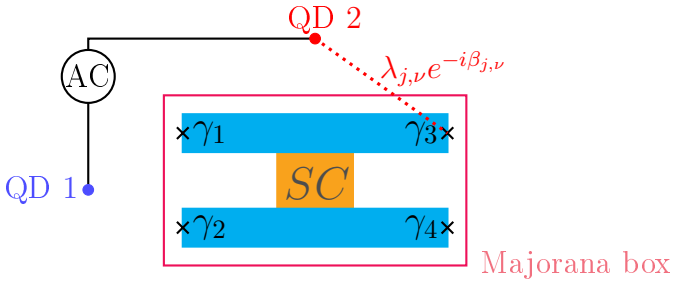

Figure 6.1: **Schematic of the Majorana Open System**. Two nanowires (represented as blue rectangles) are connected by a superconducting (SC) bridge (shown as an orange rectangle). Each nanowire hosts four edge modes known as MBSs (MBSs), labeled as γ_ν. Together, these MBSs form a Majorana box (MB), denoted by a red rectangle. These MBSs are tunnel-coupled to quantum dots QD1 and QD2, depicted by the dashed lines, where $\lambda_{j,\nu}\exp(-i\beta_{j,\nu})$ denotes the complex tunneling parameter from quantum dot $d_j^\dagger$ to MBS γ_ν. An AC voltage is applied between the two quantum dots, driving the system.

(H_{tun}). In the schematic depicted in Figure 6.1, the tunnel coupling between the quantum dot $d_j^\dagger$ and the MBS γ_ν is denoted as $\lambda_{j,\mu}\exp(-i\beta_{j,\mu})$, with $\lambda_{j,\mu}$ representing the amplitude and $\beta_{j,\mu}$ representing the phase of the coupling.

In the following sections of this chapter, we initiate our discussion by constructing the Majorana qubit within a Majorana box. Subsequently, we introduce suitable approximations and assumptions regarding the Hamiltonian to facilitate the derivation of the effective Hamiltonian. Using the Born-Markov approximation, we then proceed to derive the Lindblad equation for the Majorana sector from the effective Hamiltonian.

6.1 Constructing the Majorana qubit in a Majorana box

Within the box, the four MBSs can be paired to form two Dirac fermions. The corresponding Bogoliubov transformation that describes their relationship can be expressed as

$$c_1 = \frac{1}{2}(\gamma_1 + i\gamma_2), \qquad c_2 = \frac{1}{2}(\gamma_3 + i\gamma_4), \tag{6.2}$$

where γ denotes the MBSs, and c represents the Dirac fermions. The corresponding inverse transformations are presented below.

$$\gamma_1 = c_1^\dagger + c_1, \qquad \gamma_2 = i\left(c_1^\dagger - c_1\right); \tag{6.3}$$

$$\gamma_3 = c_2^\dagger + c_2, \qquad \gamma_4 = i\left(c_2^\dagger - c_2\right). \tag{6.4}$$

Since the Dirac fermions follow the anti-commutation relation $\left\{c_m, c_n^\dagger\right\} = \delta_{m,n}$, it is required that the Majorana operators satisfy the relation $\left\{\gamma_\mu, \gamma_\nu^\dagger\right\} = 2\delta_{\mu,\nu}$.

The total fermionic parity operator of the Majorana box is defined as

$$P = (-1)^{N_1}(-1)^{N_2} = (1-2N_1)(1-2N_2), \tag{6.5}$$

where the fermionic number operator is $N_m = c_m^\dagger c_m$ with possible eigenvalues: 0 and 1. In terms of the Majorana operators, the parity operator can be written as

$$P = \left[1 - \frac{1}{2}(\gamma_1 - i\gamma_2)(\gamma_1 + i\gamma_2)\right]\left[1 - \frac{1}{2}(\gamma_3 - i\gamma_4)(\gamma_3 + i\gamma_4)\right] \tag{6.6}$$

$$= \left[1 - \frac{1}{2}(2 + 2i\gamma_1\gamma_2)\right]\left[1 - \frac{1}{2}(2 + 2i\gamma_3\gamma_4)\right] \tag{6.7}$$

$$= -\gamma_1\gamma_2\gamma_3\gamma_4. \tag{6.8}$$

The conservation of parity implies that the parity operator P is, in fact, proportional to the identity operator: $P = \pm 1$. Without loss of generality, within the odd parity sector characterized by $P = -1$, the physical states are defined as

$$|-\rangle := |01\rangle, \qquad |+\rangle := i|10\rangle = ic_1^\dagger c_2|01\rangle, \tag{6.9}$$

where $|N_1N_2\rangle$ denotes the Fock states of the Dirac fermions, corresponding to the occupation numbers N_1 and N_2. Consequently, within any specified parity sector, the physical Hilbert space, which is two-dimensional, is spanned by the Majorana fermions, enabling the structure of a single qubit.

As shown in Figure 6.1, the entire Majorana box possesses a uniform charging energy E_C due to the superconducting bridge that connects the two nanowires. The edge states of these nanowires are regarded as MBSs. We presume the nanowires are sufficiently long to isolate the pairs of MBSs, ensuring that the hybridization energy, which decays exponentially with the separation between distinct MBSs, is negligible. Thus, the Hamiltonian of the box, in the Schrödinger picture, is written as

$$H_{\text{box}} = E_C\left(N - N_g\right)^2, \tag{6.10}$$

where the operator N signifies the total electron count within the box, and N_g represents the effect of a back-gate voltage, enabling the adjustment of the charging energy and thereby controlling the ground state of the box.

Under Coulomb blockade conditions, which imply that N_g is near integer values, the charging energy enforces a well-defined ground-state value for N. For example, when $N_g = 1$ (see Fig. 6.2), the ground states possess a fermion number $\langle N \rangle = 1$, and this condition is met for the two degenerate Majorana states characterized by odd parity. The system remains confined to the ground state subspace under the condition that the energy scale of any dynamics is less than both the charging energy E_C and the superconducting gap [126].

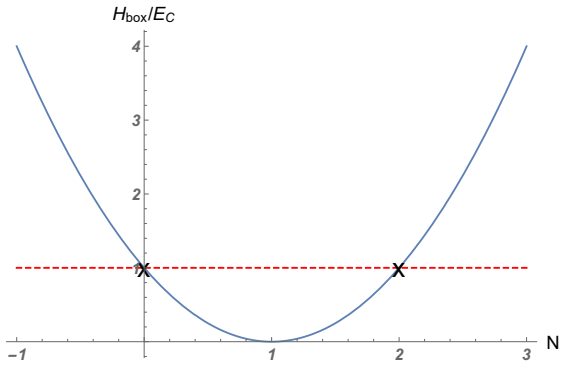

Figure 6.2: $\boldsymbol{N_g = 1}$. This diagram illustrates the relationship between the energy of the charging box and the number of particles occupying the box, when $N_g = 1$.

In the odd parity sector, the qubit states are defined by Eq. (6.9). The action of the products of Majorana operators on these states can be expressed in terms of the Pauli matrices. For example, the products of the Majorana operators, as defined by their expressions in Eqs. (6.3) and (6.4), can be identified.

$$i\gamma_1\gamma_3 = i\left(c_1^\dagger c_2^\dagger + c_1^\dagger c_2 + c_1 c_2^\dagger + c_1 c_2\right), \tag{6.11}$$

$$i\gamma_2\gamma_3 = -\left(c_1^\dagger c_2^\dagger + c_1^\dagger c_2 - c_1 c_2^\dagger - c_1 c_2\right), \tag{6.12}$$

$$i\gamma_1\gamma_2 = -\left(c_1^\dagger c_1^\dagger - c_1^\dagger c_1 + c_1 c_1^\dagger - c_1 c_1\right). \tag{6.13}$$

Applying the product, $i\gamma_1\gamma_3$ in Eq. (6.11), to the basis of states $\{|-\rangle, |+\rangle\}$, as defined in

Eq. (6.9), results in

$$i\gamma_1\gamma_3|-\rangle = ic_1^\dagger c_2|01\rangle = ic_1^\dagger c_2 c_2^\dagger|00\rangle = i|10\rangle = |+\rangle, \tag{6.14}$$

$$i\gamma_1\gamma_3|+\rangle = -c_1 c_2^\dagger|10\rangle = -c_1 c_2^\dagger c_1^\dagger|00\rangle = |01\rangle = |-\rangle. \tag{6.15}$$

Equivalently, the product of Majorana operators, $i\gamma_1\gamma_3$, can be identified as the Pauli matrix χ_x when considered within the basis $\{|-\rangle, |+\rangle\}$.

Similarly, the products of Majorana operators, as given in Eqs. (6.12) and (6.13), when applied to the qubit states, yield

$$i\gamma_2\gamma_3|-\rangle = -c_1^\dagger c_2|01\rangle = -|10\rangle = i|+\rangle, \tag{6.16}$$

$$i\gamma_2\gamma_3|+\rangle = ic_1 c_2^\dagger|10\rangle = -i|01\rangle = -i|-\rangle; \tag{6.17}$$

$$i\gamma_1\gamma_2|-\rangle = -c_1 c_1^\dagger|01\rangle = -|01\rangle = -|-\rangle, \tag{6.18}$$

$$i\gamma_1\gamma_2|+\rangle = ic_1^\dagger c_1|10\rangle = i|10\rangle = |+\rangle. \tag{6.19}$$

Thus, the bilinear forms constructed from Majorana operators correspond to the Pauli matrices when represented in the odd-parity state manifold [123, 128, 129].

$$i\gamma_1\gamma_3 = \chi_x, \qquad i\gamma_2\gamma_3 = \chi_y, \qquad i\gamma_1\gamma_2 = \chi_z. \tag{6.20}$$

For the even parity sector, when $N = 0$ or 2, the results will be analogous.

6.2 Some approximations

In the preceding section, we examined the Hamiltonian of the Majorana box and the Majorana operators within the odd parity sector, assuming a sufficiently high charging energy to confine the system to the odd-parity ground state manifold. Building on this foundation, we now turn to an analysis of the remaining contributions to the system's Hamiltonian as presented in Eq. (6.1). Through the application of suitable approximations, we simplify the system's model, allowing for a more tractable analysis and leading to the derivation of the effective Hamiltonian.

In the schematic depicted in Figure 6.1, the MBSs are coupled to two quantum dots. The Hamiltonian governing the quantum dots is given by

$$H_{\mathrm{QD}} = \sum_{j=1,2} \epsilon_j d_j^\dagger d_j, \tag{6.21}$$

where d_j is the fermionic annihilation operator, and each quantum dot is described by a single fermionic level ϵ_j. The bath Hamiltonian is modeled as a collection of bosonic harmonic oscillators, representing the environment's degrees of freedom.

$$H_{\text{env}} = \sum_m E_m b_m^\dagger b_m, \tag{6.22}$$

where b_m denotes the bosonic annihilation operator with the corresponding bosonic energy given by E_m. In practice, the bath energies E_m are significantly reduced above a certain cutoff frequency ω_c, indicating that higher energy modes of the bath have minimal impact on the system.

Next, we discuss the transport between two quantum dots as described by the driving and tunneling Hamiltonians within the comprehensive total Hamiltonian (6.1). The driving Hamiltonian encompasses the transfer of electrons between the two quantum dots through an AC field with amplitude $\mathcal{A}$ and frequency ω_0.

$$H_{\text{drive}} = 2\mathcal{A}\cos(\omega_0 t) d_1^\dagger d_2 + \text{h.c.}. \tag{6.23}$$

The tunneling between quantum dot j and MBS ν is described by the Hamiltonian presented below.

$$H_{\text{tun}} = t_0 e^{-i\hat{\phi}} \sum_{j\nu} e^{i\delta_j} \lambda_{j,\nu} e^{-i\beta_{j,\nu}} d_j^\dagger \gamma_\nu + \text{h.c.}, \tag{6.24}$$

where t_0 is the overall scale of tunnel couplings between quantum dots and MBSs, and the phase operator $\hat{\phi}$ obeys the commutator relation $\left[\hat{\phi}, N\right] = -i$, capturing the change in electron number within the Majorana box due to tunneling effects. Furthermore, the tunable tunnel amplitudes between the quantum dot electron d_j and Majorana fermions γ_ν are complex, characterized by real amplitudes $\lambda_{j,\nu}$ and phases $\beta_{j,\nu}$ within the interval $[0, \pi)$. Given that the total electron number is conserved, we consider that each of the two quantum dots contains, on average, a single electron to facilitate electron tunneling between them. δ_j represents the electromagnetic fluctuations that, in turn, affect the phases of the tunneling amplitudes between quantum dot j and the MBSs,

$$\delta_j = \sum_m g_{jm} \left(b_m + b_m^\dagger\right), \tag{6.25}$$

with real-valued constants g_{jm}.

6.2.1 Rotating-wave approximation

The rotating-wave approximation (RWA) is suitably employed when the frequency is near the resonant frequency, allowing for the neglect of oscillations that are significantly faster than the resonant frequency. We commence our analysis with the driving Hamiltonian in the interaction picture, which is given by the following expression.

$$H_{\text{drive}}(t) = 2\mathcal{A}\cos(\omega_0 t)e^{i\omega_{12}t}d_1^\dagger d_2 + 2\mathcal{A}\cos(\omega_0 t)e^{-i\omega_{12}t}d_2^\dagger d_1 \tag{6.26}$$

$$= 2\mathcal{A}\cos(\omega_0 t)\left(e^{i\omega_{12}t}\tau_+ + e^{-i\omega_{12}t}\tau_-\right), \tag{6.27}$$

where the Pauli matrix τ is the raising and lowering operators of two quantum-dot levels whose energy difference is $\omega_{12} = \epsilon_1 - \epsilon_2$.

When the AC frequency approaches the resonant frequency, the driving Hamiltonian simplifies to the following form.

$$H_{\text{drive}}(t) = \mathcal{A}\left(e^{i\omega_{12}t} + e^{-i\omega_{12}t}\right)\left(e^{i\omega_{12}t}\tau_+ + e^{-i\omega_{12}t}\tau_-\right) \tag{6.28}$$

$$= \mathcal{A}\left(\tau_+ + \tau_- + e^{2i\omega_{12}t}\tau_+ + e^{-2i\omega_{12}t}\tau_-\right). \tag{6.29}$$

We neglect the terms oscillating at $\pm 2\omega_{12}$ because they average out over time. The average value of the rapidly oscillating term over a long period is

$$\frac{1}{t}\int_0^t ds\, e^{\pm 2i\omega_{12}s} = \frac{e^{\pm 2i\omega_{12}t} - 1}{\pm 2i\omega_{12}t}. \tag{6.30}$$

Since the exponential $\exp(\pm 2i\omega_{12}t)$ bounces between complex numbers with unit magnitude, the numerator remains bounded, with a maximum value of 2. In contrast, the denominator lacks such a bound. Consequently, the average value of the rapidly oscillating term over a long period is effectively zero, and we approximate the driving Hamiltonian as follows.

$$H_{\text{drive}} \approx \mathcal{A}\left(\tau_+ + \tau_-\right). \tag{6.31}$$

By disregarding the rapid oscillations, the RWA eliminates the explicit time dependence from the driving Hamiltonian in the interaction picture.

6.2.2 Schrieffer-Wolff transformation

The Schrieffer-Wolff (SW) transformation is a type of perturbation theory approach. In general, the Hamiltonian is composed of an unperturbed Hamiltonian H_0 and a small

perturbation H_1. By selecting an anti-hermitian generator S such that $H_1 + [S, H_0] = 0$, the SW transformation yields a transformed Hamiltonian H' as

$$H' = e^S (H_0 + H_1) e^{-S} \tag{6.32}$$

$$= H_0 + H_1 + [S, H_0] + [S, H_1] + \frac{1}{2}[S, [S, H_0]] + \frac{1}{2}[S, [S, H_1]] + \dots \tag{6.33}$$

$$= H_0 + \frac{1}{2}[S, H_1] + \frac{1}{6}[S, [S, H_1]] + \dots \tag{6.34}$$

$$H' = H_0 + \sum_n \left(\frac{1}{n!} - \frac{1}{(n+1)!} \right) \underbrace{[S, [S, \dots [S}_{n}, H_1] \dots]] . \tag{6.35}$$

Because the operator S is of the order of the perturbation amplitude, a second-order perturbative approximation will yield an effective Hamiltonian as

$$H' \approx H_0 + \frac{1}{2}[S, H_1] . \tag{6.36}$$

To determine the new perturbation represented by the second term in Eq. (6.36), one may initially diagonalize the unperturbed Hamiltonian, so that the definition of the generator S can be expressed as follows.

$$(H_1)_{mn} = \sum_l \left[(H_0)_{ml} S_{ln} - S_{ml} (H_0)_{ln} \right] = \sum_l \left[\epsilon'_{ml} \delta_{m,l} S_{ln} - S_{ml} \epsilon'_{ln} \delta_{ln} \right] \tag{6.37}$$

$$\Rightarrow S_{mn} = \frac{(H_1)_{mn}}{\epsilon'_{mm} - \epsilon'_{nn}}, \tag{6.38}$$

where ϵ'_{mm} and ϵ'_{nn} denote the diagonal elements of the diagonalized unperturbed Hamiltonian H_0. Thus, the perturbed Hamiltonian in Eq. (6.36) can be expressed as

$$\frac{1}{2}[S, H_1]_{mn} = \frac{1}{2} \sum_l \left[S_{ml} (H_1)_{ln} - (H_1)_{ml} S_{ln} \right] \tag{6.39}$$

$$= \frac{1}{2} \sum_l (H_1)_{ml} (H_1)_{ln} \left(\frac{1}{\epsilon'_{mm} - \epsilon'_{ll}} + \frac{1}{\epsilon'_{nn} - \epsilon'_{ll}} \right) . \tag{6.40}$$

In the scenario of the open system depicted in Figure 6.1, we regard the tunneling Hamiltonian presented in Equation (6.24) as the perturbation, attributable to the minor energy scale of the tunnel couplings between quantum dots and MBSs, denoted by t_0. The Hamiltonian of both the box and the environment has already been diagonalized. Within the Hamiltonian $H_{\mathrm{QD}} + H_{\mathrm{drive}}$, the quantum-dot sector can be expressed in terms

of a non-interacting quantum gas Hamiltonian following its diagonalization. Therefore, the unperturbed contribution is given by $H_0 = H_{\text{box}} + H_{\text{QD}} + H_{\text{env}} + H_{\text{drive}}$, with its diagonalized form being as follows.

$$H_0 = E_C \left(N - N_g\right)^2 + \sum_{j,k=1}^{2} \epsilon_{jk} d_j^\dagger d_k + \sum_m E_m b_m^\dagger b_m \tag{6.41}$$

$$= E_C \left(N - N_g\right)^2 + \sum_{j'=1}^{4} \eta_{j'} c_{j'}^\dagger c_{j'} + \sum_m E_m b_m^\dagger b_m, \tag{6.42}$$

where ϵ_{jk} takes the value of the quantum dot energy level ϵ_j when $j = k$, and the value of the AC amplitude $\mathcal{A}$ when $j \neq k$, and the Bogoliubov transformation between the fermionic operators d_j and c_j is

$$\begin{pmatrix} d_1 \\ d_1^\dagger \\ d_2^\dagger \\ d_2 \end{pmatrix} = U_0 \begin{pmatrix} c_1 \\ c_2 \\ c_3 \\ c_4 \end{pmatrix}, \tag{6.43}$$

$$\text{where } U_0 = \begin{pmatrix} 0 & \frac{\eta_+ - 2\epsilon_2}{\sqrt{(\eta_+ - 2\epsilon_2)^2 + 4\mathcal{A}^2}} & \frac{2\mathcal{A}}{\sqrt{(\eta_+ - 2\epsilon_2)^2 + 4\mathcal{A}^2}} & 0 \\ \frac{\eta_- - 2\epsilon_2}{\sqrt{(\eta_+ - 2\epsilon_1)^2 + 4\mathcal{A}^2}} & 0 & 0 & \frac{2\mathcal{A}}{\sqrt{(\eta_+ - 2\epsilon_1)^2 + 4\mathcal{A}^2}} \\ 0 & \frac{\eta_- - 2\epsilon_2}{\sqrt{(\eta_+ - 2\epsilon_1)^2 + 4\mathcal{A}^2}} & \frac{2\mathcal{A}}{\sqrt{(\eta_+ - 2\epsilon_1)^2 + 4\mathcal{A}^2}} & 0 \\ \frac{\eta_+ - 2\epsilon_2}{\sqrt{(\eta_+ - 2\epsilon_2)^2 + 4\mathcal{A}^2}} & 0 & 0 & \frac{2\mathcal{A}}{\sqrt{(\eta_+ - 2\epsilon_2)^2 + 4\mathcal{A}^2}} \end{pmatrix}. \tag{6.44}$$

Besides, the eigenvalues corresponding to the quantum dots subspace are

$$\eta_1 = -\eta_+, \qquad \eta_2 = \eta_-, \qquad \eta_3 = -\eta_-, \qquad \eta_4 = \eta_+, \tag{6.45}$$

where $\eta_\pm = (\epsilon_1 + \epsilon_2 \pm \sqrt{4\mathcal{A}^2 + (\epsilon_1 - \epsilon_2)^2})/2$. Consequently, the diagonal elements within the unperturbed Hamiltonian comprise the charging energy E_C, the eigenvalues $\eta_1, \ldots, \eta_4$ and the bosonic energy E_m.

By applying Eq. (6.40), one can derive the second-order perturbation following the diagonalization of the unperturbed Hamiltonian.

$$\left(H_{\text{tun}}^{(2)}\right)_{mn} = \frac{1}{2} \sum_l \left(H_{\text{tun}}\right)_{ml} \left(H_{\text{tun}}\right)_{ln} \left(\frac{1}{\epsilon'_{mm} - \epsilon'_{ll}} + \frac{1}{\epsilon'_{nn} - \epsilon'_{ll}}\right), \tag{6.46}$$

where $\epsilon'_{mm} \in \{E_C, \eta_1, \ldots, \eta_4, E_m\}$. In Sec. 6.1, we have assumed that the charging energy is greater than the energy scale associated with all other dynamics within the open system, i.e.: $E_C \gg \max(\eta_1, \ldots, \eta_4, E_m)$. This assumption allows us to approximate the second-order term (6.46) as detailed below.

$$\left(H_{\text{tun}}^{(2)}\right)_{mn} \approx \frac{1}{E_C} \sum_l \left(H_{\text{tun}}\right)_{ml} \left(H_{\text{tun}}\right)_{ln} \tag{6.47}$$

$$\Rightarrow H_{\text{cot}} \approx H_{\text{tun}}^{(2)} = \frac{1}{E_C} H_{\text{tun}} H_{\text{tun}}. \tag{6.48}$$

Employing the expression of the tunneling Hamiltonian from Eq. (6.24), the cotunneling Hamiltonian is formulated as follows.

$$\begin{aligned} H_{\text{cot}}(t) &= \frac{t_0^2}{E_C} \sum_{j,k=1}^{2} \sum_{\nu \neq \mu} e^{i(\delta_j - \delta_k)} \lambda_{j,\nu} \lambda_{k,\mu} e^{i(\beta_{j,\nu} - \beta_{k,\mu})} \gamma_\nu \gamma_\mu d_j^\dagger(t) d_k(t) + \text{h.c.} \\ &= g_0 \sum_{j,k=1}^{2} e^{i(\delta_j - \delta_k)} W_{jk} \left(2 d_j^\dagger(t) d_k(t) - \delta_{j,k}\right), \end{aligned} \tag{6.49}$$

where Majorana operators are denoted with subscripts $\nu, \mu \in \{1, \ldots, 4\}$, and the energy scale $g_0 = t_0^2/E_C$, and the operator W_{jk} characterizes the transport within the Majorana sector as detailed below.

$$W_{jk} = \sum_{\nu \neq \mu} \left(\lambda_{j,\nu} \lambda_{k,\mu} e^{i(\beta_{j,\nu} - \beta_{k,\mu})} - \lambda_{j,\mu} \lambda_{k,\nu} e^{i(\beta_{j,\mu} - \beta_{k,\nu})}\right) \gamma_\nu \gamma_\mu. \tag{6.50}$$

Although the operator W_{jk} is non-Hermitian when $j \neq k$, the cotunneling Hamiltonian presented in Eq. (6.49) maintains Hermiticity because $W_{jk}^\dagger = W_{kj}$.

When considering an even occupation number in quantum dots ($N_{QD} = 0$ or 2), the occupation number is conserved at all times, which gives the cotunneling Hamiltonian (6.49) as

$$H_{cot}^{N_{QD}=0,2} = g_0 \left(N_{QD} - 1\right) \sum_{j=1}^{2} W_{jj}. \tag{6.51}$$

In this scenario, the cotunneling process does not result in dissipation. Thus, we focus on the case of an odd occupation number in quantum dots, specifically $N_{QD} = 1$, which

leads to

$$H_{\text{cot}}^{N_{QD}=1} = 2g_0 \sum_{j,k=1}^{2} W_{jk} d_j^\dagger d_k \tag{6.52}$$

$$\begin{aligned} H_{\text{cot}}^{N_{QD}=1} = {} & 2g_0 \left(e^{i(\epsilon_1-\epsilon_2)t} e^{i(\delta_1-\delta_2)} W_{12}\tau_+ + e^{-i(\epsilon_1-\epsilon_2)t} e^{i(\delta_2-\delta_1)} W_{21}\tau_- \right) \\ & + g_0 \left(W_{11} + W_{22}\right) \tau_z, \end{aligned} \tag{6.53}$$

where the quantum-dot Pauli matrices are $\tau_+ = d_1^\dagger d_2$ and $\tau_z = d_1^\dagger d_1 - d_2^\dagger d_2$. For the odd occupation number in quantum dots, the cotunneling process, specifically the first term in Eq. (6.53), induces dissipation. Hereafter, the subsequent analysis will be restricted to scenarios involving odd occupation numbers in quantum dots.

Consequently, we obtain the effective Hamiltonian in the interaction picture, derived from Eq. (6.36), as follows.

$$H_{\text{eff}}(t) = \underbrace{H_{\text{QD}} + H_{\text{drive}}}_{H_{\text{s}}} + H_{\text{env}} + H_{\text{cot}}(t), \tag{6.54}$$

where we exclude the box Hamiltonian, as it simplifies to an inconsequential constant energy shift that does not affect the dynamics of the system.

In this section, we analyze the Hamiltonian of the Majorana open system sketched in Fig. 6.1. Drawing on references [123, 126], we adopt the low-energy approximation, which posits that the charging energy E_C and the superconducting gap Δ dominate over other energy scales. Specifically, this condition is expressed as $\min(E_C, \Delta) \gg \max(\epsilon_j, t_0, \mathcal{A}, E_m, T, \omega_0, \ldots)$, where T represents the thermal energy. The substantial charging energy gives rise to the Coulomb blockade within the Majorana box. By adjusting the back-gate voltage N_g, the box can be trapped in the ground state subspace. Utilizing the RWA and the SW transformation, we derive the effective low-energy Hamiltonian presented in Eq. (6.54), taking into account the odd occupation number in quantum dots. In Table 6.1, we present a summary of the conditions under which the applied approximations are valid, as well as their influences on the Hamiltonian.

In experiments, a Majorana box can be realized using a superconductor-semiconductor heterostructure. One example of such a heterostructure is InSb/NbTiN, which operates effectively at temperatures below 15 K. In this Majorana box, both the charging energy and the maximum superconducting gap are approximately 1 meV when the InSb nanowire is several micrometers long and has a diameter on the order of tens of nanometers [63]. In the low-energy limit, where the energy scales are much lower than 1 meV except for the charging energy and the superconducting gap, the following approximations can be used.

Approximation	Constraint	Impact
Low-energy approximation	$\min(E_C, \Delta)$ is greater than $\max(\epsilon_j, t_0, \mathcal{A}, E_m, T, \omega_0, \ldots)$.	The Majorana box is confined to the ground state subspace, and the second-order term in the Schrieffer-Wolff transformation approximates to Eq. (6.48).
Rotating wave approximation	$\omega_0 \approx \lvert\epsilon_1 - \epsilon_2\rvert$.	The driving Hamiltonian can be approximated to Eq. (6.31) which is time-independent.
Schrieffer-Wolff transformation	The coupling strength between quantum dots and MBSs, t_0 or g_0, is considered to be small.	The perturbation can be written as the cotunneling Hamiltonian in Eq. (6.49).
Odd quantum-dot occupation number	$N_d = 1$.	The cotunneling Hamiltonian can be simplified to Eq. (6.53).

Table 6.1: **Approximations for the effective Hamiltonian**. The table provides a comprehensive list of the approximations applied, along with their respective impacts on the Hamiltonian. Following these approximations, we derive the effective Hamiltonian and its associated perturbation, namely the cotunneling Hamiltonian.

For weak driving of the system with amplitude $\mathcal{A} < g_0$, the RWA is valid, provided that $T < \omega_0$. Additionally, the Born-Markov approximation, which is necessary for deriving the Lindblad equation, is justified when $g_0 < T$ for weak couplings.

In the subsequent section, we will focus on a single box within the open system, as depicted in Figure 6.1. Starting from the effective Hamiltonian presented in Eq. (6.54), we will show an analysis that leads to the formulation of the Lindblad form master equation. This equation maps the system from its initial states to the steady states, all the while preserving the fundamental properties of the density matrix.

6.3 From the Von Neumann equation to the Lindblad equation

The density matrix operator, a fundamental concept in quantum mechanics, represents a quantum state as a convex combination of the outer products of the constituent states within the ensemble, each weighted by their respective probabilities. For instance, an observable operator for a physical quantity x_n, in the Schrödinger picture, gives

$$X|\psi_n\rangle = x_n|\psi_n\rangle, \text{ with } |\psi\rangle = \sum_n a_n|\psi_n\rangle. \tag{6.55}$$

Accordingly, the expectation value of X is given by

$$\langle X\rangle = \sum_n |a_n|^2 x_n. \tag{6.56}$$

The density matrix in this case is defined as

$$\rho = |\psi\rangle\langle\psi| = \sum_{n,m} a_n a_m^* |\psi_n\rangle\langle\psi_m|. \tag{6.57}$$

Given that the state function is normalized, the sum of the moduli squared of its expansion coefficients a_n must satisfy $\sum_n a_n a_n^* = 1$. This normalization condition is equivalent to the requirement that the trace of the density matrix, which is constructed from these state functions, must equal unity, ensuring the total probability is conserved. Thus, the expectation value of X is given by the trace of the product of the density matrix ρ and the corresponding observable operator X, expressed mathematically as

$$\mathrm{Tr}\,(\rho X) = \sum_{n',n,m} \langle\psi_{n'}|a_n a_m^*|\psi_n\rangle\langle\psi_m|X|\psi_{n'}\rangle = \sum_{n',n,m} a_n a_m^* x_{n'}\delta_{n,n'}\delta_{m,n'} \tag{6.58}$$

$$\Rightarrow \mathrm{Tr}\,(\rho X) = \sum_n |a_n|^2 x_n = \langle X\rangle. \tag{6.59}$$

This procedure provides a measure of the average outcome when the observable is measured on the quantum system described by the density matrix ρ. Moreover, the general form of the density matrix, as presented in Eq. (6.57), embodies two fundamental characteristics: it is Hermitian and it has a trace equal to one.

In general, the time evolution in the density matrix can be derived from the time-dependent Schrödinger equation, $id|\psi\rangle/dt = H(t)|\psi\rangle$.

$$\frac{d}{dt}\rho(t) = \left(\frac{d}{dt}|\psi\rangle\right)\langle\psi| + |\psi\rangle\left(\frac{d}{dt}\langle\psi|\right) = -iH(t)|\psi\rangle\langle\psi| + i|\psi\rangle\langle\psi|H(t) \tag{6.60}$$

$$\Rightarrow \frac{d}{dt}\rho(t) = -i\left[H(t),\rho(t)\right]. \tag{6.61}$$

Eq. (6.61) is recognized as the von Neumann or Liouville-von Neumann equation. Now, we consider the scenario where an open system is coupled to a bath, with their respective density matrices denoted as ρ_s and ρ_env. At the initial time ($t = 0$), the reduced open system and the bath are taken to be uncorrelated.

$$\rho_\mathrm{tot}(t) = \rho_\mathrm{s}(t)\otimes\rho_\mathrm{env}(t) + \rho_\mathrm{corr}(t), \text{ with } \rho_\mathrm{corr}(0) = 0, \tag{6.62}$$

where ρ_{corr} is not a quantum state but represents the correlation matrix.

The Hamiltonian for the entire system is expressed as the sum of three components: the open system Hamiltonian H_{s}, the bath H_{env}, and the interaction between them H_{int}. The interaction picture von Neumann equation (see Appendix F) for the reduced density matrix is formulated by taking the partial trace over the degrees of freedom of the bath.

$$\frac{d}{dt}\rho_{\text{s}}(t) = -i\text{Tr}_{\text{env}}\left[H_{\text{int}}(t), \rho_{\text{tot}}(t)\right] \tag{6.63}$$

By integrating both sides of the von Neumann equation (6.63) over time, we derive the following expression for the evolved density matrix.

$$\rho_{\text{s}}(t) = \rho_{\text{s}}(0) - i\int_0^t ds\ \text{Tr}_{\text{env}}\left[H_{\text{int}}(s), \rho_{\text{tot}}(s)\right], \tag{6.64}$$

Substituting this expression back into the von Neumann equation yields

$$\frac{d}{dt}\rho_{\text{s}}(t) = -\int_0^t ds\ \text{Tr}_{\text{env}}\left[H_{\text{int}}(t), \left[H_{\text{int}}(s), \rho_{\text{tot}}(s)\right]\right], \tag{6.65}$$

where we assume the initial reduced density matrix gives $\text{Tr}_{\text{env}}\left[H_{\text{int}}(t), \rho_{\text{tot}}(0)\right] = 0$. In the subsequent subsection, we will discuss the necessity of employing the Born-Markov approximation within the framework of dynamical maps, followed by an approximation of Eq. (6.65) to the Redfield equation.

6.3.1 The Born-Markov approximation

Considering the linearity of the Schrödinger equation, the time evolution of the state function is given by

$$i\frac{d}{dt}|\psi(t)\rangle = H(t)|\psi(t)\rangle, \tag{6.66}$$

$$\Rightarrow |\psi(t)\rangle = U(t,0)|\psi(0)\rangle, \text{ where } U(t,0) = \mathcal{T}e^{-i\int_0^t ds\ H(s)}, \tag{6.67}$$

where $\mathcal{T}$ represents the chronological time-ordering operator, which arranges products of time-dependent operators in increasing order of their time arguments, from 0 to t. Therefore, the time evolution of the reduced density matrix for the open system can be described by the following equation.

$$\rho_{\text{s}}(t) = \text{Tr}_{\text{env}}\left(U(t,0)\rho_{\text{tot}}(0)U^\dagger(t,0)\right) \tag{6.68}$$

$$\Rightarrow \rho_{\text{s}}(t) = \text{Tr}_{\text{env}}\left[U(t,0)\left(\rho_{\text{s}}(0)\otimes\rho_{\text{env}}(0) + \rho_{\text{corr}}(0)\right)U^\dagger(t,0)\right]. \tag{6.69}$$

The overall evolution of the system cannot be factorized into the evolutions of the individual quantum subsystems, $U(t,0) \neq U_{\mathrm{s}}(t,0) \otimes U_{\mathrm{env}}(t,0)$, due to the exchange of information between the subsystems, which indicates their mutual interaction.

Without loss of generality, we denote the density matrices of the subsystems at the initial time $t = 0$ as convex combinations of pure initial states.

$$\rho_{\mathrm{s}}(0) = \sum_n a_n |\psi_n^{\mathrm{os}}\rangle\langle\psi_n^{\mathrm{os}}|, \qquad \rho_{\mathrm{env}}(0) = \sum_m b_m |\psi_m^{\mathrm{env}}\rangle\langle\psi_m^{\mathrm{env}}|. \tag{6.70}$$

Subsequently, the reduced density matrix in Eq. (6.69) can be expressed as

$$\rho_{\mathrm{s}}(t) = \sum_{m,m'} \mathcal{U}_{m'm}(t,0)\rho_{\mathrm{s}}(0)\mathcal{U}_{m'm}^{\dagger}(t,0) + \delta\rho(t,0) \equiv \mathcal{E}_{(t,0)}\rho_{\mathrm{s}}(0), \tag{6.71}$$

where the operator $\mathcal{U}_{m'm}(t,0) = \sqrt{b_m}\langle\psi_{m'}^{\mathrm{env}}|U(t,0)|\psi_m^{\mathrm{env}}\rangle$ encapsulates the global unitary evolution, depending solely on the initial state of the bath. Besides, the correlation term yields $\delta\rho(t,0) = \mathrm{Tr}_{\mathrm{env}}\left(U(t,0)\rho_{\mathrm{corr}}(0)U^{\dagger}(t,0)\right)$, and $\mathcal{E}_{t,0}$ denote a dynamical map on the open system from time 0 to t.

Given the absence of correlations at the initial time, that is, $\rho_{\mathrm{corr}}(0) = 0$, the dynamical map simplifies to the following form, known as the universal dynamical map (UDM) [130, 131].

$$\mathcal{E}_{(t,0)}\rho_{\mathrm{s}}(0) = \sum_{m,m'} \mathcal{U}_{m'm}(t,0)\rho_{\mathrm{s}}(0)\mathcal{U}_{m'm}^{\dagger}(t,0), \tag{6.72}$$

where $\sum_{m,m'} \mathcal{U}_{m'm}^{\dagger}(t,0)\mathcal{U}_{m'm}(t,0) \equiv \mathbb{I}$ is satisfied, ensuring $\mathrm{Tr}(\rho_{\mathrm{s}}) \equiv 1$. This linear map, a type of completely positive trace-preserving map (CPTPM), guarantees the retention of the essential and intrinsic properties of the density matrix throughout the mapping process.

Fig. 6.3 shows the time evolution in the reduced density matrix ρ_{s} as described by the UDM. However, a constraint of the UDM is that it cannot be defined for an intermediate time $t = t_1$ when the subsystems exhibit correlations, i.e., $\rho_{\mathrm{corr}}(t_1) \neq 0$ in Fig. 6.3. This results in the consequence that

$$\mathcal{E}_{(0,t_2)} \neq \mathcal{E}_{(0,t_1)}\mathcal{E}_{(t_1,t_2)}, \text{ where } t_1 < t_2. \tag{6.73}$$

To re-establish the composition law for the UDMs, one might consider a scenario in which the correlation matrix decays rapidly over time, signifying that the system's evolution is memoryless. Such an evolution is characterized as a Markovian evolution, and a

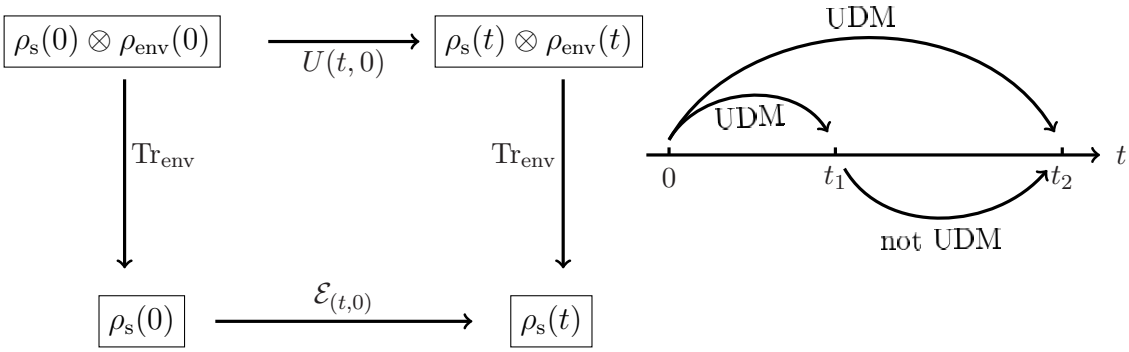

Figure 6.3: **Time evolution in the open system.** [130, 131] The left diagram shows that a dynamical map is a UDM (Universal Dynamical Map) only if it begins with a specific initial condition, $\rho_{tot}(t_0) = \rho_s(t_0) \otimes \rho_{env}(t_0)$. The right graph demonstrates the overall scenario illustrating the behavior of open quantum systems.

Markovian model is an adequate approximation when the influence of past states on the current state of the system diminishes rapidly.

The Markov approximation can also be adapted when the open system is weakly coupled to a considerably larger bath, implying the bath possesses a substantially greater number of degrees of freedom and effectively maintains equilibrium, regardless of its interactions with the open system. Furthermore, the weak coupling assumption implies that the system's back-action on the environment is negligible, thereby justifying the use of a perturbative approach. The scenario where weak couplings exist between the open system and a large bath is collectively referred to as the Born-Markov approximation. The approximation restores the composition law for UDMs, thereby preserving the fundamental properties of the density matrix throughout the mapping process.

Mathematically, under weak coupling conditions, the total density matrix can be represented as the tensor product of the subsystems' density matrices at all times, given that the memoryless bath maintains equilibrium due to the minimal influence of the system on the reservoir.

$$\rho_{tot}(t) \approx \rho_s(t) \otimes \rho_{evn}. \tag{6.74}$$

Thus, the time derivative of the density matrix in Eq. (6.65) is formulated as

$$\frac{d}{dt}\rho_s(t) = -\int_0^t ds\ \mathrm{Tr}_{env}\left[H_{int}(t), [H_{int}(s), \rho_s(s) \otimes \rho_{evn}]\right]. \tag{6.75}$$

Furthermore, the Markov approximation gives the evolution in the open system is short enough to justify the memoryless dynamics, and this leads to

$$\frac{d}{dt}\rho_{\mathrm{s}}(t) = -\int_0^t ds\ \mathrm{Tr}_{\mathrm{env}}\left[H_{\mathrm{int}}(t), [H_{\mathrm{int}}(s), \rho_{\mathrm{s}}(t)\otimes\rho_{\mathrm{evn}}]\right]. \tag{6.76}$$

This equation is also recognized as the Redfield equation, which captures the dynamics of the open system under the Born-Markov approximation.

To express the dynamics of the reduced system within the framework of a dynamical semigroup, we can perform the substitution $s \to t - s$ in the integral of Eq. (6.76). Since the Markov approximation asserts that the timescale over which the open system's state experiences significant changes is sufficiently longer than other relevant timescales, we can extend the upper limit of the integral to infinity. Consequently, we derive the Markovian quantum master equation as presented below.

$$\frac{d}{dt}\rho_{\mathrm{s}}(t) = -\int_0^\infty ds\ \mathrm{Tr}_{\mathrm{env}}\left[H_{\mathrm{int}}(t), [H_{\mathrm{int}}(t-s), \rho_{\mathrm{s}}(t)\otimes\rho_{\mathrm{evn}}]\right]. \tag{6.77}$$

The Markovian quantum master equation ensures complete positivity and trace preservation of the density matrix, and the subsequent part of this section will proceed to derive the Lindblad form master equation from this framework.

6.3.2 The Lindblad form master equation

In the open system with the Majorana architecture depicted in Fig. 6.1, the interaction dynamics are involved within the cotunneling Hamiltonian (6.53). As mentioned in Sec. 6.2.2, we have confined the system to an odd occupation number in the quantum dots. Dissipation arises when an electron transfers between the quantum dots within the framework of the cotunneling Hamiltonian, as described by Eq. (6.49).

$$V(t) = 2g_0 \sum_{j\neq k} e^{i\delta\epsilon_{jk}t} e^{i(\delta_j(t)-\delta_k(t))} W_{jk} d_j^\dagger d_k, \text{ for } j,k \in \{1,2\}, \tag{6.78}$$

where the cotunneling energy scale is represented by $g_0 = t_0^2/E_C$, and the energy difference between the levels of two quantum dots is denoted by $\delta\epsilon_{jk} = \epsilon_j - \epsilon_k$. The operator W_{jk} is defined in Eq. (6.50), and the electromagnetic fluctuations from the bath are represented by δ_j, as given in Eq. (6.25).

In this open system, the Markovian quantum master equation, as formulated in

Eq. (6.77), is expressed as follows

$$\frac{d}{dt}\rho_{\rm s}(t) = -\int_0^\infty ds\ {\rm Tr}_{\rm env}\left[V(t),[V(t-s),\rho_{\rm s}(t)\otimes\rho_{\rm evn}]\right] \tag{6.79}$$

$$= -\int_0^\infty ds\ {\rm Tr}_{\rm env}\left[V(t)V(t-s)\rho_{\rm s}(t)\otimes\rho_{\rm evn}\right. \tag{6.80}$$

$$\left.-V(t-s)\rho_{\rm s}(t)\otimes\rho_{\rm evn}V(t)+h.c.\right].$$

Using the expression of $V(t)$ as given in Eq. (6.78), the first term of the integrand in the master equation is formulated as presented below.

$$V(t)V(t-s)\rho_{\rm s}(t)\otimes\rho_{\rm evn} = 4g_0^2\sum_{j\neq k}\sum_{j'\neq k'} e^{i(\delta_j(t)-\delta_k(t))}e^{i(\delta_{j'}(t-s)-\delta_{k'}(t-s))} \tag{6.81}$$

$$\times\, e^{i(\delta\epsilon_{jk}+\delta\epsilon_{j'k'})t-i\delta\epsilon_{j'k's}}W_{jk}W_{j'k'}d_j^\dagger d_k d_{j'}^\dagger d_{k'}\rho_{\rm s}(t)\otimes\rho_{\rm evn}.$$

Once again, the occupation number of the quantum dots is restricted to one, and the tunneling processes at times t and $t-s$ should be inverses of each other.

$$V(t)V(t-s)\rho_{\rm s}(t)\otimes\rho_{\rm evn} = 4g_0^2\sum_{j\neq k} e^{i(\delta_j(t)-\delta_k(t))}e^{i(\delta_k(t-s)-\delta_j(t-s))} \tag{6.82}$$

$$\times\, e^{-i\delta\epsilon_{kj}s}W_{jk}W_{kj}d_j^\dagger d_k d_k^\dagger d_j\rho_{\rm s}(t)\otimes\rho_{\rm evn}.$$

One can distinguish between the sectors of the bath and the open system, which comprises quantum dots and the Majorana box. After performing the trace over the bath's degrees of freedom and integrating over the time s, one identifies the first term in the master equation, as shown in Eq. (6.80), as

$$\int_0^\infty ds\ {\rm Tr}_{\rm env}\left[V(t)V(t-s)\rho_{\rm s}(t)\otimes\rho_{\rm evn}\right] = \sum_{j\neq k}\Lambda_{kj}A_{jk}A_{kj}\rho_{\rm s}(t), \tag{6.83}$$

$$\text{where } A_{jk} = 2W_{jk}d_j^\dagger d_k, \tag{6.84}$$

$$\Lambda_{kj} = g_0^2\int_0^\infty ds\ e^{-i\delta\epsilon_{kj}s}{\rm Tr}_{\rm env}\left[e^{i(\delta_j(t)-\delta_k(t))}e^{i(\delta_k(t-s)-\delta_j(t-s))}\rho_{\rm evn}\right] \tag{6.85}$$

$$= g_0^2\int_0^\infty ds\ e^{-i\delta\epsilon_{kj}s}e^{J_{\rm env}(s)}.$$

Given that $W_{jk} = W_{kj}^\dagger$, as defined in Eq. (6.50), one finds that the operator $A_{jk} = A_{kj}^\dagger$.

The bath correlation function J_{env} is defined as the product of the bath operators at times t and $t-s$.

$$e^{J_{\text{env}}(t,s)} = \text{Tr}_{\text{env}}\left[e^{i(\delta_j(t)-\delta_k(t))}e^{i(\delta_k(t-s)-\delta_j(t-s))}\rho_{\text{env}}\right], \tag{6.86}$$

$$e^{J_{\text{env}}(t,s)} = \left\langle e^{i(\delta_j(t)-\delta_k(t))}e^{i(\delta_k(t-s)-\delta_j(t-s))}\right\rangle_{\text{env}}. \tag{6.87}$$

The equilibrium state of the bosonic bath is assumed to be the thermal state.

$$\rho_{\text{env}} = Z_{\text{env}}^{-1}e^{-H_{\text{env}}/T}, \text{ where } Z_{\text{env}} = \text{Tr}_{\text{env}}\left(e^{-H_{\text{env}}/T}\right). \tag{6.88}$$

Boltzmann's constant k_B is assumed to be unity. Because the bath remains in the equilibrium state and is weakly coupled with the open system, it is justified to assume a time-homogeneous bath correlation function.

$$\left\langle e^{i(\delta_j(t)-\delta_k(t))}e^{i(\delta_k(t-s)-\delta_j(t-s))}\right\rangle_{\text{env}} = \left\langle e^{i(\delta_j(s)-\delta_k(s))}e^{i(\delta_k(0)-\delta_j(0))}\right\rangle_{\text{env}} \tag{6.89}$$

$$\Rightarrow e^{J_{\text{env}}(s)} = \left\langle e^{i(\delta_j(s)-\delta_k(s))}e^{i(\delta_k(0)-\delta_j(0))}\right\rangle_{\text{env}}. \tag{6.90}$$

In Appendix G, the bath correlation function is derived with a cutoff frequency ω_c, which leads to an Ohmic bath when the frequency is below ω_c.

$$J_{\text{env}}(s) = \int \frac{d\omega}{\pi}\frac{\mathcal{J}(\omega)}{\omega^2}\left[\coth\left(\omega/2T\right)\left(\cos(\omega s)-1\right) - i\sin(\omega s)\right], \tag{6.91}$$

where the spectral density in Ohmic bath is $\mathcal{J}(\omega) = \alpha\omega\exp\left(-\omega/\omega_c\right)$, and α represents a dimensionless coupling strength between the system and the bath.

We have derived the correlation function J_{env} for a bosonic bath, which should consistently appear in each term of the expanded quantum master equation as shown in Eq. (6.80). From Appendix H, the second term of the quantum master equation has been derived and is presented as follows.

$$\int_0^\infty ds\ \text{Tr}_{\text{env}}\left[V(t)\rho_{\text{s}}(t)\otimes\rho_{\text{evn}}V(t-s)\right] = \sum_{j\neq k}\Lambda_{jk}A_{jk}\rho_{\text{s}}(t)A_{jk}^\dagger, \tag{6.92}$$

where the operator A_{jk} and the complex scalar Λ_{jk} are respectively defined in Eqs. (6.84) and (6.85). Therefore, the Markovian quantum master equation in Eq. (6.80) can be

written by Eqs. (6.83) and (6.92) and their Hermitian conjugation.

$$\frac{d}{dt}\rho_{\rm s}(t) = -\sum_{j\neq k}\Big(\Lambda_{jk}A_{jk}^{\dagger}A_{jk}\rho_{\rm s}(t) - \Lambda_{jk}A_{jk}\rho_{\rm s}(t)A_{jk}^{\dagger} + \Lambda_{jk}^{*}\rho_{\rm s}(t)A_{jk}^{\dagger}A_{jk} \tag{6.93}$$
$$-\Lambda_{jk}^{*}A_{jk}\rho_{\rm s}(t)A_{jk}^{\dagger}\Big)$$
$$= -\sum_{j\neq k}\Big(\mathrm{Re}\left\{\Lambda_{jk}\right\}\left\{A_{jk}^{\dagger}A_{jk},\rho_{\rm s}(t)\right\} + i\mathrm{Im}\left\{\Lambda_{jk}\right\}\left[A_{jk}^{\dagger}A_{jk},\rho_{\rm s}(t)\right] \tag{6.94}$$
$$-2\mathrm{Re}\left\{\Lambda_{jk}\right\}A_{jk}\rho_{\rm s}(t)A_{jk}^{\dagger}\Big).$$

The complex scalar Λ_{kj} defined in Eq. (6.85) can be decomposed into its imaginary and real parts.

$$\Lambda_{jk} = \frac{1}{2}\tilde{\Gamma}_{jk} + i\tilde{h}_{jk} \tag{6.95}$$

Finally, we have arrived at the Lindblad form of the master equation, which is presented as follows.

$$\frac{d}{dt}\rho_{\rm s}(t) = -\sum_{j\neq k}\left(\frac{1}{2}\tilde{\Gamma}_{jk}\left\{A_{jk}^{\dagger}A_{jk},\rho_{\rm s}(t)\right\} + i\tilde{h}_{jk}\left[A_{jk}^{\dagger}A_{jk},\rho_{\rm s}(t)\right]\right. \tag{6.96}$$
$$\left.-\tilde{\Gamma}_{jk}A_{jk}\rho_{\rm s}(t)A_{jk}^{\dagger}\right)$$
$$= -i\left[H_{\rm LS},\rho_{\rm s}(t)\right] + \sum_{j\neq k}\tilde{\Gamma}_{jk}\left(A_{jk}\rho_{\rm s}(t)A_{jk}^{\dagger} - \frac{1}{2}\left\{A_{jk}^{\dagger}A_{jk},\rho_{\rm s}(t)\right\}\right), \tag{6.97}$$

where the Lamb shift Hamiltonian is $H_{\rm LS} = \sum_{j\neq k}\tilde{h}_{jk}A_{jk}^{\dagger}A_{jk}$. In the Schrödinger picture, the Hamiltonian of the open system, $H_{\rm s}$ in Eq. (6.54), appears in the coherent dynamics.

$$\frac{d}{dt}\rho_{\rm s}(t) = -i\left[H'_{\rm LS},\rho_{\rm s}(t)\right] + \sum_{j\neq k}\tilde{\Gamma}_{jk}\left(A_{jk}\rho_{\rm s}(t)A_{jk}^{\dagger} - \frac{1}{2}\left\{A_{jk}^{\dagger}A_{jk},\rho_{\rm s}(t)\right\}\right), \tag{6.98}$$

where $H'_{\rm LS} = H_{\rm QD} + \mathcal{A}(\tau_{+}+\tau_{-}) + H_{\rm LS}$.

In the Lindblad equation (6.98), the commutator term represents the coherent dynamics of the system. It is expected to vanish at the steady state, characterized by $\rho_{\rm s}(t\to\infty)$, where the system reaches equilibrium and no longer exhibits coherent evolution. The second contribution within the Lindblad equation represents the dissipative dynamics, with the transition rate denoted as $\tilde{\Gamma}_{jk}$. This rate corresponds to the real part of the

complex scalar Λ_{jk} (6.85), thereby encapsulating the rate of state transitions within the system due to environmental interactions.

The process of quantum "jumping" or "collapsing" is encapsulated by the term $A_{jk}\rho_{\mathrm{s}}A_{jk}^{\dagger}$ in the Lindblad equation. Hence, the operator A_{jk} is aptly termed the "jump operator". This term accounts for the system's transitions induced by interactions with the environment, leading to a change in the system's state. The final anti-commutator term in the Lindblad equation is responsible for the "smoothing out" of the density matrix, reflecting the averaging effects induced by the environment. This term helps maintain the complete positivity and trace preservation of ρ_{s}, thereby ensuring that the density matrix describes a valid quantum state. One can prove this by taking the trace of the Lindblad equation (6.98), noting that the trace of the coherent dynamics is zero:

$$-i\mathrm{Tr}_{\mathrm{os}}\left[H'_{\mathrm{LS}},\rho_{\mathrm{s}}(t)\right]=-i\left[\mathrm{Tr}_{\mathrm{os}}\left(H'_{\mathrm{LS}}\rho_{\mathrm{s}}(t)\right)-\mathrm{Tr}_{\mathrm{os}}\left(\rho_{\mathrm{s}}(t)H'_{\mathrm{LS}}\right)\right]=0. \tag{6.99}$$

The traces of the "jump term" and the "decay terms" cancel each other out as follows.

$$\begin{aligned}&\sum_{j\neq k}\tilde{\Gamma}_{jk}\left[\mathrm{Tr}_{\mathrm{os}}\left(A_{jk}\rho_{\mathrm{s}}(t)A_{jk}^{\dagger}\right)-\frac{1}{2}\mathrm{Tr}_{\mathrm{os}}\left(A_{jk}^{\dagger}A_{jk}\rho_{\mathrm{s}}(t)\right)-\frac{1}{2}\mathrm{Tr}_{\mathrm{os}}\left(\rho_{\mathrm{s}}(t)A_{jk}^{\dagger}A_{jk}\right)\right]\\&=\sum_{j\neq k}\tilde{\Gamma}_{jk}\left[\mathrm{Tr}_{\mathrm{os}}\left(A_{jk}\rho_{\mathrm{s}}(t)A_{jk}^{\dagger}\right)-\mathrm{Tr}_{\mathrm{os}}\left(A_{jk}\rho_{\mathrm{s}}(t)A_{jk}^{\dagger}\right)\right]=0.\end{aligned} \tag{6.100}$$

Thus, the trace of the reduced density matrix is preserved in the Lindblad map as $\mathrm{Tr}_{\mathrm{os}}(d\rho_{\mathrm{s}}/dt)\equiv 0$.

The reduced density matrix, encompassing the Majorana box and the quantum dots, is observed to become factorized on a timescale that is equivalent to the inverse of the dissipative gap. This gap is associated with the reduced Lindbladian, which exclusively governs the Majorana sector. Consequently, it is justified to approximate the steady-state density matrix, $\rho_{\mathrm{s}}(t\to\infty)$, as the tensor product $\rho_M(t\to\infty)\otimes\rho_{\mathrm{QD}}$. Here ρ_{M} and ρ_{QD} denote the reduced density matrices of the MBSs and quantum dots, respectively. Given the constraint that the occupation number of the quantum dots is restricted to one, the reduced density matrix ρ_{QD} is written as a 2×2 density matrix.

$$\rho_{\mathrm{QD}}=\begin{pmatrix}1-p & p_{\perp}\\ p_{\perp}^{*} & p\end{pmatrix}, \tag{6.101}$$

where p is a real-valued probability ($0\leq p\leq 1$) of observing an electron in the occupied quantum dot 1, and $p_{\perp}$ is the coherence between two quantum dots. The driving amplitude $\mathcal{A}$ becomes apparent implicitly through its effect on the occupation

probabilities of the quantum dots, which is given by $p = p(\mathcal{A})$. In the presence of dephasing induced by the bath, it is reasonable to assume $p_\perp$ to be zero.

After performing the trace over the quantum-dot subspace when the system has reached a sufficiently long stabilization time [126], the Lindblad equation, which exclusively governs the dynamics of the Majorana sector, is formulated as follows.

$$\mathcal{L}\rho_{\mathrm{M}}(t) = -i\left[H'_{\mathrm{LS}}, \rho_{\mathrm{s}}(t)\right] + \sum_{j\neq k}\Gamma_{jk}\left(K_{jk}\rho_{\mathrm{M}}(t)K_{jk}^{\dagger} - \frac{1}{2}\left\{K_{jk}^{\dagger}K_{jk}, \rho_{\mathrm{M}}(t)\right\}\right), \tag{6.102}$$

where the jump operators and their dissipative transition rates are respectively given by

$$K_{jk} = W_{jk}, \tag{6.103}$$

$$\Gamma_{12} = p\tilde{\Gamma}_{12}, \qquad \Gamma_{21} = (1-p)\tilde{\Gamma}_{21}. \tag{6.104}$$

We reiterate that the operator W_{jk}, which encodes the Majorana operators, is explicitly defined in Eq. (6.50), and the transition rate $\tilde{\Gamma}_{jk}$ corresponds to the real part of Λ_{jk} (6.85).

The transition rate $\tilde{\Gamma}_{jk}$ is associated to the bath correction function J_{env} (6.91). This correlation function demonstrates the Kubo-Martin-Schwinger (KMS) symmetry, which is detailed in Appendix (I). The KMS symmetry indicates a periodicity in imaginary time, such that $J_{\mathrm{env}}(-s - i/T) = J_{\mathrm{env}}(s)$, when the bath is in detailed balance. By substituting $s = -s' - i/T$, the transition rate, which is the real part of Λ_{jk}, as given in Eq. (6.85), transforms accordingly.

$$\tilde{\Gamma}_{jk} = \mathrm{Re}\Lambda_{jk} = g_0^2\mathrm{Re}\int_0^\infty ds'\, e^{i\delta\epsilon_{jk}s'}e^{-\delta\epsilon_{jk}/T}e^{J_{\mathrm{env}}(-s'-i/T)} \tag{6.105}$$

$$= e^{-\delta\epsilon_{jk}/T}g_0^2\mathrm{Re}\int_0^\infty ds'\, e^{i\delta\epsilon_{jk}s'}e^{J_{\mathrm{env}}(-s')}. \tag{6.106}$$

Given that the energy difference between two quantum dots is defined as $\delta\epsilon_{jk} = \epsilon_j - \epsilon_k = -\delta\epsilon_{kj}$, the KMS symmetry in the correlation function implies that the forward and backward transition rates are exponentially related, with one being suppressed relative to the other.

$$\tilde{\Gamma}_{jk} = e^{-\delta\epsilon_{jk}/T}\mathrm{Re}2\Lambda_{kj} = e^{-\delta\epsilon_{jk}/T}\tilde{\Gamma}_{kj}. \tag{6.107}$$

There are two quantum dots, QD1 and QD2, within the open system shown in Fig. 6.1. We define the energy levels of quantum dots such that $\epsilon_2 > \epsilon_1$, which results in the following relationship between the transition rates.

$$\tilde{\Gamma}_{21} = e^{-\delta\epsilon_{21}/T}\tilde{\Gamma}_{12},\ \delta\epsilon_{21} > 0. \tag{6.108}$$

In the scenario where the temperature is sufficiently low, as outlined in the low-energy approximation in Table 6.1, the transition rate $\tilde{\Gamma}_{21}$, associated with the jump operator A_{21} that represents the transport from QD1 to QD2, becomes negligible. Therefore, dissipation described in the Lindblad equation (6.102) is solely contributed by the transport from the high energy level ϵ_2 to the low energy level ϵ_1.

$$\mathcal{L}\rho_{\mathrm{M}}(t) \approx -i\left[H_{\mathrm{LS}}^{M}, \rho_{\mathrm{s}}(t)\right] + \Gamma_{12}\left(K_{12}\rho_{\mathrm{M}}(t)K_{12}^{\dagger} - \frac{1}{2}\left\{K_{12}^{\dagger}K_{12}, \rho_{\mathrm{M}}(t)\right\}\right), \tag{6.109}$$

where $H_{\mathrm{LS}}^{M} = \sum_{j\neq k} p_j \tilde{h}_{jk} K_{jk}^{\dagger} K_{jk}$, and p_j represents the occupation probability at the quantum dot labeled by j.

When considering the overlap between adjacent MBSs, an additional term in the Hamiltonian arises

$$H_{\mathrm{overlap}} = \sum_{\nu>\mu} i\epsilon_{\nu\mu}\gamma_{\nu}\gamma_{\mu}, \tag{6.110}$$

, where $\epsilon_{\nu\mu}$ denotes the hybridization energy between the MBSs γ_{ν} and γ_{μ}. This term affects the dynamics within the Majorana box and influences the unitary time evolution described by the Lindblad equation. Typically, unitary time evolution in the Lindblad equation causes the system state to oscillate around its steady states. Such oscillations can be problematic for quantum gates because they introduce time-dependent phase shifts that may interfere with subsequent braiding operations. However, if the braiding process occurs on a timescale shorter than the oscillation timescale—determined by the inverse of the hybridization energies—the effects of these oscillations on the open system can be neglected. Given that this constraint is a well-established aspect of all braiding protocols [132], we will gracefully omit a detailed discussion of it in this work.

To concentrate on the dissipative dynamics that drive the system towards its steady state, we disregard the coherent dynamics described by the commutator term in the Lindblad equation. This simplification allows for a more direct analysis of the mechanisms that lead to the establishment of equilibrium.

$$\frac{d}{dt}\rho_{\mathrm{s}}(t) \approx \sum_{j\neq k} \tilde{\Gamma}_{jk}\left(A_{jk}\rho_{\mathrm{s}}(t)A_{jk}^{\dagger} - \frac{1}{2}\left\{A_{jk}^{\dagger}A_{jk}, \rho_{\mathrm{s}}(t)\right\}\right). \tag{6.111}$$

To determine the steady state of the Majorana box qubit, one can equate the Lindblad equation (6.109) to zero, signifying that the system has reached a state of equilibrium where the rate of change of the density matrix is nullified.

$$\mathcal{L}\rho_{\mathrm{s}} = \Gamma_{12}\left(K_{12}\rho_{\mathrm{M}}(t)K_{12}^{\dagger} - \frac{1}{2}\left\{K_{12}^{\dagger}K_{12}, \rho_{\mathrm{M}}(t)\right\}\right) = 0, \tag{6.112}$$

where the steady state of the Majorana box qubit is denoted as $\rho_s = \rho_M(t \to \infty)$. An alternative approach to understanding the system's dissipation involves identifying the dark state $|\psi_n\rangle$ [111], which is defined as

$$K_{jk}|\psi_n\rangle = 0, \ \forall K_{jk}. \tag{6.113}$$

Therefore, the Lindblad equation (6.109), when applied to the dark state, yields the condition for equilibrium, expressed as $\mathcal{L}|\psi_n\rangle\langle\psi_n| = 0$. One can conclude that the dark states represent the pure steady states of specific Liouville superoperators within the quantum system. These states are particularly stable against the specific dissipative processes described by the Liouville operators, contributing to the long-term equilibrium configuration of the quantum system. As a result, the steady state of the quantum system is anticipated to be a superposition of dark states.

$$\rho_s = \left(\sum_n a_n|\psi_n\rangle\right) \otimes h.c., \tag{6.114}$$

where the complex-valued parameters a_n are subject to the normalization condition $\sum_n |a_n|^2 = 1$ ensuring the trace preservation of ρ_s. This steady state (6.114) is distinguished by the inherent insensitivity of the dark states to the decoherence mechanisms within the system, thereby guaranteeing their stability over time.

In this chapter, we have meticulously derived the Hamiltonian for an open system employing a Majorana architecture, as illustrated in Fig. 6.1, following Ref. [126]. We demonstrated the construction of a qubit within the Majorana box, leveraging the sufficiently large charging energy. The Majorana bilinear has been adeptly expressed using Pauli operators, as detailed in Eq. (6.20). By applying the approximations detailed in Table 6.1, we have derived the effective Hamiltonian in the interaction picture, as shown in Eq. (6.54). This Hamiltonian, which incorporates the interaction between the bath and the Majorana box, specifically involves the cotunneling term described in Eq. (6.53).

The effective Hamiltonian serves as the starting point for deriving the Lindblad form master equation from the von Neumann equation (6.61), which describes the time evolution of the density matrix. The density matrix, as defined by Eq. (6.57), represents the statistical state of an open quantum system. A valid density matrix is Hermitian and has a trace of one. These properties are preserved in the Markovian quantum master equation (6.77), which serves as a universal dynamic map within the framework of the Born-Markov approximation. Utilizing the dissipative component of the cotunneling Hamiltonian, represented as $V(t)$ in Eq. (6.78), we derived the Lindblad equation (6.109) exclusively for the Majorana sector, after tracing out the quantum dot part.

As we proceed to the next chapter, we will focus on a single Majorana box, deriving its steady state using a general methodology. We will then introduce a stabilization protocol aimed at aligning the Majorana density matrix with the steady state, which exhibits topological order. Subsequently, we will build the corresponding physical tunneling system.

Chapter 7

The dissipation in a single Majorana box

In the context of open quantum systems, braiding operations occur within the decoherence-free subspace (DFS), also known as the dark space. This subspace is defined by the manifold of dark states, as described in Eq. (6.113). Our analytical focus is directed towards the steady state of the qubits. The robustness of this steady state arises from the presence of topological order, which is a crucial attribute for realizing fault-tolerant quantum computing paradigms.

To transition the system's state to the steady state, we use the Lindblad equation derived in the previous chapter. The Lindblad equation (6.109), which governs the dissipative dynamics in the Majorana sector, features the jump operator K_{jk} defined in (6.103). This operator depends on the tunneling amplitude between quantum dots and MBSs, denoted as $\lambda_{j/nu}$. Consequently, the steady state of the Majorana box can be controlled by adjusting these tunneling couplings.

This chapter primarily focuses on dissipation in the Majorana sector, described by the Lindblad equation (6.109). We begin by analyzing the simple scenario where a single Majorana box functions as the reduced open system, with its density matrix being 2×2. Following the analysis presented in Ref. [110], we demonstrate the requirements for the stabilization protocol that drives the Majorana box to steady states with topological order.

7.1 A general formalism of the steady states

To keep the discussion in general, we consider an arbitrary 2×2 density matrix in the Bloch form as follows.

$$\rho(t) = \frac{1}{2}\left(\sigma_0 + \boldsymbol{n}(t) \cdot \boldsymbol{\sigma}\right), \tag{7.1}$$

with the Pauli vector $\boldsymbol{\sigma} = (\sigma_x, \sigma_y, \sigma_z)$ and the Bloch vector $\boldsymbol{n} = (n_x, n_y, n_z)$ where $n_{x,y,z} \in \mathbb{R}$. The jump operator K_{jk}, as specified by Eq. (6.103), has a linear correspondence with the Majorana bilinear. Drawing from the representation provided in Eq. (6.20), where the Majorana bilinear is expressed in terms of Pauli operators, it becomes feasible to construct an arbitrary form of the 2×2 jump operator as follows.

$$K = K_{12} = \sum_{\nu \neq \mu} \left(\lambda_{1,\nu} \lambda_{2,\mu} e^{i(\beta_{1,\nu} - \beta_{2,\mu})} - \lambda_{1,\mu} \lambda_{2,\nu} e^{i(\beta_{1,\mu} - \beta_{2,\nu})} \right) \gamma_\nu \gamma_\mu, \tag{7.2}$$

$$\Rightarrow K = \boldsymbol{k} \cdot \boldsymbol{\sigma}, \tag{7.3}$$

with the subscripts of MBSs $\nu, \mu \in \{1, \ldots, 4\}$ and a complex-valued vector $\boldsymbol{k} = (k_x \exp(i\phi_x), k_y \exp(i\phi_y), k_z \exp(i\phi_z))$ determined by the tunneling amplitudes $\lambda_{j,\nu}$ and their respective tunneling phases $\beta_{j,\nu}$. As mentioned earlier, the jump operator does not have to be Hermitian.

Given that the products of two Pauli matrices satisfy $\sigma_a \sigma_b = \delta_{a,b} \sigma_0 + i \epsilon_{abc} \, \sigma_c$, for the Levi-Civita symbol ϵ_{abc} and $a, b, c \in \{x, y, z\}$, we can derive the following expression for the product of two vectors for two arbitrary three-dimensional vectors $\boldsymbol{v}_1$ and $\boldsymbol{v}_2$.

$$(\boldsymbol{v}_1 \cdot \boldsymbol{\sigma})(\boldsymbol{v}_2 \cdot \boldsymbol{\sigma}) = (\boldsymbol{v}_1 \cdot \boldsymbol{v}_2)\, \sigma_0 + i \boldsymbol{\sigma} \cdot (\boldsymbol{v}_1 \times \boldsymbol{v}_2) \tag{7.4}$$

By utilizing the generic expressions for the density matrix given in Eq. (7.1) and the jump operator described in Eq. (7.3), we can express the "jump term" and "decay terms" within the Lindblad equation using the vectors $\boldsymbol{n}$, $\boldsymbol{k}$ and $\boldsymbol{\sigma}$, which represent the Bloch vector, the jump operator vector, and the Pauli vector, respectively (see Appendix J).

$$K \rho K^\dagger = \frac{1}{2} \left[\left(|\boldsymbol{k}|^2 + i\, (\boldsymbol{k} \times \boldsymbol{n}) \cdot \boldsymbol{k}^* \right) \sigma_0 + \boldsymbol{\sigma} \cdot \left(i \boldsymbol{k} \times \boldsymbol{k}^* + (\boldsymbol{k} \cdot \boldsymbol{n})\, \boldsymbol{k}^* - \boldsymbol{k} \times \boldsymbol{n} \times \boldsymbol{k}^* \right) \right], \tag{7.5}$$

$$K^\dagger K \rho = \frac{1}{2} \left[\left(|\boldsymbol{k}|^2 + i\, (\boldsymbol{k} \times \boldsymbol{n}) \cdot \boldsymbol{k}^* \right) \sigma_0 + \boldsymbol{\sigma} \cdot \left(i \boldsymbol{k}^* \times \boldsymbol{k} + |\boldsymbol{k}|^2 \boldsymbol{n} - \boldsymbol{k}^* \times \boldsymbol{k} \times \boldsymbol{n} \right) \right], \tag{7.6}$$

$$\rho K^\dagger K = \frac{1}{2} \left[\left(|\boldsymbol{k}|^2 + i\, (\boldsymbol{k} \times \boldsymbol{n}) \cdot \boldsymbol{k}^* \right) \sigma_0 + \boldsymbol{\sigma} \cdot \left(i \boldsymbol{k}^* \times \boldsymbol{k} + (\boldsymbol{n} \cdot \boldsymbol{k}^*)\, \boldsymbol{k} - \boldsymbol{n} \times \boldsymbol{k}^* \times \boldsymbol{k} \right) \right]. \tag{7.7}$$

Using the expressions for the "jump term" given in Eq. (7.5) and the "decay terms" outlined in Eqs. (7.6)-(7.7), we observe that the identity terms within the Lindblad

equation cancel each other out, and the remaining terms are

$$\mathcal{L}\rho = \Gamma\left(K\rho K^\dagger - \frac{1}{2}\left\{K^\dagger K, \rho\right\}\right) \tag{7.8}$$

$$= \frac{\Gamma}{2}\boldsymbol{\sigma}\cdot\Big[(2i\boldsymbol{k}\times\boldsymbol{k}^* + (\boldsymbol{k}\cdot\boldsymbol{n})\,\boldsymbol{k}^* - \boldsymbol{k}\times\boldsymbol{n}\times\boldsymbol{k}^*) \tag{7.9}$$

$$- \frac{1}{2}\left(|\boldsymbol{k}|^2\boldsymbol{n} - \boldsymbol{k}^*\times\boldsymbol{k}\times\boldsymbol{n} + (\boldsymbol{n}\cdot\boldsymbol{k}^*)\,\boldsymbol{k} - \boldsymbol{n}\times\boldsymbol{k}^*\times\boldsymbol{k}\right)\Big].$$

Because the triple cross product is given by $(\boldsymbol{v}_1\times\boldsymbol{v}_2)\times\boldsymbol{v}_3 = (\boldsymbol{v}_1\cdot\boldsymbol{v}_3)\boldsymbol{v}_2 - (\boldsymbol{v}_2\cdot\boldsymbol{v}_3)\boldsymbol{v}_1$, the Bloch representation of the Lindblad equation can be further simplified.

$$\mathcal{L}\rho = \frac{\Gamma}{2}\boldsymbol{\sigma}\cdot\left[(2i\boldsymbol{k}\times\boldsymbol{k}^* + (\boldsymbol{k}\cdot\boldsymbol{n})\,\boldsymbol{k}^* - (\boldsymbol{k}\cdot\boldsymbol{k}^*)\,\boldsymbol{n} + (\boldsymbol{n}\cdot\boldsymbol{k}^*)\,\boldsymbol{k}) - |\boldsymbol{k}|^2\boldsymbol{n}\right] \tag{7.10}$$

$$\Rightarrow \mathcal{L}\rho = \frac{\Gamma}{2}\boldsymbol{\sigma}\cdot\left[2i\boldsymbol{k}\times\boldsymbol{k}^* + (\boldsymbol{k}\cdot\boldsymbol{n})\,\boldsymbol{k}^* + (\boldsymbol{n}\cdot\boldsymbol{k}^*)\,\boldsymbol{k} - 2|\boldsymbol{k}|^2\boldsymbol{n}\right]. \tag{7.11}$$

One can find that the Bloch form of the Liouvillian superoperator in Eq. (7.11) is Hermitian as anticipated.

The steady state ρ_s is found by solving $\mathcal{L}\rho_\mathrm{s} = 0$ as shown in Eq. (6.112). By using the Bloch form of the density matrix in Eq. (7.1) and the jump operator from Eq. (7.3) in the Lindblad equation (7.11), one can determine the Bloch vector of the steady state, denoted as $\boldsymbol{n}_s$, which can be expressed in terms of the tunneling parameters in the jump operator.

$$\mathcal{L}\rho_\mathrm{s} = \frac{\Gamma}{2}\boldsymbol{\sigma}\cdot\left[2i\boldsymbol{k}\times\boldsymbol{k}^* + (\boldsymbol{k}\cdot\boldsymbol{n}_s)\,\boldsymbol{k}^* + (\boldsymbol{n}_s\cdot\boldsymbol{k}^*)\,\boldsymbol{k} - 2|\boldsymbol{k}|^2\boldsymbol{n}_s\right] = 0 \tag{7.12}$$

$$\Rightarrow \boldsymbol{n}_s = -\left(\frac{2k_yk_z\sin(\phi_y-\phi_z)}{k_x^2+k_y^2+k_z^2}, \frac{2k_xk_z\sin(\phi_z-\phi_x)}{k_x^2+k_y^2+k_z^2}, \frac{2k_xk_y\sin(\phi_x-\phi_y)}{k_x^2+k_y^2+k_z^2}\right) \tag{7.13}$$

$$\Rightarrow (\boldsymbol{n}_s)_\mathrm{a} = -\frac{2}{|\boldsymbol{k}|}\epsilon_\mathrm{abc}k_bk_c\sin(\phi_b-\phi_c),$$

where the Levi-Civita symbol is denoted as ϵ_{abc} and $a, b, c \in \{x, y, z\}$.

Alternatively, one can calculate the steady-state Bloch vector using the ansatz $\boldsymbol{n}_s \propto \boldsymbol{k}\times\boldsymbol{k}^*$, which represents a vector normal to the complex plane spanned by the vector $\boldsymbol{k}$ and its Hermitian conjugate $\boldsymbol{k}^*$. For the steady-state Bloch vector, the right-hand side of the Lindblad equation in Eq. (7.11) reduces to zero, indicating that the system has reached equilibrium.

$$\mathcal{L}\rho_\mathrm{s} = \frac{\Gamma}{2}\boldsymbol{\sigma}\cdot\left[2i\boldsymbol{k}\times\boldsymbol{k}^* - 2|\boldsymbol{k}|^2\boldsymbol{n}_s\right] = 0 \Rightarrow \boldsymbol{n}_s = \frac{i}{|\boldsymbol{k}|^2}(\boldsymbol{k}\times\boldsymbol{k}^*). \tag{7.14}$$

Since the cross product can be expressed as $\boldsymbol{k} \times \boldsymbol{k}^* \equiv (\boldsymbol{k} \times \boldsymbol{k}^* - \boldsymbol{k}^* \times \boldsymbol{k})/2$, the Bloch operator in the density matrix can be represented by the jump operator and its Hermitian conjugate.

$$\boldsymbol{n}_s \cdot \boldsymbol{\sigma} = \frac{1}{2|\boldsymbol{k}|^2} \left[i \left(\boldsymbol{k} \times \boldsymbol{k}^* \right) \cdot \boldsymbol{\sigma} - i \left(\boldsymbol{k}^* \times \boldsymbol{k} \right) \cdot \boldsymbol{\sigma} \right] \tag{7.15}$$

$$\Rightarrow \boldsymbol{n}_s \cdot \boldsymbol{\sigma} = \frac{1}{2|\boldsymbol{k}|^2} \left(K K^\dagger - K^\dagger K \right) = \frac{1}{2|\boldsymbol{k}|^2} \left[K, K^\dagger \right], \tag{7.16}$$

where we refer to the jump operator K, as expressed in Eq. (7.3). The steady state, therefore, is written as

$$\rho_{\mathrm{s}} = \frac{1}{2} \left(\sigma_0 + \frac{1}{2|\boldsymbol{k}|^2} \left[K, K^\dagger \right] \right). \tag{7.17}$$

The general expressions for the steady state in Eq. (7.17) and its corresponding Bloch vector in Eq. (7.13) hold true under the condition that only a single transport channel is active. Since the steady state is determined by the jump operator, and the steady-state Bloch vector is determined by the vector $\boldsymbol{k}$, it becomes feasible to engineer the steady state by manipulating the tunneling parameters.

7.1.1 Pure states

A pure state is described by a density matrix that acts as a projection operator onto a single quantum state vector. Mathematically, any pure state can be expressed as $\rho_{\mathrm{pure}} = |\psi\rangle\langle\psi|$, where $|\psi\rangle$ represents the state vector. To determine whether a density matrix is pure, one can check if $\rho = \rho^2$. If this equality holds, then the density matrix is pure. Expressing this condition in the Bloch form as shown in Eq. (7.1), we derive

$$\rho^2 = \rho \tag{7.18}$$

$$\Rightarrow \frac{1}{4} \left[\sigma_0 + 2 \left(\boldsymbol{n} \cdot \boldsymbol{\sigma} \right) + \left(\boldsymbol{n} \cdot \boldsymbol{\sigma} \right) \left(\boldsymbol{n} \cdot \boldsymbol{\sigma} \right) \right] = \frac{1}{2} \left(\sigma_0 + \boldsymbol{n} \cdot \boldsymbol{\sigma} \right) \tag{7.19}$$

$$\left(\boldsymbol{n} \cdot \boldsymbol{\sigma} \right) \left(\boldsymbol{n} \cdot \boldsymbol{\sigma} \right) = \sigma_0 \tag{7.20}$$

$$|\boldsymbol{n}|^2 \sigma_0 + i \boldsymbol{\sigma} \cdot \underbrace{\left(\boldsymbol{n} \times \boldsymbol{n} \right)}_{0} = \sigma_0, \tag{7.21}$$

which leads to the conclusion that the Bloch vector corresponding to pure states must be a unit vector, denoted as $|\boldsymbol{n}_{\mathrm{pure}}| \equiv 1$.

A pure state contains complete information about a quantum system, signifying precise knowledge that the system occupies a specific, well-defined quantum state. In contrast,

a mixed state indicates incomplete knowledge of the system. Mixed states arise when the system's state is described by probabilities, reflecting uncertainty about the exact quantum state. Therefore, for braiding operations, it is crucial to ensure that the state of the Majorana sector remains pure. The condition for the pure steady state requires that its Bloch vector, given by Eq. (7.13), satisfies the following normalization constraint.

$$\left(\frac{2k_yk_z\sin(\phi_y-\phi_z)}{k_x^2+k_y^2+k_z^2}\right)^2+\left(\frac{2k_xk_z\sin(\phi_z-\phi_x)}{k_x^2+k_y^2+k_z^2}\right)^2+\left(\frac{2k_xk_y\sin(\phi_x-\phi_y)}{k_x^2+k_y^2+k_z^2}\right)^2=1. \tag{7.22}$$

Solving this normalization constraint for k_y, we find

$$k_y^2=-k_x^2e^{\pm2i(\phi_y-\phi_x)}-k_z^2e^{\pm2i(\phi_y-\phi_z)}. \tag{7.23}$$

Since the tunneling amplitudes $k_{x,y,z}$ must be real, the difference of the phases $\phi_{x,y,z}$ is restricted to discrete values. Specifically, the difference must each be an integer multiple of $\pi/2$, i.e.: $\phi_y-\phi_x=\mathbb{N}\pi/2$ and $\phi_y-\phi_z=\mathbb{N}\pi/2$ when $\mathbb{N}$ is an integer number. Thus, the normalization constraint provides the following possible solutions for a real-valued amplitude k_y.

$$k_y^2=k_x^2-k_z^2,\qquad \phi_x-\phi_y=\frac{\pi}{2}\text{ and }\phi_z-\phi_y=\pi; \tag{7.24}$$

$$k_y^2=-k_x^2+k_z^2,\qquad \phi_x-\phi_y=\pi\text{ and }\phi_z-\phi_y=\frac{\pi}{2}; \tag{7.25}$$

$$k_y^2=k_x^2+k_z^2,\qquad \phi_x-\phi_y=\frac{\pi}{2}\text{ and }\phi_z-\phi_y=\frac{\pi}{2}. \tag{7.26}$$

Clearly, the first possibility in Eq. (7.24) requires $k_x\geq k_z$ while the second possibility in Eq. (7.25) requires $k_x\leq k_z$.

Recall that our goal is to perform braiding in the dark space by adiabatically driving the system within a continuous parameter space. However, the pure steady state only provides discrete values for the difference of tunneling phases, leading to a collective variation in the phases $\phi_{x,y,z}$. Therefore, we need to drive the tunneling amplitudes $k_{x,y,z}$. Consequently, we choose the solution for k_y from Eq. (7.26), as it imposes fewer constraints on the amplitudes k_x and k_z. Additionally, we will represent the complex tunneling parameters as follows.

$$k_{x,y,z}e^{i\phi_{x,y,z}},\ k_{x,y,z}\in\mathbb{R}\text{ and }\phi_{x,y,z}\in[0,\pi); \tag{7.27}$$

$$\lambda_{j,\nu}e^{-i\beta_{j,\nu}},\ \lambda_{j,\nu}\in\mathbb{R}\text{ and }\beta_{j,\nu}\in[0,\pi). \tag{7.28}$$

With this representation, the tunneling amplitude, $k_{x,y,z}$ and $\lambda_{j,\nu}$, can now take on negative values, allowing us to explore the parameter space of all real values for the tunneling amplitudes.

To approach the solution in Eq. (7.26), the phases in the channels between the quantum dots and MBSs must be chosen such that $\phi_x - \phi_y = \phi_z - \phi_y = \pi/2$. Thus, the normalization condition of the Bloch vector implies $k_y^2 = k_x^2 + k_z^2$, and the corresponding jump vector $\boldsymbol{k}$ and the steady-state Bloch vector $\boldsymbol{n}_s$ in Eq. (7.13) are given by

$$\left.\begin{aligned}\phi_x - \phi_y &= \pi/2\\ \phi_z - \phi_y &= \pi/2\\ k_y^2 &= k_x^2 + k_z^2\end{aligned}\right\} \Rightarrow \begin{cases}\boldsymbol{k} = \left(ik_x, \mathrm{sgn}(k_y)\sqrt{k_x^2+k_z^2}, -ik_z\right) e^{i\phi_y},\\ \boldsymbol{n}_s = \left(\dfrac{k_z}{k_y}, 0, -\dfrac{k_x}{k_y}\right).\end{cases} \tag{7.29}$$

One may notice that the vector $\boldsymbol{k}$ contains a free phase ϕ_y in the vector $\boldsymbol{k}$, but this phase does not affect the steady-state Bloch vector. One can also solve the normalization condition given by Eq. (7.22) for other amplitudes such as k_x and k_z. The results obtained from these calculations are comparable to those derived in Eq. (7.29). For example, when solving the normalization constraints for k_x, the remaining free phase is ϕ_x. Importantly, the Bloch vector is unaffected by this free phase.

7.2 The steady state with topological order

To confirm the presence of topological order in the density matrix, one can demonstrate a non-zero winding number by examining the rotation of the Bloch vector on the Bloch sphere [110]. This approach is analogous to identifying a topological phase in systems such as topological superconductors, where the non-zero winding number in momentum space acts as a topological invariant in the Bogoliubov-de Gennes (BdG) Hamiltonian.

As shown in Eq. (7.29), the Bloch vector of the pure steady state is a function of the tunneling amplitudes k_x and k_z. Although adiabatically and time-periodically varying the tunneling amplitudes results in rotating the unit Bloch vector around the Bloch sphere in a closed loop (see Fig. 7.1), this process is still potentially topologically trivial. This is because any loop on a 2D surface, such as the Bloch sphere, can be continuously contracted to a point, indicating that the first homotopy group of $\boldsymbol{S}^2$ is trivial.

To preserve a non-trivial topology, we employ chiral symmetry to constrain the Bloch operator within the density matrix, as expressed in Eq. (7.1).

$$\Sigma\,(\boldsymbol{n}\cdot\boldsymbol{\sigma})\,\Sigma = -\boldsymbol{n}\cdot\boldsymbol{\sigma} \Leftrightarrow \{\Sigma, \boldsymbol{n}\cdot\boldsymbol{\sigma}\} = 0, \tag{7.30}$$

where Σ is the unitary symmetry operator, meaning that $\Sigma\Sigma = \mathbb{I}$, where $\mathbb{I}$ denotes the identity matrix. Translating this into the geometry of the Bloch sphere, we can express

the symmetry operator as

$$\Sigma = \boldsymbol{a} \cdot \boldsymbol{\sigma}, \text{ where } |\boldsymbol{a}| = 1. \tag{7.31}$$

The normalization condition for the real-valued vector $\boldsymbol{a}$ ensures the unitarity of the symmetry operator, which requires $\Sigma\Sigma = \mathbb{I}$. Thus, the constraint imposed by the chiral symmetry, as illustrated in Eq. (7.30), provides

$$\{\boldsymbol{a} \cdot \boldsymbol{\sigma}, \boldsymbol{n} \cdot \boldsymbol{\sigma}\} = 0 \tag{7.32}$$

$$(\boldsymbol{a} \cdot \boldsymbol{\sigma})(\boldsymbol{n} \cdot \boldsymbol{\sigma}) + (\boldsymbol{n} \cdot \boldsymbol{\sigma})(\boldsymbol{a} \cdot \boldsymbol{\sigma}) = 0 \tag{7.33}$$

$$2(\boldsymbol{a} \cdot \boldsymbol{n})\sigma_0 + i\boldsymbol{\sigma} \cdot \underbrace{(\boldsymbol{a} \times \boldsymbol{n} + \boldsymbol{n} \times \boldsymbol{a})}_{0} = 0 \tag{7.34}$$

$$\Rightarrow \boldsymbol{a} \cdot \boldsymbol{n} = 0. \tag{7.35}$$

This condition should be enforced throughout the rotation ($\boldsymbol{a} \cdot \boldsymbol{n}(t) = 0$ for all t), indicating that the unit Bloch vector $\boldsymbol{n}(t)$ traces a path within a unit circle whose normal vector is $\boldsymbol{a}$ (see Fig. 7.1).

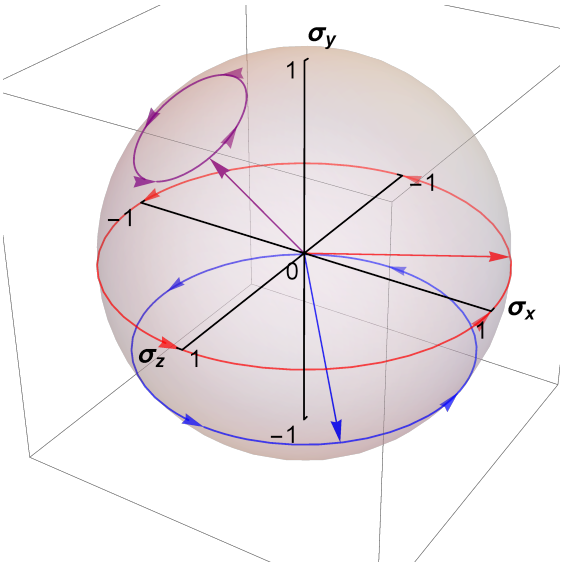

Figure 7.1: **Visualization of trajectories on the Bloch sphere**. All the purple, red, and blue vectors represent unit Bloch vectors. However, only the red Bloch vector is subject to the chiral symmetry constraint described in Eq. (7.35). Consequently, the winding number is defined as non-zero exclusively for the red Bloch vector.

The invariant, expressed in terms of the Bloch operator, is given by [110]

$$\mathcal{W} = \frac{1}{4\pi i}\int_{t_0}^{t_f} dt\ \mathrm{Tr}\left[\Sigma\left(\boldsymbol{n}\cdot\boldsymbol{\sigma}\right)\frac{d}{dt}\left(\boldsymbol{n}\cdot\boldsymbol{\sigma}\right)\right] \tag{7.36}$$

$$= \frac{1}{4\pi i}\int_{t_0}^{t_f} dt\ \mathrm{Tr}\left[\left(\boldsymbol{a}\cdot\boldsymbol{\sigma}\right)\left(\boldsymbol{n}\cdot\boldsymbol{\sigma}\right)\left(\frac{d\boldsymbol{n}}{dt}\cdot\boldsymbol{\sigma}\right)\right] \tag{7.37}$$

$$= \frac{1}{4\pi i}\int_{t_0}^{t_f} dt\ \mathrm{Tr}\left\{i\left[\left(\boldsymbol{a}\times\boldsymbol{n}\right)\cdot\frac{d\boldsymbol{n}}{dt}\right]\sigma_0 - \boldsymbol{\sigma}\cdot\left[\left(\boldsymbol{a}\times\boldsymbol{n}\right)\times\frac{d\boldsymbol{n}}{dt}\right]\right\}. \tag{7.38}$$

Since the trace of the Pauli vector $\boldsymbol{\sigma} = (\sigma_x, \sigma_y, \sigma_z)$ is a vector of zeros, the second term in the integrand above vanishes, simplifying the expression to

$$\mathcal{W} = \frac{1}{2\pi}\int_{t_0}^{t_f} dt\ \left(\boldsymbol{n}\times\frac{d\boldsymbol{n}}{dt}\right)\cdot\boldsymbol{a} \tag{7.39}$$

$$\mathcal{W} = \frac{1}{2\pi}\int_{t_0}^{t_f} dt\ \left(n_y\frac{dn_z}{dt} - n_z\frac{dn_y}{dt}, n_z\frac{dn_x}{dt} - n_x\frac{dn_z}{dt}, n_x\frac{dn_y}{dt} - n_y\frac{dn_x}{dt}\right)\cdot\boldsymbol{a}, \tag{7.40}$$

where t_0 and t_f denote the time period in the parameter space. The integral in Eq. (7.40) represents the solid angle subtended by the trajectory of the Bloch vector on the Bloch sphere as it evolves over the time interval $[t_0, t_f]$.

The steady-state Bloch vector, described by Eq. (7.29), is a unit vector confined to the $\sigma_x - \sigma_z$ plane of the Bloch sphere. Rotating this Bloch vector within the $\sigma_x - \sigma_z$ plane gives us the winding number $\mathcal{W}$ as follows.

$$\boldsymbol{n}_s = (n_x(k_x,k_z), 0, n_z(k_x,k_z)) \Rightarrow \mathcal{W} = \frac{1}{2\pi}\int_{t_0}^{t_f} dt\ \left(n_z\frac{dn_x}{dt} - n_x\frac{dn_z}{dt}\right). \tag{7.41}$$

Here, the integral limits are chosen such that the tunneling amplitudes k_x and k_z complete a closed path in parameter space, specifically satisfying the time-periodic boundary condition: $k_{x,z}(t_0) = k_{x,z}(t_f)$.

Applying the chain rule to the time derivative of the Bloch vector (7.29), we obtain

$$\frac{d}{dt}n_a(k_x(t),k_z(t)) = \frac{dk_x}{dt}\frac{\partial n_a}{\partial k_x} + \frac{dk_z}{dt}\frac{\partial n_a}{\partial k_z},\ \text{where } a \in \{x,z\}. \tag{7.42}$$

$$\Rightarrow \begin{cases} \dfrac{d}{dt}n_x(k_x(t),k_z(t)) = -\dfrac{dk_x}{dt}\dfrac{k_xk_z}{(k_x^2+k_z^2)^{\frac{3}{2}}} + \dfrac{dk_z}{dt}\dfrac{k_x^2}{(k_x^2+k_z^2)^{\frac{3}{2}}} \\ \dfrac{d}{dt}n_z(k_x(t),k_z(t)) = -\dfrac{dk_x}{dt}\dfrac{k_z^2}{(k_x^2+k_z^2)^{\frac{3}{2}}} + \dfrac{dk_z}{dt}\dfrac{k_xk_z}{(k_x^2+k_z^2)^{\frac{3}{2}}} \end{cases} \tag{7.43}$$

Inserting these expressions into Eq. (7.41), we find the winding number as follows.

$$\mathcal{W} = \frac{1}{2\pi}\int_{t_0}^{t_f} dt\ \frac{1}{k_x^2+k_z^2}\left(k_x\frac{dk_z}{dt} - k_z\frac{dk_x}{dt}\right). \tag{7.44}$$

The numerator and denominator of the integrand for the winding number in Eq. (7.44) are analogous to the cross product and dot product, respectively, of the 2D vectors (k_x, k_z) and their time derivatives$(dk_x/dt, dk_z/dt)$. Therefore, we can exploit the properties of complex numbers to unify these operations into a single calculation by taking the time derivative of the logarithm of the complex number $c = k_x + ik_z$.

$$\frac{d}{dt}\ln c = \frac{1}{c}\frac{d}{dt}c = \frac{k_x - ik_z}{|c|^2}\left(\frac{dk_x}{dt} + i\frac{dk_z}{dt}\right) \tag{7.45}$$

$$= \frac{1}{|c|^2}\left[\left(k_x\frac{dk_x}{dt} + k_z\frac{dk_z}{dt}\right) + i\left(k_x\frac{dk_z}{dt} - k_z\frac{dk_z}{dt}\right)\right] \tag{7.46}$$

$$= \frac{1}{k_x^2+k_z^2}\left[\frac{1}{2}\frac{d}{dt}\left(k_x^2+k_z^2\right) + i\left(k_x\frac{dk_z}{dt} - k_z\frac{dk_z}{dt}\right)\right] \tag{7.47}$$

$$\Rightarrow \frac{1}{k_x^2+k_z^2}\left(k_x\frac{dk_z}{dt} - k_z\frac{dk_z}{dt}\right) = -i\frac{d}{dt}\left(\ln(c) - \ln|c|\right). \tag{7.48}$$

To express the integrand in Eq. (7.44), we obtain

$$\mathcal{W} = \frac{-i}{2\pi}\int_{t_0}^{t_f} dt\ \frac{d}{dt}\left(\ln(c) - \ln|c|\right) \tag{7.49}$$

Due to the time-periodic boundary condition, we can introduce the tunneling parameters using polar coordinates.

$$k_x(t) = R\cos\theta(t), \qquad k_z(t) = R\sin\theta(t), \tag{7.50}$$

which can be equivalently transformed to the Bloch vector (7.29) with the components

$$n_x(t) = \sin\theta(t), \qquad n_z(t) = -\cos\theta(t). \tag{7.51}$$

where R is a positive constant and $\theta(t)$ is a function of time. To satisfy the periodicity in the parameter space $(k_{x,z}(t_0) = k_{x,z}(t_f))$, we define $\theta(t_f) = \theta(t_0) + 2\mathbb{N}\pi$, where $\mathbb{N}$

denotes integer numbers. Substituting this in Eq. (7.49) results in

$$\mathcal{W} = \frac{-i}{2\pi}\int_{t_0}^{t_f} dt\, \frac{d}{dt}\left(\ln\left[R\left(\cos\theta(t) + i\sin\theta(t)\right)\right] - \ln R\right) \tag{7.52}$$

$$= \frac{-i}{2\pi}\int_{t_0}^{t_f} dt\, \frac{d}{dt}\left(\ln R + \ln e^{i\theta(t)} - \ln R\right) \tag{7.53}$$

$$\Rightarrow \mathcal{W} = \frac{1}{2\pi}\left[\theta(t_f) - \theta(t_0)\right], \tag{7.54}$$

where the angle $\theta = \arctan\left(k_z/k_x\right) = -\arctan\left(n_x/n_z\right)$, which only depends on the initial and final positions of the Bloch vector. Hence, through a cyclic adiabatic change of parameters, a winding number $\mathcal{W} = 2\pi\mathbb{N}/(2\pi)$ emerges, where $\mathbb{N}$ represents integer numbers. This number is topological in nature because it is quantized and does not depend on the specific time-dependent function chosen for the adiabatic parameter change.

7.2.1 The tunneling system to a single Majorana box

In the final section of this chapter, we construct a tunneling system using a single Majorana box and outline a stabilization protocol designed to transition the Majorana box into the pure state to give rise to a topological phase. As mentioned in Sec. 6.2, we can apply the approximation described in Table. 6.1 to derive the effective Hamiltonian. Additionally, we note that we only consider the transport from QD1 to QD2, because Eq. (6.108) shows the transition rate from QD2 to QD1 is suppressed when $\epsilon_2 > \epsilon_1$ and the temperature T is sufficiently low. Thus, under the Born-Markov approximation, we can derive the Lindblad master equation. The jump operator, given in Eq. (6.103), which corresponds to the dynamics in the Majorana sector, is shown in Eq. (6.50).

Figure 7.2 illustrates one of the possible tunneling systems. By considering the possible paths from QD1 to QD2, the jump operator can be written as

$$\tilde{K}_{12} = \sum_{\nu\neq\mu}\left(\lambda_{1,\nu}\lambda_{2,\mu}e^{i(\beta_{1,\nu}-\beta_{2,\mu})} - \lambda_{1,\mu}\lambda_{2,\nu}e^{i(\beta_{1,\mu}-\beta_{2,\nu})}\right)\gamma_\nu\gamma_\mu \tag{7.55}$$

$$\begin{aligned}\Rightarrow \tilde{K}_{12} = {} & \lambda_{1,4}\lambda_{2,2}e^{i(\beta_{1,4}-\beta_{2,2})}\gamma_4\gamma_2 + \lambda_{1,4}\lambda_{2,3}e^{i(\beta_{1,4}-\beta_{2,3})}\gamma_4\gamma_3 \\ & + \lambda_{1,4}\lambda_{2,1}e^{i(\beta_{1,4}-\beta_{2,1})}\gamma_4\gamma_1.\end{aligned} \tag{7.56}$$

Since the Majorana bilinear can be written in terms of Pauli matrices as shown in Eq. (6.20), the jump operator can be expressed in the following Bloch form.

$$\tilde{K}_{12} = \left(k_x e^{i\phi_x}, k_y e^{i\phi_y}, k_z e^{i\phi_z}\right)\cdot\boldsymbol{\sigma}, \tag{7.57}$$

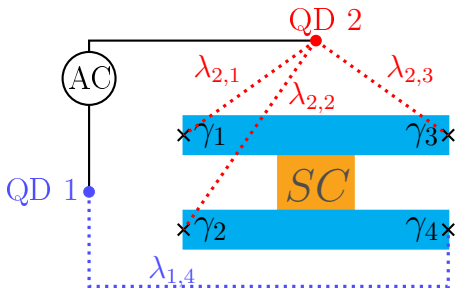

Figure 7.2: **Schematic of the tunneling system to a single Majorana box**. This setup, referred to in the notations of Fig. 6.1, operates on the principle described by the stabilization protocol in Eq. (7.29), driving the system towards its topological steady state.

where

$$k_x e^{i\phi_x} = \lambda_{1,4}\lambda_{2,2} e^{-i\beta_{1,4}+i\beta_{2,2}-i\pi/2}, \tag{7.58}$$

$$k_y e^{i\phi_y} = \lambda_{1,4}\lambda_{2,1} e^{-i\beta_{1,4}+i\beta_{2,1}-i\pi/2}, \tag{7.59}$$

$$k_z e^{i\phi_z} = \lambda_{1,4}\lambda_{2,3} e^{-i\beta_{1,4}+i\beta_{2,3}-i\pi/2}. \tag{7.60}$$

To stabilize the Majorana box in the pure state whose Bloch vector is in the form of Eq. (7.29), the tunneling parameters must satisfy the following conditions.

$$\left.\begin{aligned} &\phi_x - \phi_y = \pi/2 \\ &\phi_z - \phi_y = \pi/2 \\ &k_y^2 = k_x^2 + k_z^2 \end{aligned}\right\} \Rightarrow \begin{cases} \beta_{2,2} = \beta_{2,3} = \beta_{2,1} + \dfrac{\pi}{2}, \\ \lambda_{2,1}^2 = \lambda_{2,2}^2 + \lambda_{2,3}^2. \end{cases} \tag{7.61}$$

Thus, the jump vector $\tilde{\boldsymbol{k}}$ and the steady-state Bloch vector $\tilde{\boldsymbol{n}}_s$, as presented in Eq. (7.29), become

$$\tilde{\boldsymbol{k}} = \left(i\lambda_{2,2}, \mathrm{sgn}(\lambda_{2,1})\sqrt{\lambda_{2,2}^2+\lambda_{2,3}^2}, i\lambda_{2,3}\right)\lambda_{1,4}e^{i\tilde{\phi}_y}, \tag{7.62}$$

$$\tilde{\boldsymbol{n}}_s = \frac{\mathrm{sgn}(\lambda_{2,1})}{\sqrt{\lambda_{2,3}^2+\lambda_{2,2}^2}}\left(\lambda_{2,3}, 0, -\lambda_{2,2}\right), \tag{7.63}$$

where $\tilde{\phi}_y = \beta_{2,1} - \beta_{1,4} - \pi/2$. To rotate the Bloch vector $\tilde{\boldsymbol{n}}_s$ (7.63), we set that $\lambda_{1,4} \neq 0$, and the tunneling amplitudes $\lambda_{2,3}$ and $\lambda_{2,2}$ are adiabatically varying with a time-periodic

function. Once again, we consider the time-periodic evolution of the parameters as sine and cosine functions in the polar coordinate system.

$$\lambda_{2,2}(t) = -r\cos\varphi(t), \qquad \lambda_{2,3}(t) = r\sin\varphi(t). \tag{7.64}$$

Thus, the Bloch vector $\tilde{\boldsymbol{n}}_s(t)$ from Eq. (7.63) evolves in time as

$$\tilde{\boldsymbol{n}}_s(t) = \mathrm{sgn}(\lambda_{2,1})\,(\sin\varphi(t), 0, \cos\varphi(t))\,. \tag{7.65}$$

The periodic boundary condition for the tunneling parameters implies that $\varphi(t_f) = \varphi(t_0) + 2\pi$ for a single loop. Following the calculation of the corresponding winding number in Eq. (7.54), we find

$$\mathcal{W} = \frac{1}{2\pi}\left[\varphi(t_f) - \varphi(t_0)\right] = 1. \tag{7.66}$$

The winding trace of the Bloch vector is visualized in Fig. 7.3.

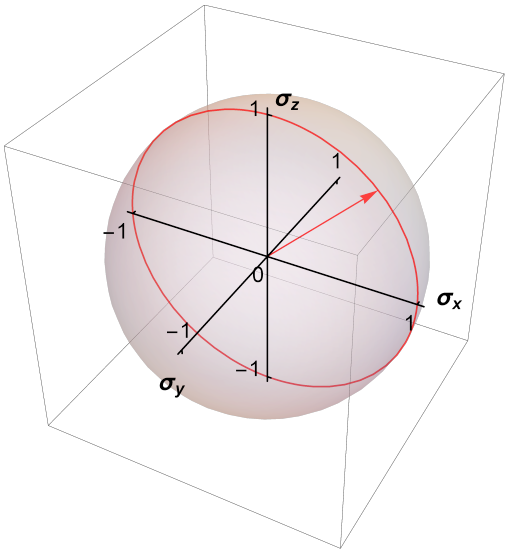

Figure 7.3: **Trajectory on the Bloch sphere.** The Bloch vector (7.65), representing a pure state, appears as a red arrow on the Bloch sphere. As we adiabatically rotate the qubits by adjusting parameters, this Bloch vector traces a path around the solid red unit circle within the $\sigma_x - \sigma_z$ plane.

At the beginning of this chapter, we solved the Lindblad form master equation for an open system consisting of a single Majorana box. Here, the transition rate from the lower

quantum-dot energy level to the higher quantum-dot energy level is suppressed. Using the general expression of the jump operator in Eq. (7.3), we derived the stabilization protocol and obtained the corresponding steady-state Bloch vector, as shown in Eq. (7.29). This steady-state Bloch vector is a unit vector, indicating that the steady state is pure.

A topological phase can emerge from adiabatic changes in the parameters of a driven-dissipative Majorana box. However, the Bloch vector must adhere to the definition of the chiral symmetry [110]. In Sec. 7.2, we showed that the Bloch vector in Eq. (7.29) exhibits chiral symmetry, as defined in Eq. (7.30). When this Bloch vector is rotated in a closed loop on the Bloch sphere, it yields a non-zero winding number, depicted as the red vector in Fig. 7.1. Subsequently, we constructed the tunneling system for a single Majorana box, as shown in Fig. 7.2. Using the stabilization protocol described in Eq. (7.61), the Majorana sector is driven to a pure state. The Bloch vector of this pure state, expressed in Eq. (7.65), exhibits an integer winding number when the tunneling amplitudes, given in Eq. (7.64) are manipulated to form a closed loop in the parameter space.

The core result of this chapter is the general driven dissipative protocol presented in Eq. (7.29), which stabilizes the Majorana box qubit into a steady state with topological order. Additionally, we demonstrated a tunneling system in Fig. 7.2 that drives the Majorana box to a topological steady state characterized by a non-zero winding number. This ensures that the information stored in the box is robust and remains stable despite slow (adiabatic) changes in the tunneling amplitudes. The timescale of adiabatic changes is sufficiently slow compared to the timescale of changes in the open system.

Braiding operations cannot be performed within a single Majorana box, as they can cause the system to transition into different topological sectors by crossing different parity subspaces. Thus, braiding in the open system necessitates additional degrees of freedom in the Majorana sector. In the next chapter, we will focus on an open system comprising multiple entangled Majorana boxes. By analyzing the fundamental requirements for braiding operations, we will develop a braiding protocol for this open system and demonstrate a potential tunneling system that can conduct a braiding rehearsal.

Chapter 8

Braiding in multiple Majorana boxes

The non-Abelian statistics of MBSs are crucial for fault-tolerant quantum computing. Unlike Abelian anyons, which only change by a simple phase factor when exchanged, non-Abelian anyons possess internal degrees of freedom that undergo transformations described by unitary matrices. This leads to more complex outcomes. Therefore, the information encoded in the braiding patterns is resistant to local errors since such errors generally do not alter the topological properties of the braids. This topological protection is crucial for quantum computing, where preserving coherence and minimizing errors are major challenges. It offers a form of fault tolerance that enhances the reliability of quantum computations.

Performing braiding operations on Majorana fermions in real space is currently highly challenging in laboratory settings. Creating and controlling these quasiparticles with high precision requires sophisticated techniques and environments. Alternatively, in this driven-dissipative system (Fig. 6.1), a braiding process can be achieved by transitioning the Majorana sector between dark states within the same parity subspace. This is accomplished by adiabatically changing the system parameters along a closed path. In this setup, the AC driving and damping due to an electromagnetic environment are important in such dissipation.

In analogy to braiding in real space, the conceptual idea of braiding in the dark space is illustrated in Fig. 8.1. For a single cycle of parameter changes, the steady state of the qubit transitions from one dark state to another. These two dark states share the same parity and are both produced by the same Lindblad dissipator. Additionally, the steady state must maintain chiral symmetry throughout the braiding operation to ensure topological protection. To achieve this, we will develop a braiding protocol that stabilizes the Majorana sector within a dark space harboring multiple dark states of the same parity. Subsequently, these dark states will be analyzed using chiral symmetry,

following the methodology outlined in Sec. 7.2.

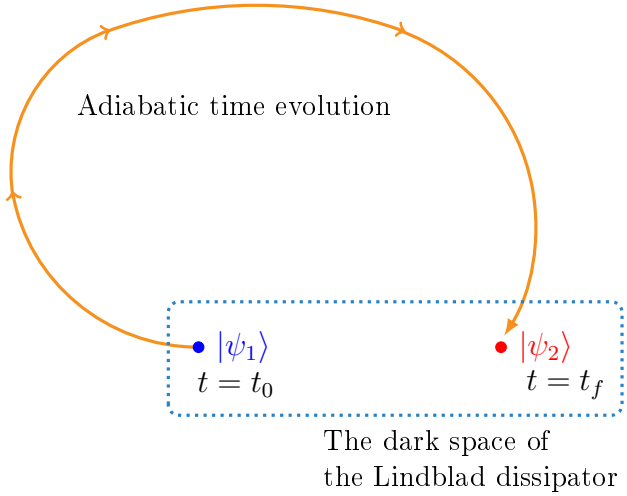

Figure 8.1: **Braiding operations in the dark space**. $|\psi_1\rangle$ and $|\psi_2\rangle$ are two dark states with the same parity in the dark space of a dissipative map represented by the blue dashed rectangle. The orange solid path indicates the adiabatically time-periodic evolution in the parameter space. Initially, at time $t = t_0$, the system is in the steady state $|\psi_1\rangle\langle\psi_1|$. By the end of the braiding process, at time $t = t_f$, the system evolves to the steady state $|\psi_2\rangle\langle\psi_2|$.

From the braiding operation in Fig. 8.1, for the dark space there are three requirements summarized as follows.

1. *The dark state subspace should contain multiple dark states with the same parity.*
2. *The dark states should be parameter-dependent.*
3. *Dark states do not disappear and do not cross when parameters are slowly tuned during braiding.*

The first requirement is to prevent the braiding operation from causing the system to transition into different topological sectors, which could interfere with the intended quantum computation. The second requirement is to ensure that the dark space changes correspondingly with variations in parameter space. Lastly, the third requirement ensures that two distinct dark states are always present in the dark space during braiding.

As discussed at the end of Chapter 7, the single Majorana box cannot meet the braiding conditions because each parity subspace contains at most one dark state. For

two Majorana boxes, each single parity subspace can have two possible states. The jump operator within this subspace can be represented by the general form as follows.

$$K_{\text{single parity}} = \begin{pmatrix} k_{00} & k_{01} \\ k_{10} & -k_{00} \end{pmatrix}, \tag{8.1}$$

where k_{00}, k_{01} and k_{10} can be complex numbers. The trace of jump operators must be zero to ensure the Lindbladian map is trace-preserving. We can find eigenvectors $|\psi_\pm\rangle$ and their corresponding eigenvalues as the following expressions.

$$K_{\text{single parity}}|\psi_\pm\rangle = \pm\sqrt{k_{00}^2 + k_{01}k_{10}}\,|\psi_\pm\rangle, \tag{8.2}$$

$$\text{where } |\psi_\pm\rangle = \left(k_{00} \pm \sqrt{k_{00}^2 + k_{01}k_{10}},\ k_{10}\right). \tag{8.3}$$

If we assume these two states to be dark states, implying their eigenvalues are zero, they will combine into a single state denoted as (k_{00}, k_{10}). Alternatively, another scenario occurs when the jump operator is a null matrix ($k_{00} = k_{01} = k_{10} = 0$), resembling a case discussed in Gau's article [126]. In this scenario, the dark states remain unaffected by the parameters, which suggests a trivial solution rather than the presence of a diabolic point. Thus, although two Majorana boxes may possess two dark states within the same parity subspace, they cannot meet the second requirement for braiding, which stipulates that these dark states must vary depending on the parameters in the jump operator.

To increase the degrees of freedom necessary to satisfy the conditions for braiding, we consider three entangled Majorana boxes. However, calculating the Lindblad equation remains time-consuming when using a general 8×8 jump operator. Unlike the methodology used for a single Majorana box in Chapter 7, we use an inverse design approach to identify a possible braiding protocol and the tunneling open system involving three Majorana boxes. This inverse design approach means that we first define a braiding-compatible jump operator whose dark states satisfy the conditions necessary for braiding. Then, we construct the tunneling system based on this braiding-compatible jump operator.

8.1 The braiding-compatible jump operator

In this chapter, as previously discussed, we address the Majorana sector involving three boxes for a braiding protocol. Since braiding operations occur within a single parity subspace, our focus in the Lindblad equation narrows to one specific parity sector. We can effectively separate the Lindblad equation into tensor products corresponding to the contributions from each parity, by initializing the density matrix of the Majorana section

and the jump operator with zeros outside the parity sectors as follows.

$$\rho_{\mathrm{M}}(t=0) = \left(\begin{array}{c|c} \rho_{\mathrm{even}}(t=0) & 0 \\ \hline 0 & \rho_{\mathrm{odd}}(t=0) \end{array}\right); \qquad K = \left(\begin{array}{c|c} K_{\mathrm{even}} & 0 \\ \hline 0 & K_{\mathrm{odd}} \end{array}\right), \tag{8.4}$$

$$\Rightarrow \mathcal{L}[K]\ \rho_{\mathrm{M}} \equiv \mathcal{L}[K_{\mathrm{even}}]\ \rho_{\mathrm{even}} \oplus \mathcal{L}[K_{\mathrm{odd}}]\ \rho_{\mathrm{odd}}. \tag{8.5}$$

Therefore, we restrict our attention to a single parity subspace, which, for three Majorana boxes, possesses a dimension of 4×4. Hereafter, we analyze dissipation exclusively within the odd-parity sector.

The braiding-compatible jump operator is defined as the operator whose dark states satisfy conditions for braiding. Specifically, multiple dark states within the same parity subspace are parameter-dependent and always distinguishable during braiding. The orthonormal states with odd parity of three entangled Majorana boxes are $\{|001\rangle, |010\rangle, |100\rangle, |111\rangle\}$. Dark states can be defined as superpositions of these orthonormal states, ensuring that the dark states remain distinguishable during braiding protocols. One possible set of linear combinations for these orthonormal states is given by

$$|\psi_1\rangle = p_1|001\rangle + p_2|111\rangle, \qquad |\psi_2\rangle = w_1|010\rangle + w_2|100\rangle, \tag{8.6}$$

where $p_1^2 + p_2^2 = 1$ and $w_1^2 + w_2^2 = 1$. According to the conditions for braiding protocols, the associated probabilities $p_{1,2}$ and $w_{1,2}$ should be functions of the parameters from the jump operator.

In the Majorana sector consisting of three boxes, the odd-parity physical Hilbert subspace has four orthonormal states: $\{|001\rangle, |010\rangle, |100\rangle, |111\rangle\}$. These orthonormal states correspond to the elements in the odd-parity sector of the reduced density matrix and the jump operator, as described below.

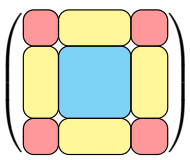

$\Rightarrow$ { Subspace spanned by $|001\rangle$ and $|111\rangle$. ; Subspace spanned by $|010\rangle$ and $|100\rangle$. ; Coherence between two subspaces $\{|001\rangle, |111\rangle\}$ and $\{|010\rangle, |100\rangle\}$. } (8.7)

In the non-Abelian braiding process illustrated in Fig. 8.1, the steady state transitions from one dark state to another within the dark subspace governed by the same Lindblad dissipator. For the dark states described in Eq. (8.6), the braiding operation moves the steady state from the subspace spanned by $\{|001\rangle, |111\rangle\}$ to the subspace spanned by $\{|010\rangle, |100\rangle\}$. This effectively changes the steady state from a mixed state of $|001\rangle$ and

$|111\rangle$ to that of $|010\rangle$ and $|100\rangle$. This transition can be implemented through coherence between the two subspaces or via the subspaces in the jump operator.

A potential choice for the jump operator feasible in the Majorana box system is to exclusively consider the coherence sector represented by the yellow blocks in the matrix described in Eq. (8.7).

$$K_{\text{odd}} = \begin{pmatrix} 0 & f_1 & -ff_1 & 0 \\ g_1 & 0 & 0 & gg_1 \\ g_2 & 0 & 0 & gg_2 \\ 0 & f_2 & -ff_2 & 0 \end{pmatrix}, \tag{8.8}$$

where $f(\lambda_{j,\nu}, \beta_{j,\nu})$ and $g(\lambda_{j,\nu}, \beta_{j,\nu})$ are real functions of the tunnel couplings. These functions encode the adiabatic time evolution. The jump operator described gives rise to two distinct dark states, $K_{\text{odd}}|\psi_{1,2}\rangle = 0$, represented as

$$|\psi_1\rangle = N_1 \left(-g|001\rangle + |111\rangle\right), \tag{8.9}$$

$$|\psi_2\rangle = N_2 \left(f|010\rangle + |100\rangle\right), \tag{8.10}$$

where N_1 and N_2 are normalization constants. These dark states are independent of the specific values of $f_{1,2}$ and $g_{1,2}$, but remain distinct when one of g_1 or g_2 is non-zero, and simultaneously, one of f_1 or f_2 is non-zero. The characteristics of these states are influenced by the tunneling parameters f and g, which are crucial for operations within the dark state subspace, particularly for braiding. Importantly, these dark states do not merge into a single state for any combination of f and g. The jump operator defined in Eq. (8.8) is referred to as the braiding-compatible jump operator. It facilitates the system's evolution into a dark space that satisfies the braiding conditions, as depicted in Fig. 8.1, through appropriate braiding protocols.

Two additional eigenstates of the braiding-compatible jump operator (8.8) exhibit symmetric pairs of eigenvalues.

$$K_{\text{odd}}|\psi_\pm\rangle = \pm\sqrt{(f_1 + f_2 g)(g_1 - f g_2)}|\psi_\pm\rangle, \tag{8.11}$$

$$\text{where } |\psi_\pm\rangle = \begin{pmatrix} f_1\sqrt{g_1 - f g_2} \\ \pm g_1\sqrt{f_1 + f_2 g} \\ \pm g_2\sqrt{f_1 + f_2 g} \\ f_2\sqrt{g_1 - f g_2} \end{pmatrix}. \tag{8.12}$$

N_3 denotes the normalizing constant. As shown in Eq. (8.11), two eigenvalues also depend on f and g, such that these eigenvalues may become zero if the conditions $f_1 = -f_2 g$ or $g_1 = f g_2$ are met during the adiabatic changes in f and g. In such a scenario, the

eigenvectors $|\psi_{\pm}\rangle$ (8.12) will coalesce with one of the dark states, $|\psi_1\rangle$ (8.9) or $|\psi_2\rangle$ (8.10). However, this does not affect the braiding protocol because the two dark states remain distinct. Hence, the jump operator (8.8) is a promising choice for braiding.

8.2 Lindblad equation incorporating the braiding-compatible jump operator

In theory, the odd-parity block in the steady state of the Lindblad equation, incorporating the braiding-compatible jump operator given by Eq. (8.8), is composed of two orthonormal dark states denoted as $|\psi_{1,2}\rangle$. Generally, the odd-parity block in a steady state, denoted as ρ_{s} in this chapter, can be expressed as follows,

$$\rho_{\mathrm{s}} = (\zeta_1|\psi_1\rangle + \zeta_2|\psi_2\rangle) \otimes \mathrm{h.c.}, \tag{8.13}$$

where $|\zeta_1|^2 + |\zeta_2|^2 = 1$, guaranteeing that the trace of the density matrix ρ_{s} equals to one. To ensure the discussion is self-consistent, we will derive the steady state in the form given by Eq. (8.13) from the Lindblad form master equation. However, the open system composed of three Majorana boxes has a greater number of degrees of freedom in its Hamiltonian compared to that of a single box. Therefore, it is necessary to rederive the Lindblad equation starting from the Hamiltonian.

8.2.1 The open system consisting of three Majorana boxes

When we introduce two additional Majorana boxes into the open system shown in Fig. 6.1, the total Hamiltonian can be written analogously to that of the single-box open system in Eq. (6.1) albeit with an increased number of degrees of freedom in the box Hamiltonian and additional tunnel couplings between the two Majorana boxes in the tunneling Hamiltonian.

$$H(t) = H_{\mathrm{box}} + H_{\mathrm{QD}} + H_{\mathrm{env}} + H_{\mathrm{drive}}(t) + H_{\mathrm{tun}}(t). \tag{8.14}$$

The remaining components of the total Hamiltonian remain unchanged from those discussed for the single-box open system in Chapter 6, including the Hamiltonians of the environment (H_{env} in Eq. (6.22), the quantum dots (H_{QD} in Eq. (6.21)), and the AC driving field (H_{drive} in Eq. (6.23)).

Recalling from the previous notations in the single-box Hamiltonian in Eq. (6.10), the box Hamiltonian in the total Hamiltonian in Eq. (8.14) can be written as

$$H_{\mathrm{box}} = E_C \sum_{n=1}^{3} (N_n - N_g)^2 , \tag{8.15}$$

where E_C denotes the charging energy, N_n represents the total electron number in Majorana box n, and N_g stands for the tunable back-gate voltage. We assume all three Majorana boxes are identical, implying they share the same charging energy. Additionally, we consider the negligible impact of overlaps between pairs of MBSs in this context.

The tunneling Hamiltonian now includes contributions not only from the tunnel couplings between the quantum dots and MBSs but also between MBSs located in different boxes. The electron tunneling between the quantum dots and Majorana box n, denoted as $H_{\text{tun,e}}$, resembles the tunneling Hamiltonian of a single-box open system, as given in Eq. (6.24), but with additional degrees of freedom in the Majorana sector.

$$H_{\text{tun,e}} = t_0 \sum_{n=1}^{3} \sum_{j=1}^{2} \sum_{\mu=1}^{4} \lambda_{j,n\mu} e^{-i\beta_{j,n\mu}} e^{-i\hat{\phi}_n + i\delta_j} d_j^\dagger \gamma_{n\mu} + \text{h.c.}. \tag{8.16}$$

Recalling the notations from the tunneling Hamiltonian in Eq. (6.24) from Chapter 6, t_0 denotes the overall scale of tunneling couplings between quantum dots and MBSs, $\hat{\phi}_n$ represents the phase operator within Majorana box n, and δ_j signifies electromagnetic fluctuations from the bath, as expressed in Eq. (6.25). The subscripts j, n and μ of the tunneling amplitudes $\lambda_{j,n\mu}$ and their corresponding phases $\beta_{j,n\mu}$ denote the specific channels connecting quantum dot d_j with MBS $\gamma_{n\mu}$ in Majorana box n.

The second term in the tunneling Hamiltonian, $H_{\text{tun},\gamma}$, describes the direct tunneling between two Majorana boxes. To avoid complications, we first consider the case where there is only a single tunnel connecting the two boxes. For Majorana box n and Majorana box n', $H_{\text{tun},\gamma}$ can be expressed as follows,

$$H_{\text{tun},\gamma} = E_C \sum_{n,n'=1}^{3} \sum_{\mu,\nu=1}^{4} i\tilde{t}_{nn'} \gamma_{n\mu} \gamma_{n'\nu}, \tag{8.17}$$

where the dimensionless parameter $\tilde{t}_{nn'} = t_{nn'}/E_C$, and $t_{nn'}$ is the tunnel coupling energy between the boxes n and n'. Here, we consider that $t_{nn} = 0$ and $t_{nn'} > 0$ for all amplitudes, because $H_{\text{tun},\gamma}$ exclusively describes the transport between two distinct boxes. Thus, the tunneling Hamiltonian in this context is the sum of $H_{\text{tun,e}}$ (as defined in Eq. (8.16)) and $H_{\text{tun},\gamma}$ (8.17).

$$H_{\text{tun}} = H_{\text{tun,e}} + H_{\text{tun},\gamma}. \tag{8.18}$$

In analogy with the approximations described in Table 6.1, we apply the RWA and the SW transformation to obtain the effective Hamiltonian in the lo-energy subspace.

In the open system with two additional boxes, the implementation of the RWA remains unchanged because the driving Hamiltonian is not altered. However, the SW transformation involves more steps due to the increased number of degrees of freedom in the Majorana sector. To accurately derive the cotunneling Hamiltonian in the low-energy regime, it is essential to extend the SW transformation up to the fourth order because second and third-order contributions alone cannot fully describe the trajectory through all three boxes.

To perform the SW transformation, we assume that the energy scales of the tunnel couplings, t_0 and $t_{nn'}$, are small. Extending the SW transformation to the fourth order allows us to obtain

$$H_{\text{eff}} = e^{S}(H_0 + H_{\text{tun}})e^{-S} \tag{8.19}$$

$$\Rightarrow H_{\text{eff}} = H_0 + H_{\text{tun}} + \sum_r \frac{1}{r!}\underbrace{[S,[S,\dots[S}_{r},\ H_0 + H_{\text{tun}}]\dots]] \tag{8.20}$$

$$\begin{aligned} &\approx H_0 + H_{\text{tun}} + [S,H_0] + [S,H_{\text{tun}}] + \frac{1}{2}[S,[S,H_0]] + \frac{1}{2}[S,[S,H_{\text{tun}}]] \\ &+ \frac{1}{6}[S,[S,[S,H_0]]] + \frac{1}{6}[S,[S,[S,H_{\text{tun}}]]] + \frac{1}{24}[S,[S,[S,[S,H_0]]]]\,, \end{aligned} \tag{8.21}$$

where the generator S is on the same order of magnitude as t_0. By choosing S such that $H_{\text{tun}} + [S,H_0] = 0$, the SW transformation results in a transformed Hamiltonian as

$$H_{\text{eff}} = H_0 + \overbrace{\underbrace{\frac{1}{2}[S,H_{\text{tun}}]}_{H_{\text{cot}}^{(2)}} + \underbrace{\frac{1}{3}[S,[S,H_{\text{tun}}]]}_{H_{\text{cot}}^{(3)}} + \underbrace{\frac{1}{8}[S,[S,[S,H_{\text{tun}}]]]}_{H_{\text{cot}}^{(4)}}}^{H_{\text{cot}}=\sum_{r=2}^{4}\frac{r-1}{r!}\overbrace{[S,[S,\dots[S}^{(r-1)},\,H_{\text{tun}}]\dots]]}. \tag{8.22}$$

$$\Rightarrow H_{\text{eff}} = H_0 + H_{\text{cot}}^{(2)} + \frac{1}{3}\left[S,2H_{\text{cot}}^{(2)}\right] + \frac{1}{8}\left[S,3H_{\text{cot}}^{(3)}\right]. \tag{8.23}$$

Regarding the low-energy approximation outlined in Table 6.1, Appendix K presents the derivation of the cotunneling contribution in Eq. 8.23 as follows.

$$H_{\text{cot}} = \sum_{r=2}^{4}\left(\frac{r-1}{r!}\right)\left(\frac{2}{E_C}\right)^{r-1}(H_{\text{tun}})^{r}\,. \tag{8.24}$$

In addition to the tunnel couplings between quantum dots and Majorana boxes, the tunneling Hamiltonian now incorporates an extra term due to the tunnel couplings

between the boxes themselves, labeled as $H_{\mathrm{tun},\gamma}$ in Eq. (8.17). Therefore, the second-order term in the cotunneling contribution can be expressed as

$$H_{\mathrm{cot}}^{(2)} = \frac{1}{E_C}\left(H_{\mathrm{tun}}H_{\mathrm{tun}}\right) = \frac{1}{E_C}\left(H_{\mathrm{tun,e}} + H_{\mathrm{tun},\gamma}\right)\left(H_{\mathrm{tun,e}} + H_{\mathrm{tun},\gamma}\right) \tag{8.25}$$

$$\Rightarrow H_{\mathrm{cot}}^{(2)} = \frac{1}{E_C}\left(H_{\mathrm{tun,e}}H_{\mathrm{tun,e}} + H_{\mathrm{tun},\gamma}H_{\mathrm{tun},\gamma} + \{H_{\mathrm{tun,e}}, H_{\mathrm{tun},\gamma}\}\right). \tag{8.26}$$

Only the first term, $(H_{\mathrm{tun,e}}H_{\mathrm{tun,e}})$, traces a complete trajectory between the two quantum dots, akin to the situation in a single Majorana box scenario. Terms involving incomplete trajectories would contribute only minor corrections to higher-order tunneling processes. Therefore, by focusing on this term up to the second order, we derive the second-order cotunneling Hamiltonian as

$$H_{\mathrm{cot}}^{(2)} \approx \frac{t_0^2}{E_C}\sum_{n=1}^{3}\left(e^{i(\delta_1-\delta_2)}e^{i(\epsilon_2-\epsilon_1)t}W_{12}^{n}d_2^{\dagger}d_1 + \mathrm{h.c.}\right). \tag{8.27}$$

The operator W_{jk}^{n}, analogous to the operator W_{jk} in Eq. (6.50), describes the dynamics within Majorana box n, where both quantum dots j and k participate in transport processes.

$$W_{jk}^{n} = \sum_{\nu\neq\mu}\left(\lambda_{j,n\nu}\lambda_{k,n\mu}e^{i(\beta_{j,n\nu}-\beta_{k,n\mu})} - \lambda_{j,n\mu}\lambda_{k,n\nu}e^{i(\beta_{j,n\mu}-\beta_{k,n\nu})}\right)\gamma_{n\nu}\gamma_{n\mu}. \tag{8.28}$$

Here, $\lambda_{j,n\nu}$ denotes the tunneling amplitudes between the quantum dot j and the MBS $\gamma_{n\nu}$ in the Majorana box n, and $\beta_{j,n\nu}$ is the associated to the corresponding tunneling phase.

For the third and fourth-order terms in Eq. (8.24), we exclusively consider contributions from the complete trajectory between two quantum dots. These contributions are derived as follows,

$$H_{\mathrm{cot}}^{(3)} \approx \frac{4}{3E_C^2}\left(H_{\mathrm{tun,e}}H_{\mathrm{tun},\gamma}H_{\mathrm{tun,e}}\right), \tag{8.29}$$

$$H_{\mathrm{cot}}^{(4)} \approx \frac{1}{E_C^3}\left(H_{\mathrm{tun,e}}H_{\mathrm{tun},\gamma}H_{\mathrm{tun},\gamma}H_{\mathrm{tun,e}}\right). \tag{8.30}$$

From the expressions $H_{\mathrm{tun,e}}$ and $H_{\mathrm{tun},\gamma}$ in Eqs. (8.16) and (8.17), we derive the formulas for the third and fourth-order cotunneling involving the second quantization of Majorana

and fermion operators.

$$H_{\text{cot}}^{(3)} \approx \frac{4t_0^2}{3E_C} \sum_{n \neq n'} \left(e^{i(\delta_1 - \delta_2)} e^{i(\epsilon_2 - \epsilon_1)t} W_{12}^{n,n'} d_2^\dagger d_1 + \text{h.c.} \right), \tag{8.31}$$

$$H_{\text{cot}}^{(4)} \approx \frac{t_0^2}{E_C} \sum_{n \neq n' \neq n''} \left(e^{i(\delta_1 - \delta_2)} e^{i(\epsilon_2 - \epsilon_1)t} W_{12}^{n,n',n''} d_2^\dagger d_1 + \text{h.c.} \right). \tag{8.32}$$

The third and fourth-order terms involve trajectories through two and three Majorana boxes, respectively. The operators $W_{jk}^{n,n'}$ and $W_{jk}^{n,n',n''}$ represent the dynamics within the Majorana boxes. Specifically, $W_{jk}^{n,n'}$ corresponds to the dynamics involving boxes n and n', while $W_{jk}^{n,n',n''}$ involves the dynamics across boxes n, n', and n''.

$$\begin{aligned} W_{jk}^{n,n'} &= -i\tilde{t}_{nn'} \sum_{\nu \neq \mu} \sum_{\nu' \neq \mu'} \gamma_{n\nu}\gamma_{n\mu}\gamma_{n'\nu'}\gamma_{n'\mu'} \\ &\quad \times \left(\lambda_{j,n\nu}\lambda_{k,n'\mu'} e^{i(\beta_{j,n\nu} - \beta_{k,n'\mu'})} - \lambda_{j,n'\mu'}\lambda_{k,n\nu} e^{i(\beta_{j,n'\mu'} - \beta_{k,n\nu})} \right), \end{aligned} \tag{8.33}$$

$$\begin{aligned} W_{jk}^{n,n',n''} &= -\tilde{t}_{nn'}\tilde{t}_{n'n''} \sum_{\nu \neq \mu} \sum_{\nu' \neq \mu'} \sum_{\nu'' \neq \mu''} \gamma_{n\nu}\gamma_{n\mu}\gamma_{n'\nu'}\gamma_{n'\mu'}\gamma_{n''\nu''}\gamma_{n''\mu''} \\ &\quad \times \left(\lambda_{j,n\nu}\lambda_{k,n''\mu''} e^{i(\beta_{j,n\nu} - \beta_{k,n''\mu''})} - \lambda_{j,n''\mu''}\lambda_{k,n\nu} e^{i(\beta_{j,n''\mu''} - \beta_{k,n\nu})} \right), \end{aligned} \tag{8.34}$$

where the dimensionless scalar $\tilde{t}_{nn'} = t_{nn'}/E_C$, first introduced in Eq. (8.17), represents the strength of the tunneling between the Majorana boxes n and n'. The tunneling operators within the Majorana boxes, labeled as W_{jk}^{n}, $W_{jk}^{n,n'}$ and $W_{jk}^{n,n',n''}$, will later serve as the jump operators in the Lindblad equation, which governs the dissipation in the Majorana box. They will become significant later on, particularly when we explore the braiding-compatible jump operator within the context of the real tunneling system.

As shown in Eq. (K.15), fourth-order cotunneling adequately describes the transport across three boxes and between two quantum dots. Thus, we expand the Hamiltonian up to the fourth order in perturbation theory using the SW transformation. The effective Hamiltonian is then given by

$$H_{\text{eff}} \approx \underbrace{H_{\text{QD}} + H_{\text{env}} + H_{\text{drive}}}_{H_0} + \underbrace{H_{\text{cot}}^{(2)} + H_{\text{cot}}^{(3)} + H_{\text{cot}}^{(4)}}_{H_{\text{cot}}}, \tag{8.35}$$

where $H_{\text{cot}}^{(2)}$, $H_{\text{cot}}^{(3)}$ and $H_{\text{cot}}^{(4)}$ are the cotunneling contributions of the second, third, and fourth-order, respectively, as detailed in Eqs. (8.27), (8.31) and (8.32). The rest of the

effective Hamiltonian, excluding the Majorana sector represented by W_{jk}^{n} in Eq. (8.28), $W_{jk}^{n,n'}$ in Eq. (8.33) and $W_{jk}^{n,n',n''}$ in Eq. (8.34), remains unchanged because the only modification is the addition of two boxes. Applying the Born-Markov approximation to the effective Hamiltonian (8.35) is similar to the computation for the single-box system described in Sec. 6.3.1. In comparison to the single-box case, the Lindblad equation for the dissipative dynamics in three Majorana boxes involves the same transition rates Γ_{jk} as specified in Eq. (6.104), but uses different jump operators.

$$\mathcal{L}\rho_M(t) = \sum_{j\neq k} \Gamma_{jk} \left(K_{jk}\rho_{\mathrm{M}}(t)K_{jk}^{\dagger} - \frac{1}{2}\left\{ K_{jk}^{\dagger}K_{jk}, \rho_{\mathrm{M}}(t) \right\} \right), \tag{8.36}$$

where the jump operator K_{jk}, which represents the possible routes from quantum dot j to quantum dot k via Majorana boxes, is expressed as

$$K_{jk} = \sum_{n} W_{jk}^{n} + \sum_{n'>n} W_{jk}^{n,n'} + W_{jk}^{1,2,3}, \text{ where } n, n' \in \{1,2,3\}. \tag{8.37}$$

Once again, we consider an Ohmic bath at low temperature. As shown in Eq. (6.107), under these conditions, the transition rate from the lower quantum dot level to the higher quantum dot level is suppressed by the inverse transition rate. Therefore, we focus exclusively on transport from quantum dot 1 to quantum dot 2, which leads to the following Lindblad equation.

$$\mathcal{L}\rho_M(t) \approx \Gamma_{12} \left(K_{12}\rho_{\mathrm{M}}(t)K_{12}^{\dagger} - \frac{1}{2}\left\{ K_{12}^{\dagger}K_{12}, \rho_{\mathrm{M}}(t) \right\} \right). \tag{8.38}$$

As the steady-state of the Majorana sector, denoted as $\rho_s = \rho_M(t \to \infty)$, is immune to the dissipation described by the Lindblad equation (8.38), we can state that $\mathcal{L}\rho_s = 0$. As discussed in Eq. (8.5), we can consider exclusively the odd-parity block when the coherence between the two parity blocks of the initial density matrix and the jump operators is absent.

8.2.2 The steady states with topological order

In the equilibrium state, the odd-parity block of the Lindblad equation can be written as

$$\mathcal{L}[K_{\mathrm{odd}}]\rho_{\mathrm{odd}} = 0 \Rightarrow \Gamma_{12} \left(K_{\mathrm{odd}}\rho_{\mathrm{odd}}K_{\mathrm{odd}}^{\dagger} - \frac{1}{2}\left\{ K_{\mathrm{odd}}^{\dagger}K_{\mathrm{odd}}, \rho_{\mathrm{odd}} \right\} \right) = 0, \tag{8.39}$$

where ρ_{odd} represents the odd-parity block of the steady-state density matrix $\rho_M(t \to \infty)$, and K_{odd} represents the odd-parity block of the jump operator K_{12}. By employing the braiding-compatible jump operator defined in Eq. (8.8), we will investigate how the Lindblad equation, which incorporates this operator, guides the Majorana boxes towards a steady state spanned by the dark states shown in Eqs. (8.9) and (8.10).

Without loss of generality, any arbitrary 4×4 density matrix can be expressed as

$$\rho_{4\times4} = \sum_{n=0}^{3} a_{nn}|n\rangle\langle n| + \sum_{n>m} \left[(a_{nm} + i\, b_{nm})\, |n\rangle\langle m| + \text{h.c.}\right], \tag{8.40}$$

where a_{nm} and b_{nm} are real numbers, and $\{|0\rangle, |1\rangle, |2\rangle, |3\rangle\}$ here denote the four basis states corresponding to odd-parity states. For the matrix $\rho_{4\times4}$ to be a valid density matrix, the coefficients must satisfy $\sum_{n=0}^{3} a_{nn} \equiv 1$ and $a_{nn} \geq 0$. We represent the steady state ρ_{odd} using the general form given by Eq. (8.40) in the Lindblad equation (8.39) incorporating the braiding-compatible jump operator (8.8), then we obtain the following matrix coefficients corresponding to the steady states.

$$\mathcal{L}[K_{\text{odd}}]\rho_{\text{odd}} = 0 \Rightarrow \begin{cases} a_{00} = -g a_{03}, & a_{11} = \dfrac{f^2\left(a_{03}g^2 + a_{03} + g\right)}{\left(f^2+1\right)g}, \\ a_{33} = -\dfrac{a_{03}}{g}, & a_{22} = \dfrac{a_{03}g^2 + a_{03} + g}{f^2 g + g}; \\ a_{01} = -fg a_{23}, & a_{02} = -g a_{23}, \\ a_{13} = f a_{23}, & \dfrac{1+f^2}{f}a_{12} + \dfrac{1+g^2}{-g}a_{03} = 1; \\ b_{01} = fg b_{23}, & b_{02} = g b_{23}, \\ b_{03} = b_{12} = 0, & b_{13} = f b_{23}. \end{cases} \tag{8.41}$$

For the matrix coefficients a_{12} and a_{03}, which correspond to the coherence between states $|010\rangle$ and $|100\rangle$, and states $|001\rangle$ and $|111\rangle$ respectively, we introduce a function $F(f, g)$ to substitute them using the following formulas.

$$a_{12} = F^2 \frac{f}{1+f^2}, \qquad a_{03} = \left(1 - F^2\right)\frac{-g}{1+g^2}, \tag{8.42}$$

where $F \in [-1, 1]$ ensures satisfaction of the corresponding equation in Eq. (8.41). By inserting Eqs. (8.41) and (8.42) into the general expression for the density matrix given

in Eq. (8.40), we obtain the steady state ρ_{odd}.

$$\rho_{\text{odd}} = \begin{pmatrix} \frac{(1-F^2)g^2}{g^2+1} & fg(-a_{23}+ib_{23}) & g(-a_{23}+ib_{23}) & \frac{(F^2-1)g}{g^2+1} \\ fg(-a_{23}-ib_{23}) & \frac{f^2F^2}{f^2+1} & \frac{fF^2}{f^2+1} & f(a_{23}+ib_{23}) \\ g(-a_{23}-ib_{23}) & \frac{fF^2}{f^2+1} & \frac{F^2}{f^2+1} & a_{23}+ib_{23} \\ \frac{(F^2-1)g}{g^2+1} & f(a_{23}-ib_{23}) & a_{23}-ib_{23} & \frac{1-F^2}{g^2+1} \end{pmatrix}. \tag{8.43}$$

As mentioned previously, the steady state is always spanned by the dark states, which can be shown through a unitary transformation. For the braiding-compatible jump operator, this unitary transformation consists of the column vectors representing the dark states $|\psi_1\rangle$ (8.9) and $|\psi_2\rangle$ (8.10), along with their corresponding orthonormal vectors $|\psi_3\rangle$ and $|\psi_4\rangle$, respectively, that complete the orthonormal basis.

$$\begin{aligned} U &= (|\psi_1\rangle\ |\psi_2\rangle\ |\psi_3\rangle\ |\psi_4\rangle) \\ &= \begin{pmatrix} -g/\sqrt{1+g^2} & 0 & 1/\sqrt{1+g^2} & 0 \\ 0 & f/\sqrt{1+f^2} & 0 & -1/\sqrt{1+f^2} \\ 0 & 1/\sqrt{1+f^2} & 0 & f/\sqrt{1+f^2} \\ 1/\sqrt{1+g^2} & 0 & g/\sqrt{1+g^2} & 0 \end{pmatrix}. \end{aligned} \tag{8.44}$$

As anticipated, the steady-state density matrix ρ_{odd} (8.40) yields zero vectors when applied to the orthonormal vectors $|\psi_3\rangle$ and $|\psi_4\rangle$. In other words, $\rho_{\text{odd}}|\psi_3\rangle = 0$ and $\rho_{\text{odd}}|\psi_4\rangle = 0$. On the other hand, the dark states, $|\psi_1\rangle$ and $|\psi_2\rangle$, are eigenstates of the steady-state density matrix. Thus, the unitary transformation to the orthonormal basis $\{|\psi_1\rangle, |\psi_2\rangle, |\psi_3\rangle, |\psi_4\rangle\}$ results in

$$\begin{aligned} U^\dagger \rho_{\text{odd}} U &= \begin{pmatrix} 1-F^2 & r_{23}e^{-i\theta_{23}}\sqrt{(f^2+1)(g^2+1)} & 0 & 0 \\ r_{23}e^{i\theta_{23}}\sqrt{(f^2+1)(g^2+1)} & F^2 & 0 & 0 \\ 0 & 0 & 0 & 0 \\ 0 & 0 & 0 & 0 \end{pmatrix} \\ \Rightarrow \rho_{\text{odd}} &= \left(1-F^2\right)|\psi_1\rangle\langle\psi_1| + r_{23}e^{-i\theta_{23}}\sqrt{(f^2+1)(g^2+1)}|\psi_1\rangle\langle\psi_2| \\ &\quad + r_{23}e^{i\theta_{23}}\sqrt{(f^2+1)(g^2+1)}|\psi_2\rangle\langle\psi_1| + F^2|\psi_2\rangle\langle\psi_2|, \end{aligned} \tag{8.45}$$

where $r_{23} = \text{sgn}(a_{23})\sqrt{a_{23}+b_{23}}$ and $\theta_{23} = \arctan(b_{23}/a_{23})$ with $\theta_{23} \in [0,\ \pi)$.

In the case of the pure steady state, where $\rho_{\text{odd}}^2 = \rho_{\text{odd}}$, we find that

$$r_{23} = \frac{F\sqrt{1-F^2}}{\sqrt{(f^2+1)(g^2+1)}} \tag{8.46}$$

$$\Rightarrow \rho_{\text{odd}} = \left(\sqrt{1-F^2}e^{i\alpha_1}|\psi_1\rangle + Fe^{i\alpha_2}|\psi_2\rangle\right) \otimes \text{h.c.}, \tag{8.47}$$

where $\alpha_1 - \alpha_2 = \theta_{23}$, and it is assumed that F and r_{23} have the same sign. The expression for the steady state ρ_{odd} given in Eq. (8.47) was anticipated and outlined earlier in Eq. (8.13) at the beginning of this section.

The same results can also be obtained by expressing the density matrix in vector form and representing the Liouvillian superoperator $\mathcal{L}$ as a matrix [126]. In Appendix L, we provide four dark states, denoted as $|\mathcal{D}_{1,\ldots,4}\rangle$ in Eqs. (L.4)-(L.7), which correspond to the vectorized forms of $|\psi_l\rangle\langle\psi_m|$, with l, $m \in \{1,2\}$. The remaining eigenstates of the Liouvillian have negative eigenvalues, leading to their exponential decay over time. The smallest non-zero eigenvalue is referred to as the dissipative gap. The rate at which the Majorana sector transitions to the dark states is governed by the inverse of this dissipative gap.

To demonstrate the topological invariant in the steady state, we reintroduce the same chiral symmetry discussed in Eq. (7.30) in Sec. 7.2. To satisfy the constraints imposed by chiral symmetry, one approach is to set $\theta_{23} = 0$, which is equivalent to setting $b_{23} = 0$, the pure-state constraint given by Eq. (8.46) becomes

$$a_{23}^2 = \frac{(F^2 - F^4)}{(f^2+1)(g^2+1)}. \tag{8.48}$$

This can be achieved by adjusting the coherence phase between the two dark states $|\psi_1\rangle$ and $|\psi_2\rangle$ using quantum gates. Consequently, the pure state described by Eq. (8.47) becomes

$$\begin{aligned}\rho_{\text{odd}} = &\left(1-F^2\right)|\psi_1\rangle\langle\psi_1| + F\sqrt{1-F^2}\,|\psi_1\rangle\langle\psi_2| \\ &+ F\sqrt{1-F^2}\,|\psi_2\rangle\langle\psi_1| + F^2|\psi_2\rangle\langle\psi_2|,\end{aligned} \tag{8.49}$$

whose Bloch vector $(2F\sqrt{1-F^2}, 0, 1-2F^2)$ lies in the $\sigma_x - \sigma_z$ plane. On the Bloch sphere, this vector can only move within a unit circle in the $\sigma_x - \sigma_z$ plane, similar to the red vector shown in Fig. 7.1.

In a manner analogous to the approach described in Sec. 7.2, we can determine the topological invariant of the same class for the Bloch vector n_{odd} as the winding number

$\mathcal{W}$ expressed in Eqs. (7.41) and (7.54).

$$\boldsymbol{n}_{\text{odd}} = \left(2F\sqrt{1-F^2}, 0, 1-2F^2\right) \tag{8.50}$$

$$\Rightarrow \mathcal{W} = \frac{1}{\pi}\int_{t_0}^{t_f} dt \left((1-2F^2)\frac{d(F\sqrt{1-F^2})}{dt} - (F\sqrt{1-F^2})\frac{d(1-2F^2)}{dt}\right) \tag{8.51}$$

$$= \frac{1}{2\pi}\left[\theta(t_f) - \theta(t_0)\right], \tag{8.52}$$

where the angle $\theta = -\arctan\left(n_x/n_z\right) = -\arctan\left[2F\sqrt{1-F^2}/(1-2F^2)\right]$. The function F, as defined in Eq. (8.42), depends on f and g which are components of the jump operator K_{odd} given in Eq. (8.8). These components f and g are functions of the tunneling parameters, as detailed in Eq. (8.37). This relationship is derived from the Hamiltonian and is crucial for the Lindblad equation described in Eq. (8.36). While the expression for the jump operator in Eq. (8.37) is essential for understanding the structure of the braiding-compatible jump operator in a physical tunneling system, we will first focus on calculating the winding number. The construction of the real tunneling system that yields the braiding-compatible jump operator will be addressed in the next section.

According to the braiding operation illustrated in Fig. 8.1, the Bloch vector (8.50) traces a semicircular path for each closed loop in the parameter space associated with f and g. In polar coordinates, the time-periodic driving functions $f(t)$ and $g(t)$ are given by

$$f(t) = r\cos\varphi(t), \qquad g(t) = r\sin\varphi(t), \tag{8.53}$$

where $\varphi(t_f) = \varphi(t_0) + 2\pi$ for the time-periodic boundary condition. To achieve a different periodicity in the function $F(f,g)$, we can use the following expression.

$$F(\varphi(t)) = \sin\left(\frac{\varphi(t)}{4}\right) = \sin\left[\frac{1}{4}\sin^{-1}\left(\frac{g}{\sqrt{f^2+g^2}}\right)\right]. \tag{8.54}$$

This function F in Eq. (8.54) satisfies the initial definition of F provided in Eq. (8.42), where $F(f,g) \in [-1,1]$. This function can be realized using quantum gates to adjust the coherence between two dark states. Consequently, the angle θ, as defined in the winding number (8.52), becomes

$$\theta = -\arctan\left(\frac{2F\sqrt{1-F^2}}{1-2F^2}\right) \tag{8.55}$$

$$\Rightarrow \theta = -\arctan\left[\frac{2\sin\left(\varphi(t)/4\right)\cos\left(\varphi(t)/4\right)}{1-2\sin^2\left(\varphi(t)/4\right)}\right] = -\frac{\varphi(t)}{2}. \tag{8.56}$$

By applying the time-periodic boundary condition to $\varphi(t)$ as defined in Eq. (8.53), the corresponding winding number, given by Eq. (8.52), transforms into

$$\mathcal{W} = -\frac{1}{2\pi}\left[\frac{\varphi(t_f)}{2} - \frac{\varphi(t_0)}{2}\right] = -\frac{1}{2\pi}\left[\frac{\varphi(t_0)+2\pi}{2} - \frac{\varphi(t_0)}{2}\right] \tag{8.57}$$

$$\Rightarrow \mathcal{W} = -\frac{\pi}{2\pi}. \tag{8.58}$$

In a closed loop within the parameter space of $f(t)$ and $g(t)$, the dissipative system returns to its original dark space. However, the density matrix transitions to a different dark state because the Bloch vector $\boldsymbol{n}_{\text{odd}}$ evolves according to the dynamics specified as follows,

$$\boldsymbol{n}_{\text{odd}} = \left(\sin\left(\frac{\varphi(t)}{2}\right), 0, \cos\left(\frac{\varphi(t)}{2}\right)\right) \tag{8.59}$$

$$\Rightarrow \begin{cases} \varphi(t_0) = 0,\ \boldsymbol{n}_{\text{odd}}(t = t_0) = (0,0,1)\,, \\ \varphi(t_f) = 2\pi,\ \boldsymbol{n}_{\text{odd}}(t = t_f) = (0,0,-1)\,. \end{cases} \tag{8.60}$$

The braiding operation can be described using a braiding operator or the Pauli-Y gate $B = \sigma_y$, which acts on the Hilbert space spanned by the two dark states: $|\psi_1\rangle$ (8.9) and $|\psi_2\rangle$ (8.10). When the braiding operation is applied, it transforms the steady state of the Majorana sector in the following way.

$$B\left[\boldsymbol{n}_{\text{odd}}(t = t_0)\cdot\boldsymbol{\sigma}\right]B = \boldsymbol{n}_{\text{odd}}(t = t_f)\cdot\boldsymbol{\sigma} \Rightarrow B\sigma_z B = -\sigma_z. \tag{8.61}$$

In this section, we have derived the Lindblad equation for an open system containing three Majorana boxes, using the same approximations as outlined in Table 6.1. The Lindblad equation, given by Eq. (8.38), features additional degrees of freedom in the jump operator, as shown in Eq. (8.37). By applying the braiding-compatible jump operator (8.8) to this Lindblad equation, we find that the steady state, given by Eq. (8.47), is spanned by the dark states $|\psi_1\rangle$ (8.9) and $|\psi_2\rangle$ (8.10). Through adjusting the coherence between these two dark states following Eqs. (8.48) and (8.54)we attain a pure steady state that exhibits chiral symmetry. The Bloch vector, provided in Eq. (8.59), demonstrates non-Abelian braiding, as illustrated through a time-periodic and adiabatic change in the parameter space (see Eq. (8.60)). In the following section, we will illustrate how to achieve the braiding-compatible jump operator in a real tunneling system.

8.3 A potential tunneling system with its corresponding braiding protocol

To implement the braiding-compatible jump operator and the associated stabilization protocol in an open system, we need to recall the general form of the jump operator for a system with three Majorana boxes, as given in Eq. (8.37), which includes contributions from transport through one box (W_{jk}^{n} (8.28)), two boxes ($W_{jk}^{n,n'}$ (8.33)), and three boxes ($W_{jk}^{n,n',n''}$ (8.34)). These contributions are constructed using the Majorana bilinears discussed in Sec. (6.1), which can be represented by the Pauli matrices shown in Eq. (6.20). Here, we define the operator $\mathcal{S}_{abc}$ associated with the Kronecker product of three Pauli matrices.

$$\mathcal{S}_{abc} = \chi_a^1 \otimes \chi_b^2 \otimes \chi_c^3, \text{ and } \chi_a^n = i\gamma_{n\nu}\gamma_{n\mu}, \tag{8.62}$$

where $a, b, c \in \{0, x, y, z\}$ and $n \in \{1, 2, 3\}$. Then, the operators W_{jk}^{n}, $W_{jk}^{n,n'}$ and $W_{jk}^{n,n',n''}$ can be expressed in terms of the operator $\mathcal{S}_{abc}$ as follows,

$$\sum_{n} W_{jk}^{n} = \sum_{\nu\neq\mu} \big(- \underbrace{i\Upsilon_{jk}^{1\nu,1\mu}\mathcal{S}_{a00}}_{W_{jk}^{1}} - \underbrace{i\Upsilon_{jk}^{2\nu,2\mu}\mathcal{S}_{0b0}}_{W_{jk}^{2}} - \underbrace{i\Upsilon_{jk}^{3\nu,3\mu}\mathcal{S}_{00c}}_{W_{jk}^{3}} \big), \tag{8.63}$$

$$\sum_{n\neq n'} W_{jk}^{n,n'} = \sum_{\nu\neq\mu}\sum_{\nu'\neq\mu'} \big(\underbrace{i\tilde{t}_{12}\Upsilon_{jk}^{1\nu,2\mu'}\mathcal{S}_{ab0}}_{W_{jk}^{1,2}} + \underbrace{i\tilde{t}_{13}\Upsilon_{jk}^{1\nu,3\mu'}\mathcal{S}_{a0c}}_{W_{jk}^{1,3}} + \underbrace{i\tilde{t}_{23}\Upsilon_{jk}^{2\nu,3\mu'}\mathcal{S}_{0bc}}_{W_{jk}^{2,3}} \big), \tag{8.64}$$

$$W_{jk}^{1,2,3} = -\sum_{\nu\neq\mu}\sum_{\nu'\neq\mu'}\sum_{\nu''\neq\mu''} i\tilde{t}_{12}\tilde{t}_{23} \left(\sum_{n\neq n'} \Upsilon_{jk}^{n\nu,n'\mu'} \right) \mathcal{S}_{abc}. \tag{8.65}$$

The notation $\Upsilon_{jk}^{n\nu,n'\mu'}$ represents the tunneling parameters of the channel connecting quantum dots and MBSs. To determine $\Upsilon_{jk}^{n\nu,n'\mu'}$, we focus exclusively on the initial and final MBSs involved in the transport process. Specifically, $\Upsilon_{jk}^{n\nu,n'\mu'}$ characterizes the tunneling process where transport enters the Majorana sector at the MBS $\gamma_{n\nu}$ and exits at the MBS $\gamma_{n'\mu'}$, which can be expressed as

$$\Upsilon_{jk}^{n\nu,n'\mu'} = \lambda_{j,n\nu}\lambda_{k,n'\mu'} e^{i(\beta_{j,n\nu}-\beta_{k,n'\mu'})} - \lambda_{j,n'\mu'}\lambda_{k,n\nu} e^{i(\beta_{j,n'\mu'}-\beta_{k,n\nu})}. \tag{8.66}$$

where $\lambda_{j,n\nu}$ and $\beta_{j,n\nu}$ denote the tunneling amplitude and phase, respectively, as explained in Eq. (8.28).

The structure of the jump operator, constituting the operators W^{n}_{jk} (8.63), $W^{n,n'}_{jk}$ (8.64) and $W^{n,n',n''}_{jk}$ (8.65), is actually determined by the operator $\mathcal{S}_{abc}$. For three entangled boxes, there are 4^3 distinct $\mathcal{S}_{abc}$ matrices. However, some of these matrices vanish in the single-parity subspace, requiring the exclusion of these trajectories since braiding does not change the parity of states. Through algebraic manipulations, one can identify a total of 16 associated trajectories in the Majorana sector, with their corresponding $\mathcal{S}_{abc}$ matrices encompassed in the set s as outlined below.

$$\begin{aligned}&\mathcal{S}_{abc} = \chi^1_a \otimes \chi^2_b \otimes \chi^3_c, \\ &\text{where } (a,b,c) \in s, \text{ and } s = \big\{(0,x,x),\ (0,x,y),\ (0,y,x),\ (0,y,y),\\ &\qquad\qquad (x,0,x),\ (x,0,y),\ (x,z,x),\ (x,z,y),\\ &\qquad\qquad (y,0,x),\ (y,0,y),\ (y,z,x),\ (y,z,y),\\ &\qquad\qquad (z,x,x),\ (z,x,y),\ (z,y,x),\ (z,y,y)\big\}.\end{aligned} \tag{8.67}$$

To realize these 16 trajectories, the tunneling system has been constructed as shown in Fig. 8.2. In this tunneling setup, the coherence between the even and odd parity states of the jump operator K_{12} vanishes, as demonstrated by Eq. (8.4). We can therefore focus exclusively on the odd-parity block when the initial state of the Majorana sector, ρ_M, is spanned in the odd-parity subspace.

We denote the odd-parity block of the jump operator as $\tilde{K}_{\text{odd}}$. In the tunneling system illustrated in Fig. 8.2, the jump operator, which governs the dynamics from QD1 to QD2, can be divided into a set of components $\{\tilde{K}^{n\nu}_{\text{odd}}\}$. The superscript in $\tilde{K}^{n\nu}_{\text{odd}}$ corresponds to the MBSs $\gamma_{n\nu}$. This notation indicates that the component $\tilde{K}^{n\nu}_{\text{odd}}$ within the jump operator $\tilde{K}_{\text{odd}}$ is responsible for the transport dynamics initiated by the MBS $\gamma_{n\nu}$. Since there are four MBSs directly coupled to QD1, we need to consider four components which are $\tilde{K}^{11}_{\text{odd}}$, $\tilde{K}^{12}_{\text{odd}}$, $\tilde{K}^{21}_{\text{odd}}$, and $\tilde{K}^{22}_{\text{odd}}$. To compute these components, one can visualize their transport using a tree diagram. For example, the possible trajectories from the MBS γ_{11} to the MBSs coupled to QD2 are illustrated in the following tree diagram.

$$\begin{array}{lllll} & \gamma_{13} & \xrightarrow{t_{12}} \gamma_{24}\gamma_{23} & \xrightarrow{t_{23}} \gamma_{31} & \nearrow \gamma_{33} \\ \gamma_{11} & \nearrow & & & \searrow \gamma_{34} \\ & \gamma_{14} & \xrightarrow{t_{13}} \gamma_{32} & \nearrow \gamma_{33} & \\ & & & \searrow \gamma_{34} & \end{array} \tag{8.68}$$

As illustrated in the tree diagram 8.68, the component $\tilde{K}^{11}_{\text{odd}}$ can be expressed in terms

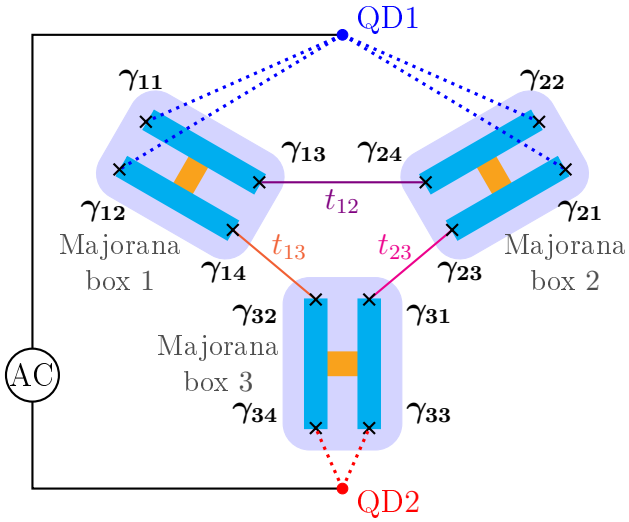

Figure 8.2: The setup involves three Majorana boxes interconnected by tunneling amplitudes t_{12}, t_{13} and t_{23}, with Majorana operators $\gamma_{n\mu}$ representing the MBS μ in the box n. Two quantum dots (QD1 and QD2) are tunnel-coupled to these MBSs. The quantum dots, driving field, and environment mirror those in a single Majorana box setup shown in Fig. 7.2. These tunneling couplings are engineered to achieve the jump operator in Eq. (8.8), with odd-parity dark states depending on parameters f and g as shown in Eqs. (8.9)-(8.10).

of the operators $W_{jk}^{n,n'}$ (8.64) and $W_{jk}^{n,n',n''}$ (8.65).

$$\tilde{K}_{\text{odd}}^{11} = W_{12}^{1,3} + W_{12}^{1,2,3} \tag{8.69}$$

$$\begin{aligned} \Rightarrow \tilde{K}_{\text{odd}}^{11} = \Big[& \lambda_{2,33} e^{i\beta_{2,33}} \left(i\tilde{t}_{12}\tilde{t}_{23}\mathcal{S}_{xzx}^{\text{odd}} + i\tilde{t}_{13}\mathcal{S}_{y0y}^{\text{odd}} \right) \\ & + \lambda_{2,34} e^{i\beta_{2,34}} \left(i\tilde{t}_{12}\tilde{t}_{23}\mathcal{S}_{xzy}^{\text{odd}} - i\tilde{t}_{13}\mathcal{S}_{y0x}^{\text{odd}} \right) \Big] \lambda_{1,11} e^{-i\beta_{1,11}}, \end{aligned} \tag{8.70}$$

where $\mathcal{S}_{abc}^{\text{odd}}$ denotes the component of $\mathcal{S}_{abc}$ (8.62) that has odd parity. Using the same

method, we can express the remaining contributions in the jump operator $\tilde{K}_{\text{odd}}$ as follows,

$$\tilde{K}^{12}_{\text{odd}} = \Big[\lambda_{2,33}e^{i\beta_{2,33}}\left(-i\tilde{t}_{12}\tilde{t}_{23}\mathcal{S}^{\text{odd}}_{yzx} + i\tilde{t}_{13}\mathcal{S}^{\text{odd}}_{x0y}\right) \\ -\lambda_{2,34}e^{i\beta_{2,34}}\left(i\tilde{t}_{12}\tilde{t}_{23}\mathcal{S}^{\text{odd}}_{yzy} + i\tilde{t}_{13}\mathcal{S}^{\text{odd}}_{x0x}\right)\Big]\lambda_{1,12}e^{-i\beta_{1,12}}, \tag{8.71}$$

$$\tilde{K}^{21}_{\text{odd}} = \Big[\lambda_{2,33}e^{i\beta_{2,33}}\left(-i\tilde{t}_{23}\mathcal{S}^{\text{odd}}_{0xx} + i\tilde{t}_{12}\tilde{t}_{13}\mathcal{S}^{\text{odd}}_{zyy}\right) \\ -\lambda_{2,34}e^{i\beta_{2,34}}\left(i\tilde{t}_{23}\mathcal{S}^{\text{odd}}_{0xy} + i\tilde{t}_{12}\tilde{t}_{13}\mathcal{S}^{\text{odd}}_{zyx}\right)\Big]\lambda_{1,21}e^{-i\beta_{1,21}}, \tag{8.72}$$

$$\tilde{K}^{22}_{\text{odd}} = \Big[\lambda_{2,33}e^{i\beta_{2,33}}\left(i\tilde{t}_{23}\mathcal{S}^{\text{odd}}_{0yx} + i\tilde{t}_{12}\tilde{t}_{13}\mathcal{S}^{\text{odd}}_{zxy}\right) \\ +\lambda_{2,34}e^{i\beta_{2,34}}\left(i\tilde{t}_{23}\mathcal{S}^{\text{odd}}_{0yy} - i\tilde{t}_{12}\tilde{t}_{13}\mathcal{S}^{\text{odd}}_{zxx}\right)\Big]\lambda_{1,22}e^{-i\beta_{1,22}}. \tag{8.73}$$

To obtain the jump operator, $\tilde{K}$odd, we sum these components: $\tilde{K}_{\text{odd}} = \tilde{K}^{11}_{\text{odd}} + \tilde{K}^{12}_{\text{odd}} + \tilde{K}^{21}_{\text{odd}} + \tilde{K}^{22}_{\text{odd}}$.

To ensure that $\tilde{K}_{\text{odd}}$ has the same structure as the braiding-compatible jump operator described in Eq. (8.8), we need to define certain tunneling parameters appropriately. To begin with, the phases of tunneling are defined as follows,

$$\beta_{1,11} = \beta_{2,33} + \frac{\pi}{2}, \qquad \beta_{1,12} = \beta_{2,33} + \pi, \\ \beta_{1,21} = \beta_{2,33} - \frac{\pi}{2}, \qquad \beta_{1,22} = \beta_{2,33} + \pi, \qquad \beta_{2,34} = \beta_{2,33} + \frac{\pi}{2}. \tag{8.74}$$

The tunneling amplitudes between the Majorana boxes are given by $t_{12} = (t_{13}+t_{23})/(t_{13}-t_{23})$ for $t_{13} > t_{23}$. Introducing new notations for the tunneling amplitudes,

$$\lambda_{1,1\pm} = \lambda_{1,12} \pm \lambda_{1,11}, \qquad \lambda_{1,2\pm} = \lambda_{1,21} \pm \lambda_{1,22}, \qquad \lambda_{2,3\pm} = \lambda_{2,33} \pm \lambda_{2,34}, \tag{8.75}$$

the jump operator takes the form

$$\tilde{K}_{\text{odd}} = \frac{t_{13}^2 + t_{23}^2}{t_{23} - t_{13}} \begin{pmatrix} 0 & \lambda_{1,2-}\lambda_{2,3-} & -\lambda_{1,1+}\lambda_{2,3-} & 0 \\ \lambda_{1,2+}\lambda_{2,3+} & 0 & 0 & \lambda_{1,1+}\lambda_{2,3+} \\ \lambda_{1,1-}\lambda_{2,3+} & 0 & 0 & \lambda_{1,2-}\lambda_{2,3+} \\ 0 & -\lambda_{1,1-}\lambda_{2,3-} & \lambda_{1,2+}\lambda_{2,3-} & 0 \end{pmatrix}. \tag{8.76}$$

To obtain the structure of the braiding-compatible jump operator (8.8), the final key factor for the tunneling amplitudes is

$$\lambda_{1,1+}\lambda_{1,1-} = \lambda_{1,2+}\lambda_{1,2-} \Leftrightarrow \lambda^2_{1,12} - \lambda^2_{1,11} = \lambda^2_{1,21} - \lambda^2_{1,22}. \tag{8.77}$$

To simplify notation, we introduce the following symbols

$$\tilde{f} = \frac{\lambda_{1,1+}}{\lambda_{1,2-}} = \frac{\lambda_{1,2+}}{\lambda_{1,1-}}, \qquad \tilde{g} = \frac{\lambda_{1,2-}}{\lambda_{1,1-}} = \frac{\lambda_{1,1+}}{\lambda_{1,2+}}, \tag{8.78}$$

which allow the jump operator (8.76) to be expressed as

$$\tilde{K}_{odd} = \Lambda \begin{pmatrix} 0 & \tilde{g}\lambda_{2,3-} & -\tilde{f}\tilde{g}\lambda_{2,3-} & 0 \\ \tilde{f}\lambda_{2,3+} & 0 & 0 & \tilde{f}\tilde{g}\lambda_{2,3+} \\ \lambda_{2,3+} & 0 & 0 & \tilde{g}\lambda_{2,3+} \\ 0 & -\lambda_{2,3-} & \tilde{f}\lambda_{2,3-} & 0 \end{pmatrix}, \tag{8.79}$$

with $\Lambda = \lambda_{1,1-}(t_{13}^2 + t_{23}^2)/(t_{23} - t_{13})$. Given the definitions

$$\tilde{f}_1 = \tilde{g}\lambda_{2,3-}, \qquad \tilde{f}_2 = -\lambda_{2,3-}, \qquad \tilde{g}_1 = \tilde{f}\lambda_{2,3+}, \qquad \tilde{g}_2 = \lambda_{2,3+}, \tag{8.80}$$

the jump operator $\tilde{K}_{\text{odd}}$ as defined in Eq. (8.79) can be expressed in the form of the braiding-compatible jump operator (8.8). As expected, the dark states of $\tilde{K}_{\text{odd}}$ (8.79), denoted as $|\tilde{\psi}_1\rangle$ and $|\tilde{\psi}_2\rangle$, are given by $|\psi_1\rangle$ (8.9) and $|\psi_2\rangle$ (8.10).

$$|\tilde{\psi}_1\rangle = \tilde{N}_1 \left(-\tilde{g}|001\rangle + |111\rangle\right) = \tilde{N}_1 \left(\frac{\lambda_{1,22} - \lambda_{1,21}}{\lambda_{1,12} - \lambda_{1,11}}|001\rangle + |111\rangle\right), \tag{8.81}$$

$$|\tilde{\psi}_2\rangle = \tilde{N}_2 \left(\tilde{f}|010\rangle + |100\rangle\right) = \tilde{N}_2 \left(\frac{\lambda_{1,21} + \lambda_{1,22}}{\lambda_{1,12} - \lambda_{1,11}}|010\rangle + |100\rangle\right). \tag{8.82}$$

In a manner analogous to the formulae for the other two eigenstates given in Eq. (8.12), it can be shown that the remaining two eigenstates, denoted $|\tilde{\psi}_\pm\rangle$, of the operator $\tilde{K}_{\text{odd}}$ (8.79) coalesce into a null vector in this scenario.

The choice of tunneling parameters specified by Eqs. (8.74) and (8.77) ensures that the jump operator produces two parameter-dependent dark states within the odd-parity subspace. However, the tunneling system must avoid two specific conditions: $\lambda_{2,3+} = 0$ and $\lambda_{2,3-} = 0$. This means that the tunneling amplitudes involving QD2 should neither be in phase, $\lambda_{2,33} = \lambda_{2,34}$, nor exactly out of phase, $\lambda_{2,33} = -\lambda_{2,34}$. When $\lambda_{2,3\pm}$ is zero, the dark subspace would contain only one parameter-dependent dark state, which cannot support a braiding transformation. Therefore, we vary the tunneling amplitudes $\lambda_{1,2\pm}$ adiabatically while keeping $\lambda_{2,3\pm}$ as non-zero constants during the braiding process.

8.3.1 Braiding operations

In a manner comparable to the general scenario discussed in Sec. 8.2.2, the Lindblad dissipator associated with the jump operator $\tilde{K}_{\text{odd}}$ (8.79) drives the system to a steady

state spanned by the dark states $|\tilde{\psi}_1\rangle$ (8.81) and $|\tilde{\psi}_2\rangle$ (8.82). These dark states are dependent on the tunneling parameters. During the braiding operation, the parameters $\lambda_{1,2\pm}$ are varied adiabatically, which in turn causes the parameters $\lambda_{1,1\pm}$ to adjust according to the relationship given in Eq. (8.77). Considering the time-periodic boundary conditions from t_0 to t_f, we establish polar coordinate systems for the tunnel amplitudes.

$$\lambda_{1,2-}(t) = r_2 \sin[\theta_2(t)], \qquad \lambda_{1,2+}(t) = r_2 \cos[\theta_2(t)]; \tag{8.83}$$

$$\lambda_{1,1-}(t) = r_1 \cos[\theta_1(t)], \qquad \lambda_{1,1+}(t) = r_1 \sin[\theta_1(t)], \tag{8.84}$$

where time-periodic boundary condition is given by $\theta_l(t_f) = \theta_l(t_0) + 2\pi$ for $l \in \{1, 2\}$. This implies that the equation $r_2^2 \cos(\theta_2)\sin(\theta_2) \equiv r_1^2 \cos(\theta_1)\sin(\theta_1)$ must be satisfied according to Eq. (8.77).

As outlined in Sec. 8.2.2, the pure steady state, denoted as $\tilde{\rho}_{\text{odd}}$, in this context is represented by ρ_{odd} as given in Eq. (8.49). Similarly, the function $F(f, g)$, as described in Eq. (8.54) for the steady state ρ_{odd}, is translated into a corresponding function $\tilde{F}$ to ensure that the steady state $\tilde{\rho}_{\text{odd}}$ remains a pure state with topological order. Specifically, $\tilde{F}$ is derived from $F(f, g)$ according to the translation process outlined.

$$\tilde{F}(\lambda_{1,21}, \lambda_{1,22}) = \sin\left[\frac{1}{4}\sin^{-1}\left(\frac{\lambda_{1,21} - \lambda_{1,22}}{\sqrt{2\lambda_{1,21}^2 + 2\lambda_{1,22}^2}}\right)\right]. \tag{8.85}$$

In the polar coordinate systems defined by Eq. (8.83)-(8.84), the function $\tilde{F}$ can be expressed as

$$\tilde{F}(\theta_2) = \sin(\theta_2/4). \tag{8.86}$$

Referring to the Bloch vector $\boldsymbol{n}_{\text{odd}}$ from Eq. (8.50), we find that in this context the Bloch vector is given by

$$\tilde{\boldsymbol{n}}_{\text{odd}} = \left(\sin\frac{\theta_2}{2}, 0, \cos\frac{\theta_2}{2}\right). \tag{8.87}$$

This shows that the Bloch vector is parametrized by θ_2, indicating that its behavior depends on θ_2 rather than on time t. Consequently, the steady state described by this Bloch vector transitions from $|\tilde{\psi}_2\rangle$ to $|\tilde{\psi}_1\rangle$ after the parameters are varied over one cycle: $\theta_2(t_f) = \theta(t_0) + 2\pi$. This process gives rise to the braiding operator $B = \sigma_y$ as detailed in Eq. (8.61).

In Fig. 8.3, we provide a numerical example where $r_1 = 2r_2$ and $\theta_1(t) = \theta_2(t)$, with θ varying linearly with time. This figure illustrates the trajectory of the Bloch vector alongside the periodic changes in the parameters. The rotation of the Bloch vector corresponds to the braiding illustrated in the dark space, as shown in Fig. 8.1.

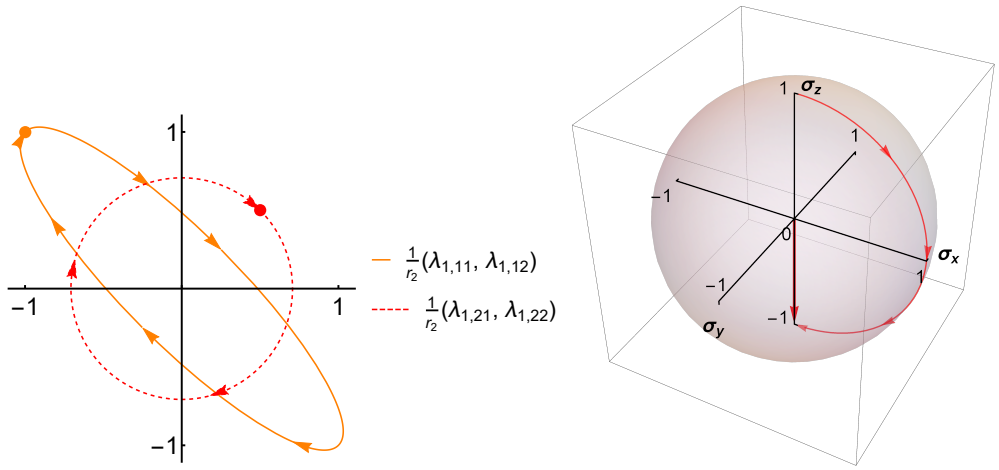

Figure 8.3: The left diagram shows how tunneling amplitudes change as θ_2 varies from 0 to 2π with $r_1 = 2r_2$ and $\theta_1(t) = \theta_2(t)$ in Eqs. (8.83)-(8.84). The solid dots mark the initial and final parameter values in the cyclic adiabatic evolution. The right diagram depicts the rotation of the Bloch vector $\tilde{\boldsymbol{n}}_{\text{odd}}$ (8.87).

8.4 Summary

To summarize this chapter, we first established that the braiding operation, as shown in Fig. 8.1, requires a minimum of three Majorana boxes. These boxes collectively form an open quantum system that can potentially possess two parameter-dependent dark states with the same parity. In Sec. 8.1, we introduced the braiding-compatible jump operator (8.8), which includes two dark states (8.9) - (8.10) within the odd-parity subspace. According to the Lindblad equation with this jump operator, the dissipation should drive the Majorana sector into a state within the subspace spanned exclusively by these two dark states, as shown in Eq. (8.47).

To maintain chiral symmetry in the steady state, the function $F(f, g)$ in Eq. (8.47) must be real and satisfy $F \in [-1,\ 1]$. The presence of chiral symmetry leads to topological order in the steady state, characterized by the Bloch vector (8.50) described in Sec. 8.2.2. As anticipated, this topological order is captured by the invariant $\mathcal{W}$ given in Eq. (8.52). When the function F is specified as in Eq. (8.54), the steady state exhibits a non-trivial transformation as the parameters vary along a periodic circle. This transformation is detailed by Eq. (8.60) and corresponds to the non-Abelian braiding illustrated in Fig. 8.1.

For a system involving three Majorana boxes, the Lindblad equation governing the Majorana sector can be expressed in terms of the jump operator shown in Eq. (8.37).

To achieve the structure of the braiding-compatible jump operator given in Eq. (8.8), we constructed the tunneling system depicted in Fig. 8.2. Although other tunneling systems could also realize the braiding-compatible jump operator, the configuration shown in Fig 8.2 is the simplest one that achieves the desired form of the jump operator. By appropriately selecting the tunneling parameters, as described in Eqs. (8.74) and (8.77), the setup depicted in Fig. 8.2 can yield the jump operator (8.79). This jump operator produces two odd-parity dark states, which are parameter-dependent and are given in Eqs. (8.81) and (8.82). However, it is crucial to avoid having in-phase or opposite-phase tunneling amplitudes between QD2 and MBSs, i.e., $\lambda_{2,33} \neq \pm\lambda_{2,34}$. If these conditions are not met, braiding in the corresponding dark space will not be feasible.

For the tunnel amplitudes, their periodic variation is described by sinusoidal functions in polar coordinates, as shown in Eqs. (8.83) and (8.84). When the tunneling amplitude varies with a linearly time-dependent angle $\theta_{1,2}$, the Bloch vector, according to Eq. (8.87), traces out a semicircle. This behavior is shown in Fig. 8.3, which confirms the expected pattern. However, the performance of the Bloch vector is independent of the specific time-dependent functions, $\theta_1(t)$ and $\theta_2(t)$, used in the adiabatic and time-periodic change of parameters.

There are several forms of jump operators compatible with braiding. We specifically use the form given in Eq. (8.8) because it is relatively straightforward to implement in practical tunneling systems. Braiding can also be achieved using different sets of braiding operators, depending on how the parameters F and $\alpha_{1,2}$ are defined in Eq. (8.47). These parameters represent the coherence between two dark states in the steady state. To achieve non-Abelian braiding in the dark space, we generally need to adhere to the requirements summarized in Fig. 8.1, which outline the conditions necessary for successful non-Abelian braiding in this context. In the context of open systems, the ability to freely adjust tunneling parameters allows for adiabatic changes along closed loops in parameter space. This adiabatic evolution ensures that the resulting braiding transformation is topological, reflecting the robustness and stability of the braiding process in the reduced parameter space.

Chapter 9

Conclusions

In revisiting the goals set out at the beginning of this research, the study has met its objectives and contributed to two areas: quantum friction and topological quantum computing. The results are not only consistent with previous research but also offer new insights from different perspectives. Moreover, the theoretical findings have a strong potential to influence future research on observing quantum friction and advancing the implementation of quantum computers. Both areas are of great importance, especially as people are relentlessly working to create functional quantum chips.

9.1 Quantum friction between metals in the hydrodynamic regime

This study on quantum friction investigates how the frictional force is affected by the dispersion of materials, focusing on the impact of their frequency-dependent dielectric properties. The dispersion relation is a key characteristic of the hydrodynamic model, with the sound speed serving as a critical parameter that describes how excitations propagate within the medium. By integrating recent developments in the field [40–42] with established studies of the electric hydrodynamic model, we can demonstrate that the hydrodynamic regime in conductors, such as graphene, can be realized when electron-electron interactions are the dominant factor.

In this study, we revisited the electric hydrodynamic model discussed in Barton's review [39] and incorporated this model into the calculation of quantum friction using time-dependent perturbation theory [25]. The quantum friction system involves a single atom moving parallel to the interface of a metallic substrate. When the dipole moment d is sufficiently small to be treated as a perturbative constant, time-dependent perturbation theory is applicable. As a result, we derived the frictional force as a series of terms in perturbative order.

In the analytic derivation of the second-order and fourth-order forces, we have examined the dispersion relation, which leads to a Heaviside step function and modifies the delta function that enforces energy conservation in these forces. Consequently, we have found that the speed of sound acts as the threshold velocity for the frictional force at each order of perturbation. This enlightens our understanding of how frictional force arises. It suggests that there is a mirror image of the atom in the substrate within a vacuum. The speed of sound represents the maximum speed at which this mirror image can propagate through the substrate. When the atom moves faster than the speed of sound, the mirror image cannot align vertically with the moving atom at the interface, leading to a frictional force due to the misalignment between the real atom and its image in the substrate.

Our numerical results indicate that dispersion significantly affects the frictional force when the atom moves at relatively low velocities, which is consistent with the claim made in Ref. [33]. Additionally, within appropriate ranges of relevant parameters, such as plasma frequency and Bohr transition frequency, the effects arising from the dispersion relation become negligible when the atom's velocity exceeds ten times the speed of sound. This will be important for future studies, as the dispersion effect reduces the magnitude of the frictional force.

Overall, this study enhances our understanding of quantum friction, particularly within the framework of electronic hydrodynamic models that account for significant dispersion effects. While quantum friction remains a debatable topic, it is an active area of research with promising potential for experimental observation. This frictional force is expected to be especially significant at scales approaching the nanometer or smaller. Furthermore, the dissipation associated with quantum friction can be beneficial in certain occasions.

9.2 Braiding protocols in the dissipative-driven Majorana boxes

In this work, we explore the possibility of implementing braiding operations in dissipative-driven Majorana boxes. These boxes are connected to quantum dots positioned in a bosonic environment. Rather than performing non-Abelian braiding within the manifold of ground states, we propose conducting the topological braiding operation in the context of open systems within a "dark space". This dark space is composed of dark states that are immune to environmental interactions and resist decay.

Due to the constraints imposed by topological braiding, the dark space must always contain *multiple* dark states that share the *same parity* and are dependent on system parameters. These dark states are the eigenstates of the jump operator with zero eigenvalues. By adiabatically tuning certain parameters, it is possible to manipulate quantum states within the Majorana sector, allowing for braiding operations within this

dark space. Although it might seem intuitive that two Majorana boxes would suffice to construct such a dark space, the Lindblad equation, as a CPTP map, imposes limitations on the structure of the jump operators that prevent the possibility of braiding with just two Majorana boxes. The limitations of a CPTP map ensure that certain non-physical behaviors are prevented.

To address the constraints of both topological braiding and the CPTP map, we decided to extend the degrees of freedom in the Majorana sector by adding additional Majorana boxes. In the analysis of the open system composed of three boxes, a braiding-compatible jump operator was first identified, which has two orthonormal odd-parity dark states as its eigenstates. These eigenstates are influenced by the tunneling amplitude between the Majorana boxes and quantum dots. Subsequently, a tunneling system was constructed to approach the braiding-compatible jump operator by adjusting certain parameters. Ultimately, a "braiding rehearsal" was conducted in which the relevant tunneling amplitudes were modulated by sinusoidal functions to satisfy the time-periodic boundary condition.

In the braiding protocols demonstrated in this work, the Majorana sector was driven to a steady state as a superposition of orthonormal dark states in the odd-parity subspace, given that the system was initially set up in a state with odd parity. To determine the constraints arising from chiral symmetry, which can be a characteristic of certain topologically ordered phases, we expressed the steady state spanned by the dark states in Bloch form through a unitary transformation. As stated in Ref. [110], the geometry of the Bloch sphere indicates that chiral symmetry confines the winding of the Bloch vector to a unit circle. To satisfy this additional constraint, specific parameters of the system must be adjusted to particular symmetric values. However, the remaining available parameters still permit an adiabatic change along closed loops in the parameter space. Consequently, the resulting braiding transformation is topological within this reduced parameter space.

This study demonstrated one of the simplest methods for performing topological braiding operations in dissipative-driven Majorana boxes. While we focused on a system of three Majorana boxes, it is important to note that multiple braiding-compatible jump operators exist. Additionally, there are various tunneling systems and braiding protocols that can be explored. The primary aim of this research was to confirm the feasibility of braiding implementations within the Majorana open system and to provide a comprehensive guideline for constructing a braiding-compatible jump operator along with its associated braiding protocols in the tunneling system.

In contrast to braiding operations performed in real space, braiding in the dark space can be implemented simply by adiabatically adjusting the tunneling amplitudes, without the need for the more complex processes required in quantum mechanics. This

approach appears more feasible in practice, but it requires AC driving and damping from the electromagnetic environment, necessitating adjustments to the current experimental platforms. Once a functional platform has been established to efficiently manage the Majorana boxes within this damping system, this work will provide a clear guideline for performing braiding operations in the dark space. The implications of this research extend beyond theoretical constructs, suggesting practical pathways for developing robust quantum computing systems.

Acknowledgments

I would like to express my heartfelt gratitude to all those who have supported me throughout my journey to completing this thesis. First and foremost, I wish to thank my supervisors, Prof. Dr. Thomas L. Schmidt and Dr. M. Belén Farias, for their invaluable guidance, patience, and encouragement during the research process. Their insightful feedback and unwavering support have been instrumental in shaping this work. I am grateful for the support of my colleagues in the research group: Theory of Mesoscopic Quantum Systems, who provided a collaborative and stimulating environment. Special thanks to Sadeq S. Kadijani and Johan Ekström for their assistance and insightful discussions. I also appreciate the support and friendship of the other members of the group throughout this process

I would like to acknowledge the financial support from the National Research Fund Luxembourg under grant C18/MS/12704391/QUTHERM, which made this research possible. Additionally, I am thankful for the resources provided by the University of Luxembourg that facilitated my work. I also wish to thank the large language models, OpenAI and Kimi.ai, for their valuable suggestions on language corrections in this literature. Finally, I would like to dedicate this thesis to my research group and university, whose inspiration and support have been invaluable to me.

Appendix A Normalizing constants of the surface and bulk modes in the HD regime

In field theory, the commutator of the normalized Φ in both modes and the canonical form's first element yields the following formulas.

$$\left[\Phi_s(\boldsymbol{r}), \Pi_s^0(\boldsymbol{r}')\right] = i\delta(\boldsymbol{r}-\boldsymbol{r}') \tag{A.1}$$
$$\left[\Phi_b(\boldsymbol{r}), \Pi_b^0(\boldsymbol{r}')\right] = i\delta(\boldsymbol{r}-\boldsymbol{r}'), \tag{A.2}$$

where $\Pi_s^0 = \partial\Phi_s/\partial t$, as well as in the bulk modes.

$$\Pi_s^0 = \frac{m}{e} N_k \int d\boldsymbol{k}\; i\Omega_s\; e^{i\boldsymbol{k}\cdot\boldsymbol{r}-kz-i\Omega_s t} a_{\boldsymbol{k}} (\Omega_s^2 p_s - \omega_p^2 k) + h.c.. \tag{A.3}$$

Thus, one can obtain

$$\Phi_s\Pi_s^0 = \frac{m^2 N_k^2}{e^2} \int d\boldsymbol{k}\; i\Omega_s\; (\Omega_s^2 p_s - \omega_p^2 k)^2 \left(a_{\boldsymbol{k}} a_{\boldsymbol{k}}^\dagger e^{i\boldsymbol{k}\cdot(\boldsymbol{r}-\boldsymbol{r}')} - a_{\boldsymbol{k}}^\dagger a_{\boldsymbol{k}} e^{i\boldsymbol{k}\cdot(\boldsymbol{r}'-\boldsymbol{r})}\right) \tag{A.4}$$
$$\Pi_s^0\Phi_s = \frac{m^2 N_k^2}{e^2} \int d\boldsymbol{k}\; i\Omega_s\; (\Omega_s^2 p_s - \omega_p^2 k)^2 \left(a_{\boldsymbol{k}}^\dagger a_{\boldsymbol{k}} e^{i\boldsymbol{k}\cdot(\boldsymbol{r}-\boldsymbol{r}')} - a_{\boldsymbol{k}} a_{\boldsymbol{k}}^\dagger e^{i\boldsymbol{k}\cdot(\boldsymbol{r}'-\boldsymbol{r})}\right). \tag{A.5}$$

Straightforwardly, we can determine the commutation of normalized fields in surface modes.

$$\Phi_s\Pi_s^0 - \Pi_s^0\Phi_s = \frac{m^2 N_k^2}{e^2} \int d\boldsymbol{k}\; i\Omega_s\; (\Omega_s^2 p_s - \omega_p^2 k)^2 \left(e^{i\boldsymbol{k}\cdot(\boldsymbol{r}-\boldsymbol{r}')} + e^{i\boldsymbol{k}\cdot(\boldsymbol{r}'-\boldsymbol{r})}\right) \left(a_{\boldsymbol{k}} a_{\boldsymbol{k}}^\dagger - a_{\boldsymbol{k}}^\dagger a_{\boldsymbol{k}}\right). \tag{A.6}$$

This formula should turn into $i\delta(\boldsymbol{r}-\boldsymbol{r}')$ which can be written as

$$i\delta(\boldsymbol{r}-\boldsymbol{r}') = i \int d\boldsymbol{k}\; e^{i\boldsymbol{k}\cdot(\boldsymbol{r}-\boldsymbol{r}')}. \tag{A.7}$$

To satisfy $\left[\Phi_s(\boldsymbol{r}), \Pi_s^0(\boldsymbol{r}')\right] \equiv i\delta(\boldsymbol{r}-\boldsymbol{r}')$, the normalizing constant becomes:

$$N_k^2 = \frac{\omega_p^2(2\Omega_s^2-\omega_p^2)^2}{16\pi^2 mn\Omega_s k^3(\omega_p^2+2\Omega_s^2)(\Omega_s^2-\omega_p^2)^2}. \tag{A.8}$$

With the same procedures, the normalizing constant of the bulk mode is also obtained.

$$M_k^2 = \frac{\beta^4 p_b^2(2\Omega_b^2-\omega_p^2)^2}{4\pi^3 mn\Omega_b(\Omega_b^2-\omega_p^2)^2((2\Omega_b^2-\omega_p^2)^2-4\beta^2k^2\Omega_b^2)}. \tag{A.9}$$

Appendix B Perturbative coefficients

B.1 The second perturbative order coefficients

Here we derive the perturbative coefficients from $b_0^{(2)}$ and $b_2^{(2)}$ in Eqs. (3.38)-(3.39) to obtain the exact state function.

$$b_0^{(2)} = \mathcal{F}_{01}^{(1)} = -i \int_{-\infty}^{t} ds\ W_{01} b_1^{(1)}(s) e^{i\omega_{01} s}, \tag{B.1}$$

$$b_2^{(2)} = \mathcal{F}_{21}^{(1)} = -i \int_{-\infty}^{t} ds\ W_{21} b_1^{(1)}(s) e^{i\omega_{21} s}. \tag{B.2}$$

Starting with the relatively easier one, $b_0^{(2)}$, because $W(t) = V(t)/d$ is a Hermitian operator, we can obtain $W_{01} = (W_{10})^*$ from W_{10} in Eq. (3.35).

$$W_{01}(t) = i \left(\boldsymbol{\eta} \cdot \vec{k}\right) \phi_k e^{-kz} e^{-i(\omega'(k)+\omega_b)t}. \tag{B.3}$$

Combining the expression for $b_1^{(1)}$ in Eq. (3.37), we can obtain the integral in $b_0^{(2)}$ as follows

$$b_0^{(2)} = \mathcal{F}_{01}^{(1)} = i \sum_{\boldsymbol{\eta}} \int d\boldsymbol{k} \frac{|\boldsymbol{\eta} \cdot \vec{k}|^2 \phi_k^2 e^{-2kz}}{\omega'(k) + \omega_b - i\delta^+} \int_{-\infty}^{t} ds\ e^{\delta^+ s} \tag{B.4}$$

To calculate $b_2^{(2)}$, we firstly derive W_{21} from the operator $V(t)$ in Eq. (3.6).

$$W_{21}(t) = \frac{1}{d} \langle \mathrm{g}, \boldsymbol{k}_1 \boldsymbol{k}_2 | V(t) | \boldsymbol{\eta}, \boldsymbol{k} \rangle \tag{B.5}$$

$$= \frac{1}{d} \int d\boldsymbol{k}'\ \langle \mathrm{g} | \boldsymbol{D}(t) | \boldsymbol{\eta} \rangle \cdot \left(i\vec{k}'\right)^* e^{i\omega'(k')t - k'z} \phi_{k'} \langle \boldsymbol{k}_1 \boldsymbol{k}_2 | a_{\boldsymbol{k}'}^\dagger | \boldsymbol{k} \rangle \tag{B.6}$$

$$= -i \int d\boldsymbol{k}'\ e^{i(\omega'(k') - \omega_b)t - k'z} \left(\boldsymbol{\eta} \cdot \vec{k}'\right)^* \phi_{k'} \langle \boldsymbol{k}_1 \boldsymbol{k}_2 | a_{\boldsymbol{k}'}^\dagger | \boldsymbol{k} \rangle. \tag{B.7}$$

To find the expectation of the bosonic sector, one can apply the Wick theorem which leads to

$$\langle \boldsymbol{k}_1 \boldsymbol{k}_2 | a^\dagger_{\boldsymbol{k}'} | \boldsymbol{k} \rangle = \langle a_{\boldsymbol{k}_1} a_{\boldsymbol{k}_2} a^\dagger_{\boldsymbol{k}'} a^\dagger_{\boldsymbol{k}} \rangle_{\text{vac}} \tag{B.8}$$

$$= \langle a_{\boldsymbol{k}_1} a^\dagger_{\boldsymbol{k}'} \rangle \langle a_{\boldsymbol{k}_2} a^\dagger_{\boldsymbol{k}} \rangle + \langle a_{\boldsymbol{k}_1} a^\dagger_{\boldsymbol{k}} \rangle \langle a_{\boldsymbol{k}_2} a^\dagger_{\boldsymbol{k}'} \rangle \tag{B.9}$$

$$= \delta(\boldsymbol{k}_1 - \boldsymbol{k}')\delta(\boldsymbol{k}_2 - \boldsymbol{k}) + \delta(\boldsymbol{k}_1 - \boldsymbol{k})\delta(\boldsymbol{k}_2 - \boldsymbol{k}'). \tag{B.10}$$

Thus, the element $W_{21}(t)$ becomes

$$W_{21}(t) = -i \int d\boldsymbol{k}' \; e^{i(\omega'(k') - \omega_b)t - k'z} \left(\boldsymbol{\eta} \cdot \vec{k}' \right)^* \phi_k \tag{B.11}$$

$$\times \delta(\boldsymbol{k}_1 - \boldsymbol{k}')\delta(\boldsymbol{k}_2 - \boldsymbol{k}) + \delta(\boldsymbol{k}_1 - \boldsymbol{k})\delta(\boldsymbol{k}_2 - \boldsymbol{k}')$$

$$W_{21}(t) = -i \left(e^{i(\omega'(k_1) - \omega_b)t - k_1 z} \left(\boldsymbol{\eta} \cdot \vec{k}_1 \right)^* \phi_{k_1} \delta(\boldsymbol{k}_2 - \boldsymbol{k}) + \{k_1 \leftrightarrow k_2\} \right), \tag{B.12}$$

where $\{k_1 \leftrightarrow k_2\}$ represents the same formalism but exchanging the momenta k_1 and k_2. Then, one can use the equations of W_{21} and $b_1^{(1)}$ to obtain the expression for $b_2^{(2)}$.

$$b_2^{(2)} = -i \int_{-\infty}^{t} ds \; W_{21} b_1^{(1)}(s) e^{i\omega_{21} s} \tag{B.13}$$

$$= -ie^{-k_1 z - k_2 z} \left(\vec{k}_2 \cdot \vec{k}_1 \right)^* \phi_{k_1} \phi_{k_2} \int_{-\infty}^{t} ds \; \left(\frac{e^{i(\omega'(k_1) + \omega'(k_2) - i\delta^+)s}}{\omega'(k_2) + \omega_b - i\delta^+} + \{k_1 \leftrightarrow k_2\} \right) \tag{B.14}$$

$$b_2^{(2)} = -\frac{e^{-k_1 z - k_2 z} \left(\vec{k}_2 \cdot \vec{k}_1 \right)^* \phi_{k_1} \phi_{k_2}}{\omega'(k_1) + \omega'(k_2) - i\delta^+} \left(\frac{e^{i(\omega'(k_1) + \omega'(k_2))t}}{\omega'(k_2) + \omega_b - i\delta^+} + \{k_1 \leftrightarrow k_2\} \right). \tag{B.15}$$

In the Sec. 3.2, the expressions of $b_0^{(2)}$ (B.4) and $b_2^{(2)}$ (B.15) will be used to analyze the state functions of the quantum-friction system.

B.2 The third perturbative coefficients

For the third perturbative order coefficient $b_1^{(3)}$ in Sec. 3.2, we derive it from Eq. (3.44)

$$b_1^{(3)}(t) = \mathcal{F}_{10}^{(2)} + \mathcal{F}_{12}^{(2)} = -i \int_{-\infty}^{t} ds \; W_{10} b_0^{(2)} e^{i\omega_{10} s} - i \int_{-\infty}^{t} ds \; W_{12} b_2^{(2)} e^{i\omega_{12} s}. \tag{B.16}$$

With the expressions of W_{10} in Eq. (3.35) and $b_0^{(2)}$ in Eq. (3.42), the first term, $\mathcal{F}_{10}^{(2)}$, can be obtained as follows.

$$\mathcal{F}_{10}^{(2)} = -\frac{1}{d^2}\int_{-\infty}^{t} ds\ \left(\boldsymbol{\eta}\cdot\vec{k}\right)^* \phi_k e^{-kz} e^{i(\omega'(k)+\omega_b)s}\left(-i\delta\omega_g s - \frac{\gamma_g s}{2}\right) e^{i\omega_{10}s} \tag{B.17}$$

$$= -\frac{\left(\boldsymbol{\eta}\cdot\vec{k}\right)^* \phi_k e^{-kz}}{d^2}\left(-i\delta\omega_g - \frac{\gamma_g}{2}\right)\int_{-\infty}^{t} ds\ e^{i(\omega'(k)+\omega_b-i\delta^+)s} s. \tag{B.18}$$

One can solve the time integral by parts.

$$\mathcal{F}_{10}^{(2)} = -\frac{\left(\boldsymbol{\eta}\cdot\vec{k}\right)^* \phi_k e^{-kz}}{d^2}\left(-i\delta\omega_g - \frac{\gamma_g}{2}\right)\left(\left[\frac{e^{i(\omega'(k)+\omega_b-i\delta^+)s} s}{i(\omega'(k)+\omega_b-i\delta^+)}\right]_{s=-\infty}^{t}\right. \tag{B.19}$$

$$\left. - \int_{-\infty}^{t} ds\ \frac{e^{i(\omega'(k)+\omega_b-i\delta^+)s}}{i(\omega'(k)+\omega_b-i\delta^+)}\right)$$

$$\mathcal{F}_{10}^{(2)} = -\frac{i\left(\boldsymbol{\eta}\cdot\vec{k}\right)^* \phi_k e^{-kz} e^{i(\omega'(k)+\omega_b)t}}{d^2(\omega'(k)+\omega_b-i\delta^+)}\left(i\delta\omega_g + \frac{\gamma_g}{2}\right)\left(t + \frac{i}{\omega'(k)+\omega_b-i\delta^+}\right) \tag{B.20}$$

The second part, $\mathcal{F}_{12}^{(2)}$, can be rewritten using W_{21} (B.12).

$$\mathcal{F}_{12}^{(2)} = -i\int_{-\infty}^{t} ds \int d\boldsymbol{k}_1 d\boldsymbol{k}_2\ W_{21}^*(s,\boldsymbol{k}_1,\boldsymbol{k}_2,\boldsymbol{k}) b_2^{(2)}(s,\boldsymbol{k}_1,\boldsymbol{k}_2) e^{i\omega_{12}s} \tag{B.21}$$

$$= \int_{-\infty}^{t} ds \int d\boldsymbol{k}_1 d\boldsymbol{k}_2 \left(e^{-i(\omega'(k_1)-\omega_b)s-k_1 z}\left(\boldsymbol{\eta}\cdot\vec{k}_1\right)^* \phi_{k_1}\delta(\boldsymbol{k}_2-\boldsymbol{k})\right. \tag{B.22}$$

$$\left. + \{k_1 \leftrightarrow k_2\}\right) \times b_2^{(2)}(s,\boldsymbol{k}_1,\boldsymbol{k}_2) e^{i\omega_{12}s}$$

$$= \int_{-\infty}^{t} ds \int d\boldsymbol{k}_1\ e^{-i(\omega'(k_1)-\omega_b+i\delta^+)s-k_1 z}\left(\boldsymbol{\eta}\cdot\vec{k}_1\right)^* \phi_{k_1} b_2^{(2)}(s,\boldsymbol{k}_1,\boldsymbol{k}) \tag{B.23}$$

$$+ \int_{-\infty}^{t} ds \int d\boldsymbol{k}_2 \{k_1 \leftrightarrow k_2\} b_2^{(2)}(s,\boldsymbol{k},\boldsymbol{k}_2).$$

Since k_1 and k_2 are dummy variables, one can rewrite them as $\boldsymbol{k}'$ in the integral of $\mathcal{F}_{12}^{(2)}$.

$$\mathcal{F}_{12}^{(2)} = \int_{-\infty}^{t} ds \int d\boldsymbol{k}'\ e^{-i(\omega'(k')-\omega_b+i\delta^+)s-k' z}\left(\boldsymbol{\eta}\cdot\vec{k}'\right)^* \phi_{k'} \tag{B.24}$$

$$\times \left(b_2^{(2)}(s,\boldsymbol{k}',\boldsymbol{k}) + b_2^{(2)}(s,\boldsymbol{k},\boldsymbol{k}')\right).$$

Using the coefficient $b_2^{(2)}$ (3.41), we obtain the second part in the third perturbative order coefficient as follows.

$$\mathcal{F}_{12}^{(2)} = -e^{-kz}\phi_k \int d\boldsymbol{k'}\, e^{-2k'z} \frac{\left(\vec{k}\cdot\vec{k'}\right)^* \left(\boldsymbol{\eta}\cdot\vec{k'}\right)^* \phi_{k'}^2}{\omega'(k)+\omega'(k')-i\delta^+} \tag{B.25}$$
$$\times \left(\frac{1}{\omega'(k')+\omega_b-i\delta^+} + \{k \leftrightarrow k'\}\right) \int_{-\infty}^{t} ds\, e^{i\left(\omega'(k)+\omega_b-i\delta^+\right)s}$$
$$= \frac{i\phi_k e^{-kz} e^{i(\omega'(k)+\omega_b)t}}{\omega'(k)+\omega_b-i\delta^+} \int d\boldsymbol{k'}\, e^{-2k'z} \frac{\left(\vec{k}\cdot\vec{k'}\right)^* \left(\boldsymbol{\eta}\cdot\vec{k'}\right)^* \phi_{k'}^2}{\omega'(k)+\omega'(k')-i\delta^+} \tag{B.26}$$
$$\times \left(\frac{1}{\omega'(k')+\omega_b-i\delta^+} + \{k \leftrightarrow k'\}\right)$$

Therefore, we compute the third perturbative order coefficient $b_1^{(3)}$ as the sum of $\mathcal{F}_{10}^{(2)}$ (B.20) and $\mathcal{F}_{12}^{(2)}$ (B.26).

$$b_1^{(3)} = \frac{i\phi_k e^{-kz} e^{i(\omega'(k)+\omega_b)t}}{\omega'(k)+\omega_b-i\delta^+} \Bigg[-\frac{\left(\boldsymbol{\eta}\cdot\vec{k}\right)^*}{d^2} \left(i\delta\omega_g + \frac{\gamma_g}{2}\right) \left(t + \frac{i}{\omega'(k)+\omega_b-i\delta^+}\right) \tag{B.27}$$
$$+ \int d\boldsymbol{k'}\, e^{-2k'z} \frac{\left(\vec{k}\cdot\vec{k'}\right)^* \left(\boldsymbol{\eta}\cdot\vec{k'}\right)^* \phi_{k'}^2}{\omega'(k)+\omega'(k')-i\delta^+} \left(\frac{1}{\omega'(k')+\omega_b-i\delta^+} + \{k \leftrightarrow k'\}\right) \Bigg].$$

Appendix C Sokhotski-Plemelj theorem

The Sokhotski-Plemelj theorem states that

$$\lim_{\lambda\to 0}\int_a^b dx\frac{f(x)}{x\pm i\lambda} = \mp i\pi f(0)+\mathcal{P}\int_a^b dx\frac{f(x)}{x}, \tag{C.1}$$

where $\mathcal{P}$ is the notation of the Cauchy principal value. Its proof is as following.

$$\lim_{\lambda\to 0}\int_a^b dx\frac{f(x)}{x\pm i\lambda} = \int_a^b dx\frac{(x\mp i\lambda)}{(x\pm i\lambda)(x\mp i\lambda)}f(x) \tag{C.2}$$

$$= \int_a^b dx\frac{x}{x^2+\lambda^2}f(x)\mp\int_a^b dx\frac{i\lambda}{x^2+\lambda^2}f(x) \tag{C.3}$$

$$= \int_a^b dx\frac{x}{x^2+\lambda^2}f(x)\mp i\pi\int_a^b dx\frac{\lambda}{\pi\left(x^2+\lambda^2\right)}f(x). \tag{C.4}$$

The fraction in the second imaginary term is known as the nascent delta function in the limit as $\lambda\to 0$.

$$\lim_{\lambda\to 0}\int_a^b dx\frac{f(x)}{x\pm i\lambda} = \int_a^b dx\frac{x}{x^2+\lambda^2}f(x)\mp i\pi\int_a^b dx\;\delta(x)f(x). \tag{C.5}$$

In Sec. 3.2, one can find the real part of the coefficient $b_0^{(2)}$ in Eq. (3.40) can be expressed as the nascent delta function in Eq. (3.43).

$$\int d^2k\ \mathrm{Re}\left[\lim_{\lambda\to 0}\frac{i}{\omega_b+\omega'(k)-i\lambda}\right] = \int d^2k\ \mathrm{Re}\left[i\times i\pi\delta\left(\omega_b+\omega'(k)\right)\right] \tag{C.6}$$

$$= -\pi\int d^2k\;\delta\left(\omega_b+\omega'(k)\right). \tag{C.7}$$

Appendix D The integral in the second-order force

Here, we perform the substitution in the integral of the second-order force as shown in Eq. (4.12) by the dispersion relation in Eq. (4.15).

$$\langle F_x\rangle^{(2)} = \frac{2d^2\omega_p^4}{v}\int_0^\infty dk\ \frac{k^2e^{-2kz}}{\Omega_s(k)\left(\omega_p^2+2\Omega_s^2(k)\right)}\frac{(\Omega_s(k)+\omega_b)\Theta\left(kv-\Omega_s(k)-\omega_b\right)}{\sqrt{(kv)^2-(\Omega_s(k)+\omega_b)^2}}, \tag{D.1}$$

$$k = \frac{2\tilde{\Omega}^2-1}{2\tilde{\Omega}}\frac{\omega_p}{\beta}, \qquad dk = \frac{2\tilde{\Omega}^2+1}{2\tilde{\Omega}^2}\frac{\omega_p}{\beta}d\tilde{\Omega}. \tag{D.2}$$

Before the substitution, we also replace the parameters with the dimensionless parameters defined in Eq. (4.14).

$$\langle F_x\rangle^{(2)} = \frac{2d^2\omega_p}{\tilde{v}\beta}\int_0^\infty dk\ \frac{k^2e^{-2kz}}{\tilde{\Omega}\left(2\tilde{\Omega}^2+1\right)}\frac{(\tilde{\Omega}+\tilde{\omega})\Theta\left(kv-\Omega_s-\omega_b\right)}{\sqrt{(kv/\omega_p)^2-(\tilde{\Omega}+\tilde{\omega})^2}}. \tag{D.3}$$

Then, with the substitution in Eq. (D.2), one can further determine

$$\frac{kv}{\omega_p} = \frac{2\tilde{\Omega}^2-1}{2\tilde{\Omega}}\tilde{v}, \qquad kz = \frac{2\tilde{\Omega}^2-1}{2\tilde{\Omega}}\tilde{z}, \tag{D.4}$$

and the second force becomes

$$\langle F_x\rangle^{(2)} = \frac{d^2\omega_p^4}{2\tilde{v}\beta^4}\int_{1/\sqrt{2}}^\infty d\tilde{\Omega}\ \Theta\left(\frac{2\tilde{\Omega}^2-1}{2\tilde{\Omega}}\tilde{v}-\tilde{\Omega}-\tilde{\omega}\right)\frac{(\tilde{\Omega}+\tilde{\omega})(2\tilde{\Omega}^2-1)^2e^{-\left(2\tilde{\Omega}^2-1\right)\tilde{z}/\tilde{\Omega}}}{\tilde{\Omega}^4\sqrt{(2\tilde{\Omega}^2\tilde{v}-\tilde{v})^2-4\tilde{\Omega}^2(\tilde{\Omega}+\tilde{\omega})^2}}. \tag{D.5}$$

Appendix E The integral in the fourth-order force

One can use the expressions for $c_1^{(1)}$ in Eq. (3.46) and $c_2^{(2)}$ (3.48) to derive the second integral in $\langle F_x \rangle_2^{(4)}$ (4.4).

$$\mathrm{Re}\sum_\eta \int d\boldsymbol{k}_1 d\boldsymbol{k}_2 \, \langle \boldsymbol{\eta}, \boldsymbol{k}|F_x|\mathrm{g}, \boldsymbol{k}_1\boldsymbol{k}_2\rangle c_1^{(1)*}(t,\boldsymbol{k}) c_2^{(2)}(t,\boldsymbol{k}_1,\boldsymbol{k}_2) \tag{E.1}$$

$$= \mathrm{Re}\sum_\eta \int d\boldsymbol{k}_1 d\boldsymbol{k}_2 \, \langle \boldsymbol{\eta}, \boldsymbol{k}|F_x|\mathrm{g}, \boldsymbol{k}_1\boldsymbol{k}_2\rangle i d^3 \left(\boldsymbol{\eta}\cdot\vec{k}\right) \phi_k e^{-kz} \frac{e^{-i(\omega'(k)+\omega_b)t}}{\omega'(k)+\omega_b+i\delta^+} \tag{E.2}$$

$$\times \frac{e^{-k_1 z - k_2 z}\left(\vec{k}_2\cdot\vec{k}_1\right)^* \phi_{k_1}\phi_{k_2}}{\omega'(k_1)+\omega'(k_2)-i\delta^+} \left(\frac{e^{i(\omega'(k_1)+\omega'(k_2))t}}{\omega'(k_2)+\omega_b-i\delta^+} + \{k_1 \leftrightarrow k_2\} \right).$$

The force operator is defined as $F_x = \partial V/\partial t$, so that

$$\langle \boldsymbol{\eta}, \boldsymbol{k}|F_x|\mathrm{g}, \boldsymbol{k}_1\boldsymbol{k}_2\rangle = \frac{\partial}{\partial x}\langle \boldsymbol{\eta}, \boldsymbol{k}|V|\mathrm{g}, \boldsymbol{k}_1\boldsymbol{k}_2\rangle = d\frac{\partial}{\partial x}\langle \boldsymbol{\eta}, \boldsymbol{k}|W|\mathrm{g}, \boldsymbol{k}_1\boldsymbol{k}_2\rangle = d\frac{\partial W_{12}}{\partial x}. \tag{E.3}$$

As the matrix W should be hermitian, $W_{12} = W_{21}^*$, and using the expression for W_{21} in Eq. (B.12), one obtains

$$\langle \boldsymbol{\eta}, \boldsymbol{k}|F_x|\mathrm{g}, \boldsymbol{k}_1\boldsymbol{k}_2\rangle = -d\Big(e^{-i(\omega'(k_1)-\omega_b)t - k_1 z} k_1 \cos(\theta_1) \left(\boldsymbol{\eta}\cdot\vec{k}_1\right) \phi_{k_1} \delta(\boldsymbol{k}_2 - \boldsymbol{k}) \tag{E.4}$$

$$+ \{k_1 \leftrightarrow k_2\}\Big).$$

Inserting this into the integral in Eq. (E.2) yields

$$\mathrm{Re}\sum_{\eta}\int d\boldsymbol{k}_1 d\boldsymbol{k}_2\ \langle \boldsymbol{\eta},\boldsymbol{k}|F_x|\mathrm{g},\boldsymbol{k}_1\boldsymbol{k}_2\rangle c_1^{(1)*}(t,\boldsymbol{k})c_2^{(2)}(t,\boldsymbol{k}_1,\boldsymbol{k}_2) \tag{E.5}$$

$$= -d^4\mathrm{Re}\int d\boldsymbol{k}_1 d\boldsymbol{k}_2\ \phi_{k_1}^2\phi_{k_2}^2\left|\vec{k}_1\cdot\vec{k}_2\right|^2\left(\frac{k_1\cos(\theta_1)}{\omega'(k_2)+\omega_b+i\delta^+}+\{k_1\leftrightarrow k_2\}\right) \tag{E.6}$$

$$\times\, e^{-2k_1z-2k_2z}\frac{i}{\omega'(k_1)+\omega'(k_2)-i\delta^+}\left(\frac{1}{\omega'(k_2)+\omega_b-i\delta^+}+\{k_1\leftrightarrow k_2\}\right).$$

Again, one can define a delta function in the integral by the Sokhotski-Plemelj theorem illustrated in Appendix C.

$$\mathrm{Re}\sum_{\eta}\int d\boldsymbol{k}_1 d\boldsymbol{k}_2\ \langle \boldsymbol{\eta},\boldsymbol{k}|F_x|\mathrm{g},\boldsymbol{k}_1\boldsymbol{k}_2\rangle c_1^{(1)*}(t,\boldsymbol{k})c_2^{(2)}(t,\boldsymbol{k}_1,\boldsymbol{k}_2) \tag{E.7}$$

$$= \pi d^4\int d\boldsymbol{k}_1 d\boldsymbol{k}_2\ \phi_{k_1}^2\phi_{k_2}^2\left|\vec{k}_1\cdot\vec{k}_2\right|^2 e^{-2k_1z-2k_2z}\left(\frac{k_1\cos(\theta_1)}{\omega'(k_2)+\omega_b}+\frac{k_2\cos(\theta_2)}{\omega'(k_1)+\omega_b}\right) \tag{E.8}$$

$$\times\,\delta\left(\omega'(k_1)+\omega'(k_2)\right)\left(\frac{1}{\omega'(k_2)+\omega_b}+\{k_1\leftrightarrow k_2\}\right).$$

Appendix F The density matrix in the interaction picture

The density matrix operator in the Schrödinger picture is written as

$$\rho(t) = |\psi(t)\rangle\langle\psi(t)|, \tag{F.1}$$

where $|\psi(t)\rangle$ is the state function of the total Hamiltonian as $H = H_0 + H_{\text{int}}(t)$, and H_0 consists of the Hamiltonian of each subsystem. Thus, the time evolution in the state function should be

$$|\psi(t,t')\rangle = U(t,t')|\psi(t')\rangle, \text{ where } U(t,t') = \mathcal{T}e^{-i\int_{t'}^{t} ds\, H(s)}. \tag{F.2}$$

$\mathcal{T}$ is the time-ordering operator. Therefore, the density matrix in the Schrödinger picture can be expressed as

$$\rho(t) = U(t,t')\rho(t')U^{\dagger}(t,t'). \tag{F.3}$$

Therefore, the time derivative of the density matrix gives the von Neumann equation as expected.

$$\frac{d}{dt}\rho(t) = \frac{dU(t,t')}{dt}\rho(t')U^{\dagger}(t,t') + U(t,t')\rho(t')\frac{dU^{\dagger}(t,t')}{dt} \tag{F.4}$$

$$= -iH(t)\rho(t) + i\rho(t)H^{\dagger}(t) = -i\left[H(t),\rho(t)\right]. \tag{F.5}$$

In the interaction picture, the density matrix operator is expressed in a manner analogous to other observable operators.

$$\rho_I(t) = U_0^{\dagger}(t,t')\rho(t)U_0(t,t') \tag{F.6}$$

$$= U_I(t,t')\rho(t')U_I^{\dagger}(t,t'), \tag{F.7}$$

$$\text{where } U_0(t,t') = e^{-iH_0(t-t')} \text{ and } U_I(t,t') = \mathcal{T}e^{-i\int_{t'}^{t} ds\, H_{\text{int}}(s)}. \tag{F.8}$$

One can also obtain this result by analyzing the state function in the interaction picture as follows.

$$|\psi_I(t)\rangle = e^{iH_0(t-t')}|\psi(t)\rangle = e^{iH_0(t-t')}U(t,t')|\psi(t')\rangle = U_I(t,t')|\psi(t')\rangle. \tag{F.9}$$

Thus, we obtain the corresponding von Neumann equation in the interaction picture as follows.

$$\frac{d}{dt}\rho_I(t) = \frac{dU_I(t,t')}{dt}\rho(t')U_I^\dagger(t,t') + U_I(t,t')\rho(t')\frac{dU_I^\dagger(t,t')}{dt} \tag{F.10}$$

$$= -iH_{\text{int}}\rho_I(t) + i\rho_I(t)H_{\text{int}}^\dagger \tag{F.11}$$

$$\frac{d}{dt}\rho_I(t) = -i\left[H_{\text{int}}, \rho_I(t)\right]. \tag{F.12}$$

Appendix G The bath correlation functions

The bath correlation function, which is homogenous in time, is expressed as Eq. (6.90).

$$e^{J_{\text{env}}(s)} = \left\langle e^{i(\delta_j(s)-\delta_k(s))} e^{i(\delta_k(0)-\delta_j(0))} \right\rangle_{\text{env}}, \tag{G.1}$$

where $\delta_j(t) = \sum_m g_{jm}\left(b_m^\dagger(t) + b_m(t)\right)$ with the bosonic annihilation operators $b_m(t) = b_m \exp\left(-iE_m t\right)$. Therefore, $\delta_j(s) - \delta_k(s)$ can be written as

$$\delta_j(s) - \delta_k(s) = \sum_m \delta g_{jk,m}\left(b_m^\dagger(s) + b_m(s)\right), \text{ where } \delta g_{jk,m} = g_{jm} - g_{km}. \tag{G.2}$$

The state of the bath remains at equilibrium, which is characterized as a thermal state.

$$\rho_{\text{env}} = Z_{\text{env}}^{-1} e^{-H_{\text{env}}/T}, \text{ where } Z_{\text{env}} = \text{Tr}_{\text{env}}\left(e^{-H_{\text{env}}/T}\right). \tag{G.3}$$

As anticipated, the expectation value of the electromagnetic fluctuation from the bath is zero, i.e.: $\langle \delta_j(t) \rangle = 0$. For a Gaussian random variable $\delta_j(t)$ with mean zero, the bath correlation function is given by [122]

$$J_{\text{env}}(s) = \langle \{\delta_j(s) - \delta_k(s) - [\delta_j(0) - \delta_k(0)]\} [\delta_j(0) - \delta_k(0)] \rangle_{\text{env}} \tag{G.4}$$

$$= \sum_{m,m'} \delta g_{jk,m} \delta g_{jk,m'} \left\langle b_m^\dagger b_{m'} \left(e^{iE_m s} - 1\right) + b_m b_{m'}^\dagger \left(e^{-iE_m s} - 1\right) \right\rangle_{\text{env}}. \tag{G.5}$$

The bosonic distribution corresponding to the Hamiltonian in Eq. (6.22) should be

$$\left\langle b_m^\dagger b_{m'} \right\rangle_{\text{env}} = \delta_{m,m'} \frac{1}{e^{E_m/T} - 1} \tag{G.6}$$

$$\left\langle b_m b_{m'}^\dagger \right\rangle_{\text{env}} = \delta_{m,m'} \left(1 + \frac{1}{e^{E_m/T} - 1}\right) = \delta_{m,m'} \frac{e^{E_m/T}}{e^{E_m/T} - 1}. \tag{G.7}$$

The correlation function is then expressed as

$$J_{\text{env}}(s) = \sum_m \delta g_{jk,m}^2 \frac{e^{iE_m s} - 1 + e^{E_m/T}\left(e^{-iE_m s} - 1\right)}{e^{E_m/T} - 1} \tag{G.8}$$

$$= \sum_m \delta g_{jk,m}^2 \left[\frac{e^{E_m/T} + 1}{e^{E_m/T} - 1}\left(\cos(E_m s) - 1\right) - i\sin(E_m s)\right] \tag{G.9}$$

$$= \sum_m \delta g_{jk,m}^2 \left[\coth\left(E_m/2T\right)\left(\cos(E_m s) - 1\right) - i\sin(E_m s)\right] \tag{G.10}$$

Here we introduce the energy spectral density $\mathcal{J}(\omega)$,

$$\mathcal{J}(\omega) = \pi \sum_m \delta g_{jk,m}^2 E_m^2 \delta(\omega - E_m), \tag{G.11}$$

which effectively characterizes the distribution of the bosonic bath modes in terms of their frequencies and the strength of their coupling to the open system. In terms of the spectral density function, the correlation function is written as

$$J_{\text{env}}(s) = \int \frac{d\omega}{\pi} \frac{\mathcal{J}(\omega)}{\omega^2} \left[\coth\left(\omega/2T\right)\left(\cos(\omega s) - 1\right) - i\sin(\omega s)\right]. \tag{G.12}$$

We can apply the concept of an Ohmic bath to model the spectral density $\mathcal{J}(\omega)$, which is characterized by a linear relationship $\mathcal{J}(\omega) \propto \omega$. However, to adhere to physical constraints, especially to prevent divergence at high frequencies, the spectral density must be refined. This refinement is accomplished by incorporating a cutoff frequency ω_c, which ensures convergence and limits the energy of the bath. Mathematically, this is done by including an exponential decay term, resulting in the following form for the Ohmic spectral density.

$$\mathcal{J}(\omega) = \alpha\omega e^{-\omega/\omega_c}, \tag{G.13}$$

where α is a dimensionless parameter that quantifies the system-bath coupling strength.

Appendix H The expansion of the Markovian quantum master equation

The expansion of the Markovian quantum master equation is detailed in Eq. (6.80), which captures the dynamics of the open quantum system under the influence of a bosonic bath.

$$\frac{d}{dt}\rho_{\mathrm{s}}(t) = -\int_0^\infty ds\ \mathrm{Tr}_{\mathrm{env}}\left[V(t)V(t-s)\rho_{\mathrm{s}}(t)\otimes\rho_{\mathrm{evn}}\right. \\ \left. -V(t-s)\rho_{\mathrm{s}}(t)\otimes\rho_{\mathrm{evn}}V(t) + h.c.\right]. \tag{H.1}$$

Using the expression of V as presented in Eq. (6.78), we have systematically derived each term that constitutes the quantum master equation as follows.

$$V(t-s)\rho_{\mathrm{s}}(t)\otimes\rho_{\mathrm{evn}}V(t) = 4g_0^2\sum_{j\neq k} e^{-i\delta\epsilon_{kj}s}W_{jk}d_j^\dagger d_k\rho_{\mathrm{s}}(t)W_{kj}d_k^\dagger d_j \\ \otimes e^{i(\delta_k(t-s)-\delta_j(t-s))}\rho_{\mathrm{evn}}e^{i(\delta_j(t)-\delta_k(t))}. \tag{H.2}$$

Taking the trace over the bath and applying the cyclic property of the trace, we obtain the same bath correlation function defined in Eq. (6.86).

$$\mathrm{Tr}_{\mathrm{env}}\left[e^{i(\delta_k(t-s)-\delta_j(t-s))}\rho_{\mathrm{evn}}e^{i(\delta_j(t)-\delta_k(t))}\right] = \mathrm{Tr}_{\mathrm{env}}\left[e^{i(\delta_j(t)-\delta_k(t))}e^{i(\delta_k(t-s)-\delta_j(t-s))}\rho_{\mathrm{evn}}\right] \\ \mathrm{Tr}_{\mathrm{env}}\left[e^{i(\delta_k(t-s)-\delta_j(t-s))}\rho_{\mathrm{evn}}e^{i(\delta_j(t)-\delta_k(t))}\right] = e^{J_{\mathrm{env}}}, \tag{H.3}$$

Then integrating over time s leads to

$$\int_0^\infty ds\ \mathrm{Tr}_{\mathrm{env}}\left[V(t)\rho_{\mathrm{s}}(t)\otimes\rho_{\mathrm{evn}}V(t-s)\right] = \sum_{j\neq k}\Lambda_{jk}A_{jk}\rho_{\mathrm{s}}(t)A_{jk}^\dagger, \tag{H.4}$$

$$\text{where } A_{jk} = 2W_{jk}d_j^\dagger d_k \text{ and } \Lambda_{kj} = g_0^2\int_0^\infty ds\ e^{-i\delta\epsilon_{kj}s}e^{J_{\mathrm{env}}(s)}. \tag{H.5}$$

For the Hermitian conjugation of the terms in the quantum master Eq. (H.1), one can directly identify the corresponding Hermitian adjoint, which is essential for ensuring the complete positivity of the density matrix evolution.

$$\int_0^\infty ds\ \mathrm{Tr}_{\mathrm{env}}\left[\rho_{\mathrm{s}}(t)\otimes\rho_{\mathrm{evn}}V(t)V(t-s)\right]=\sum_{j\neq k}\Lambda_{jk}^{*}\rho_{\mathrm{s}}(t)A_{jk}^{\dagger}A_{jk}, \tag{H.6}$$

$$\int_0^\infty ds\ \mathrm{Tr}_{\mathrm{env}}\left[V(t-s)\rho_{\mathrm{s}}(t)\otimes\rho_{\mathrm{evn}}V(t)\right]=\sum_{j\neq k}\Lambda_{jk}^{*}A_{jk}\rho_{\mathrm{s}}(t)A_{jk}^{\dagger}. \tag{H.7}$$

Appendix I Kubo-Martin-Schwinger symmetry

The transition rate $\tilde{\Gamma}_{jk}$ is associated with the bath correlation function $J_{\text{env}}(s)$ expressed in Eq. (6.91). The integrand of the correlation function $J_{\text{env}}(-s - i/T)$ is given by $\coth(\omega/2T)\,(\cos(-\omega s - i\omega/T) - 1) - i\sin(-\omega s - i\omega/T)$. Using Euler's formula,

$$\cos(i\omega/T) = \cosh(\omega/T), \qquad \sin(i\omega/T) = i\sinh(\omega/T), \tag{I.1}$$

we can express the trigonometric functions with complex arguments as

$$\begin{aligned} \cos(\omega s + i\omega T) &= \cos(\omega s)\cos(i\omega/T) - \sin(\omega s)\sin(i\omega/T) && \text{(I.2)}\\ &= \cos(\omega s)\cosh(\omega/T) - i\sin(\omega s)\sinh(\omega/T), \\ \sin(\omega s + i\omega/T) &= \sin(\omega s)\cos(i\omega/T) + \sin(i\omega/T)\cos(\omega s) && \text{(I.3)}\\ &= \sin(\omega s)\cosh(\omega/T) + i\sinh(\omega/T)\cos(\omega s). \end{aligned}$$

Subsequently, we derive the integrand $J_{\text{env}}(-s - i/T)$ of the bath correlation function, which is initially given by the following expression.

$$\begin{aligned} \mathcal{I}(-s - i/T) = \coth(\omega/2T)\,(\cos(\omega s)\cosh(\omega/T) - 1) - \sinh(\omega/T)\cos(\omega s) \\ - i\sin(\omega s)\,(\sinh(\omega/T)\coth(\omega/2T) - \cosh(\omega/T))\,. \end{aligned} \tag{I.4}$$

Employing the hyperbolic identities $\sinh(2x) = 2\sinh(x)\cosh(x)$, $\cosh(2x) = \cosh^2(x) + \sinh^2(x)$ and $1 = \cosh^2(x) - \sinh^2(x)$, we proceed to simplify the integrand.

$$\begin{aligned} \mathcal{I}(-s - i/T) &= \coth(\omega/2T)\left[\cos(\omega s)\left(\cosh(\omega/T) - 2\sinh^2(\omega/2T)\right) - 1\right] && \text{(I.5)}\\ &\quad - i\sin(\omega s)\left(2\cosh^2(\omega/2T) - \cosh^2(\omega/2T) - \sinh^2(\omega/2T)\right) \\ &= \coth(\omega/2T)\left[\cos(\omega s)\left(\cosh^2(\omega/2T) - \sinh^2(\omega/2T)\right) - 1\right] && \text{(I.6)}\\ &\quad - i\sin(\omega s)\left(\cosh^2(\omega/2T) - \sinh^2(\omega/2T)\right) \\ \Rightarrow \mathcal{I}(-s - i/T) &= \coth(\omega/2T)\,[\cos(\omega s) - 1] - i\sin(\omega s) = \mathcal{I}(s). && \text{(I.7)} \end{aligned}$$

Hence, the bath correlation function, as defined in Eq. (6.86) exhibits that $J_{\text{env}}(-s - i/T) \equiv J_{\text{env}}(s)$ which is known as the Kubo-Martin-Schwinger (KMS) symmetry [133]. KMS symmetry characterizes the thermal equilibrium state of a quantum system at a specific temperature T. This symmetry fundamentally confirms that the correlation functions of the system, when in thermal equilibrium, display a specific periodicity in imaginary time. This periodicity is directly related to the inverse of the temperature.

Appendix J The Bloch form of Lindblad equation

We consider the open system consisting of a single Majorana box whose density matrix is 2×2. Without loss of generality, one can express the 2×2 density matrix and the corresponding jump operator using the generic forms given by Eqs. (7.1) and (7.3),

$$\rho = \frac{1}{2}\left(\sigma_0 + \boldsymbol{n}\cdot\boldsymbol{\sigma}\right) = \frac{1}{2}\left[\sigma_0 + (n_x, n_y, n_z)\cdot(\sigma_x, \sigma_y, \sigma_z)\right], \tag{J.1}$$

$$K = \boldsymbol{k}\cdot\boldsymbol{\sigma} = (k_x \exp(i\phi_x), k_y \exp(i\phi_y), k_z \exp(i\phi_z))\cdot(\sigma_x, \sigma_y, \sigma_z), \tag{J.2}$$

where $n_{x,y,z} \in \mathbb{R}$, and $k_{x,y,z}$ and $\phi_{x,y,z}$ are determined by the tunneling amplitudes $\lambda_{j,\nu}$ and tunneling phases $\beta_{j,\nu}$, respectively. In the Lindblad equation (6.111), the contributions of quantum jumps and the anti-commutator can be expressed as

$$K\rho K^\dagger = (\boldsymbol{k}\cdot\boldsymbol{\sigma})\frac{1}{2}\left(\sigma_0 + \boldsymbol{n}\cdot\boldsymbol{\sigma}\right)(\boldsymbol{k}^*\cdot\boldsymbol{\sigma}), \tag{J.3}$$

$$K^\dagger K\rho = (\boldsymbol{k}^*\cdot\boldsymbol{\sigma})(\boldsymbol{k}\cdot\boldsymbol{\sigma})\frac{1}{2}\left(\sigma_0 + \boldsymbol{n}\cdot\boldsymbol{\sigma}\right), \tag{J.4}$$

$$\rho K^\dagger K = \frac{1}{2}\left(\sigma_0 + \boldsymbol{n}\cdot\boldsymbol{\sigma}\right)(\boldsymbol{k}^*\cdot\boldsymbol{\sigma})(\boldsymbol{k}\cdot\boldsymbol{\sigma}). \tag{J.5}$$

Given that the product of Pauli matrices can be written as $\sigma_a\sigma_b = \delta_{a,b}\sigma_0 + i\epsilon_{abc}\,\sigma_c$, where ϵ_{abc} is the Levi-Civita symbol and $a, b, c \in \{x, y, z\}$, it follows that for two arbitrary vectors $\boldsymbol{v}_1$ and $\boldsymbol{v}_2$, there is $(\boldsymbol{v}_1\cdot\boldsymbol{\sigma})(\boldsymbol{v}_2\cdot\boldsymbol{\sigma}) = (\boldsymbol{v}_1\cdot\boldsymbol{v}_2)\,\sigma_0 + i\boldsymbol{\sigma}\cdot(\boldsymbol{v}_1\times\boldsymbol{v}_2)$. Thus, we

proceed to derive the expression for quantum jumps as follows.

$$K\rho K^\dagger = (\boldsymbol{k}\cdot\boldsymbol{\sigma})\frac{1}{2}(\sigma_0 + \boldsymbol{n}\cdot\boldsymbol{\sigma})(\boldsymbol{k}^*\cdot\boldsymbol{\sigma}) \tag{J.6}$$

$$= \frac{1}{2}\left[\boldsymbol{k}\cdot\boldsymbol{\sigma} + (\boldsymbol{k}\cdot\boldsymbol{n})\sigma_0 + i\boldsymbol{\sigma}\cdot(\boldsymbol{k}\times\boldsymbol{n})\right](\boldsymbol{k}^*\cdot\boldsymbol{\sigma}) \tag{J.7}$$

$$= \frac{1}{2}\left[(\boldsymbol{k}\cdot\boldsymbol{k}^*)\sigma_0 + i\boldsymbol{\sigma}\cdot(\boldsymbol{k}\times\boldsymbol{k}^*) + \boldsymbol{\sigma}\cdot\boldsymbol{k}^*(\boldsymbol{k}\cdot\boldsymbol{n})\right. \tag{J.8}$$

$$\left. + i\left[(\boldsymbol{k}\times\boldsymbol{n})\cdot\boldsymbol{k}^*\right]\sigma_0 - \boldsymbol{\sigma}\cdot(\boldsymbol{k}\times\boldsymbol{n})\times\boldsymbol{k}^*\right]$$

$$K\rho K^\dagger = \frac{1}{2}\left[\left(|\boldsymbol{k}|^2 + i(\boldsymbol{k}\times\boldsymbol{n})\cdot\boldsymbol{k}^*\right)\sigma_0 + \boldsymbol{\sigma}\cdot(i\boldsymbol{k}\times\boldsymbol{k}^* + (\boldsymbol{k}\cdot\boldsymbol{n})\boldsymbol{k}^* - (\boldsymbol{k}\times\boldsymbol{n})\times\boldsymbol{k}^*)\right]. \tag{J.9}$$

We apply the same approach to the terms from the anti-commutator and obtain their expressions as

$$K^\dagger K\rho = (\boldsymbol{k}^*\cdot\boldsymbol{\sigma})(\boldsymbol{k}\cdot\boldsymbol{\sigma})\frac{1}{2}(\sigma_0 + \boldsymbol{n}\cdot\boldsymbol{\sigma}) \tag{J.10}$$

$$= \frac{1}{2}\left[\left(|\boldsymbol{k}|^2 + i(\boldsymbol{k}^*\times\boldsymbol{k})\cdot\boldsymbol{n}\right)\sigma_0 + \boldsymbol{\sigma}\cdot\left(i\boldsymbol{k}^*\times\boldsymbol{k} + |\boldsymbol{k}|^2\boldsymbol{n} - \boldsymbol{k}^*\times\boldsymbol{k}\times\boldsymbol{n}\right)\right],$$

$$\rho K^\dagger K = \frac{1}{2}(\sigma_0 + \boldsymbol{n}\cdot\boldsymbol{\sigma})(\boldsymbol{k}^*\cdot\boldsymbol{\sigma})(\boldsymbol{k}\cdot\boldsymbol{\sigma}) \tag{J.11}$$

$$= \frac{1}{2}\left[\left(|\boldsymbol{k}|^2 + i(\boldsymbol{n}\times\boldsymbol{k}^*)\cdot\boldsymbol{k}\right)\sigma_0 + \boldsymbol{\sigma}\cdot(i\boldsymbol{k}^*\times\boldsymbol{k} + (\boldsymbol{n}\cdot\boldsymbol{k}^*)\boldsymbol{k} - \boldsymbol{n}\times\boldsymbol{k}^*\times\boldsymbol{k})\right].$$

Using the properties of the scalar triple product and the cyclic nature of the cross product and dot product, $(\boldsymbol{v}_1\times\boldsymbol{v}_2)\cdot\boldsymbol{v}_3 = (\boldsymbol{v}_3\times\boldsymbol{v}_1)\cdot\boldsymbol{v}_2$, we can align the identity terms in the contribution of the anti-commutator to that of the quantum jumps. Thereby, we obtain

$$K^\dagger K\rho = \frac{1}{2}\left[\left(|\boldsymbol{k}|^2 + i(\boldsymbol{k}\times\boldsymbol{n})\cdot\boldsymbol{k}^*\right)\sigma_0 + \boldsymbol{\sigma}\cdot\left(i\boldsymbol{k}^*\times\boldsymbol{k} + |\boldsymbol{k}|^2\boldsymbol{n} - \boldsymbol{k}^*\times\boldsymbol{k}\times\boldsymbol{n}\right)\right], \tag{J.12}$$

$$\rho K^\dagger K = \frac{1}{2}\left[\left(|\boldsymbol{k}|^2 + i(\boldsymbol{k}\times\boldsymbol{n})\cdot\boldsymbol{k}^*\right)\sigma_0 + \boldsymbol{\sigma}\cdot(i\boldsymbol{k}^*\times\boldsymbol{k} + (\boldsymbol{n}\cdot\boldsymbol{k}^*)\boldsymbol{k} - \boldsymbol{n}\times\boldsymbol{k}^*\times\boldsymbol{k})\right]. \tag{J.13}$$

Writing the Lindblad equation in Bloch form simplifies the analytical solution for its steady state. The steady state, denoted as ρ_s, can be determined by $\mathcal{L}\rho_\mathrm{s} = 0$ as shown in Eq. (6.112).

Appendix K The Schrieffer-Wolff transformation up to the fourth order

To derive the SW transformation for the Hamiltonian given in Eq. (8.23),

$$H_{\text{eff}} = H_0 + H_{\text{cot}}^{(2)} + \frac{1}{3}\left[S, 2H_{\text{cot}}^{(2)}\right] + \frac{1}{8}\left[S, 3H_{\text{cot}}^{(3)}\right], \tag{K.1}$$

analogous to the method discussed in Sec. 6.2.2, we begin by diagonalizing the unperturbed Hamiltonian H_0 to isolate the cotunneling contribution H_{cot}. Applying the rotating wave approximation to eliminate rapidly oscillating terms in the driving Hamiltonian, the unperturbed Hamiltonian from Eq. (8.14) becomes time-independent and can be expressed as follows,

$$\begin{aligned} H_0 &= H_{\text{box}} + H_{\text{QD}} + H_{\text{env}} + H_{\text{drive}} \\ &= E_C \sum_n \left(\hat{N}_n - N_g\right)^2 + \sum_{j=1,2} \epsilon_j d_j^\dagger d_j + \sum_m E_m b_m^\dagger b_m + \mathcal{A}(d_2^\dagger d_1 + h.c.), \end{aligned} \tag{K.2}$$

where $\mathcal{A}$ is the amplitude of the driving field. Although this unperturbed Hamiltonian H_0 (K.2) in a higher-dimensional Hilbert space due to additional Majorana boxes, the box Hamiltonian in Eq. (8.15) exhibits three degenerate eigenvalues. Since the Hamiltonians of the environment, quantum dots, and AC driving field remain unchanged, the diagonalization of H_0 (K.2) results in the identical set of eigenvalues as in the case of the single-box open system: $\{E_C, \eta_1, \ldots, \eta_4, E_m\}$, where $\eta_{1,2,3,4}$ are detailed in Eq. (6.45).

In Eq. (6.37), we recall the derivation for the generator S in the context of the diagonalized Hamiltonian H_0, and the generator is expressed as

$$H_{\text{tun}} + [S, H_0] = 0 \tag{K.3}$$

$$\Rightarrow (H_{\text{tun}})_{ab} = \left(\epsilon'_{aa} - \epsilon'_{bb}\right) S_{ab}, \tag{K.4}$$

where $\epsilon'_{mm} \in \{E_C, \eta_1, \ldots, \eta_4, E_m\}$. Consequently, the second-order terms in Eq. (K.1)

can be expressed in terms of the tunneling Hamiltonian and the eigenvalues of ϵ'_{aa}.

$$\left(H^{(2)}_{\text{cot}}\right)_{ab} = \frac{1}{2}\left[S, H_{\text{tun}}\right]_{ab} \tag{K.5}$$

$$\Rightarrow \left(H^{(2)}_{\text{cot}}\right)_{ab} = \frac{1}{2}\sum_{c}\left(H_{\text{tun}}\right)_{ac}\left(H_{\text{tun}}\right)_{cb}\left(\frac{1}{\epsilon'_{aa}-\epsilon'_{cc}}+\frac{1}{\epsilon'_{bb}-\epsilon'_{cc}}\right). \tag{K.6}$$

As shown in Table 6.1, the low-energy regime imposes that the charging energy is the largest among the various energy scales, making it appropriate to adopt the following approximation,

$$\left.\begin{aligned}\left(H_{\text{tun}}\right)_{ab} &= \pm\left(E_m - \eta_{1,\ldots,4}\right)S_{ab},\\ \left(H_{\text{tun}}\right)_{ab} &= \pm\left(E_C - \eta_{1,\ldots,4}\right)S_{ab},\\ \left(H_{\text{tun}}\right)_{ab} &= \pm\left(E_C - E_m\right)S_{ab}.\end{aligned}\right\} \Rightarrow \begin{cases}\left(H_{\text{tun}}\right)_{ab} \approx 0,\\ \left(H_{\text{tun}}\right)_{ab} \approx \pm E_C S_{ab},\\ \left(H_{\text{tun}}\right)_{ab} \approx \pm E_C S_{ab}.\end{cases} \tag{K.7}$$

Therefore, one can further simplify the second-order term by these approximations, and one obtain the second-order term as

$$\left(H^{(2)}_{\text{cot}}\right)_{ab} \approx \frac{1}{E_C}\sum_{c}\left(H_{\text{tun}}\right)_{ac}\left(H_{\text{tun}}\right)_{cb} \Rightarrow H^{(2)}_{\text{cot}} = \frac{1}{E_C}\left(H_{\text{tun}}H_{\text{tun}}\right). \tag{K.8}$$

This expression matches what we derived for the cotunneling Hamiltonian in the single-box case in Chapter 7, but now includes an additional contribution from the tunnel couplings between boxes, denoted as $H_{\text{tun},\gamma}$ in Eq. (8.17). Before deriving the specific expression for the second-order term, we can also apply this low-energy approximation to the third and fourth-order terms in the cotunneling Hamiltonian, as shown in Eq. (K.1).

The third-order terms in the expansion formula of Eq. (K.1) can be rewritten using the expression for the generator S given in Eq. (K.4) and the second-order cotunneling terms $H^{(2)}_{\text{tun}}$ from Eq. (K.8).

$$\left(H^{(3)}_{\text{cot}}\right)_{ab} = \frac{1}{3}\left[S, 2H^{(2)}_{\text{cot}}\right]_{ab}, \tag{K.9}$$

$$\Rightarrow \left(H^{(3)}_{cot}\right)_{ab} = \frac{2}{3E_C}\sum_{c}\left(H_{\text{tun}}\right)_{ac}\left(H_{\text{tun}}H_{\text{tun}}\right)_{cb}\left(\frac{1}{\epsilon'_{aa}-\epsilon'_{cc}}+\frac{1}{\epsilon'_{bb}-\epsilon'_{cc}}\right). \tag{K.10}$$

By adopting the consequence in Eq. (K.7) from the low-energy limit once more, we can reduce the third-order cotunneling term to the following expressions.

$$\left(H^{(3)}_{\text{cot}}\right)_{ab} \approx \frac{2}{3E_C}\frac{2}{E_C}\sum_{c}\left(H_{\text{tun}}\right)_{ac}\left(H_{\text{tun}}H_{\text{tun}}\right)_{cb} \tag{K.11}$$

$$\Rightarrow H^{(3)}_{\text{cot}} = \frac{4}{3E_C^2}\left(H_{\text{tun}}H_{\text{tun}}H_{\text{tun}}\right). \tag{K.12}$$

We can use the previously derived expression for $H_{cot}^{(3)}$ to calculate the fourth-order term in Eq. (K.1).

$$\left(H_{\mathrm{cot}}^{(4)}\right)_{ab} = \frac{1}{8}\left[S, 3H_{\mathrm{cot}}^{(3)}\right]_{ab} \tag{K.13}$$

$$\Rightarrow \left(H_{\mathrm{cot}}^{(4)}\right)_{ab} = \frac{1}{2E_C^2}\sum_c \left(H_{\mathrm{tun}}\right)_{ac}\left(H_{\mathrm{tun}}^3\right)_{cb}\left(\frac{1}{\epsilon'_{aa}-\epsilon'_{cc}}+\frac{1}{\epsilon'_{bb}-\epsilon'_{cc}}\right). \tag{K.14}$$

The approximation in Eq. (K.7) further simplifies fourth-order cotunneling to

$$H_{\mathrm{cot}}^{(4)} \approx \frac{1}{E_C^3}\left(H_{\mathrm{tun}}H_{\mathrm{tun}}H_{\mathrm{tun}}H_{\mathrm{tun}}\right). \tag{K.15}$$

Accordingly, to derive the cotunneling contribution up to the fourth order, we sum equations Eqs. (K.8), (K.12) and (K.15).

$$H_{\mathrm{cot}} = \sum_{r=2}^{4}\left(\frac{r-1}{r!}\right)\left(\frac{2}{E_C}\right)^{r-1}\left(H_{\mathrm{tun}}\right)^r. \tag{K.16}$$

Appendix L The vector formalism of the Liouvillian superoperator

In Sec. 8.2, we derive the Lindblad equation for an open system comprising three Majorana boxes. When the dissipation is characterized by the braiding-compatible jump operator K_{odd} given by Eq. (8.8),

$$K_{\text{odd}} = \begin{pmatrix} 0 & f_1 & -ff_1 & 0 \\ g_1 & 0 & 0 & gg_1 \\ g_2 & 0 & 0 & gg_2 \\ 0 & f_2 & -ff_2 & 0 \end{pmatrix}, \tag{L.1}$$

The steady state ρ_{odd} can be determined by solving the equation $\mathcal{L}[K_{\text{odd}}]\rho_{\text{odd}} = 0$, where $\mathcal{L}$ denotes the Lindbladian superoperator. By representing the density matrix as a vector and the Liouvillian superoperator as a matrix, the Lindblad equation given by Eq. (8.38) can be expressed as

$$\mathcal{L}[K_{\text{odd}}] = \Gamma_{12}\left[K_{\text{odd}} \otimes K_{\text{odd}}^{\dagger} - \frac{1}{2}\left(\mathbb{I} \otimes K_{\text{odd}}^{\dagger}K_{\text{odd}} + K_{\text{odd}}^{\dagger}K_{\text{odd}} \otimes \mathbb{I}\right)\right], \tag{L.2}$$

where Γ_{12} is the transition rate defined in Eq. (6.104), and $\mathbb{I}$ is the identity matrix. In the case of three Majorana box qubits, the Liouvillian superoperator is represented as a 16×16 matrix, and the density matrix $|\rho_{\text{odd}}\rangle$ is a 16-dimensional vector.

In principle, when an eigenvalue of the Liouvillian superoperator (L.2) is zero, the corresponding eigenstate is unaffected by damping and is immune to dissipation. Therefore, the stationary state associated with zero eigenvalues represents the dark state of the Liouvillian superoperator.

$$\mathcal{L}[K_{\text{odd}}]|\rho_{\text{odd}}\rangle \equiv 0. \tag{L.3}$$

By diagonalizing the Liouvillian superoperator, we can identify four dark states.

$$\mathcal{L}[K_{\text{odd}}]|\mathcal{D}_1\rangle = \mathcal{L}[K_{\text{odd}}]\left(g^2,0,0,-g,0,0,0,0,0,0,0,0,-g,0,0,1\right)^T = 0 \tag{L.4}$$

$$\mathcal{L}[K_{\text{odd}}]|\mathcal{D}_2\rangle = \mathcal{L}[K_{\text{odd}}]\left(0,-fg,-g,0,0,0,0,0,0,0,0,0,0,f,1,0\right)^T = 0 \tag{L.5}$$

$$\mathcal{L}[K_{\text{odd}}]|\mathcal{D}_3\rangle = \mathcal{L}[K_{\text{odd}}]\left(0,0,0,0,-fg,0,0,f,-g,0,0,1,0,0,0,0\right)^T = 0 \tag{L.6}$$

$$\mathcal{L}[K_{\text{odd}}]|\mathcal{D}_4\rangle = \mathcal{L}[K_{\text{odd}}]\left(0,0,0,0,0,f^2,f,0,0,f,1,0,0,0,0,0\right)^T = 0. \tag{L.7}$$

The remaining eigenvalues of the Liouvillian superoperator are negative, which implies that the corresponding eigenstates decay exponentially over time. The dissipative gap in this Lindblad equation is determined by the nearest non-zero eigenvalue of the Liouvillian superoperator. As a result, the steady state of the system is characterized by a combination of these dark states.

$$|\rho_{\text{odd}}\rangle = \sum_{\alpha=1}^{4} \zeta_\alpha |\mathcal{D}_\alpha\rangle. \tag{L.8}$$

To ensure that the diagonal elements of the matrix ρ_{ss} sum to one, the prefactor ζ_α must be chosen appropriately.

Bibliography

[1] Hendrick BG Casimir. On the attraction between two perfectly conducting plates. *Front. Phys.*, 100:61–63, 1948.

[2] Hendrik BG Casimir and Dirk Polder. The influence of retardation on the london-van der waals forces. *Physical Review*, 73(4):360, 1948.

[3] EM Lifshitz. The theory of molecular attraction forces between solid bodies. *Zhurnal Eksperimentalnoi Teoreticheskoi Fiziki*, 29:94–110, 1955.

[4] Igor E Dzyaloshinskii, Efrat M Lifshitz, and Lev P Pitaevskii. The general theory of van der waals forces. *Advances in Physics*, 10(38):165–209, 1961.

[5] Evgeny Mikhailovich Lifshitz and Lev Petrovich Pitaevskii. Statistical physics part 2, landau and lifshitz course of theoretical physics. *ed: Pergamon Press, Oxford*, 1980.

[6] Marcus J Sparnaay. Measurements of attractive forces between flat plates. *Physica*, 24(6-10):751–764, 1958.

[7] Steven K Lamoreaux. Demonstration of the casimir force in the 0.6 to 6 μ m range. *Physical Review Letters*, 78(1):5, 1997.

[8] Umar Mohideen and Anushree Roy. Precision measurement of the casimir force from 0.1 to 0.9 μ m. *Physical Review Letters*, 81(21):4549, 1998.

[9] PD Nation, JR Johansson, MP Blencowe, and Franco Nori. Stimulating uncertainty: Amplifying the quantum vacuum with superconducting circuits. *Reviews of Modern Physics*, 84(1):1–24, 2012.

[10] Viktor Dodonov. Fifty years of the dynamical casimir effect. *Physics*, 2(1):67–104, 2020.

[11] JB Pendry. Shearing the vacuum-quantum friction. *Journal of Physics: Condensed Matter*, 9(47):10301, 1997.

[12] JB Pendry. Quantum friction–fact or fiction? *New Journal of Physics*, 12(3):033028, 2010.

[13] Diego AR Dalvit, Paulo A Maia Neto, and Francisco Diego Mazzitelli. Fluctuations, dissipation and the dynamical casimir effect. In *Casimir Physics*, pages 419–457. Springer, 2011.

[14] Daniel Reiche, Francesco Intravaia, and Kurt Busch. Wading through the void: Exploring quantum friction and nonequilibrium fluctuations. *APL Photonics*, 7(3), 2022.

[15] Thomas G Philbin and Ulf Leonhardt. No quantum friction between uniformly moving plates. *New Journal of Physics*, 11(3):033035, 2009.

[16] Ulf Leonhardt. Comment on 'quantum friction—fact or fiction?'. *New Journal of Physics*, 12(6):068001, 2010.

[17] F Intravaia, RO Behunin, and Diego AR Dalvit. Quantum friction and fluctuation theorems. *Physical Review A*, 89(5):050101, 2014.

[18] Francesco Intravaia, RO Behunin, Carsten Henkel, Kurt Busch, and Diego Alejandro Roberto Dalvit. Failure of local thermal equilibrium in quantum friction. *Physical review letters*, 117(10):100402, 2016.

[19] Juliane Klatt, M Belén Farías, Diego Alejandro Roberto Dalvit, and SY Buhmann. Quantum friction in arbitrarily directed motion. *Physical Review A*, 95(5):052510, 2017.

[20] F Intravaia, M Oelschläger, D Reiche, Diego Alejandro Roberto Dalvit, and K Busch. Quantum rolling friction. *Physical Review Letters*, 123(12):120401, 2019.

[21] Daniel Reiche, Francesco Intravaia, Jen-Tsung Hsiang, Kurt Busch, and Bei-Lok Hu. Nonequilibrium thermodynamics of quantum friction. *arXiv preprint arXiv:2007.04857*, 2020.

[22] AI Volokitin and BNJ Persson. Quantum friction. *Physical review letters*, 106(9):094502, 2011.

[23] Alexandr Ivanovich Volokitin. Casimir friction force between a sio 2 probe and a graphene-coated sio 2 substrate. *JETP letters*, 104:504–509, 2016.

[24] M Belén Farías, Fernando C Lombardo, Alejandro Soba, Paula I Villar, and Ricardo S Decca. Towards detecting traces of non-contact quantum friction in the corrections of the accumulated geometric phase. *npj Quantum Information*, 6(1):1–7, 2020.

[25] Gabriel Barton. On van der waals friction. ii: Between atom and half-space. *New Journal of Physics*, 12(11):113045, 2010.

[26] M. Belén Farías, César D. Fosco, Fernando C. Lombardo, Francisco D. Mazzitelli, and Adrián E Rubio López. Functional approach to quantum friction: Effective action and dissipative force. *Phys. Rev. D*, 91(10):105020, 2015.

[27] Juliane Klatt, Robert Bennett, and Stefan Yoshi Buhmann. Spectroscopic signatures of quantum friction. *Physical Review A*, 94(6):063803, 2016.

[28] F Intravaia, RO Behunin, and DAR Dalvit. Quantum friction and fluctuation theorems. *Physical Review A*, 89(5):050101, 2014.

[29] M Belén Farías and Fernando C Lombardo. Dissipation and decoherence effects on a moving particle in front of a dielectric plate. *Phys. Rev. D*, 93(6):065035, 2016.

[30] Ludmila Viotti, M. Belén Farías, Paula I. Villar, and Fernando C. Lombardo. Thermal corrections to quantum friction and decoherence: A closed-time-path approach to atom-surface interaction. *Phys. Rev. D*, 99:105005, May 2019.

[31] PW Langhoff, ST Epstein, and M Karplus. Aspects of time-dependent perturbation theory. *Reviews of Modern Physics*, 44(3):602, 1972.

[32] Alberto Galindo and Pedro Pascual. *Quantum mechanics I.* Springer Science & Business Media, 2012.

[33] Daniel Reiche, Diego Alejandro Roberto Dalvit, Kurt Busch, and Francesco Intravaia. Spatial dispersion in atom-surface quantum friction. *Physical Review B*, 95(15):155448, 2017.

[34] LD Landau and EM Lifshitz. *Course of theoretical physics. Vol. 5: Statistical physics.* London, 1958.

[35] Lev Davidovich Landau. *Collected papers of LD Landau.* Pergamon, 1965.

[36] Andrew Lucas and Kin Chung Fong. Hydrodynamics of electrons in graphene. *Journal of Physics: Condensed Matter*, 30(5):053001, 2018.

[37] Philippe Nozieres. *Theory of quantum liquids: Superfluid bose liquids*. CRC Press, 2018.

[38] Sean A Hartnoll, Andrew Lucas, and Subir Sachdev. *Holographic quantum matter*. MIT press, 2018.

[39] G Barton. Some surface effects in the hydrodynamic model of metals. *Reports on Progress in Physics*, 42(6):963, 1979.

[40] D Svintsov. Hydrodynamic-to-ballistic crossover in dirac materials. *Physical Review B*, 97(12):121405, 2018.

[41] Derek YH Ho, Indra Yudhistira, Nilotpal Chakraborty, and Shaffique Adam. Theoretical determination of hydrodynamic window in monolayer and bilayer graphene from scattering rates. *Physical Review B*, 97(12):121404, 2018.

[42] Marco Polini and Andre K. Geim. Viscous electron fluids. *Physics Today*, 73(6):28–34, June 2020.

[43] M Belén Farias, César D Fosco, Fernando C Lombardo, and Francisco D Mazzitelli. Quantum friction between graphene sheets. *Phy. Rev. D*, 95(6):065012, 2017.

[44] M Belén Farias, César D Fosco, Fernando C Lombardo, and Francisco D Mazzitelli. Quantum friction between graphene sheets. *Phys. Rev. D*, 95(6):065012, 2017.

[45] Ettore Majorana. Teoria simmetrica dell'elettrone e del positrone. *Il Nuovo Cimento (1924-1942)*, 14(4):171–184, 1937.

[46] Steven R Elliott and Marcel Franz. Colloquium: Majorana fermions in nuclear, particle, and solid-state physics. *Reviews of Modern Physics*, 87(1):137–163, 2015.

[47] J Schechter and José WF Valle. Majorana neutrinos and magnetic fields. *Physical Review D*, 24(7):1883, 1981.

[48] CWJ Beenakker. Search for Majorana fermions in superconductors. *Annu. Rev. Condens. Matter Phys.*, 4(1):113–136, 2013.

[49] Nicholas Read and Dmitry Green. Paired states of fermions in two dimensions with breaking of parity and time-reversal symmetries and the fractional quantum Hall effect. *Physical Review B*, 61(15):10267, 2000.

[50] Liang Fu and Charles L Kane. Superconducting proximity effect and Majorana fermions at the surface of a topological insulator. *Physical Review Letters*, 100(9):096407, 2008.

[51] Liang Fu and Charles L Kane. Josephson current and noise at a superconductor/quantum-spin-Hall-insulator/superconductor junction. *Physical Review B*, 79(16):161408, 2009.

[52] Sean Hart, Hechen Ren, Timo Wagner, Philipp Leubner, Mathias Mühlbauer, Christoph Brüne, Hartmut Buhmann, Laurens W Molenkamp, and Amir Yacoby. Induced superconductivity in the quantum spin Hall edge. *Nature Physics*, 10(9):638–643, 2014.

[53] Vlad S Pribiag, Arjan JA Beukman, Fanming Qu, Maja C Cassidy, Christophe Charpentier, Werner Wegscheider, and Leo P Kouwenhoven. Edge-mode superconductivity in a two-dimensional topological insulator. *Nature Nanotechnology*, 10(7):593–597, 2015.

[54] Masatoshi Sato and Satoshi Fujimoto. Topological phases of noncentrosymmetric superconductors: Edge states, Majorana fermions, and non-Abelian statistics. *Physical Review B*, 79(9):094504, 2009.

[55] Yuval Oreg, Gil Refael, and Felix Von Oppen. Helical liquids and Majorana bound states in quantum wires. *Physical Review Letters*, 105(17):177002, 2010.

[56] Roman M Lutchyn, Jay D Sau, and S Das Sarma. Majorana fermions and a topological phase transition in semiconductor-superconductor heterostructures. *Physical Review Letters*, 105(7):077001, 2010.

[57] Vincent Mourik, Kun Zuo, Sergey M Frolov, SR Plissard, Erik PAM Bakkers, and Leo P Kouwenhoven. Signatures of Majorana fermions in hybrid superconductor-semiconductor nanowire devices. *Science*, 336(6084):1003–1007, 2012.

[58] Leonid P Rokhinson, Xinyu Liu, and Jacek K Furdyna. The fractional AC Josephson effect in a semiconductor–superconductor nanowire as a signature of Majorana particles. *Nature Physics*, 8(11):795–799, 2012.

[59] Anindya Das, Yuval Ronen, Yonatan Most, Yuval Oreg, Moty Heiblum, and Hadas Shtrikman. Zero-bias peaks and splitting in an Al–InAs nanowire topological superconductor as a signature of Majorana fermions. *Nature Physics*, 8(12):887–895, 2012.

[60] MT Deng, CL Yu, GY Huang, Marcus Larsson, Philippe Caroff, and HQ Xu. Anomalous zero-bias conductance peak in a Nb–InSb nanowire–Nb hybrid device. *Nano Letters*, 12(12):6414–6419, 2012.

[61] HOH Churchill, V Fatemi, Kasper Grove-Rasmussen, MT Deng, Philippe Caroff, HQ Xu, and Charles M Marcus. Superconductor-nanowire devices from tunneling to the multichannel regime: Zero-bias oscillations and magnetoconductance crossover. *Physical Review B*, 87(24):241401, 2013.

[62] ADK Finck, DJ Van Harlingen, PK Mohseni, K Jung, and X Li. Anomalous modulation of a zero-bias peak in a hybrid nanowire-superconductor device. *Physical Review Letters*, 110(12):126406, 2013.

[63] Roman M Lutchyn, Erik PAM Bakkers, Leo P Kouwenhoven, Peter Krogstrup, Charles M Marcus, and Yuval Oreg. Majorana zero modes in superconductor–semiconductor heterostructures. *Nature Reviews Materials*, 3(5):52–68, 2018.

[64] Hao Zhang, Dong E Liu, Michael Wimmer, and Leo P Kouwenhoven. Next steps of quantum transport in Majorana nanowire devices. *Nature communications*, 10(1):5128, 2019.

[65] Elsa Prada, Pablo San-Jose, Michiel WA de Moor, Attila Geresdi, Eduardo JH Lee, Jelena Klinovaja, Daniel Loss, Jesper Nygård, Ramón Aguado, and Leo P Kouwenhoven. From Andreev to Majorana bound states in hybrid superconductor–semiconductor nanowires. *Nature Reviews Physics*, 2(10):575–594, 2020.

[66] Haining Pan and S Das Sarma. Physical mechanisms for zero-bias conductance peaks in Majorana nanowires. *Physical Review Research*, 2(1):013377, 2020.

[67] Morteza Aghaee, Arun Akkala, Zulfi Alam, Rizwan Ali, Alejandro Alcaraz Ramirez, Mariusz Andrzejczuk, Andrey E Antipov, Pavel Aseev, Mikhail Astafev, Bela Bauer, et al. InAs-Al hybrid devices passing the topological gap protocol. *Physical Review B*, 107(24):245423, 2023.

[68] T-P Choy, Jonathan M Edge, Anton R Akhmerov, and Carlo WJ Beenakker. Majorana fermions emerging from magnetic nanoparticles on a superconductor without spin-orbit coupling. *Physical Review B*, 84(19):195442, 2011.

[69] Morten Kjaergaard, Konrad Wölms, and Karsten Flensberg. Majorana fermions in superconducting nanowires without spin-orbit coupling. *Physical Review B*, 85(2):020503, 2012.

[70] Ivar Martin and Alberto F Morpurgo. Majorana fermions in superconducting helical magnets. *Physical Review B*, 85(14):144505, 2012.

[71] Stevan Nadj-Perge, Ilya K Drozdov, B Andrei Bernevig, and Ali Yazdani. Proposal for realizing Majorana fermions in chains of magnetic atoms on a superconductor. *Physical Review B*, 88(2):020407, 2013.

[72] Falko Pientka, Leonid I Glazman, and Felix Von Oppen. Topological superconducting phase in helical Shiba chains. *Physical Review B*, 88(15):155420, 2013.

[73] Jelena Klinovaja, Peter Stano, Ali Yazdani, and Daniel Loss. Topological superconductivity and Majorana fermions in RKKY systems. *Physical Review Letters*, 111(18):186805, 2013.

[74] Bernd Braunecker and Pascal Simon. Interplay between classical magnetic moments and superconductivity in quantum one-dimensional conductors: toward a self-sustained topological Majorana phase. *Physical Review Letters*, 111(14):147202, 2013.

[75] MM Vazifeh and Marcel Franz. Self-organized topological state with Majorana fermions. *Physical Review Letters*, 111(20):206802, 2013.

[76] Stevan Nadj-Perge, Ilya K Drozdov, Jian Li, Hua Chen, Sangjun Jeon, Jungpil Seo, Allan H MacDonald, B Andrei Bernevig, and Ali Yazdani. Observation of Majorana fermions in ferromagnetic atomic chains on a superconductor. *Science*, 346(6209):602–607, 2014.

[77] Younghyun Kim, Meng Cheng, Bela Bauer, Roman M Lutchyn, and S Das Sarma. Helical order in one-dimensional magnetic atom chains and possible emergence of Majorana bound states. *Physical Review B*, 90(6):060401, 2014.

[78] Kim Pöyhönen, Alex Weststrom, Joel Röntynen, and Teemu Ojanen. Majorana states in helical Shiba chains and ladders. *Physical Review B*, 89(11):115109, 2014.

[79] Yang Peng, Falko Pientka, Leonid I Glazman, and Felix Von Oppen. Strong localization of Majorana end states in chains of magnetic adatoms. *Physical Review Letters*, 114(10):106801, 2015.

[80] Michael Ruby, Falko Pientka, Yang Peng, Felix Von Oppen, Benjamin W Heinrich, and Katharina J Franke. End states and subgap structure in proximity-coupled chains of magnetic adatoms. *Physical Review Letters*, 115(19):197204, 2015.

[81] Rémy Pawlak, Marcin Kisiel, Jelena Klinovaja, Tobias Meier, Shigeki Kawai, Thilo Glatzel, Daniel Loss, and Ernst Meyer. Probing atomic structure and Majorana wavefunctions in mono-atomic Fe chains on superconducting Pb surface. *NPJ Quantum Information*, 2(1):1–5, 2016.

[82] Benjamin E Feldman, Mallika T Randeria, Jian Li, Sangjun Jeon, Yonglong Xie, Zhijun Wang, Ilya K Drozdov, B Andrei Bernevig, and Ali Yazdani. High-resolution studies of the Majorana atomic chain platform. *Nature Physics*, 13(3):286–291, 2017.

[83] Sangjun Jeon, Yonglong Xie, Jian Li, Zhijun Wang, B Andrei Bernevig, and Ali Yazdani. Distinguishing a Majorana zero mode using spin-resolved measurements. *Science*, 358(6364):772–776, 2017.

[84] Howon Kim, Alexandra Palacio-Morales, Thore Posske, Levente Rózsa, Krisztián Palotás, László Szunyogh, Michael Thorwart, and Roland Wiesendanger. Toward tailoring Majorana bound states in artificially constructed magnetic atom chains on elemental superconductors. *Science Advances*, 4(5):eaar5251, 2018.

[85] A Cook and M Franz. Majorana fermions in a topological-insulator nanowire proximity-coupled to an s-wave superconductor. *Physical Review B—Condensed Matter and Materials Physics*, 84(20):201105, 2011.

[86] AM Cook, MM Vazifeh, and M Franz. Stability of majorana fermions in proximity-coupled topological insulator nanowires. *Physical Review B—Condensed Matter and Materials Physics*, 86(15):155431, 2012.

[87] Henry F Legg, Daniel Loss, and Jelena Klinovaja. Majorana bound states in topological insulators without a vortex. *Physical Review B*, 104(16):165405, 2021.

[88] Falko Pientka, Anna Keselman, Erez Berg, Amir Yacoby, Ady Stern, and Bertrand I Halperin. Topological superconductivity in a planar Josephson junction. *Physical Review X*, 7(2):021032, 2017.

[89] Michael Hell, Martin Leijnse, and Karsten Flensberg. Two-dimensional platform for networks of majorana bound states. *Physical review letters*, 118(10):107701, 2017.

[90] Antonio Fornieri, Alexander M Whiticar, F Setiawan, Elías Portolés, Asbjørn CC Drachmann, Anna Keselman, Sergei Gronin, Candice Thomas, Tian Wang, Ray Kallaher, et al. Evidence of topological superconductivity in planar Josephson junctions. *Nature*, 569(7754):89–92, 2019.

[91] Hechen Ren, Falko Pientka, Sean Hart, Andrew T Pierce, Michael Kosowsky, Lukas Lunczer, Raimund Schlereth, Benedikt Scharf, Ewelina M Hankiewicz, Laurens W Molenkamp, et al. Topological superconductivity in a phase-controlled josephson junction. *Nature*, 569(7754):93–98, 2019.

[92] Matthieu C Dartiailh, William Mayer, Joseph Yuan, Kaushini S Wickramasinghe, Alex Matos-Abiague, Igor Žutić, and Javad Shabani. Phase signature of topological transition in josephson junctions. *Physical Review Letters*, 126(3):036802, 2021.

[93] Katharina Laubscher and Jelena Klinovaja. Majorana bound states in semiconducting nanostructures. *Journal of Applied Physics*, 130(8), 2021.

[94] A Yu Kitaev. Unpaired Majorana fermions in quantum wires. *Physics-Uspekhi*, 44(10S):131, 2001.

[95] Michael Freedman, Alexei Kitaev, Michael Larsen, and Zhenghan Wang. Topological quantum computation. *Bulletin of the American Mathematical Society*, 40(1):31–38, 2003.

[96] Chetan Nayak, Steven H Simon, Ady Stern, Michael Freedman, and Sankar Das Sarma. Non-Abelian anyons and topological quantum computation. *Reviews of Modern Physics*, 80(3):1083, 2008.

[97] Zhenghan Wang. *Topological quantum computation*. Number 112. American Mathematical Soc., 2010.

[98] David Aasen, Michael Hell, Ryan V Mishmash, Andrew Higginbotham, Jeroen Danon, Martin Leijnse, Thomas S Jespersen, Joshua A Folk, Charles M Marcus, Karsten Flensberg, et al. Milestones toward Majorana-based quantum computing. *Physical Review X*, 6(3):031016, 2016.

[99] Dmitri A Ivanov. Non-Abelian statistics of half-quantum vortices in p-wave superconductors. *Physical Review Letters*, 86(2):268, 2001.

[100] Ady Stern and Netanel H Lindner. Topological quantum computation—from basic concepts to first experiments. *Science*, 339(6124):1179–1184, 2013.

[101] Tudor D Stanescu and Sumanta Tewari. Majorana fermions in semiconductor nanowires: fundamentals, modeling, and experiment. *Journal of Physics: Condensed Matter*, 25(23):233201, 2013.

[102] Jason Alicea, Yuval Oreg, Gil Refael, Felix Von Oppen, and Matthew PA Fisher. Non-Abelian statistics and topological quantum information processing in 1D wire networks. *Nature Physics*, 7(5):412–417, 2011.

[103] Fenner Harper, Aakash Pushp, and Rahul Roy. Majorana braiding in realistic nanowire Y-junctions and tuning forks. *Physical Review Research*, 1(3):033207, 2019.

[104] Paolo Zanardi and Mario Rasetti. Holonomic quantum computation. *Physics Letters A*, 264(2-3):94–99, 1999.

[105] Shogo Tanimura, Mikio Nakahara, and Daisuke Hayashi. Exact solutions of the isoholonomic problem and the optimal control problem in holonomic quantum computation. *Journal of Mathematical Physics*, 46(2):022101, 2005.

[106] Jiang Zhang, Simon J Devitt, JQ You, and Franco Nori. Holonomic surface codes for fault-tolerant quantum computation. *Physical Review A*, 97(2):022335, 2018.

[107] Alessio Calzona, Nicolas Bauer, and Björn Trauzettel. Holonomic implementation of CNOT gate on topological Majorana qubits. *SciPost Physics Core*, 3(2):014, 2020.

[108] B Van Heck, AR Akhmerov, F Hassler, M Burrello, and CWJ Beenakker. Coulomb-assisted braiding of Majorana fermions in a Josephson junction array. *New Journal of Physics*, 14(3):035019, 2012.

[109] MB Plenio and SF Huelga. Entangled light from white noise. *Physical Review Letters*, 88(19):197901, 2002.

[110] Sebastian Diehl, Enrique Rico, Mikhail A Baranov, and Peter Zoller. Topology by dissipation in atomic quantum wires. *Nature Physics*, 7(12):971–977, 2011.

[111] C-E Bardyn, M A Baranov, C V Kraus, E Rico, A İmamoğlu, P Zoller, and S Diehl. Topology by dissipation. *New Journal of Physics*, 15(8):085001, aug 2013.

[112] Dong E Liu. Proposed method for tunneling spectroscopy with Ohmic dissipation using resistive electrodes: a possible Majorana filter. *Physical Review Letters*, 111(20):207003, 2013.

[113] Gu Zhang and Harold U Baranger. Stabilization of a Majorana zero mode through quantum frustration. *Physical Review B*, 102(3):035103, 2020.

[114] Gu Zhang and Christian Spånslätt. Distinguishing between topological and quasi Majorana zero modes with a dissipative resonant level. *Physical Review B*, 102(4):045111, 2020.

[115] Crispin Gardiner and Peter Zoller. *Quantum noise: a handbook of Markovian and non-Markovian quantum stochastic methods with applications to quantum optics*. Springer Science & Business Media, 2004.

[116] Raul A Santos, Fernando Iemini, Alex Kamenev, and Yuval Gefen. A possible route towards dissipation-protected qubits using a multidimensional dark space and its symmetries. *Nature Communications*, 11(1):5899, 2020.

[117] Fernando Iemini, Leonardo Mazza, Davide Rossini, Rosario Fazio, and Sebastian Diehl. Localized Majorana-like modes in a number-conserving setting: An exactly solvable model. *Physical Review Letters*, 115(15):156402, 2015.

[118] Fernando Iemini, Davide Rossini, Rosario Fazio, Sebastian Diehl, and Leonardo Mazza. Dissipative topological superconductors in number-conserving systems. *Physical Review B*, 93(11):115113, 2016.

[119] Goran Lindblad. On the generators of quantum dynamical semigroups. *Communications in Mathematical Physics*, 48:119–130, 1976.

[120] C Lindblad. *Non-equilibrium entropy and irreversibility*, volume 5. Springer Science & Business Media, 2001.

[121] Heinz-Peter Breuer and Francesco Petruccione. *The theory of open quantum systems*. Oxford University Press, USA, 2002.

[122] Ulrich Weiss. *Quantum dissipative systems*. World Scientific, 2012.

[123] Stephan Plugge, Asbjørn Rasmussen, Reinhold Egger, and Karsten Flensberg. Majorana box qubits. *New Journal of Physics*, 19(1):012001, 2017.

[124] Parsa Bonderson, Michael Freedman, and Chetan Nayak. Measurement-only topological quantum computation. *Physical review letters*, 101(1):010501, 2008.

[125] Torsten Karzig, Christina Knapp, Roman M Lutchyn, Parsa Bonderson, Matthew B Hastings, Chetan Nayak, Jason Alicea, Karsten Flensberg, Stephan Plugge, Yuval Oreg, et al. Scalable designs for quasiparticle-poisoning-protected topological quantum computation with Majorana zero modes. *Physical Review B*, 95(23):235305, 2017.

[126] Matthias Gau, Reinhold Egger, Alex Zazunov, and Yuval Gefen. Towards dark space stabilization and manipulation in driven dissipative Majorana platforms. *Phys. Rev. B*, 102:134501, Oct 2020.

[127] Matthias Gau, Reinhold Egger, Alex Zazunov, and Yuval Gefen. Driven dissipative Majorana dark spaces. *Physical Review Letters*, 125(14):147701, 2020.

[128] LA Landau, S Plugge, E Sela, A Altland, SM Albrecht, and R Egger. Towards realistic implementations of a Majorana surface code. *Physical Review Letters*, 116(5):050501, 2016.

[129] S Plugge, LA Landau, E Sela, A Altland, K Flensberg, and R Egger. Roadmap to Majorana surface codes. *Physical Review B*, 94(17):174514, 2016.

[130] Heinz-Peter Breuer and Francesco Petruccione. *The theory of open quantum systems*. Oxford University Press on Demand, 2002.

[131] Angel Rivas and Susana F Huelga. *Open quantum systems*, volume 10. Springer, 2012.

[132] Jason Alicea. New directions in the pursuit of Majorana fermions in solid state systems. *Reports on Progress in Physics*, 75(7):076501, 2012.

[133] R Kubo. Soc. jpn 12, 570 (1957). pc martin and j. schwinger. *Phys. Rev*, 115:1342, 1959.